TECHNICAL REVIEW

No. 73

Eco-consciousness

Safety

Comfort

General Research & Development Center Established in an Effort to Enhance New Product Development Capabilities

In September 2005, **NTN**'s General Research & Development Center was completed in Iwata City, Shizuoka Prefecture, Japan, as the keystone of **NTN**'s R&D network of four R&D bases globally. Having a total floor area of 16,775 m^2, the Center's five-story building possesses a seismically isolated steel structure that incorporates Super Sliding Bearings manufactured by **NTN** Engineering Plastics Corporation. The Center Building also has an engine driven power generator so that **NTN**'s global research and development system will not be affected by the Tokai Earthquake, a strong earthquake that is expected to occur in the near future in this region.

NTN considers the General R&D Center to be the core of **NTN**'s R&D efforts to create new products and technologies for the world. The researchers at the Center work around the clock in cooperation with local engineers and technicians to cope with technical assistance requests from customers around the world. Through this work the Center seeks to accelerate development of new products and ensure swift technical support for customers around the globe. Furthermore, the Center will help **NTN** develop new products in cutting-edge industrial fields, including next generation automobiles, environmental and energy applications, medicines and robotics. In particular, **NTN** has been augmenting the team of engineers that specializes in electronics applications and research in order to develop promising new products.

On the fifth floor of the Center, an exhibition hall displays **NTN**'s newest products and technologies. We hope that visiting customers will fully appreciate **NTN**'s capabilities for proposing and developing novel products and recognizing **NTN** as a valuable engineering partner.

[Features of the General Research & Development Center]

Location: On site at **NTN** Iwata Works (1578 Higashi Kaizuka, Iwata-shi, Shizuoka Prefecture, Japan)

Total floor area: 5 stories, 16,775 m^2

Structure: Seismically resistant building that incorporates elastic Super Sliding Bearings (SSB) manufactured by **NTN** Engineering Plastics Corporation

Equipment: Emergency relief equipment including an engine driven power generator and a well-water utilization system; roof garden; eco air-conditioning system

For New Technology Network

CONTENTS

[Preface]

Introduction to this Special Feature Issue –

NTN's Automotive Products

Kenji OKADA
Managing Director

The Kyoto Protocol, adopted in the 3rd session of the Conference of the Parties to the United Nations Framework Convention on Climate Change (COP3) held in Kyoto in 1997, came into effect in February 2005, and Japan is now facing its obligation to reduce its emissions of greenhouse gases. Recent automotive technologies are increasingly focused on the challenges of environmental issues. As evidenced by the rapid growth in the sales of hybrid cars, the auto industry in Japan and around the world is experiencing dramatic changes in customer preferences. At the 39th Tokyo Motor Show, held from October 21 to November 11, 2005, a variety of novel eco-friendly products and technologies from various car manufacturers around the world were exhibited. As an eco-conscious bearing manufacturer, **NTN** exhibited unique products that will, we believe, offer solutions that meet the needs of our customers.

This special issue, **NTN** Technical Review No. 73 (2005), focuses particularly on three types of concerns that automobiles must satisfy – environmental, comfort, and safety. For this issue, we invited Mr. Iwai Nobuo, Senior Chief Researcher of the Japan Automobile Research Institute FC-EV Center, to provide an overview of new trends in the automotive industry with a focus on environmental-protection technologies for automobiles. This issue also summarizes new eco-friendly products and eco-conscious technologies associated with major **NTN** products, including constant velocity joints, hub unit bearings and needle bearings, as well as unit-built and modular products that incorporate electronics technologies and other unique automotive bearing products.

Our major products, bearings and constant velocity joints, are essentially eco-friendly products that help reduce energy loss and increase energy efficiency. While constantly seeking quality and safety, **NTN** is committed to the development of eco-friendly products that promote greater compactness, lower torque, higher efficiency and longer service life. In developing these new products, we not only consider energy savings during use by our customers, but also aim to reduce environmental impacts during product lifecycles from design, production and sales to use and final disposal. To fulfill these goals, we are making efforts to eliminate the use of substances with harmful environmental impacts in our products, to introduce highly efficient production lines, to rationalize logistics systems and to achieve zero waste emissions.

In September 2005, **NTN** established the General Research & Development Center at our Iwata Works to further enhance our product development capabilities in high technology fields including next generation automobiles, environmental protection, energy, medicine and robotics. In the 21st century, which is being called the century of the environment, **NTN** is following the motto "For New Technology Network" in promoting its new R&D projects and contributing to society.

FOR NEW TECHNOLOGY NETWORK

[Contribution]

Technology on Environmental Protection for The Next Decade

Nobuo IWAI

Senior Chief Researcher FC・EV Center, Japan Automobile Research Institute

Exhaust emission purification on both gasoline engine vehicles and diesel engine vehicles could be solved by 2010 using exhaust catalysts and low sulfur fuels. Global warming gases and energy diversifications for sustainable mobility will be major issues in the next decade. Use of electric power devices will be continued in the major technologies of both hybrid and fuel cell vehicles. Power unit configuration, traction control four-wheel drive using a traction motor could increase not only energy savings, but driving safety as well. Advancement of R&D on secure utilities, such as assembly of the transmission and motor/generator into a single unit is one key technology for environmentally friendly vehicles.

1. Introduction

Think about the typical fuels and energies used in Japan before the industrialization and westernization that took place toward the end of the 19th century. Average Japanese people used candles and rapeseed oil for illumination, wood and charcoal for cooking and heating, and traveled on foot. Cargo carts were driven by people, oxen and horses, while boats and ships were powered by people and wind. In short, renewable energy resources were used in every aspect of everyday lives in Japan. In those days, petroleum and coal were available in very limited areas in small quantities. For nearly three centuries before industrialization and westernization, Japan maintained a unique seclusion policy in which the country conducted trade with only Holland and China. During this period, industrial resources and raw materials were rarely imported into Japan. People continued to live in a closed land of a limited area on renewable resources.

In the average farming village, eldest sons inherited land from their parents. If land had been passed on not only to eldest sons but also to second and third sons, the land would have been split into halves and even thirds and in the generation of grandsons, the

land would have been further split. To avoid this, the established practice was for only the eldest son to inherit the land. A person who violated this tradition and passed his land not only to his eldest son but also to his younger sons was called "tawake", a foolish person who splits up his paddy fields. This wise tradition of our ancestors was intended to preserve limited assets and resources.

If lands and resources are limitless, however, production expansion is possible and the idea of "tawake" does not apply.

In Europe, the Industrial Revolution offered greater power, amounts which had not previously been available from human energy alone. Eventually, mobility developed by use of transportation means, typified by automobiles. This revolution in mobility was triggered by the discovery of an affordable energy source-petroleum. According to statistical data from the Petroleum Association of Japan, global annual production of this resource reached 413 million kiloliters in 2004. This great amount of crude oil is collected from oil fields annually, and a large portion of it is burned, generating gaseous substances, including greenhouse gases and particulate matters that are released into the air. A portion of it is converted into solids in the form of polymers that are recycled and

finally disposed of as refuse or burned and gasified. Though essential for the present-day economy, as the occurrence of pollution shows, the development of petroleum resources also has negative impacts.

Current challenges for automotive environmental protection technologies are gas emissions reduction and global warming prevention, while mid and long-term challenges are expected to be related to the steady acquisition of resources and energies. The very purpose of automobiles is transportation, that is, mobility. Maintaining this mobility is necessary even if the shapes, engines and energy sources of future automobiles differ from those of current cars. For this purpose, we need to address the challenges associated with environmental protection technologies for automobiles.

2. Gas emissions control

Gas emissions control for gasoline-engine cars has been nearly solved as the NOx emission level of low-polluting gasoline-engine cars is now as low as 1.6% of the level of conventional gasoline-engine cars, thanks to highly advanced exhaust gas catalysts. For diesel-engine cars that emit not only gaseous substances including NOx but also particulate matters (PM), emissions will be successfully controlled in the near future through improved combustion and catalyst technologies. The petroleum industry in Japan decided to reduce the sulfur content in diesel oil to 50 ppm or lower by the end of 2004 and 10 ppm or lower

during 2007. According to the new 2005 long-term regulation, the combination of low-sulfur diesel oil and low-pollution diesel engines will help reduce NOx emissions to 12% and PM emissions to 3% compared to conventional diesel-engine cars. Furthermore, according to the 8th Report from the Central Environmental Council of Japan, NOx emissions will be reduced to 5% and PM emissions to 1% by 2009. In other words, virtually all the technological challenges related to automotive gas emissions control will be solved in the first decade of the 21st century. Though these gas emissions control initiatives are limited to the Japanese auto market, Japanese automakers, having grown into multinational companies, must now take responsibility for conservation of the global environment. These Japanese-born environmental protection technologies will contribute to environmental conservation in developing nations where rapid economic growth is taking place. Japanese contributions to international society in the form of military power and financial support are often discussed in Japan. However, I hope that Japan's unique environmental protection technologies will contribute to the prosperity and welfare of the world.

3. Recent energy source situation

As can be understood from the statistical data of the Petroleum Association of Japan illustrated in **Fig. 1**, the price of petroleum, which was cheaper and
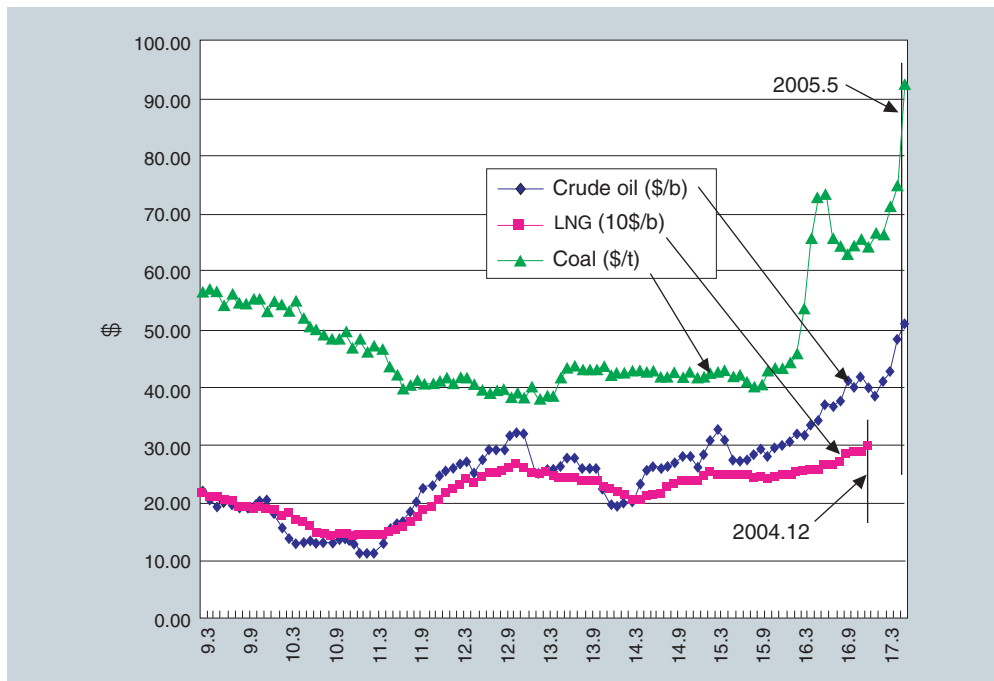

Fig.1 CIF basis import prices of crude oil, LNG and coal
(Graph formation using home page data of Petroleum Association of Japan)

available in a greater amount, has been skyrocketing along with the CIF basis import prices of LNG and coal. We need to remember the old idea of "**tawake**," which is a theory of finiteness, if this situation continues for a prolonged period. So far, according to the statistical data, the CIF based import price of crude oil has been proportional to that of LNG. However, the CIF based import price of crude oil has not been synchronous with that of coal. Recently, however, the change in resource and energy consumption patterns resulting from dramatic economic growth in developing nations including China, has resulted in increased prices for many resources and raw materials. In the 2000-2020 time span, the demand for crude oil in China seems to have nearly doubled due to China's dramatic economic growth. Currently, about 90% of crude oil, the raw material of automotive fuel, comes from the Middle East. Likewise, the major sources of crude oil for the northeast Asian nations of Taiwan, South Korea and China are the countries of the Middle East.

Another uncertain factor about petroleum supply is the special situation in America. Unlike the OPEC basket, the crude oil price OPEC uses as a standard

price, the price of West Texas Intermediate (WTI), a standard US market brand that is produced in Texas, has always been about $5 per barrel higher. Recently, the difference between the two prices has been increasing. For instance, crude oil spot prices as of October 2004 were $37.54 per barrel for the OPEC basket and $53.24 per barrel for WTI, a difference of $15.70 per barrel.

This is because WTI is a superior light crude oil that contains less sulfur content, and because the facilities that produce light oil from heavy oil lack capacity. As a result, the supply capacity for light oils, including gasoline, kerosene and diesel oil, is insufficient compared to their demand.

According to the estimated amounts of crude oil deposits and mining years summarized in **Fig. 2**, the total number of mining years left worldwide is 49 and 69.3% of proven reserves are in the OPEC nations.

What we should remain aware of is that the mining years for the USA, China, and Norway and the UK combined, oil producing nations that also consume large amounts of petroleum, are 11, 14 and 7 years, respectively≳surprisingly small reserves. These mining years have been obtained by simply dividing the
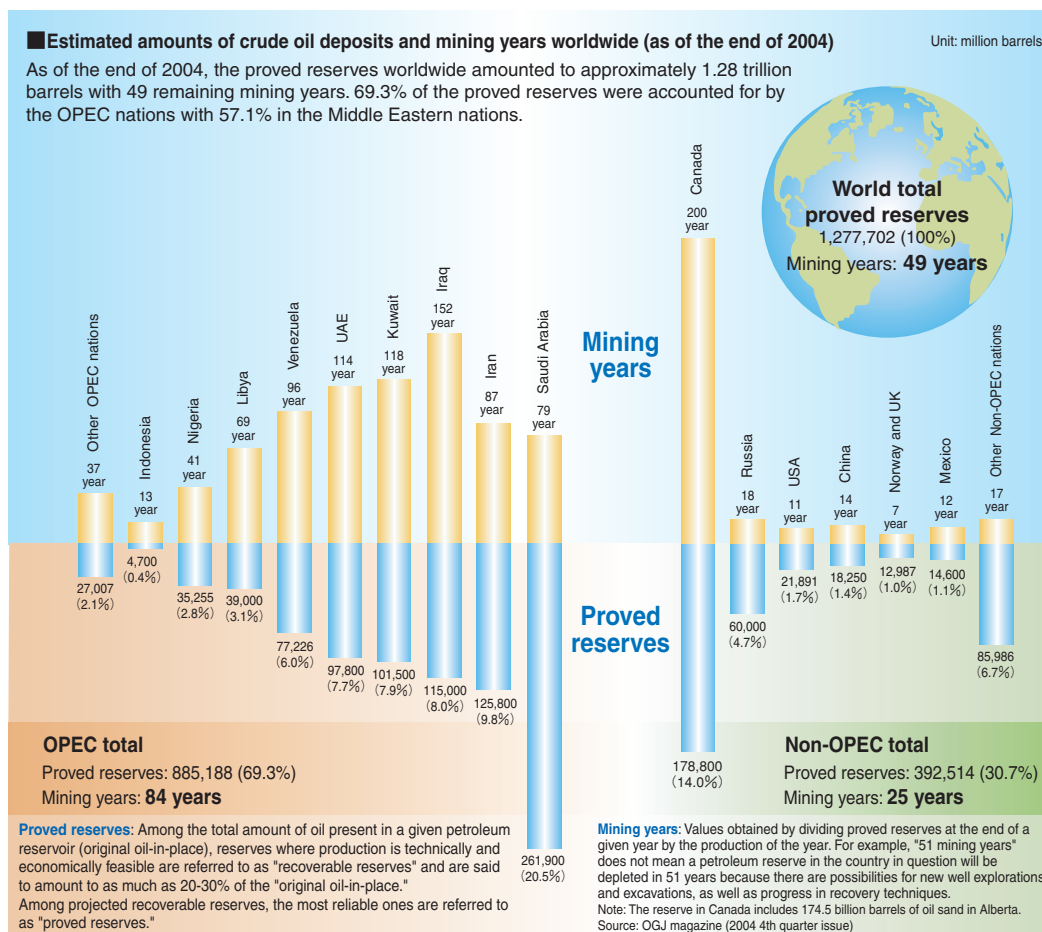

Fig.2 The estimated amount of crude oil deposits and mining years in the world
(Home page of Petroleum Association of Japan)

proven reserves by the amounts produced in a given year. The petroleum supply profile is often said to have a bell-curve shape. When the peak of the bell-curve is reached and the supply and demand equilibrium breaks, petroleum prices will skyrocket and petroleum supply will become unstable.

4. Emission control for greenhouse gases and energy conservation measures for automobiles

Emission of greenhouse gases released from any country in the world, whether or not the country has ratified the Kyoto Protocol, can affect not only neighboring countries but also the global environment. Currently, only people in a handful of nations, a minority among the living beings on the earth, are enjoying high energy consumption and the benefits of mobility, and also emitting greenhouse gases in the process. Though we tend to think that human economic activities only jeopardize the living environments of people, we should be aware that such activities also damage the whole of nature.

So that we can continue utilizing convenient automobiles to maintain mobility while minimizing greenhouse gas emissions, we must run engines with low fuel consumption and use sustainable energy sources to achieve our travel and transportation purposes. The very task of engineers who specialize in automobiles is to realize highly efficient engines that operate on fuels and energies obtained from resources with stable supplies in order to achieve this objective. More specifically, we must realize the costs and systems that are acceptable to society and bring

them into common use in order to contribute to energy conservation and reduction of greenhouse gas emissions.

If we can reduce energy consumption for production and use (traveling) by 50%, greenhouse gas emissions from automobiles will also be reduced by 50% and the mining years for crude oil will be doubled. The information in **Fig. 3**, released by the Japanese Ministry of Land, Infrastructure and Transport, summarizes the fuel consumption of gasoline passenger cars by vehicle weight. As is apparent from this diagram, lighter cars (downsizing) and hybrid cars boost lower fuel consumption.

(1) Downsizing

Usually, users prefer heavy, expensive, large luxury cars. If most hours of car use are for commuting, cars often carry only one passenger. For example, imagine a car that weighs 1.5 tons or more traveling with only one passenger, leaving four or more seats vacant. Suppose that user purchases a less expensive lightweight car weighing 1 ton or less, dramatic reductions in both fuel costs and consumption are achieved simply. For the Academy Awards ceremony in Hollywood, movie stars arrive in hybrid cars instead of full-sized luxury cars. This is now regarded as a symbol of status among movie stars. We have analyzed the preferences of car users (tendencies may vary depending on age group or sex) and learned that certain users are satisfied with smaller cars, or, in certain cases, even motorcycles. For this reason, the author believes that we have many possibilities for investigation, research and development into technologies that help realize downsizing.
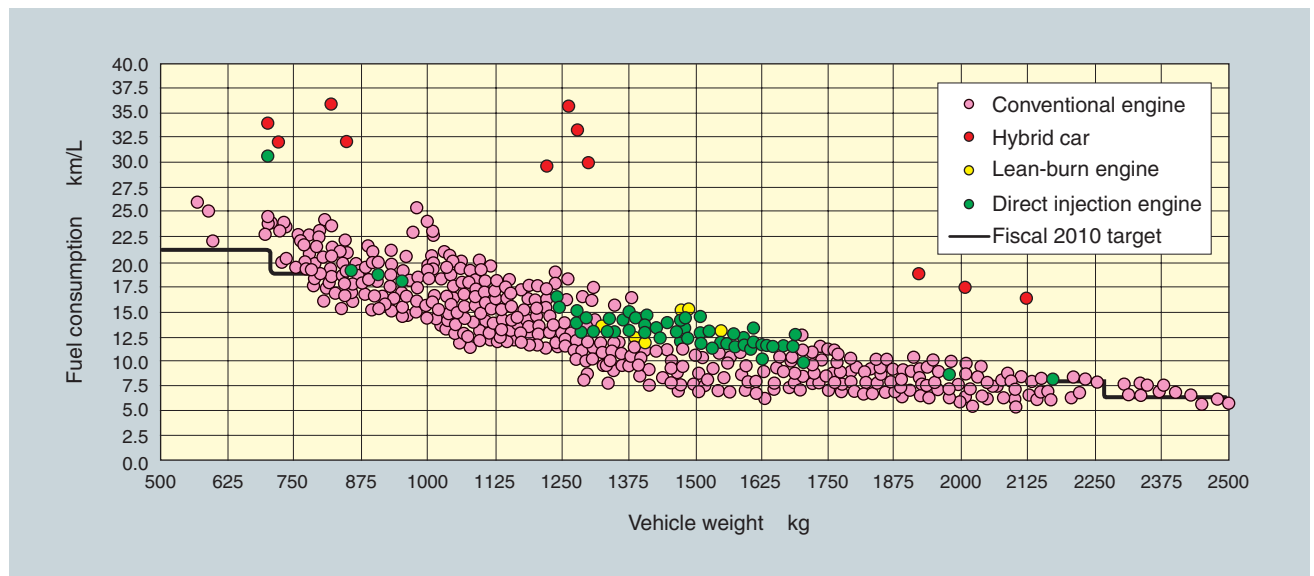

Fig.3 Fuel consumption on gasoline passenger cars
(Home page of Ministry of Land, Infrastructure and Transport)

(2) Hybrid cars

Stationary engines for driving power generators, etc. can be used as cogeneration systems that offer exhaust heat and cooling heat for hot water supply. As a result, such stationary engines boast a total thermal efficiency of approximately 80%. In contrast, the maximum net thermal efficiency of automotive engines is usually in the range of 35 to 45% since the waste heat of these engines cannot be used for hot water supply. However, in city running modes, typically in the 10-15 mode, the thermal efficiency drops to approximately 15 to 17% since partial loads, including idling with a thermal efficiency of 0%, are often used and accumulated motion energy is dissipated as thermal energy during braking.

The improved efficiency of hybrid cars is the result of the following. (1) During deceleration, a regenerative brake uses the accumulated motion energy to drive the power generator without dissipating that energy as thermal energy. This electricity is accumulated and reused for acceleration of the car. (2) The engine stops while the car is not running. (3) In low load operations when thermal efficiency is low, the car runs on electricity that was previously generated and stored during medium and high load operations when the engine was running at higher thermal efficiency. If the net thermal efficiency reaches approximately 30% by these measures, fuel efficiency is doubled.

The description above is the basic concept of hybrid cars. To realize this concept, systems that store energy and convert it into motive power are necessary. Examples of previous R&D efforts for energy storage include those for compressed gas and flywheels. Currently, efforts are centered on electricity storage systems including nickel hydrogen batteries, lithium ion batteries and ultracapacitors. From the utility viewpoint, the mountability of storage systems is important. One of the advantages of hybrid cars over electric cars is that the size and weight of batteries mounted in them are less than those in electric cars. This situation may change if energy storage systems that are more efficient and useful than electricity storage systems are successfully developed. However, electricity storage systems will maintain their prevalence for the near future.

One of the challenges associated with alleviating automobile environmental impacts is reducing greenhouse gas emissions. In regions where a larger portion of power generation is accounted for by nuclear and hydraulic power stations, which have lower CO_2 emissions, electric cars are more eco-friendly than hybrid cars. However, the drawback of electric cars is that the distance they can travel on one charge is limited, a problem that prevents them from being used more widely. In Europe, to overcome this drawback, a "plug-in hybrid" system is being considered. These plug-in hybrid cars would function as externally charged electric cars in urban areas and as internal combustion cars in suburban areas. In certain situation, they would also operate in hybrid mode.

There is also the possibility that a novel type of hybrid car that features a new concept for reducing greenhouse gas emissions could be developed.

Having two prime movers, that is, an engine and a motor, hybrid cars can use the driving force of both when a larger output is needed, such as when accelerating or climbing a slope. As a result, engines that are more compact and powerful can be designed to meet fuel efficiency performance requirements. For example, the Honda Civic gasoline passenger car has an engine capacity of 1688 cc and maximum torque of 155 N-m, whereas the Honda Civic Hybrid features an engine capacity of 1339 cc, maximum engine torque of 119 N-m and maximum system torque of 146 N-m. In other words, the Honda hybrid boasts a maximum system torque equivalent to that of the conventional Civic. In the case of the Toyota Lexus RX300 and Highlander models, the hybrid system consists of the 3310 cc engine with a maximum output of 155 kW and front and rear motors that boost the maximum system output to as much as 200 kW. Though being SUVs, these cars feature both the low fuel consumption associated with popularly priced compact cars and the higher power of sports cars.

The Toyota Lexus RX300, the Highlander and the Estima Hybrid employ electrically driven 4WD systems. The front wheels are driven by the engine and the front motor, while the rear wheels are powered by the rear motor in response to the current running state. In the normal state, these cars are driven by their front wheels. However, during starting, acceleration with full throttle, deceleration and braking, and when slipping is detected on a snow-covered or slippery road surface, the rear wheels also initiate driving power and the cars switch to 4WD mode. These cars are good examples of how low fuel-consumption power train technology can be fully utilized to ensure safe driving.

5. In pursuit of sustainable fuel energies

Another solution to these social needs of energy conservation and greenhouse gas emissions reduction that also uses sustainable fuel energies is the hydrogen fuel cell vehicle (FCV).

In January 2002, the US Department of Energy (DOE) announced the FreedomCAR (Cooperative Automotive Research) program, which is centered on the engineering development of hydrogen fuel cells, as the program to succeed the Partnership for a New Generation of Vehicles (PNGV). In February 2003, President Bush announced the Hydrogen Fuel Initiative that supports the fuel aspect of the FreedomCAR program, and accordingly, a demonstration program has been in progress that covers hydrogen production, storage and transport as well as FCVs. The numerical engineering targets of the DOE are a durability of 2000 hours for the stack, a range of 250 miles or farther, a hydrogen supply cost of $3 per kilogram, and the capability to travel in any US weather conditions, including low temperatures and high temperatures with both low and high humidity, by the end of 2009. The goals for the end of 2015 are a stack durability of 5000 hours, a 300-mile or greater range, a hydrogen supply cost of $1.5 per kilogram, and a fuel cell cost of $30 per kilowatt power unit. In 2015, the DOE will make a decision on whether or not to commercialize the FCV, based on the achievements of these engineering challenges.

Automakers and energy supply companies are making joint efforts in fleet tests in various nations. Examples of such efforts include the California Fuel Cell Partnership (CaFCP) in the USA, the Clean Urban Transport for Europe (CUTE) FC bus demonstration program, and the Ecological City Transport System (ECTOS) in Europe, and the Japan Hydrogen & Fuel Cell Demonstration Project (JHFC).

The FCV commercialization scenario of the Japanese Ministry of Economy, Trade and Industry defines that the period up to the end of 2005 was for preparation of engineering fundamentals, demonstration of engineering aspects, establishing the engineering development strategy, providing legal frameworks, performing demonstration tests and developing fuel quality standards. In the introductory phase from 2005 - 2010, the fuel supply system will be established, 50,000 FCV units will be introduced to public organizations and enterprises, and the second-stage FC technology development strategy will be developed. In the 2010 - 2020 full commercialization phase, the fuel supply system will be further enhanced and 5,000,000 FCV units will be sold to ordinary users

in order to decrease the price of FCVs. To fulfill these targets, government agencies and private corporations are jointly continuing research and development activities.

As has been demonstrated in the JHFC project and elsewhere in Japan, FCVs already have performance sufficient for running in urban streets. Freezing of water at cold temperatures is reported to have been solved by decreasing thermal capacity with a metal separator and improving the warming capability by using reaction heat. The operating temperature of the stack is approximately 80°C. This means smaller differences with the outside temperature in the hot summer climate, so efficient cooling performance needs to be provided. If a solid polymer membrane capable of withstanding higher temperatures is developed, the stack will be able to function normally at higher operating temperatures, which should make greater efficiency, improved performance and cooling solutions easier to attain. The most demanding challenge for full commercialization of FCVs is achieving a two-digit reduction in price. To realize this dramatic price reduction, we need to return to the very basics for research into stack components, such as solid polymer membranes, catalysts and separators where dramatic breakthroughs are expected. Another challenge remaining to be solved is increasing the range on one charge of hydrogen. There have been research efforts and deregulation attempts to increase the permissible fill pressure of hydrogen containers from 35 MPa to 70 MPa or greater. However, even if a hydrogen container were charged to 70 MPa, the range of one hydrogen charge would still be insufficient. A breakthrough is also expected with hydrogen storage technology. For example, high-pressure methane hydride stored in high-pressure containers appears to be promising.

For some years, the possible methods for producing hydrogen will be onsite production at hydrogen supply stations and offsite production and shipment from petrochemical complexes. These will require the modification of petroleum fuels and gases, with coke gas as a byproduct and the electrolysis of water. In the future, solar heat, a renewable energy, will be used for steam reforming coal and natural gas to produce hydrogen without releasing CO_2. Japan has virtually no useable renewable energy sources, including solar energy. In the future, nations and regions situated in the sunbelt where abundant solar energy is available, such as the USA, Australia, the Middle East and Africa, which are also blessed with coal and natural gas, could become hydrogen supply sources. Methanol and dimethyl ether seem promising as carriers for the maritime transportation of hydrogen.

If this transportation scheme is commercialized, reformed fuel cells using these carriers as automotive fuels may be reconsidered.

6. Conclusion

During the next 10 years, hybrid cars will be more commonly used and fuel cell cars will be increasingly introduced. **Fig. 4** summarizes the comparison of the 10-15 mode fuel consumption of gasoline vehicles (catalog data), hybrid vehicles (catalog data), and hydrogen fuel cell vehicles (actual measurements obtained from the JHFC project converted to gasoline equivalents). In each vehicle group, the vehicle weights have been adjusted to a common value and the average 10-15 mode fuel consumption values and top runner values are indicated. Since there is variation in the data of actual cars, comparing the average fuel consumption values and the top runner values (best values available with the present-day technologies) of all the groups will be useful in order to evaluate the

fuel efficiency improvements in each group.

As this chart shows, in terms of both the average and top runner fuel efficiency values, the hybrid vehicles are better than the gasoline vehicles, and the hydrogen fuel cell vehicles are superior to the hybrid vehicles. Note, however, that this data only shows the degree of efficiency in the particular period ranging from the fuel tank to the travel of cars (tank to wheel). In terms of greenhouse gas emissions, the efficiency of the whole life of oil, ranging from drilling to fuel production and transportation and then operation of cars (well to wheel) needs to be considered. The author believes that data on ever-diversifying fuel production techniques will be thoroughly reviewed and automotive engines will be optimized for the fuel types used.

In a certain sense, fuel cell vehicles are series hybrid vehicles whose engines and generators are replaced with fuel cells. Many components, including secondary batteries and motors, are commonly used in both fuel cell vehicles and hybrid vehicles. If higher
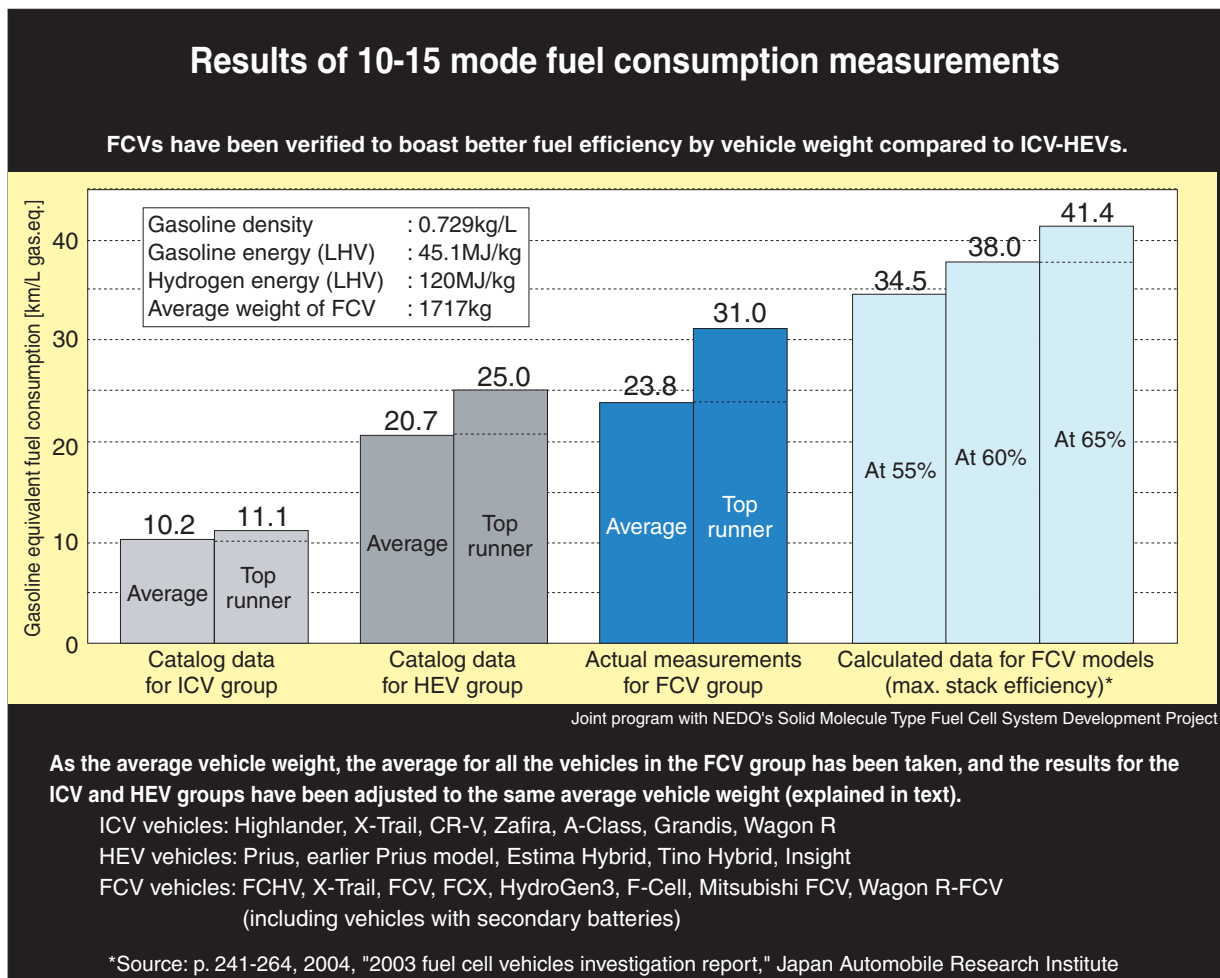
Results of 10-15 mode fuel consumption measurements

FCVs have been verified to boast better fuel efficiency by vehicle weight compared to ICV-HEVs.

Gasoline density : 0.729kg/L
Gasoline energy (LHV) : 45.1MJ/kg
Hydrogen energy (LHV) : 120MJ/kg
Average weight of FCV : 1717kg

Gasoline equivalent fuel consumption [km/L gas.eq.]

- Catalog data for ICV group: Average 10.2, Top runner 11.1
- Catalog data for HEV group: Average 20.7, Top runner 25.0
- Actual measurements for FCV group: Average 23.8, Top runner 31.0
- Calculated data for FCV models (max. stack efficiency)*: At 55% 34.5, At 60% 38.0, At 65% 41.4

Joint program with NEDO's Solid Molecule Type Fuel Cell System Development Project

As the average vehicle weight, the average for all the vehicles in the FCV group has been taken, and the results for the ICV and HEV groups have been adjusted to the same average vehicle weight (explained in text).

ICV vehicles: Highlander, X-Trail, CR-V, Zafira, A-Class, Grandis, Wagon R
HEV vehicles: Prius, earlier Prius model, Estima Hybrid, Tino Hybrid, Insight
FCV vehicles: FCHV, X-Trail, FCV, FCX, HydroGen3, F-Cell, Mitsubishi FCV, Wagon R-FCV
(including vehicles with secondary batteries)

*Source: p. 241-264, 2004, "2003 fuel cell vehicles investigation report," Japan Automobile Research Institute

Fig.4 Japanese 10-15 mode fuel consumption on gasoline, hybrid and fuel cell vehicles (Home page of JHFC)

energy density in energy storage media including batteries and capacitors is achieved, for example, or other higher functionality is realized, the number of batteries mounted on cars can be decreased, allowing lighter-weight vehicle design.

Furthermore, cost reduction, through improvement in manufacturing techniques for batteries and other components, is key to realizing greater use of fuel cell vehicles.

One of the technologies that helped create hybrid vehicles is a unique packaging technology in which previously independent power units, including an engine, motors, and a transmission are built into single lightweight assembly that is readily mounted on a car. The Toyota Hybrid System (THS) in which the electric CVT is configured using planetary gearing is a good example of overcoming various engineering challenges.

Currently, an increasing number of models of hybrid cars are being introduced into the car market. Some analysts predict that more than one million hybrid cars will be produced annually. This technical field naturally involves bearing technology, which is a strongpoint of **NTN** Corporation. The component technology for hybrid cars will be increasingly used for motive power in electric 4WD vehicles, electrically driven wheelchairs and construction machinery. **NTN**'s unique component technologies, including constant velocity joints, are vital technologies for power transmission systems on machines including automobiles. The efforts of the **NTN** staff to improve their technologies to realize more compact, lightweight, low-loss products support environmental protection technologies and are reflected in both conventional and hybrid cars. Examples of such efforts include their E series high-efficiency constant velocity joints, PTJ low-vibration constant velocity joints and mechanical clutch units (MCU).

[Technical Article]

The Reduction of Hazardous Substances

Kiyoshi NAKANISHI*
Masakazu HIRATA**

The **NTN** Group has continued to achieve environmental harmony according to its Environmental Policy by alleviating environmental impacts arising from its business activities, products and services.

This paper introduces the present and future goals of **NTN**'s efforts to reduce of hazardous materials in **NTN** products. These items would include rolling bearings and constant velocity joints, as well as many other **NTN** products.

1. Introduction

Believing that coexistence with the global environment is our most important challenge, **NTN** undertakes eco-conscious management aimed at the reduction of environmental impacts and the realization of a recycling-oriented society. With these goals, **NTN** is striving to reduce CO_2 emissions, the prevention of air, water and soil pollution, the reduction of wastes, and the promotion of green procurement.

This report describes current and future **NTN** efforts to reduce hazardous substances in its products.

2. Trend in elimination of the use of specific hazardous substances

In 2001, electronic equipment built in Europe contained high amounts of cadmium, a hazardous substance exceeding regulated level standards. This triggered increased consciousness about green procurement.

Consequently, EU issued a series of directives that control or ban the use of hazardous substances in these and other products. These include the ELV (End of Life Vehicle) directive that totally bans the heavy metals lead, mercury, cadmium and hexavalent chromium in cars. The RoHS (Restriction of the use of certain Hazardous Substances in electrical and electronics equipment) directive also imposes a total ban on six hazardous substances, including the heavy metals above and fire retardants for plastics (PBB's and PBDE's), in electrical and electronics equipment, beginning in July, 2006.

In addition, some manufacturers have already started various self-imposed efforts to ban certain organic substances that could harm humans.

---

*Environmental Management Dept.
**Research & Development Center　Technical Research Dept.

3. Elimination of controlled substances

3.1 Hexavalent chromium: total ban of use in shields and seal cores

Previously, hexavalent chromium had often been used in **NTN** product components, including shields and rubber seal cores on bearings.

To prevent outward leakage of grease and inward ingress of foreign matter, a shield and a core metal rubber seal are installed on the side faces of sealed rolling bearings. Conventionally, the metal used in shields and cores has been galvanized sheet steel and the surfaces of the pieces have been chromate-treated with a material containing hexavalent chromium.

In 2002, **NTN** introduced a safe tin-plated sheet steel for shield use with anti-rusting qualities. Two safe materials for seal core metal to ensure good adhesion with rubber were also introduced - galvanized sheet steel with a special electrolytic treatment layer and galvanized sheet steel with a phosphate film.

Photo 1 shows examples of tin-plated sheet steel and conventional chromate-treated (hexavalent chromium) galvanized sheet steel after undergoing a salt spray test. The tin-plated sheet steel samples exhibit higher anti-rusting performance compared to the conventional material.

3.2 Lead: total ban of lead-based extreme pressure agents in grease

Lead naphthenate, lead dithiophosphate and lead dithiocarbamate are excellent extreme pressure agents that have long been used as additives in high-load greases.

Constant velocity joints, one of our major products, are used in high surface pressure and rolling-sliding conditions. Therefore, greases containing lead-based extreme pressure additives have often been used on them to prevent wear and achieve low friction. In cooperation with a grease manufacturer, we have developed alternative greases to address this environmental challenge[1], and started to offer alternative lead-free greases to our customers in 2002.

Our newly developed greases have unique combinations of additives that enhance bearing performance and contain organic molybdenum, molybdenum bisulfide and similar substances instead of lead-based extreme pressure additives.

	(Conventional) Galvanization + chromating	(Improved) Tin plating
24 hours later		
Rust occurrence	5/5 parts	0/5 parts
48 hours later		
Rust occurrence	5/5 parts	5/5 parts

<Salt spray test: in accordance with JIS Z 2371> Sample shield plate: 6203 Z, w/ external rust-preventive oil
Test conditions: 5% salt water, spray rate 1-2 ml/h
Test duration: 24 h and 48 h

Photo 1. Shield appearance after (neutral) salt spray test

Performance data for greases developed for the slidable joint TJ series are summarized in **Fig. 1** and **Table 1**. The results for the 3rd order component of induced cyclic axial load that serves as an index for NVH (Noise, Vibration, Harshness) performance affecting automobile riding comfort, as well as for durability, are better than those of a conventional grease that contains a lead-based extreme pressure additive.

In addition, the bearings used in low-speed, high-load conditions, such as for steel-making and construction machinery, had employed lithium-mineral oil based greases containing lead-based extreme pressure additives. We have already replaced these conventional greases with lead-free greases that we developed in cooperation with a grease manufacturer.
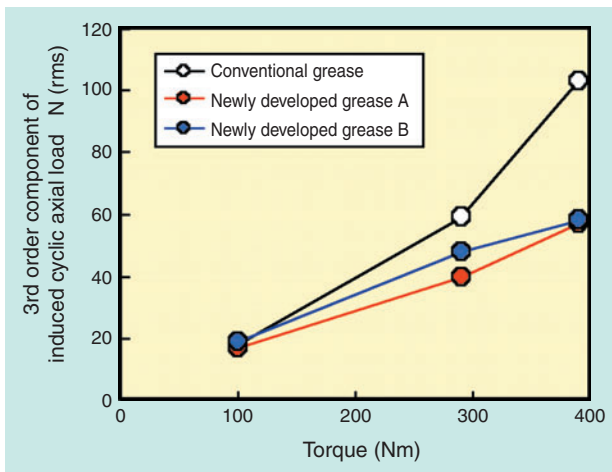
Fig.1 The 3rd order component of induced cyclic axial load of TJ

Table 1 Light load durability of TJ

Type of grease	T.P	Running time h		
		90	125	300
Newly developed grease A	No.1	○	○	○
	No.2	○	○	○
Newly developed grease B	No.1	○	○	○
	No.2	○	○	○
Conventional grease	No.1	△	△	✕
	No.2	△	△	△

Target hours
(○: No problem △: Minor problem ✕: Severe problem)

3.3 Cadmium: ban of use in resin colorant

A yellow or red cadmium-based pigment has been used often as a colorant for resins. NTN previously used a cadmium-based pigment in certain resin sliding material BEAREE products and in the band resin for expansion-compensating bearings. The cadmium-based pigment for the former application was replaced with an alternative material by 1993, and for the latter application in 2002.

4. Efforts to eliminate possible toxic substances

4.1 Sodium nitrite: ban of use in greases

Sodium nitrite has been used often as a rust-preventive agent because of its excellent performance in this role. It also has high performance as an antiseptic and it is a food additive approved by the US Food and Drug Administration (FDA). However, it can generate nitrosamine, a carcinogenic substance, in the presence of a secondary amine (**Fig. 2**).

During the late 1970's, **NTN** totally banned the use of sodium nitrite-containing coolant as a water-soluble grinding coolant because grinding machine operators frequently come into direct contact with such coolants.

Sodium nitrite-containing greases have remained in use because operators directly touch them less frequently, they boast good performance as rust-preventive agents and oxidation inhibitors, and there have been no reliable alternative greases. Recently, however, attempts are being made to regulate this type of grease, especially in Europe. To cope with this trend, we have already switched most outsourced greases to alternative safe greases.

In the 1980's, peeling phenomenon accompanied by the occurrence of a white structure occasionally appeared on bearings for automotive electrical equipment. This appears to result from hydrogen brittleness caused by the ingress of hydrogen to the bearings due to the decomposition of the base oils in greases.
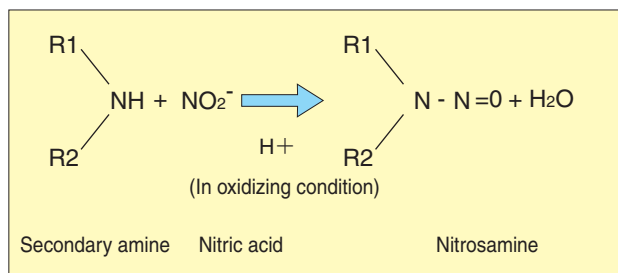

Fig.2 Reaction of secondary amine and nitrite

Table 2 Composition and properties of sodium nitrite free grease

	Conventional grease	**Newly developed grease**
Base oil	Ether + PAO	Ether
Base oil viscosity mm^2/s	72	100
Thickener	Diurea	Diurea
Consistency	300	300
Life h (at 150°C)	2100	3800
Resistance against brittleness-induced peeling h	＞300（n=5）	＞300（n=11）
Rust-preventive performance (rust occurrence %)	1	1

We have verified that sodium nitrite helps create a passive condition on steel material surfaces, preventing the ingress of hydrogen. Therefore, sodium nitrite additive is highly effective in preventing this type of peeling phenomenon. **NTN** had previously developed and been using a high-temperature grease that contained sodium nitrite additives for use in electrical accessories. To cope with the trend toward regulation of sodium nitrite, we have developed a new unique grease. This grease, whose composition and performance are summarized in **Table 2**, features brittleness-induced peeling resistance and rust prevention qualities comparable to those of the previous grease, with the advantage of longer high-temperature life.

4.2 Phthalates: ban of use in boots and rubber seals for constant velocity joints

Phthalates are often used as plasticizers for plastics and rubbers. In 2003, certain phthalates were added to the EU list of regulated substances (EU directive 2003/36/EC) as CMR substances (Substances classified as Carcinogens, Mutagens or substances toxic to Reproduction). More specifically, sales of dibutyl phthalate (DBP) and diethyl hexyl phthalate (DEHP) and preparations containing these substances were banned in the EU region from the end of 2004.*

Certain **NTN** bearing seals and constant velocity joint boots contain phthalates as plasticizers. We are replacing these with phthalate-free components in cooperation with associated component manufacturers with the goal of eliminating phthalates by the end of 2007.

>   *Sales of products containing these substances to general consumers are permitted.

4.3 Water-soluble barium compounds

Water-soluble barium compounds are listed as Class 1 designated chemical substances in the Pollutant Release and Transfer Register (PRTR) Law.

There is no move toward their regulation in Japan, but in Europe and the USA, attempts are being made to regulate them.

Rust-preventative oils and greases often contain water-insoluble barium sulfonate. Insoluble in water, this substance is not yet regulated by the PRTR Law. However, some researchers suspect that water-insoluble barium sulfonate can generate water-soluble salts. Therefore, we are going to introduce rust-preventive oils and newly developed greases that do not contain barium sulfonate.

5. Conclusion

As stated at the beginning of this report, **NTN** makes coexistence with in the global environment a top priority and implements eco-conscious management aimed at reducing environmental impacts and realizing a recycling-oriented society. In this report, the authors have introduced **NTN**'s proactive efforts to reduce the use of regulated substances.

Though not described in this report, **NTN** wishes to contribute to reducing global environmental impacts and is fully committed to developing eco-friendly products that boast smaller sizes, lower torques, higher efficiency and longer life. Bearings are essentially eco-products that decrease friction and reduce energy loss. **NTN** will remain dedicated to the development of environmentally friendly products and reduction of substances with environmental impacts - two areas that are crucial to our eco-conscious management activities.

References
1) Shinichi Takabe: **NTN** Technical Review, 68 (2000), 44

Photos of authors

Kiyoshi NAKANISHI
Environmental
Management Dept.

Masakazu HIRATA
Technical Research Dept.
Research & Development Center

[**Technical Article**]

Application of Topology Optimization and Shape Optimization for Development of Hub-Bearing Lightening

Haruo NAGATANI*
Tsuyoshi NIWA*

From the perspective of global environmental protection and conservation of resources, the development of lighter automobile parts for fuel cost savings is a worldwide initiative. In this abstract, we seek the ultra-lightweight Hub-Bearing, and succeed in its development. In the development of this product, two optimization methods are used: First is a topology optimization; the second is shape optimization. We introduce the process of the development by explaining the two optimization methods shown above.

1. Introduction

The enactment of the US CAFE (Corporate Average Fuel Economy) regulations in 1975 triggered increased demand for lightweight designs for every automotive component. Lighter components lead to better automobile fuel efficiency, which in turn contributes to energy conservation and global environmental preservation. In manufacturing industries, various efforts to achieve lightweight designs are in progress and bearing manufacturers are committed to decreasing the weights of hub bearings.[1] [2]

NTN has also been working to lighten various products. By applying shape optimization techniques to the development of lightweight 3rd generation hub bearings, we have succeeded in dramatic weight reductions. This report describes our optimization techniques as well as examples of lightening effects.

2. Development goal

The hub bearing being developed is for low weight cars and its target mass is 1.0 kg, which would make it the lightest in the world. In the initial stage of development, a prototype hub bearing weighing 1.3 kg failed a durability test, while one weighing 1.4 kg, illustrated in **Fig. 1**, succeeded in achieving functional targets including for mechanical strength. This result marked the starting point of our analysis for optimal bearing shape.
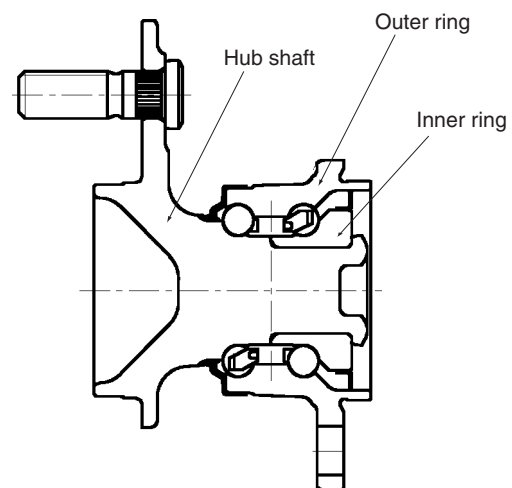
Fig.1 Hub-Bearing original design

*Automotive Sales Headquarters   Automotive Engineering Dept.

3. Overview of shape optimization

The basic concept of shape optimization design is to place material in areas that truly need it and thin out unnecessary material from areas that are not important for correct function in order to obtain the minimum shape that satisfies all the necessary functional requirements, such as mechanical strength and rigidity. Spurred by the lightening needs mentioned above, recently the demand for the ability to determine optimal shapes easily has been mounting. However, currently available software packages are not powerful enough to fulfill this demand.

The currently available analysis techniques can be roughly categorized into (1) topology optimization and (2) shape optimization (these techniques will be described in detail later). For topology optimization, an optimal structure for carrying an external load is determined, while for shape optimization, the areas to be altered and the ranges for possible dimensions are set in advance and optimal values are determined accordingly.

Since each type of technique has advantages and disadvantages, we should utilize the strengths of both to attain our goals. In our development project, topology optimization was executed first to develop a rough shape (basic shape), and then adjustments were made as necessary to achieve optimal dimensions that do not greatly differ from those of that basic shape. The reasons for this two-step scheme are as follows.

Necessity of two-step analysis scheme

(1) Topology optimization analysis is essentially linear analysis,* and does not offer sufficiently accurate results for a boundary nonlinear problem such as stress analysis for hub bearings where contacts between a flange and a brake rotor or between an inner ring and a hub ring are treated. For this reason, high-precision nonlinear analysis is necessary to verify the results obtained from topology optimization.

(2) Optimal shapes obtained from topology optimization are complicated 3D forms that may not be obtainable by machining at reasonable costs or may not be obtainable at all. Therefore, a process to develop a machining-ready shape based on the results of topology optimization is necessary. This new basic shape is again subjected to shape optimization to realize the final optimal shape.

*Certain software packages are now capable of analysis using gap elements. However, even with these packages, setup for an object with a complicated shape is time-consuming, and areas with complicated profiles must be set as unalterable. As a result, these packages are insufficient in terms of analytical accuracy.

4. Topology optimization (1st step)

In the topology optimization step, an optimal structure to achieve the functions necessary for the part in question is obtained. In some cases, dramatic changes in the structure are possible. We used a homogenization method [3] as a topology optimization technique.

Analysis model

The analysis model we used is illustrated in **Fig. 2**. The hub ring was integrated with the inner ring, mesh was plotted and the 3 translational degrees of freedom for the bolthole nodes on the flange were constrained. For the external load working on the hub ring, load concentration was assumed to occur on the rolling
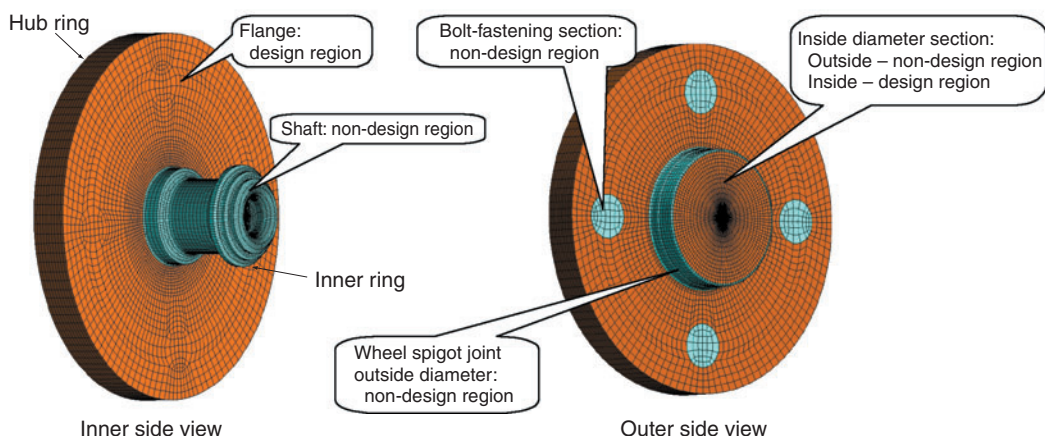
Fig.2 Topology optimization model

surface and a rolling element load value obtained from a bearing internal force analysis program was utilized.

As shown in **Fig. 2**, regions where the shape can be altered (design regions) were set larger, and regions where the shape cannot be changed (such as the wheel spigot joint outside diameter and bearing outside diameter) due to interactions with counterpart members were defined as unalterable regions (non-design regions).

Furthermore, analysis was executed considering the forging draft, cyclic symmetry conditions of boltholes and symmetricalness relative to the straight lines connecting the boltholes and the flange center. The object function and restricting conditions were as follows.

Objective function: Distortion energy minimization
Restricting conditions: 22.5%, 27.5% and 30% relative to the volume (or mass) of initial shape

The analysis was performed with two hub bolt patterns - 0° (cross-pattern) and 45° (X-pattern) relative to the vertical direction. Since the stress was greater in the 0° direction, further analysis was limited to this direction.

Analysis results

The shapes and principal stresses shown in **Figs. 3** and **4** were attained. As shown in **Fig. 4**, with greater weight reduction, stress rapidly increased. We adopted a shape that was 27.5% the initial volume and near the stress limit as the basis for the basic structure of the hub bearing.
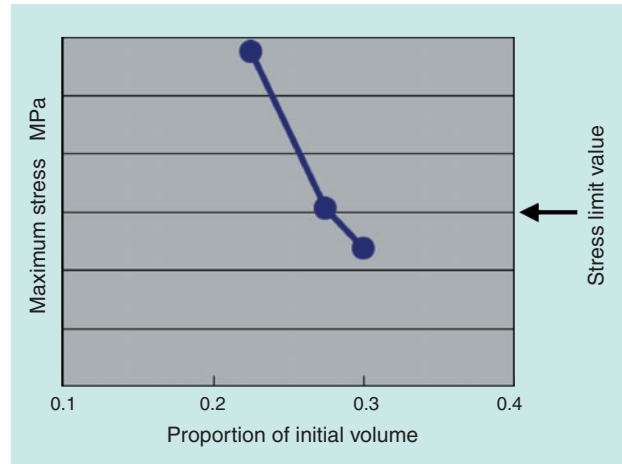
Fig.4 Principal stress of each design
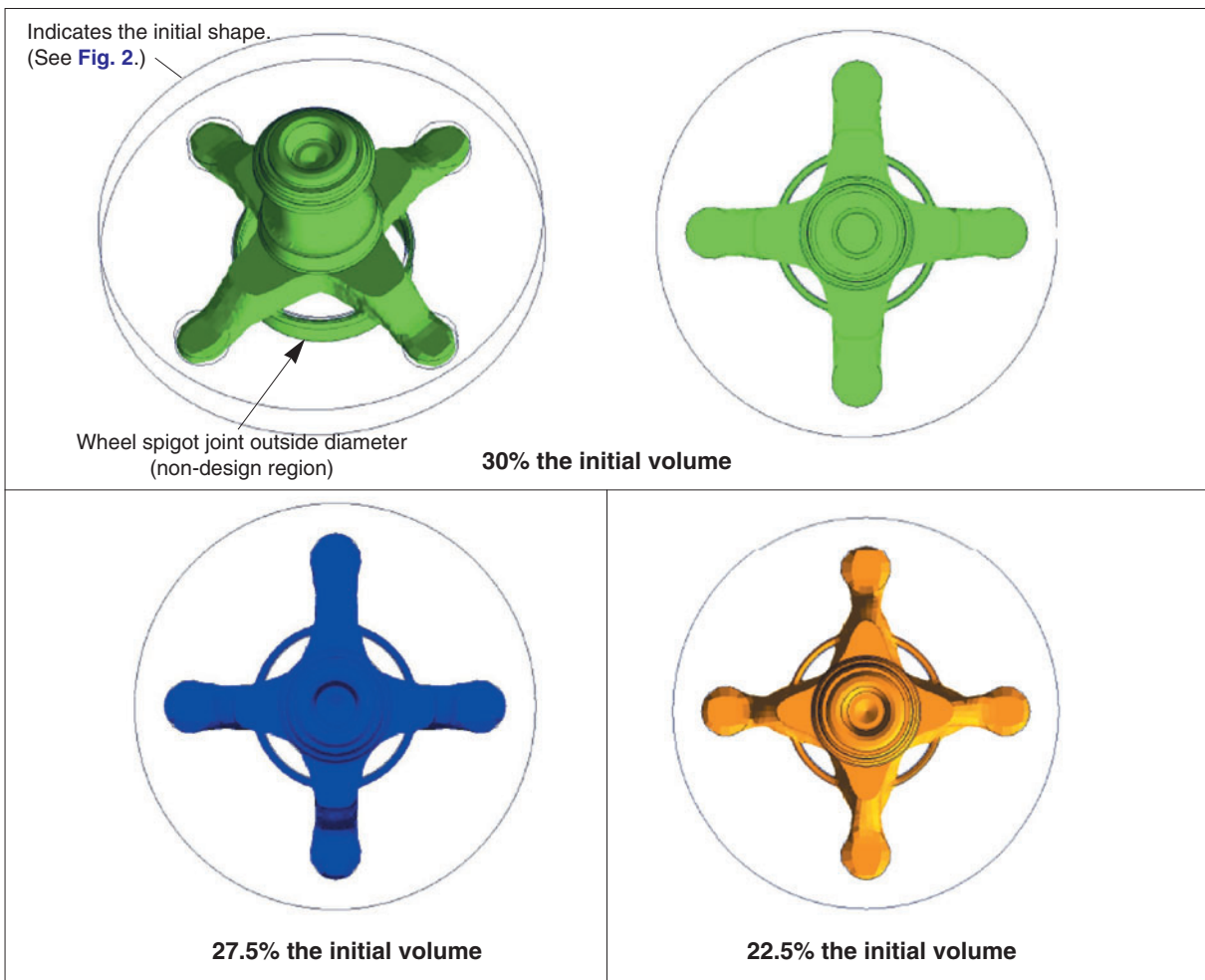
Fig.3 Result of topology optimization

-16-

5. Shape Optimization (2nd Step)

Analysis model

Using the shape obtained from the previously described topology analysis as a basis, the basic shape was set as in **Fig. 5** and shape optimization analysis was executed by varying the dimensions at the seven locations (h, b, y_1, x_2, y_2, x_3, y_3) shown in **Fig. 6**. The fully automatic analysis system summarized in **Fig. 7** was developed and the analysis was executed based on the L_{27} experiment plan method.

> **Objective function: Volume (mass) minimization**
> **Restricting conditions: Principle stress at three designated nodes (yellow dots in Fig. 6) below the current level**

The software of the shape optimization analysis system drives the nonlinear analysis solver to calculate stress values while altering the shape according to the mesh data.

In altering the shape, the shape base vectors* were set using the morphing software so that alteration of the mesh could be synchronized with alteration of the shape in order to maintain the cyclic symmetry of the bolt holes as well as the symmetricalness relative to the straight lines connecting the bolt holes and the flange center.

The calculation was executed on a 2.8 GHz Pentium 4 computer and took 2.5 days to complete.

From this result, a response curved surface approximation model was developed to achieve an optimal solution.

*Vectors that defines how each node shifts when the nodes used as parameters are shifted.
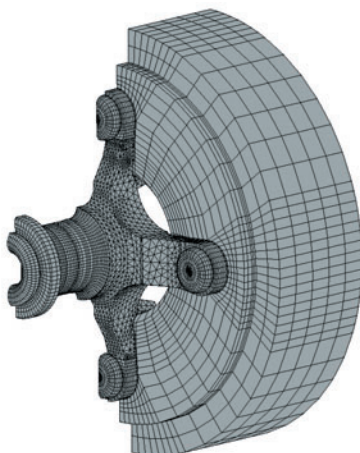
Fig. 5 Basic design of shape optimization
(As installed to the flange of test rig)
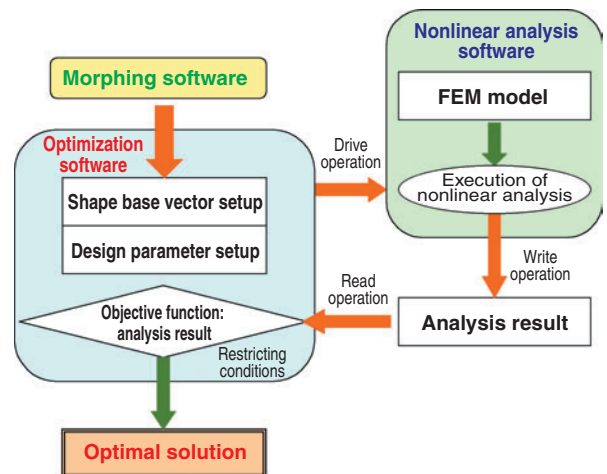
Fig. 7 Shape optimization systems
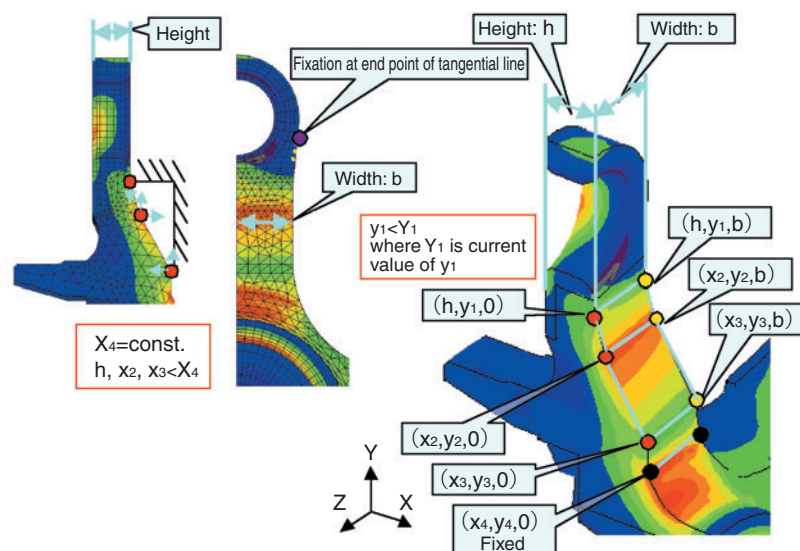
Fig. 6 Parameter of DOE

(a) Volume
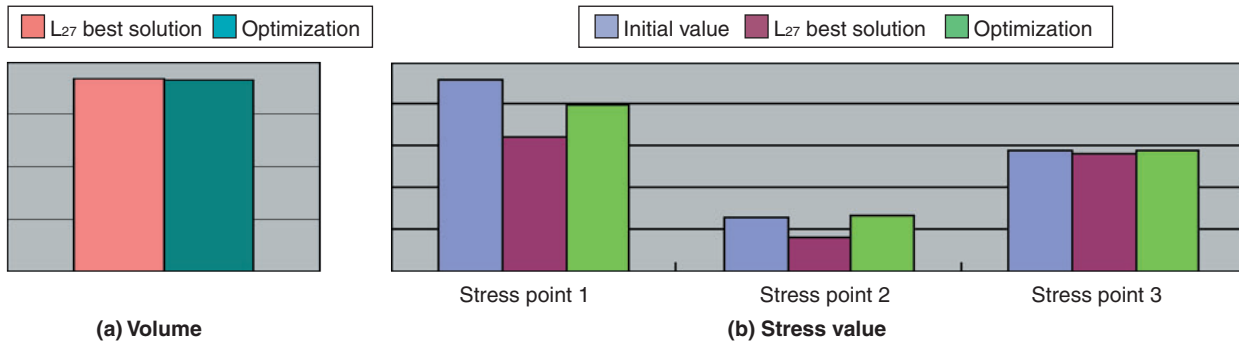
(b) Stress value

Fig. 8 Result of shape optimization

Analysis results

In **Fig. 8**, (a) summarizes volumes, while (b) shows stress values. "L_{27} best solution" represents the combination that performed most effectively in the calculations performed according to the experimental method while "Optimization" represents the optimal solution obtained by calculation in accordance with the response curved surface approximation. As a result of this series of calculation operations, many of the optimal values obtained coincided with the upper or lower limits (limits in terms of avoidance of interaction with counterpart parts). Consequently, as can be understood from **Fig. 8(a)**, there was no apparent difference between the L_{27} best solution and the optimal values obtained from the response curved surface. We cannot deny the possibility of obtaining better optimal values, but we believe that we have successfully determined values very near the ideal optimal values.

Fig. 8(b) summarizes stress values associated with varying shapes. At every evaluation point, the stress value is lower than the current level.

From these findings, we determined the shape of our final design.

6. Final Design

In the development work, we also applied the analysis technique described above to the outer ring. In addition to shape optimization, we attempted to achieve lightening in the finalized bearing specification through alteration of bearing internal design and development of new materials and grease. The newly developed hub bearing shape, which is illustrated in **Fig. 9,** has

achieved the target mass of 1.0 kg and cleared the target values for strength, durability and rigidity. In addition, the hub ring and outer ring have also achieved lightening targets as illustrated in **Fig. 10.**
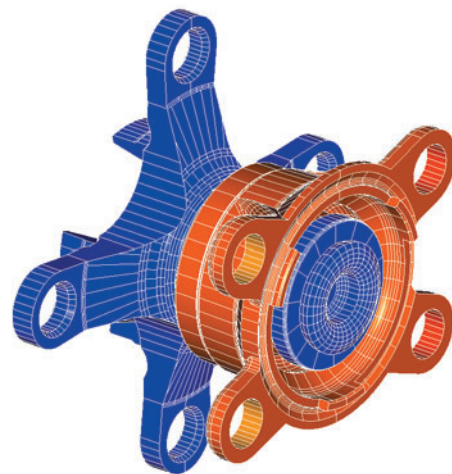
Fig. 9 Shape of final design

Outer ring

−100g

Hub ring

−240g
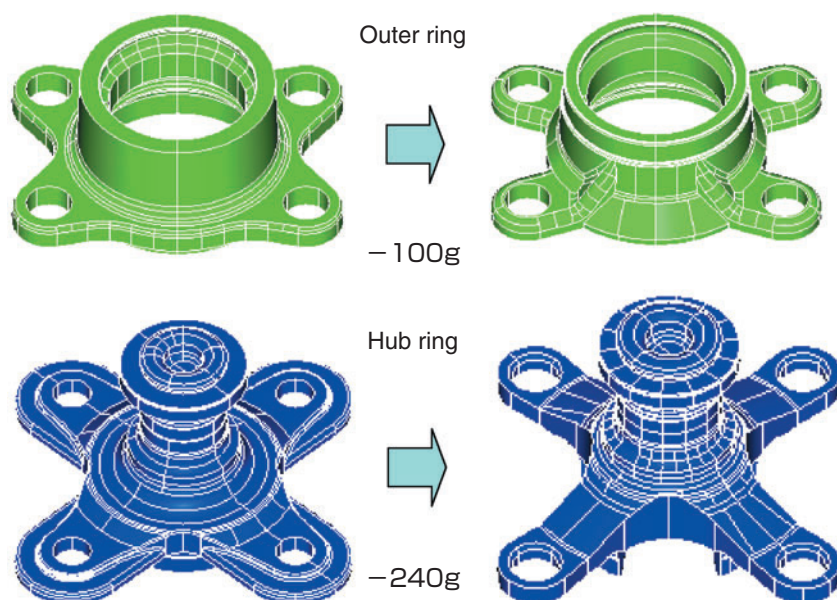
Fig. 10 Amount of each component Lightening

7. Conclusion

This report has introduced the shape optimization analysis executed for lightening hub bearings for reduced weight cars. With this technique, we have succeeded in achieving a target mass of 1.0 kg, attaining dramatic lightening that was previously considered impossible. Note, however, that this newly developed hub bearing is not suitable for drum brake structures in which the hub bearing also functions as a brake seal.* For such applications, another hub bearing type developed through use of our shape optimization technique should be used (at a penalty of additional 50 g weight).

Our analysis in this report was centered on mechanical strength. However, we also need to set targets for hub bearing rigidity. Therefore, we will aim for multi-faceted optimization in which we attempt to promote further lightening while maintaining sufficient bearing rigidity so that we can establish hub bearing technology to cope with the needs of various car manufacturers.

*As shown in **Fig. 9**, the newly developed hub bearing has four pawls that radially guide the members installed to the hub ring. If the hub bearing is applied to a drum brake, the pawls need to be replaced with a circumferential rim to provide sealing function.

References

1) J. Sakamoto, "Hub unit bearing market and technology trends," Monthly Tribology, October 2004

2) K. Kajihara, "Improved hub unit analysis simulation techniques," Koyo Engineering Journal No. 167 (2005)

Photos of authors

Haruo NAGATANI

Automotive Sales Headquarters
Automotive Engineering Dept.

Tsuyoshi NIWA

Automotive Sales Headquarters
Automotive Engineering Dept.

Dynamic Analysis of a High-Load Capacity Tapered Roller Bearing

Kazuyoshi HARADA*
Tomoya SAKAGUCHI*

It is necessary to predict forces acting on a cage when designing rolling element bearings. It requires a dynamic simulation that can evaluate interaction forces between the bearing components including the cage as well as real-time behaviors of these components.

NTN had already developed a 2-dimensional dynamic analysis code for cylindrical roller bearings using a commercial, versatile dynamic analysis software. At this time, **NTN** has developed a 3-dimensional analysis code for tapered roller bearings by extending its dynamic analysis technology.

Additionally, **NTN** has proposed a tapered roller bearing that accommodates more rollers with a larger outside diameter cage to increase its load carrying capacity. The cage geometry change may affect the interactions between the cage and rollers, and the experimental verification of these interactions is generally beyond accurate measurement. Accordingly, the developed code is implemented to investigate the difference between the conventional tapered roller bearings and the newly proposed one in terms of the interaction forces between the cage and rollers and the resulting cage behavior. This report outlines the physical model of this analysis tool, and shows the analytical results where any significant difference is not found from the above viewpoint. Developers have confirmed that the newly designed high-load capacity tapered roller bearing is quite effective for use.

1. Introduction

When designing a cage for a roller bearing, advanced clarification of the forces acting on the cage is necessary. To analyze the forces acting on the cage, determining the dynamic behavior of the rolling elements and the cage itself as well as the resultant forces occurring between the bearing components is necessary. In short, dynamic analysis is needed.

NTN had previously developed a dynamic analysis tool for cylindrical roller bearings limited to two-dimensional freedom by using the general-purpose mechanism analysis software ADAMS(R).[1) 2) 3)] By enhancing this dynamic analysis technique, we have recently developed a three-dimensional dynamic analysis tool for tapered roller bearings.[4)]

NTN has developed a high-load capacity tapered roller bearing with greater load bearing capacity that consists of a cage with a larger outside diameter and an increased number of rollers. The unique geometric shape of this high-load capacity type cage can affect the interaction between the rollers and the cage, but verification of this problem through experiments is difficult. Therefore, we investigated the differences in the cage behavior and the interaction between the rollers and the cage by comparing this new type and standard tapered roller bearings using our newly developed 3D dynamic analysis tool. As a result, we learned that the new type does not greatly affect the cage behavior or the interaction between the rollers and the cage.

This report summarizes the 3D dynamic analysis tool and describes the results of our analysis.

---

*New Product Development R&D Center   Mechatronics Research Dept.

2. Symbols

b : Half the Hertz contact length, m
D : Cage outside diameter
D_{iso} : Deborah Number $= \eta_0 e^{\alpha \bar{P}} \bar{u}/(Gb)$
G : Dimensionless material parameter $= \alpha_0 E'$
E' : Equivalent Young's modulus, Pa
F_a : Axial load, N
F_{EHLr} : EHL rolling viscous drag, N
F_{px} : Rolling direction component in EHL oil film pressure, N
F_r : Radial load, N
f_c : Cage running frequency, Hz
f_T : Friction force at contact area, N
h_c : Oil film thickness at center, m
k : $= 1.03\, \alpha_r^{2/\pi}$
k' : Thermal conductivity of lubricant, W/(mk)
L_t : Thermal load coefficient $= \eta_0 \beta \bar{u}^2/k'$
l : Width of roller slice, m
N_{sl} : Number of roller slices
$\bar{P}$: Mean surface pressure on Hertzian contact, Pa
P_{max} : Maximum surface pressure on Hertzian contact, Pa
q : Contact force on sliced piece, N
R_e : Equivalent radius of curvature, m
s : Slip ratio
$\bar{S}$: Mean dimensionless shear stress on the whole contact area
U : Dimensionless representative velocity $= \eta_0 \bar{u}/(E'R_e)$
$\bar{u}$: Mean surface velocity, m/s
u_s : Sliding velocity on contact area
W : Dimensionless load parameter
X_c : Dimensionless length on EHL contact area $= (D_{iso}/\Sigma_{iso})\sinh^{-1}\Sigma_{iso}$
x_c^* : Dimensionless x-direction displacement at cage mass center $= x/\delta_{Pr}$
y_c^* : Dimensionless y-direction displacement at cage mass center $= y/\delta_{Pr}$
z_c^* : Dimensionless z-direction displacement at cage mass center $= z/\delta_{Pa}$
α : Pressure coefficient of viscosity, 1/Pa
α_0 : Pressure viscosity index of lubricant under normal pressure, 1/Pa
α_r : Ratio of curvature radius vertically intersecting the rolling direction to curvature radius in rolling direction
α_p : Pocket angle
β : Temperature increase dependent coefficient of viscosity, 1/K
δ : Geometric interference amount, m
η_0 : Viscosity under normal temperature and pressure, $Pa \cdot s$
ψ : $[1+2/(3\,\alpha_r)]$

Λ : Film thickness parameter $= h_c/\sigma_e$
Λ_{bd} : Upper limit film thickness parameter under boundary lubrication
Λ_{hd} : Lower limit film thickness parameter under hydrodynamic lubrication
μ_{bd} : Friction coefficient under boundary lubrication
μ_{hd} : Traction coefficient with oil film
μ_r : Friction coefficient on contact area
Σ_{iso} : Dimensionless sheer velocity with isothermal lubricant
σ_e : Equivalent roughness of contact areas between two objects, m
δ_{Pa} : Cage axial clearance
δ_{Pr} : Cage pocket radial clearance
τ_0 : Lubricant characteristic stress, Pa
ϕ_T : Temperature compensation coefficient of oil film

Subscript characters

b : Roller(s)
IR : Equivalent viscosity-solid body mode
i : Inner ring
PE : High viscosity-elastic body mode
o : Outer ring

Boldfaced characters represent vectors.

3. Analysis method

The conditions assumed for our analysis are summarized below.

- The rollers and cage are provided with six degrees of freedom.
- The inner ring is subjected unconditionally to translational displacement equivalent to rotation at specific velocities and preset loads (zero degree of freedom).
- The outer ring is fixed in space.
- All the apparent forces, such as centrifugal force, are included.
- Gravity is considered.
- Each component is regarded as a rigid body, but local elastic contact between elements is taken into account.
- Interaction force distribution on the roller rolling contact surface is evaluated with the slice method.
- For the friction force between the rollers and the raceway, the friction component resulting from the oil film and the metal contact is considered. Also, in the elastohydrodynamic lubrication (EHL) condition, the rolling viscous resistance[5] is considered (**Fig. 1**).
- The squeeze effect of the EHL film (speed-dependent term) is not considered.
- All the interaction force between the roller large end face and the inner ring large rib face is assumed to
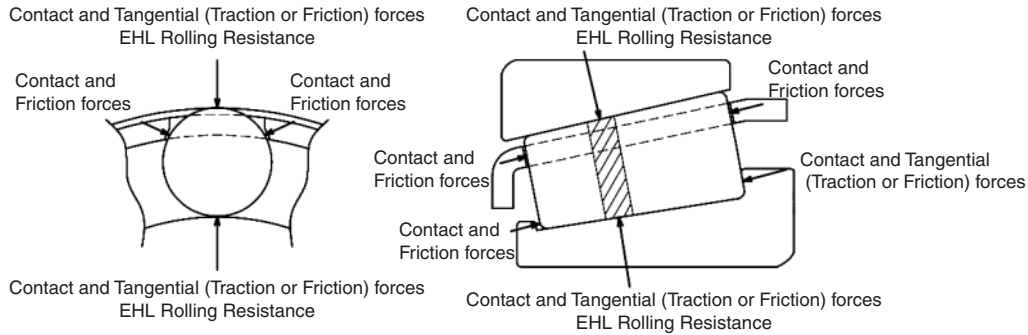
Fig. 1 Considered interaction forces in this dynamic analysis

be applied to the maximum neighboring point. The friction coefficient is handled in the same manner as that of the raceway surface. However, because of the sliding contact, the EHL rolling viscous resistance is not considered (**Fig. 1**).

● For the friction force between the rollers and the cage, boundary lubrication alone is assumed (**Fig. 1**). In the case of contact with the roller end face, all the contact force and friction force of the maximum interaction point is applied.

3.1 Dynamic interaction forces between the roller contact surface and the raceway surface

The dynamic interaction force model for the interaction between the roller contact surface and the raceway surface is based on the following assumptions.

1) Only when an elastic deformation amount (geometric interaction amount δ) occurs against the relative position of the rollers and the bearing ring that is governed by the time t, a contact-induced normal force, friction force and rolling viscous resistance occur between the roller rolling contact surface and the raceway surface.

2) The slice method is applied to the roller rolling contact surface, thereby the distribution of the interaction force is considered. If the interaction vector δ on each slice is given, then Palmgren's simple formula is employed and the expression (1) is used to determine the contact force vector $\mathbf{q}$ for each slice.

$$\mathbf{q}=0.356 E' N_{sl}^{-1/9} l^{8/9} \delta^{10/9} \frac{\delta}{|\delta|} \quad \cdots\cdots\cdots\cdots (1)$$

3) The friction coefficient is calculated for each lubrication mode in the manner shown by expression (2), based on the film thickness parameter.[3] The friction force vector $\mathbf{f}_T$ acting on each roller slice is determined with expression (3) using the roller-dependent sliding velocity vector $\mathbf{u}_s$.

$$\mu_r = \begin{cases} \mu_{bd} & \text{if } \Lambda < \Lambda_{bd} \\ \left\{ \dfrac{\mu_{bd} - \mu_{hd}}{(\Lambda_{bd} - \Lambda_{hd})^6}(\Lambda - \Lambda_{hd})^6 + \mu_{hd} \right\} & \text{if } \Lambda_{bd} \leqq \Lambda < \Lambda_{hd} \\ \mu_{hd} & \text{if } \Lambda_{hd} \leqq \Lambda \end{cases}$$

$$\cdots\cdots\cdots\cdots\cdots\cdots\cdots\cdots\cdots\cdots (2)$$

$$\mathbf{f}_t = \mu_r \mathbf{q} \cdot \frac{\mathbf{u}_s}{|\mathbf{u}_s|} \quad \cdots\cdots\cdots\cdots\cdots\cdots (3)$$

For this purpose, $\Lambda_{bd}=0.01$ and $\Lambda_{hd}=1.5$ were used. The above-mentioned film thickness parameter is essentially the center oil film thickness. The center oil film thickness was determined by assuming that the contact area was in the hydrodynamic lubrication mode (either the high viscosity-elastic body mode (PE mode) or the equivalent viscosity-rigid body mode (IR mode), as necessary) as described in expression (4). For the PE mode, Pan's formula (5)[6] was used while for the IR mode, Martin's formula (6)[7] was used.

Furthermore, considering the inlet temperature, the temperature compensation coefficient ϕ_T[8] defined by expression (8) was used. Usually, the IR mode is necessary when the rollers are in contact with the outer ring in the non-load region. Additionally, through comparison of the oil film thicknesses of the two fluid lubrication modes, the relevant mode was determined, and this mode was used to judge whether the EHL rolling viscous resistance, described later, was necessary.

$$h_c = \begin{cases} \phi_T \cdot h_{c,PE} & \text{if } h_{c,PE} > h_{c,IR} \\ \phi_T \cdot h_{c,IR} & \text{otherwise} \end{cases} \quad \cdots\cdots (4)$$

$$h_{c,PE} = 2.922 \, W^{-0.166} U^{0.692} G^{0.47} R_e \quad \cdots\cdots (5)$$

$$h_{c,IR} = 4.9 \, UW^{-1} R_e \quad \cdots\cdots\cdots\cdots (6)$$

Provided that,

$$R_e^{-1}=\begin{cases}\dfrac{1}{R_b}+\dfrac{1}{R_i} & \text{for Roller / Inner race}\\[2mm]\dfrac{1}{R_b}-\dfrac{1}{R_o} & \text{for Roller / Outer race}\end{cases}\cdots(7)$$

$$\phi_T=\left[\frac{1-13.2(P_{\max}/E')L_T^{0.42}}{1+0.213(1+2.23s^{0.83})L_T^{0.64}}\right]\cdots\cdots(8)$$

For the friction coefficient μ_{bd} under the boundary lubrication condition ($\Lambda<\Lambda_{bd}$) shown by the expression (2), the function[9] of Kragelskii's solid contact friction coefficient was modified and used as shown in **Fig. 2**. The modification was such that the variable was changed from a sliding velocity to a sliding parameter and the friction coefficient was set to 0 when sliding was also 0.

$$\mu_{bd}=(-0.1+22.28s)\exp(-181.46s)+0.1\cdots(9)$$

The friction coefficient μ_{hd} for the fluid lubrication condition ($\Lambda<\Lambda_{hd}$) was calculated with Muraki's simple theoretical formula[10] given below. To reduce the amount of numerical calculations, the temperature was assumed to be constant. In addition, it was assumed that this traction model could also be effective even in the IR mode.

$$X_c\geqq2:\bar{S}=\Sigma_{iso}/D_{iso}\quad\cdots\cdots\cdots\cdots\cdots(10)$$

$$X_c<2:\bar{S}=\sinh^{-1}\Sigma_{iso}\{1-(D_{iso}/4\Sigma_{iso})\sinh^{-1}\Sigma_{iso}\}$$
$$\cdots\cdots\cdots\cdots\cdots(11)$$

$$\mu_{hd}=\tau_0\bar{S}/\bar{P}\quad\cdots\cdots\cdots\cdots\cdots\cdots\cdots(12)$$

Here, the dimensionless length of the elastic area is represented as $X_c=(D_{iso}/\Sigma_{iso})\sinh^{-1}\Sigma_{iso}$.
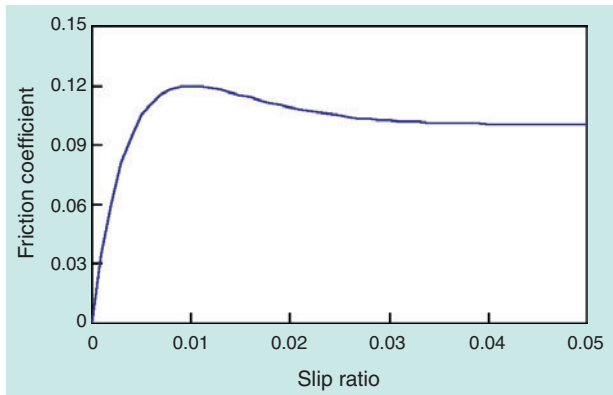
The mixed lubrication region ($\mu_{bd}\pm\Lambda<\mu_{hd}$) was determined by smoothly interpolating the friction coefficients μ_{hd} and μ_{bd} of the above-mentioned fluid lubrication and boundary lubrication, respectively, as shown by expression (2). **Fig. 3** shows two cases of variation in friction coefficients, with μ_{hd} of 0.001 and 0.06, determined through expression (2).

4) To determine the EHL rolling viscous resistance, Zhou's regressive formula (13) was used, but this operation was not performed when the applicable fluid lubrication mode was the IR mode. The force of EHL rolling viscous resistance was assumed to be opposite that of the mean surface velocity vector $\bar{\mathbf{u}}$ Also, with two rotating objects, it is necessary to consider the force F_{px} (expression (14)) that results from the pressure component in the rolling direction on the EHL oil film.[5] Note, however, that the sign for the rollers and inner ring must be a plus sign, and that for the outer ring must be a minus sign. Being compensated for by the component force of pressure in the normal direction, this force does not affect the moment.

$$\mathbf{F}_{EHLr}=\begin{cases}-\phi_T\dfrac{29.2R_el\,(GU)^{0.648}W^{0.246}}{\alpha_0}\cdot\dfrac{\bar{\mathbf{u}}}{|\bar{\mathbf{u}}|} & \text{if }h_{c,\,PE}>h_{c,\,IR}\\[2mm]0 & \text{otherwise}\end{cases}$$
$$\cdots\cdots\cdots\cdots\cdots\cdots\cdots\cdots\cdots\cdots\cdots(13)$$

$$\mathbf{F}_{px_{b,r}}=\pm\frac{2R_e}{R_{b,r}}\left|\mathbf{F}_{EHLr}\right|\frac{\bar{\mathbf{u}}}{|\bar{\mathbf{u}}|}\quad\cdots\cdots\cdots\cdots(14)$$

As such, the contact force, friction force and EHL rolling viscous resistance acting on each roller slice dynamic contact surface were calculated. In addition, the moment on each slice was calculated. The total of forces and moments working on all the slices act on the roller.

Fig. 2 Friction coefficient under boundary lubrication
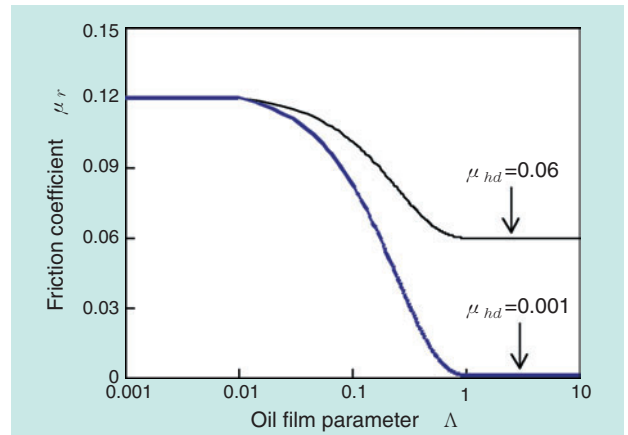
Fig. 3 Relationship between friction coefficient and oil film parameter

3.2 Interaction forces between the roller large end face and the inner ring large rib face

Generally, the contact area between the roller large end face and the inner ring large rib face has 30-40% slip. For this reason, the rolling viscous resistance is approximately one tenth of that of the traction force or friction force and can therefore be ignored.

1) The roller large end face of the bearing is round-shaped and the inner ring large rib face is cone-shaped. As a result, elliptical contact occurs. Because the length of elliptical contact is smaller than the contact length between the roller and the raceway surface, it can be assumed that all the interaction forces act on the geometrical maximum interaction point.

2) From the geometrical interaction amount δ, the contact force can be calculated with Hertz's point contact formula. The friction coefficient for the roller large end face and inner ring large rib face can be calculated in a manner identical to that for the raceway surface. Note, however, for the calculation of oil film thickness, Brewe's[11] formula (16) is used in the IR mode, and Chittenden's[12] formula (17) is used in the PE mode, as described below.

$$h_c = \begin{cases} \phi_T \cdot h_{c,PE} & \text{if } h_{c,PE} > h_{c,IR} \\ \phi_T \cdot h_{c,IR} & \text{otherwise} \end{cases} \quad \cdots\cdots\cdots (15)$$

$$h_{c,IR} = 128\alpha_r \left[0.131\tan^{-1}\left(\frac{\alpha_r}{2}\right) + 1.683 \right]^2 \left[\psi \frac{U}{W} \right]^2 R_e \quad \cdots\cdots (16)$$

$$h_{c,PE} = 4.31 U^{0.68} G^{0.49} W^{-0.073} \left[1 - \exp(-1.23 k^{2/3}) \right] R_e \cdots (17)$$

3.3 Interaction forces between the roller small end face and the inner ring small rib face

Generally, contact between the roller small end face and the inner ring small rib face rarely occurs. However, if gravity and external vibration act on this area in the non-load region, the roller small end face can contact the inner ring small rib face on rare occasions. Again, assuming that the entire interaction force is applied to the maximum contact point, we calculated the interaction force using Hertz's point contact formula. Because the mode of contact in this area was considered to be edge contact, we used a friction coefficient under constant boundary lubrication for the friction force calculation.

3.4 Interaction forces between the dynamic roller contact surface and the cage pocket surface

The interaction force between the dynamic roller contact surface and the cage pocket surface (shown with diagonal lines in **Fig. 4**) is similar to the interaction force between a roller and a bearing ring, and, therefore, was evaluated with the slice technique.
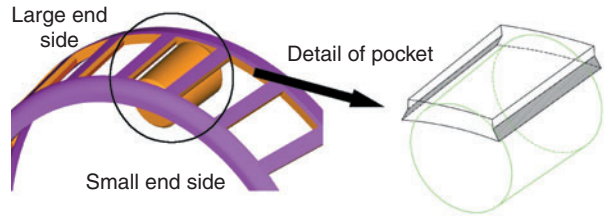
Fig. 4 Geometrical shape of cage pocket

Because the roughness of the pocket surface is great, the friction force when the roller rolling contact surface is in contact with the cage pocket surface was calculated assuming that the lubrication mode was boundary lubrication. In addition, because the width of the bar of the pocket in contact with the roller rolling contact surface is finite, a case where the roller was in contact with the edge of the bar was considered.

3.5 Interaction forces between the roller end face and the cage pocket surface

The interaction forces between the roller large end face and the cage pocket surface and between the roller small end face and the cage pocket surface are in sphere-to-plane and plane-to-plane contact modes, respectively. Therefore, we subjected all the representative points where contact could occur to a series of calculations, and took the sum of the contact and friction forces at each point as the interaction force at that point. Because the roughness of the pocket surface is great, the friction force when the roller end face was in contact with the cage pocket surface was calculated assuming that the lubrication mode was boundary lubrication.

4. Analysis model

The analysis model and coordinate systems used are shown in **Fig. 5**. Every coordinate system used was a right-hand coordinate system. Two types of bearings "standard specification and high-load capacity" were subjected to dynamic analysis to determine the differences in the cage behavior and interaction force between them. The high-load capacity type has inner and outer rings and rollers whose diameters were the same as those on the standard specification type, but its newly developed cage has an outside diameter greater than that of the standard specification bearing. The bearing data and operating conditions for these bearing types are summarized in **Table 1**, and the area that includes the dimensions in Table 1 is illustrated in **Fig. 6**.

The radial load was applied such that the inner ring was displaced in the +y direction and the topmost roller received the maximum load.
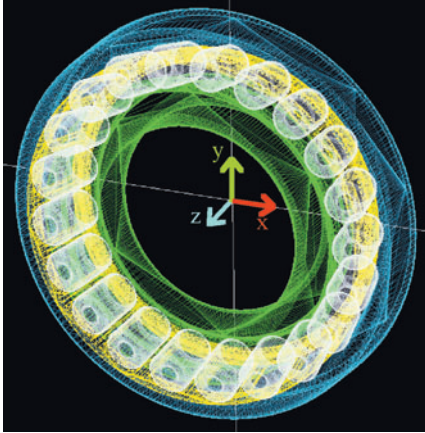
Fig. 5 Analyzed bearing schematic and its coordinate system

Table 1 Test bearing and operating conditions

Bearing (inside dia.×outside dia.×width, mm)	Standard specification bearing (φ40×φ76.2×17.5)	High-load capacity bearing*
Cage type	Standard cage	Newly developed cage
Number of rollers	21	23
Basic rated dynamic load, kN	46.5	50.0
Pocket angle α_p, deg	45	56
Cage outside dia ϕD, mm	61.39	62.22
Lubricant temperature ˚C	100	
Lubricant dynamic viscosity, mm²/s {cSt}	2.52 @ 100˚C	
Inner ring running speed, rpm	5000	
Load, kN	$F_r = 5,\ F_a = 2.5$	

*The inner ring, outer ring and rollers are identical to those used on the standard specification bearing.
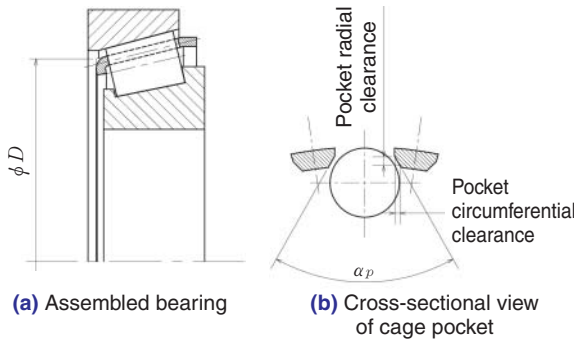
(a) Assembled bearing

(b) Cross-sectional view of cage pocket

Fig. 6 Cage geometry
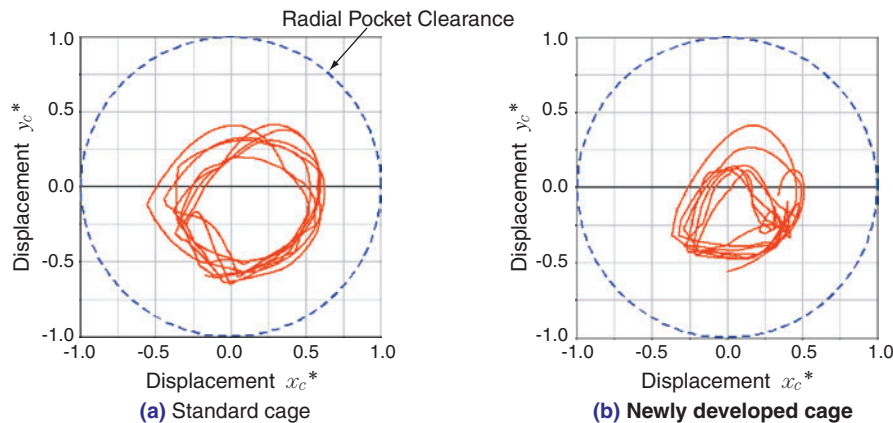
5. Analysis results

In further analysis, to eliminate the influence of the initial conditions the data acquired during the 0.5 s time-span after the start of calculation (for approximately 40 revolutions of the inner ring) was deleted, and the data obtained during the next 0.2 s (for approximately 17 revolutions of the inner ring) was utilized for evaluation.

5.1 Translational displacement on the radial plane at the cage mass center

On the cage used for the analysis, the pocket radial clearance is larger than the pocket circumferential clearance as illustrated in **Fig. 6(b)**, and the maximum translational displacement of the cage is the radial clearance on the pocket [4]. The trajectories of the cage mass centers on their radial planes with the standard bearing and the newly developed bearing are plotted in **Fig. 7**. The red solid lines in the charts represent the radial plane positions of the cage mass centers that were made dimensionless with the radial pocket clearances. The blue dotted lines indicate circles that took the radial pocket clearances of the cages as a radius. The areas of trajectories of cage mass centers are smaller than the radial pocket clearances, and match the characteristics of cage behavior under complex load conditions described in previous research[4, 13]. The displacement of the newly developed cage is slightly smaller than that of the standard cage.

The pattern of interaction force between the roller rolling contact surface and the cage is illustrated in **Fig. 8**. **Fig. 8(a)** shows the cage/roller interaction force and the interaction position in the case where the cage mass center is displaced to the position shown in **Fig. 8(b)**. The red vector in this chart is an interference force which the cage exerts onto the rollers and originates from the center of gravity of each roller. As can be understood from this chart,

(a) Standard cage

(b) Newly developed cage

Fig. 7 Numerical results of cage mass center behavior in radial plane

(a) Roller/cage interference position

(b) Position of cage mass center
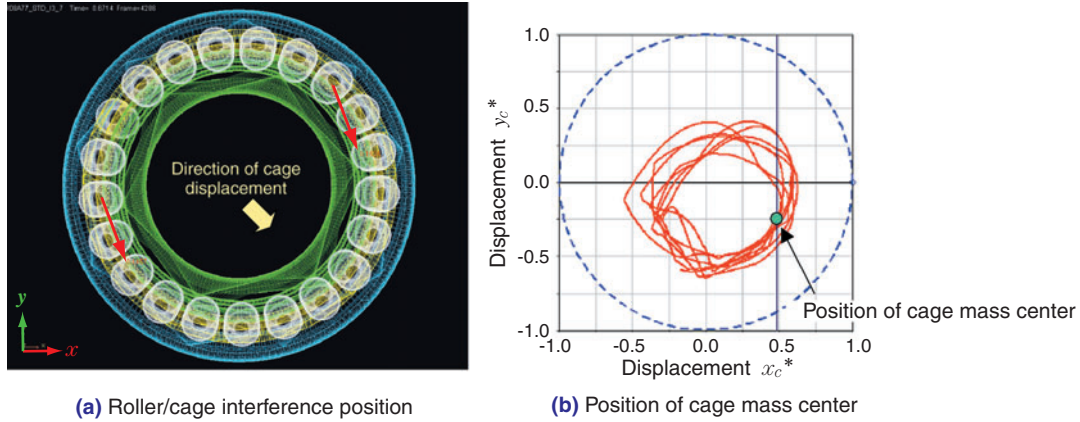
Fig. 8 Relationship between the direction of cage displacement and cage/roller interaction position (standard cage)

under this operating condition, multiple rollers that are square to the displacement direction of the cage are interacting with the cage.

In this situation, the direction of displacement within the pockets of the rollers in contact with the cage is the circumferential direction shown in **Fig. 6(b)**. As a result, the displacement of the cage is smaller than the pocket radial clearance.

A time-dependent record of the interaction force between the dynamic roller contact surface and the cage is given in **Fig. 9** for both the standard cage and

the newly developed cage. The charts in **Fig. 9** were obtained by plotting the absolute values of the interaction forces between the dynamic roller contact surfaces and all the cage bars. The interaction between the dynamic roller contact surface and the cage appears to be non-cyclic. The mean and maximum values of the interaction forces are summarized in **Fig. 10**. The mean value with the newly developed cage is 14% smaller than that with the standard cage. We believe this is because the normal load from the raceway surface on each roller

(a) Standard cage

(b) Newly developed cage
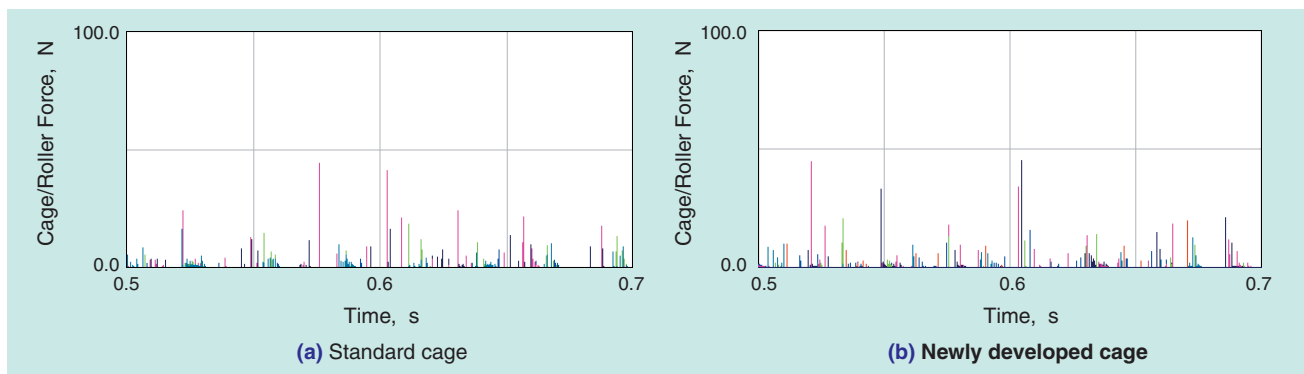
Fig. 9 Cage/roller (rolling surface) interaction forces
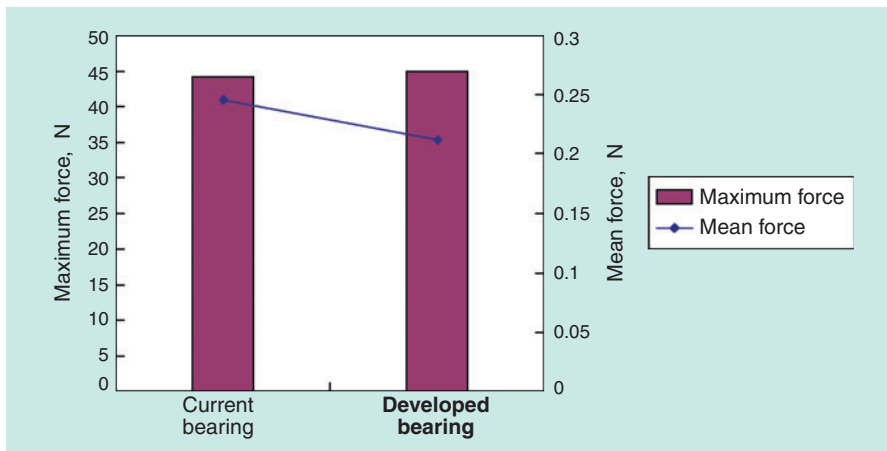
Fig. 10 Mean value and the maximum value of cage/roller (rolling surface) interaction forces

has decreased due to the increased number of rollers. The greater number of rollers has caused the traction force from the raceway surface that drives the rollers to decrease and resulted in decreasing the mean interaction force between the dynamic roller contact surface and the cage.

The driving force from the cage stems from the interaction force on the rollers, and the time-integration value of this interaction force governs the behavior of the cage. For this reason, the difference in the amplitude of the mass center trajectories of the cages, as shown in **Fig. 7**, seems to result from the difference in the mean interaction forces.

The difference in the maximum interaction forces of the standard cage and the newly developed cage was 2%. The maximum interaction force can be affected by accidental interaction. However, when all the data obtained from approximately 57 revolutions of the inner ring was evaluated, the maximum interaction force with the newly developed cage did not exceed that of the standard cage by more than 2%. Thus, we can judge that the maximum interaction force is roughly the same for both cage types.

5.2 Axial displacement of the cage mass center

Next, the time-dependent trend of the axial displacement of the mass centers of both cages is illustrated in **Fig. 11**. As shown in **Fig. 12**, the vertical axis took the cage mass center as the zero point when the roller was in contact with the raceway surface and the large rib face of the inner ring and the cage were in contact with the roller large end face. The vertical axis was also made dimensionless with the axial clearance of the cage pocket. As can be seen in **Fig. 11**, the axial displacement of the cage was approximately 1/2 the maximum axial clearance of the cage. In **Fig. 13**, cage/roller interaction force patterns in the cage pocket are illustrated. The red arrow in the diagram shows the interaction force from the cage acting on the roller. As a result, a reaction force in response to the illustrated interaction force acts on the cage. Due to the geometrical shape of the cage pocket, if the dynamic roller contact surface interferes with the cage pocket (**Fig. 13(a)**), the cage shifts in the -z direction due to the z-direction component of the above-mentioned interaction force. On the other hand, when the roller large end face interferes with the cage pocket (**Fig. 13(b)**), the cage shifts in the +z direction.

(a) Standard cage   (b) Newly developed cage
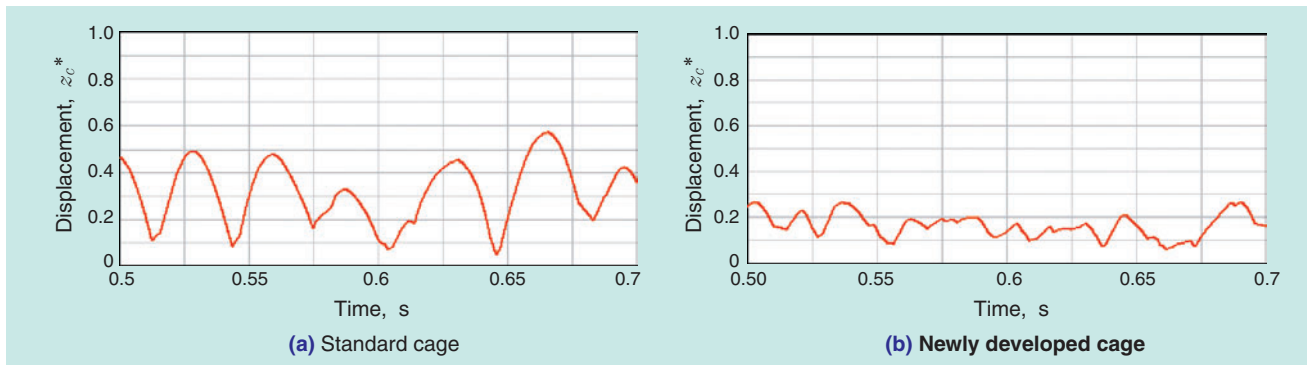
Fig. 11 Axial behavior of cage mass center
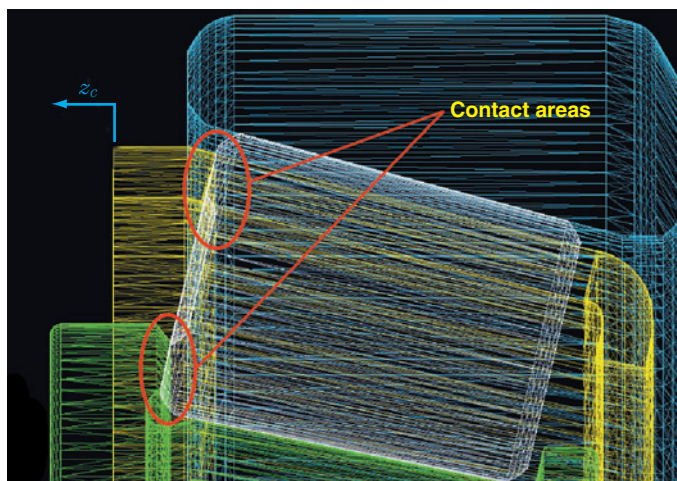
Fig. 12 Datum point for axial displacement of cage mass center
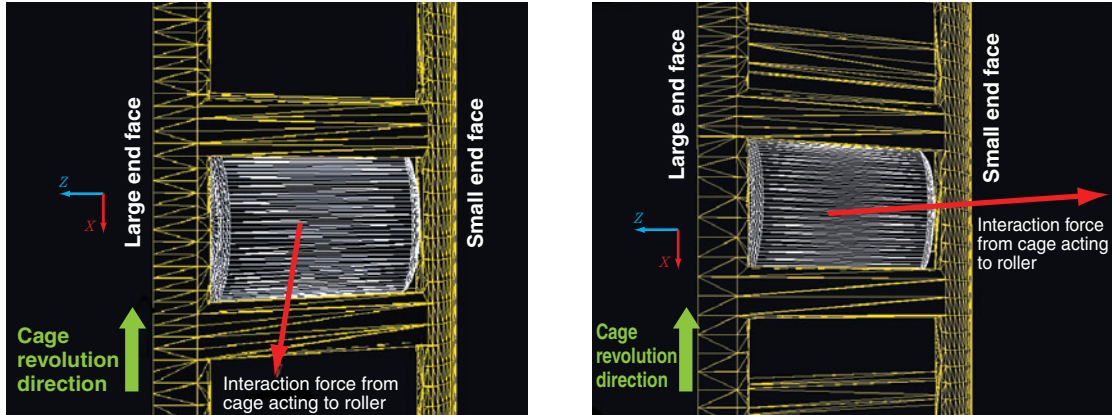
(a) Contact between roller rolling surface and cage pocket (b) Contact between roller large end and cage pocket

Fig. 13 Graphic example of cage/roller interaction forces (standard cage)

The roller large end face/cage pocket interaction force is summarized in **Fig. 14**. This chart was obtained by plotting the absolute values of the interaction forces between the large end faces of the rollers and the cage pockets. On the standard bearing, interaction occurs at about the cage running frequency fc while on the newly developed bearing, the magnitude of the interaction force is approximately 1/2 that of the standard bearing and this means the interaction occurs more frequently on the newly developed cage. In terms of axial displacement, the difference between the standard cage and the newly developed cage in **Fig. 11** results from the difference between interaction patterns given in **Fig. 14**. Under our analysis conditions, no collision between the roller small end face and the cage pocket occurred.

As described above, the behavior of the newly developed cage is the same as that of the standard cage, while the roller/cage interaction force with the newly developed cage is smaller than that with the standard cage. The effect of the cage outside diameter and pocket angle on the roller/cage interaction force is small within the scope of this analysis.

6. Conclusion

Using a 3D dynamic analysis tool optimized for tapered roller bearings, we have compared a standard tapered roller bearing and a high-load capacity tapered roller bearing that has an increased number of rollers. As a result, we have found that the behavior of the cage with the high-load capacity bearing is very similar to that of the standard bearing and that the roller/cage interaction force with the high-load capacity bearing is equivalent to or smaller than that of the standard bearing. We also found that the effect of the geometrical shape of the cage unique to the high-load capacity bearing onto the roller/cage interaction force is small within the scope of our analysis.

It is difficult to experimentally compare the levels of roller/cage interaction force. Therefore, our analysis technique, as an alternative to an experiment-based technique, is a useful means for verifying the functions of high-load capacity bearings.
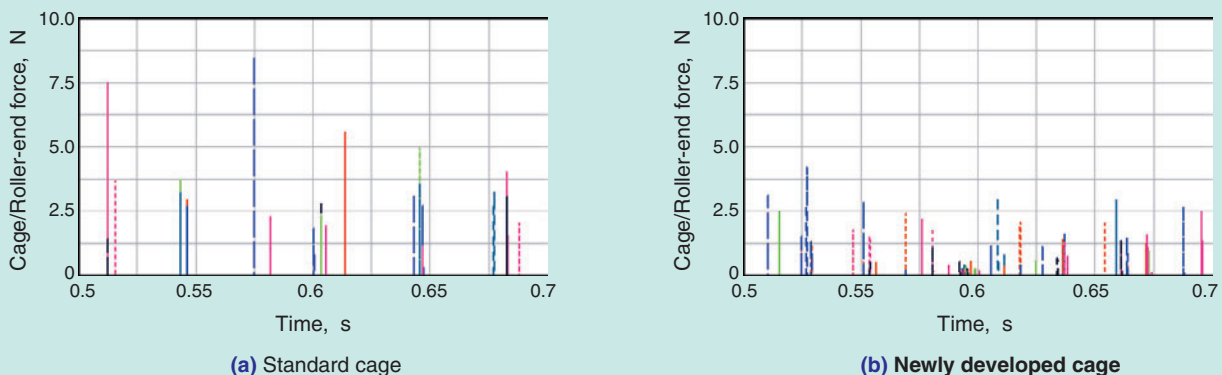
(a) Standard cage   (b) **Newly developed cage**

Fig. 14 Cage/roller large end interaction forces

References

1）MSC.Software，HP Address：
http://www.mscsoftware.co.jp/（2005.05.23）

2) Tomoya Sakaguchi, Kaoru Ueno, Takuji Kobayashi:
Analysis of cage behavior on cylindrical roller
bearings, Japanese Society of Tribologists, Tribology
Conference Preprints (Sendai 2002-10) 415.

3) Tomoya Sakaguchi, Kaoru Ueno: Analysis of cage
behavior on cylindrical roller bearings, **NTN**
Technical Review, No. 71 (2003) 8-17.

4) Tomoya Sakaguchi, Kazuyoshi Harada: Analysis of
cage behavior on tapered roller bearings (2nd report,
calculation result), Japanese Society of Tribologists,
Tribology Conference Preprints (Tottori 2004-11)
503.

5）Zhou, R. S., Hoeprich, M. R.：Torque of Tapered
Roller Bearings, Trans. ASME, J. Trib., 113, 7
（1991） 590-597.

6) Pan, P., Hamrock, B.J.: Simple Formulae for
Performance Parameters Used in
Elastohydrodynamically Line Contacts, Trans.
ASME, J. Trib., 111, 2（1989） 246-251.

7) Martin, H. M., :Lubrication of Gear Teeth,
Engineering, London, 102（1916）119-121.

8）Gupta, P. K. et al., : Visco-Elastic Effects in Mil-L-
7808 Type Lubricant, Part I; Analytical Formulation,
STLE Tribol. Trans., 34, 4（1991） 608-617.

9）Kragelskii, I. V., : Friction and Wear, Butterworths,
London（1965）178-184.

10) Masayoshi Muraki, Yoshitsugu Kimura: Research into
traction characteristics of lubricant (2nd report),
Junkatsu, 28, 10 (1983), 730-760.

11）Brewe, D. E., Hamrock, B. J., Taylor, C. M., : Effects
of Geometry on Hydrodynamic Film Thickness,
ASME J. Lubr. Technol., 101,2（1979） 231-239.

12）Chittenden, R. J., Dowson, D., Dunn, J. F., Taylor,
C. M., : A theoretical analysis of the isothermal
elastohydrodynamic lubrication of concentrated
contacts I. Direction of lubricant entrainment
coincident with the major axis of the Hertzian contact
ellipse, Proc. Roy. Soc., London, A397（1985）245-
269.

13) Kazuyoshi Harada, Tomoya Sakaguchi: Analysis of
cage behavior on tapered roller bearings (1st report,
behavior measurement), Japanese Society of
Tribologists, Tribology Conference Preprints (Tottori
2004-11) 501.

Photos of authors

Kazuyoshi HARADA

New Product Development
R&D Center
Mechatronics Research Dept.

Tomoya SAKAGUCHI

New Product Development
R&D Center
Mechatronics Research Dept.

High Capacity Tapered Roller Bearings
- Super Low Torque · High Rigidity Tapered Roller Bearings -
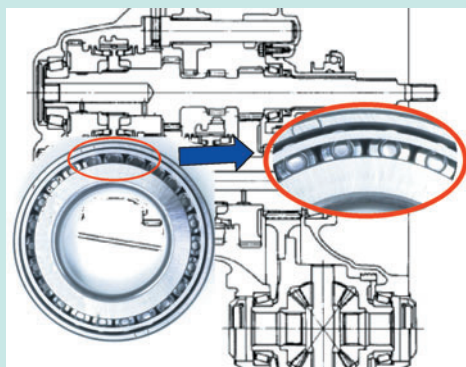
Takashi TSUJIMOTO*
Jiro MOCHIZUKI*

Tapered roller bearing have greater capacity for carrying not only pure radial or axial loads but also combined loads, and feature greater bearing rigidity. Therefore, they are found in numerous applications in various industries such as the automotive industry.

Recent advancements in transmissions for low fuel consumption have resulted in lower oil viscosities and reduction in transmission size. Therefore, it is necessary to reduce the size of the bearings, which can result in bearing life and rigidity problems.

High capacity tapered roller bearings were developed in order to suppress the life reduction effect associated with reduction in bearing size. This is accomplished by increasing the number of rollers (similar to a full compliment type bearing) by using a special cage. By doing this, the dynamic load rating can be increased by up to 10%, and the static load rating can be increased by up to 15%. As a result, bearing life under severe lubrication conditions can be improved in addition to increasing the bearings rigidity.

Super low torque bearings that maintain bearing life and rigidity can be designed by combining high capacity tapered roller bearings and FA tapered roller bearing features.

1. Introduction

In order to reduce automobile fuel consumption, efforts are in progress to introduce low-viscosity oils and compact, lightweight designs for automotive transmissions and differential gears. The sizes of bearings used in transmissions and differential gears have been getting much smaller, and, as a result, the need to ensure bearing life and rigidity has been increasing. To address this challenge, we have developed a unique high-load capacity, compact tapered roller bearing that has a usage life just as long as traditional bearings.

This bearing type incorporates a special cage and has an increased number of rollers, nearly the same number as a full complement roller bearing, to increase the load carrying capacity. As a result, the contact pressure is decreased, higher bearing rigidity is achieved and bearing life is extended even under severe lubrication conditions, including contaminated lubricant. In this report, the authors introduce the structure and features of this bearing and the results of evaluation tests, as well as examples of applications of this low-torque, high-rigidity design.

---

*Automotive Sales Headquaters   Automotive Engineering Dept.

2. Structure of high-load capacity tapered roller bearing

Employing a smaller clearance between the cage and the outer ring to increase the cage PCD allows the cage bar width to remain the same as that of a standard bearing. At the same time, a narrower roller-to-roller clearance was adopted so that the bearing cage can incorporate almost as many rollers as the number used in full complement bearings.
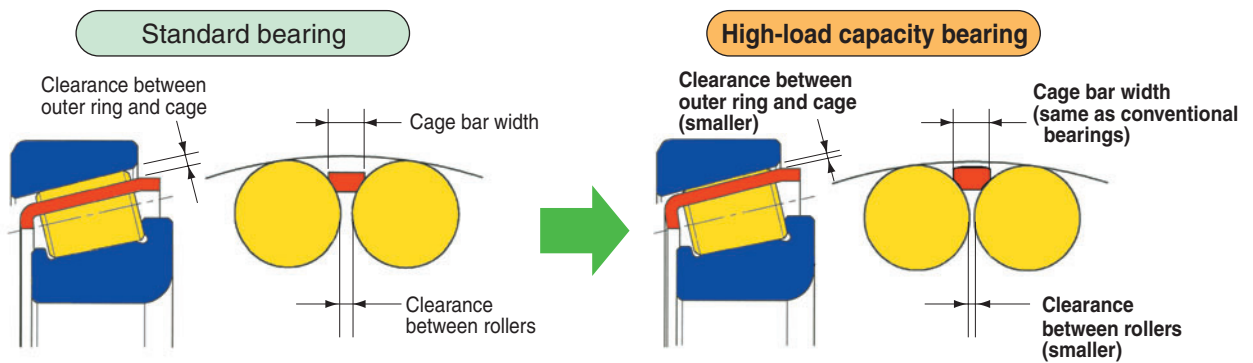
Fig. 1 Structure of high capacity tapered roller bearing

Standard bearing

24 rollers
Dynamic rated load Cr= 42.0 kN
Static rated load Cor= 52.0 kN

High-load capacity bearing

27 rollers (**increase of 3 rollers**)
Dynamic rated load Cr= 45.5 kN (**increase of 8%**)
Static rated load Cor= 58.0 kN (**increase of 11%**)
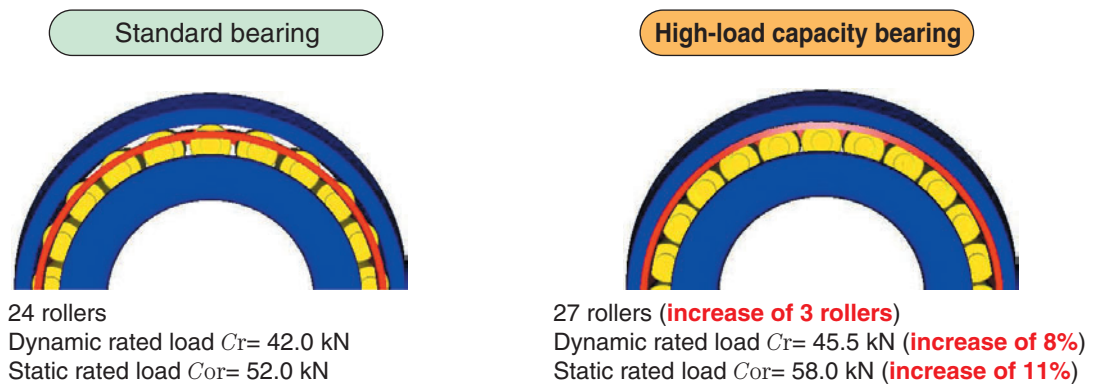
Fig. 2 Example of bearing design (size : $\phi 45 \times \phi 81 \times 16$)

3. Features of high-load capacity tapered roller bearing

The increased number of rollers gives our high-load capacity tapered roller bearing the following improved functions:

1) Increased rated load
- Up to 10% increase in dynamic rated load (maximum improvement of 37% in terms of calculated life)
- Up to 15% increase in static rated load (maximum improvement of 15% in terms of safety)

2) Higher rigidity
- Up to 10% increase in bearing rigidity (up to 9% decrease in elastic displacement)

3) Longer bearing life
- Improved practical bearing life under clean lubricating conditions

  The greater number of rollers contributes to reducing the maximum contact surface pressure, increasing the oil film thickness, and stress relief in metal-to-metal contact situations. Thus, surface-initiated flaking, which results from metal-to-metal contact in lubricating conditions when an oil film is not readily formed, is inhibited resulting in the extension of practical bearing life.

- Improved practical bearing life under contaminated lubricating conditions

  The increased number of rollers contributes to reducing the maximum contact surface pressure, thereby decreasing the size of dents caused by trapped foreign matter are and the stress occurring on the rims around dents is reduced. As a result, the bearing life under contaminated conditions is also extended.

4. Performance of high-load capacity tapered roller bearing

Table 1 Test bearing

	Standard bearing	High-load capacity bearing
Bearing size	ϕ 45 $\times$ ϕ 81 $\times$ 16 mm	
Rated load	Dynamic rated load C_r =42.0 kN	Dynamic rated load C_r =45.5 kN
	Static rated load C_{or} =52.0 kN	Static rated load C_{or} =58.0 kN
Number of rollers	24 rollers	27 rollers

1) Results of a bearing life test under a clean lubricating condition of $\varLambda$*0.2

Fig. 3 illustrates the results of a bearing life test under $\varLambda$*0.2 clean oil lubricating conditions in which oil film formation was extremely poor.

Our high-load capacity tapered roller bearing was less prone to developing surface-initiated flaking, which results from metal-to-metal contact in poor oil film formation conditions, and boasted a bearing life approximately 15 times longer than standard tapered roller bearings.

$\varLambda$*: Oil film parameter (oil film thickness/combined rolling contact surface roughness)

2) Results of bearing life test for use with contaminated lubricant

The results of the life test under use with contaminated lubricant are summarized in **Fig. 4.**

Our high-load capacity tapered roller bearing was less prone to develop dent-initiated flaking in use with contaminated lubricant and boasts a bearing life approximately 3 times longer than standard tapered roller bearings under the same conditions.

3) Results of bearing life test in use with low-viscosity lubricant

Generally, the viscosity grade of the oils currently used on automotive MT and differentials is in the range of VG75 to VG90, while the viscosity level of oils on automotive CVT and AT is at the VG32 level. The lowest viscosity grade oils currently available on the market are VG20 level oils. Because transmission oils with much lower viscosity will be increasingly used, we executed a bearing life test using viscosity grade VG10 oil under both clean oil lubrication and contaminated oil lubrication conditions.

Load conditions:
  radial load F_r= 19.1 kN
  axial load: F_a= 0 kN
  (axial clearance 0.20-0.25 mm)
Speed: 2500 min⁻¹
Lubricant: Jomo High Speed Fluid VG1.5
Lubrication method: oil bath
Oil film parameter: $\varLambda$ = 0.2
Calculated life:
  standard bearing L_{10}= 92.2 h
  High-load capacity bearing L_{10}= 120.4 h

slope e
● 1.546
■ 4.231

$L_{(50)}$
● 22.4
■ 152.9

$L_{(10)}$
● 6.6
■ 98.0

Fig. 3 Life test results under clean lubrication

Load conditions:
  radial load: F_r= 19.1 kN
  axial load: F_a= 0 kN
  (axial clearance 0.20-0.25 mm)
Speed: 2500 min⁻¹
Lubricant: Turbine Oil VG56
Contaminants: steel beads + gas-atomization 0.5 g/L
  Contaminant grain size
  50 μ m or smaller, 90wt%
  100-180 μ m, 10wt%
Lubrication method: oil bath
Oil film parameter: $\varLambda$ = 2.0
Calculated life:
  standard bearing L_{10}= 92.2 h
  high-load capacity bearing L_{10}= 120.4 h

slope e
● 1.971
■ 3.275

$L_{(50)}$
● 22.5
■ 49.0

$L_{(10)}$
● 8.7
■ 27.6

Fig. 4 Life test results under contaminated lubrication

The results of the life test under the Λ=0.8 clean oil lubrication condition are shown in **Fig. 5**.

Our high-load capacity tapered roller bearing was less prone to develop surface-initiated flaking because of metal-to-metal contact due to poor oil film formation conditions and boasts a bearing life approximately twice as long as standard tapered roller bearings.

The results of the life test under the Λ=0.8 contaminated oil lubrication condition are shown in **Fig. 6**.

We performed a market study of the contaminants in lubricating oils and found the size of contaminants was 50 μ m or smaller and that the amount of contaminants was less than 0.3 g/L even on MT cars. Therefore, we employed severe contamination conditions with contaminants sized 50 μ m or smaller in amounts of 0.3 g/L.

Our high-load capacity tapered roller bearing was less prone to developing dent-initiated flaking during use with contaminated lubricant and boasts a bearing life approximately 3 times the length of the standard tapered roller bearing.

5. Application to extremely low torque/high rigidity design

Our high-load capacity tapered roller bearing can be combined with a long-life bearing, such as the **NTN** FA tapered roller bearing [2] that features a special heat treatment process (FA), to obtain finer crystal grains and optimized bearing interior design technologies.

The FA tapered roller bearing offers longer bearing life, greater seizure resistance and improved dent resistance. If it is designed for a bearing life equivalent to standard tapered roller bearings, its size can be more compact than that of standard bearings, resulting in lower torque. However, loss in bearing rigidity was unavoidable when we attempted to achieve a significantly lower torque. By combining the FA tapered roller bearing with our newly developed high-load capacity tapered roller bearing, it is possible to avoid loss in bearing rigidity and achieve a lower torque.
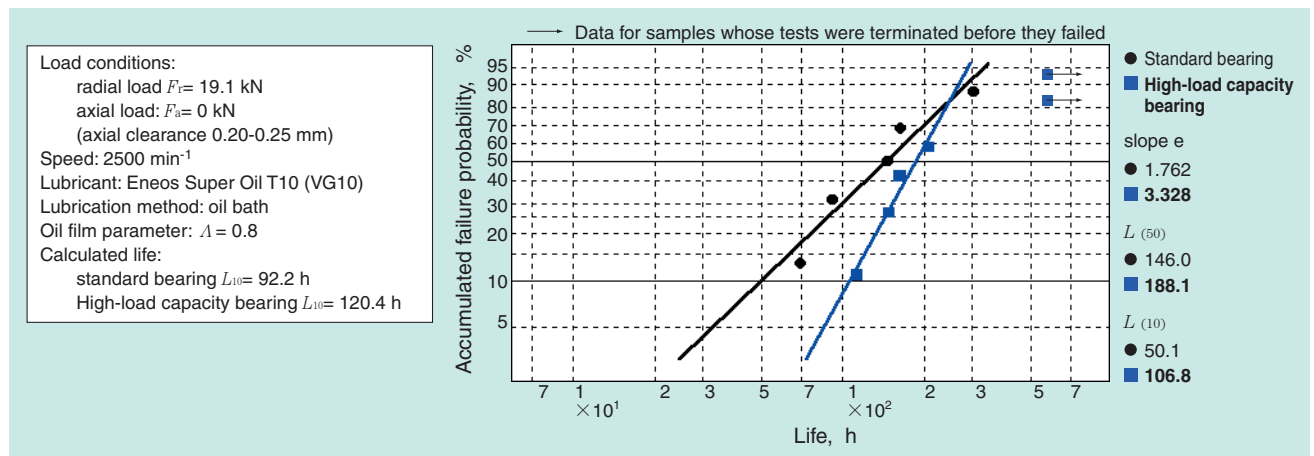
Fig. 5 Life test results under clean lubrication
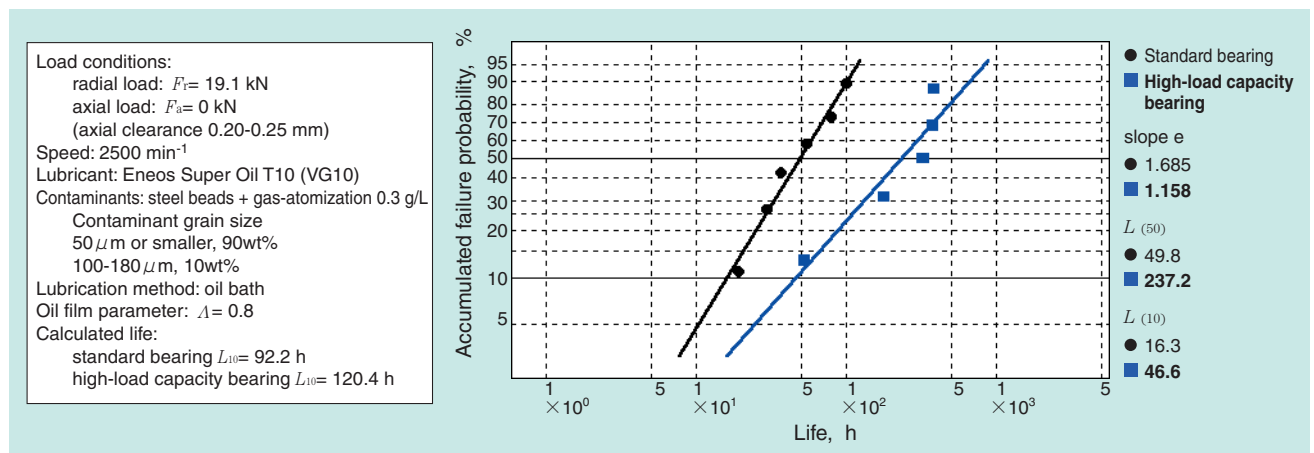
Fig. 6 Life test results under contaminated lubrication

Furthermore, it is possible to decrease the torque to 50% by greatly reducing the lubricant stirring drag in the bearing through optimization of the cage shape. Applications of 50% low torque design that also ensure bearing life and rigidity are described below.

5.1 Tested bearing

Since the tapered roller bearings for pinion shaft supports in near axle differentials are used under high loads, bearings capable of carrying large loads are used. Since the torque loss caused by the bearings is a relatively large part of the total loss, the need for low-torque tapered roller bearings is growing.

To address this problem, we have attempted to achieve lower torque for a bearing used for pinion shaft support in near axle differentials with model #30306D.

5.2 Torque factors on tapered roller bearings

The torque factors on tapered roller bearing are shown in **Fig. 7**.

To decrease the torque occurring on tapered roller bearings, factors ① through ⑤ need to be reduced.
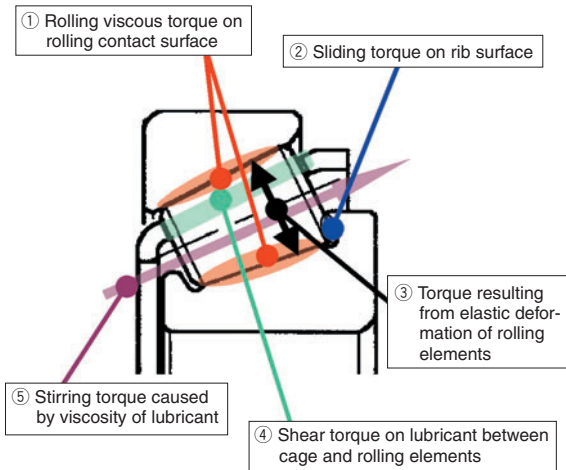
Fig. 7 Torque factor of tapered roller bearing

5.3 Torque factors and their contribution to torque on tapered roller bearings for near axle differentials

Among the torque factors working on a tapered roller bearing, the magnitude of the stirring torque caused by lubricant viscosity greatly varies depending on the amount and temperature of the lubricant oil. We executed tests with various oil levels, as shown in **Fig. 9**, to determine the magnitude of stirring torque on tapered roller bearings used for pinion shaft support in near axle differentials. As a result, we have learned that in a normal bearing running speed range of 2000-3000 r/min, the lubricant stirring torque accounts for approximately 30% of the whole torque.

Based on this finding, we have summarized the torque factors and contribution rates of a tapered roller bearing used on a pinion shaft support in a near axle differential in the pie chart below.

When the amount of lubricant on a bearing is relatively large and its viscosity is relatively high, the major contributing factors are "stirring torque caused by lubricant viscosity," "rolling viscous torque on rolling contact surface" and "shear torque on lubricant between cage and rolling elements."
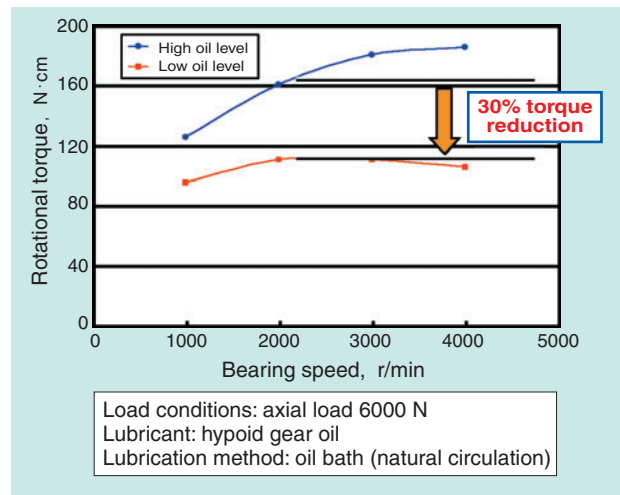
Fig. 8 Torque of tapered roller bearing used for pinion shaft support in near axle differential
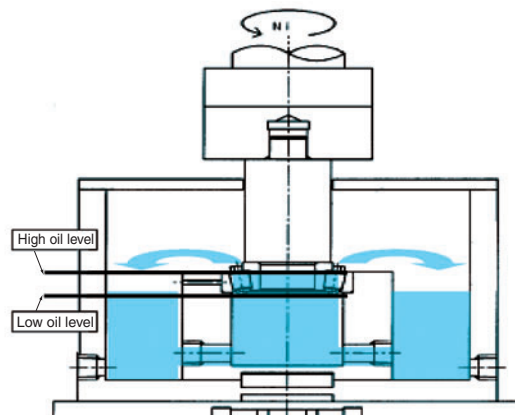
Fig. 9 Torque measurement method
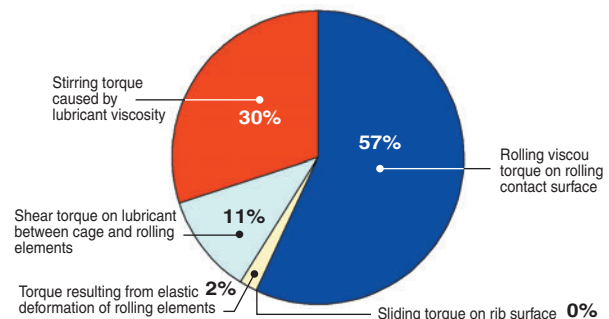
Fig. 10 Factors contributing to friction torque of tapered roller bearing used for pinion shaft support in near axle differential

5.4 Torque reduction techniques

Reduction of the major contributing torque types is necessary to decrease the torque on tapered roller bearings used on pinion shaft support in near axle differentials. These include "rolling viscous torque on rolling contact surface", "shear torque on lubricant between cage and rolling elements" and "stirring torque caused by lubricant viscosity".

① **Decrease in rolling viscous torque on rolling contact surface**

Optimization of the bearing interior design and the crowning of rollers is effective for decreasing the rolling viscous torque on a rolling contact surface. Our torque reduction techniques that can ensure bearing rigidity are described below.

1) Alteration of bearing internal design

To achieve a lower torque while maintaining bearing rigidity, we have checked the bearing internal design's contribution to torque and bearing rigidity. The results are summarized in **Fig. 11**. To achieve a high-rigidity low-torque design, smaller roller pitches and greater contact angles are advantageous.
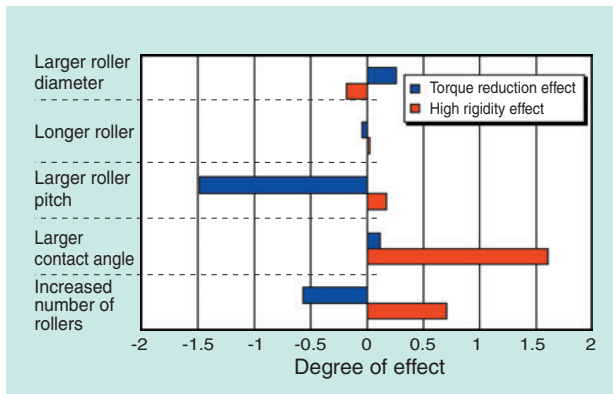
Fig. 11 Effect of internal design factors in torque and rigidity

2) Alteration of crowning shape

Fig. 12 summarizes the torque reduction (calculated values and actual measurements) that result from the 17% reduction in the effective contact length between the rollers and the raceway surface through alteration of the crowning shape. The torque can be decreased by altering the crowning shape to reduce the effective contact length. The actual effect nearly matches our calculated values.

However, as summarized in **Fig. 13**, a lower torque attained by alteration of the crowning shape can decrease the bearing rigidity. Therefore, bearing rigidity must be considered to determine an
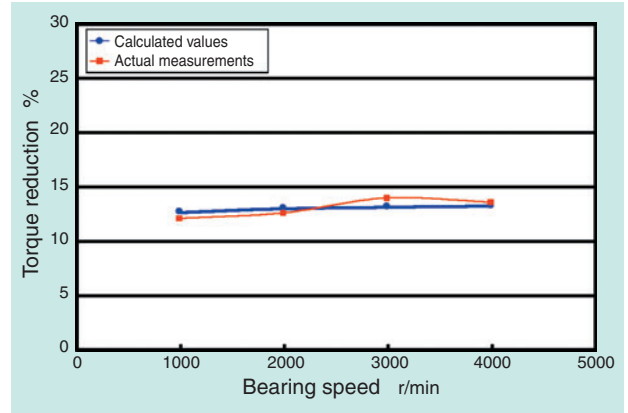
Fig. 12 Torque reduce percentage by changing crowning

Crowning shape examples
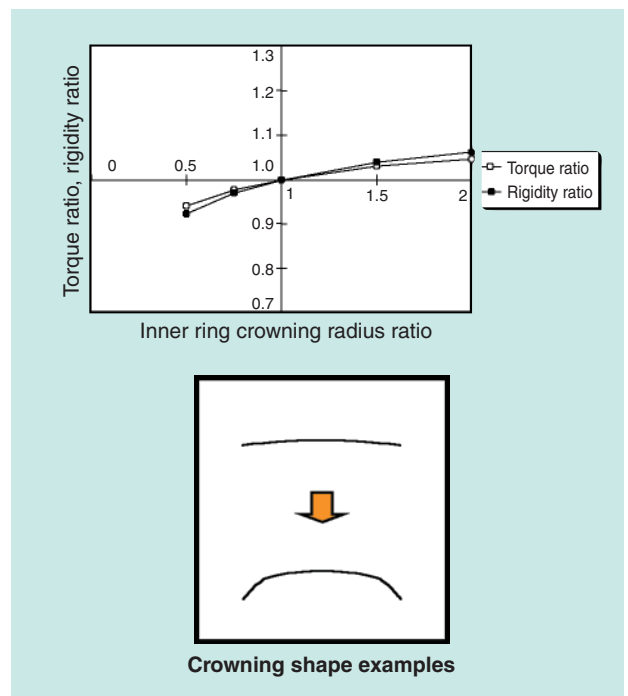
Fig. 13 Factors contributing to friction torque and rigidity of inner ring crowning

optimal crowning shape.

② **Reduction of shear torque on lubricant between cage and rolling elements**

As summarized in **Table 2**, compared to a standard cage, the shape A cage with straight bars results in a lower shear torque on the lubricant between the cage and rolling elements. The actual shear torque measurements match our calculations well. In the case of shape B, the grooves on the ribs help promote oil flow toward the outer ring. This arrangement can lower the lubricant stirring torque compared to cases where lubricant oil tends to remain stagnant in the bearing inner ring.

Table. 2 Type of cage and torque reduction ratio

		Standard cage	Shape A	Shape B
Smaller diameter side ↑ Larger diameter side ↓				
Torque reduction percentage	Actual measurements	—	10%	12%
	Calculated values	0%	10%	10%

Oil flow
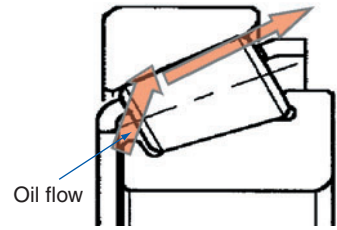
③ **Decrease in stirring torque caused by viscosity of lubricant**

1) Effect by modified bearing internal design

A low torque design with a more compact bearing results in reduced roller rolling area volume as shown in **Fig. 14**, thereby reducing the lubricant stirring torque inside the bearing. An example of reduced roller rolling area volume is described below.

Fig. 15 shows a comparison between the standard bearing and a new bearing with a modified internal design. As summarized in **Table 3**, the rolling area volume in the bearing with a modified internal design is 31% smaller than the standard bearing.

The torque reduction percentage resulting from the modified internal design is summarized in **Fig. 16**. Since the calculated values do not include the reduction in stirring torque caused by the low viscosity of the lubricant, the reduction effect in the calculated values is lower than the actual measurements. However, when the reduction in the lubricant stirring torque due to the roller rolling area reduction is considered, as demonstrated by expression (1), the calculated reduction in bearing torque coincides well with the actual measurement.

Lubricant stirring torque rate　　Roller rolling area volume reduction rate　　Rolling viscosity torque reduction rate

$$\text{Bearing torque} = 30\% \times (100\% - 31\%) + 70\%$$
$$\times (100\% - 13\%) = 82\% \,(\textbf{18\% reduction}) \cdots \text{Expression (1)}$$

Rolling viscosity torque rate

Calculated value coincides well with actual measurement.

Fig. 14 Roller rolling area volume

Standard bearing　　　　New bearing with modified internal design

Fig. 15 Comparison of bearing form

Table. 3 Comparison of bearing internal design

	Roller length	Avg. roller dia.	Roller pitch dia.	Roller rolling area volume ratio
Standard bearing	13	9.22	51.54	1.00
Bearing with modified internal design	11	8.04	48.46	0.69
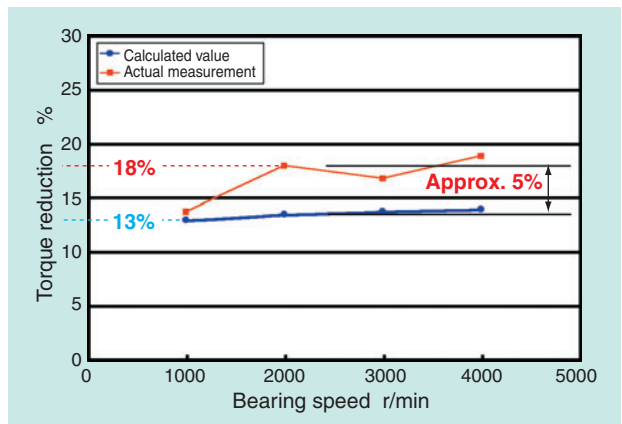
Fig. 16 Relationship between torque and torque reduce percentage

2) Alteration to cage inside diameter

To reduce the lubricant stirring drag by decreasing the amount of lubricant flowing into the bearing, we verified the torque reduction effect with a bearing that has a small diameter cage. The resultant torque reduction effect is summarized in **Fig. 17**. At a bearing speed of 2500 r/min, approximately 25% reduction in torque is achieved. The lubricant stirring torque accounts for approximately 30% of the whole bearing torque. In other words, the lubricant stirring torque was reduced by 83%.

Standard cage   **Small diameter cage**
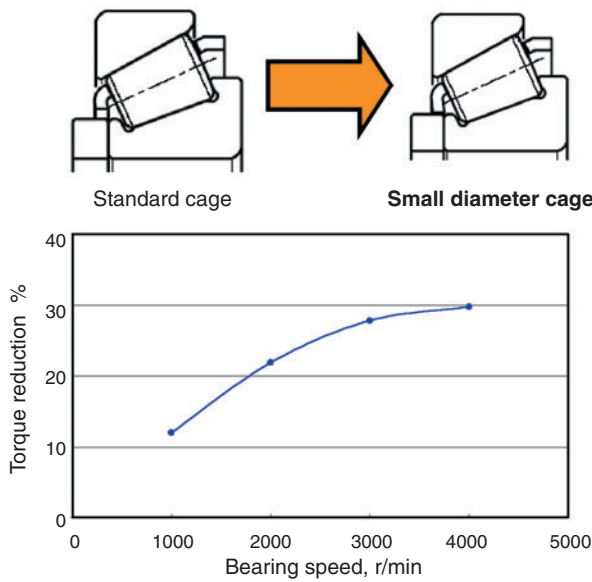
Fig. 17 Relationship between speed and torque reduce percentage of bearing with small diameter cage

5.5 Ultra-low torque/high-rigidity tapered roller bearing design example

By combining the FA bearing, the high-load capacity design, and the torque reduction techniques, it is possible to reduce bearing torque by 50% while ensuring bearing life and rigidity (**Fig. 18**, **Table 4**).

Standard bearing   **Low-torque bearing**

More compact bearing design is possible.
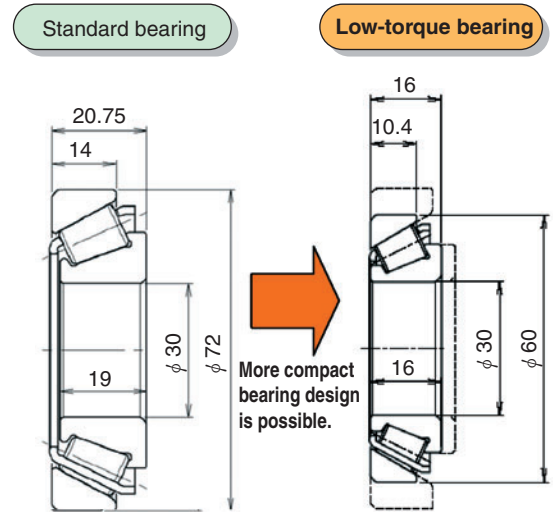
Fig. 18 Comparison of bearing size

Table 4 Bearing internal design

	Standard bearing	Low-torque design
Rated load	Dynamic rated load C_r =49.0 kN Static rated load C_{or}=52.5 kN	Dynamic rated load C_r =33.0 kN Static rated load C_{or}=35.5 kN
Roller PCD (mm)	ϕ 51.54	ϕ 44.44
Number of rollers	15	17
Contact angle	28° 48′ 39″	30° 30′
Roller length (mm)	13	10.1
Mean roller dia. (mm)	ϕ 9.22	ϕ 7.25
Mass (kg)	0.393	0.223

1) Torque reduction effect by factor (calculated value)

Fig. 19 summarizes the running torque reduction effect (expected value) for each torque reduction factor. In the practical speed range of 2000 to 3000 r/min, it is possible to reduce running torque by 50%.

① Effect of modified internal design
② ①+crowning effect
③ ②+effect of reduction in shear torque on lubricant between cage and rolling elements
④ ③+effect of reduction in lubricant stirring toque by modified internal design
⑤ ④+effect of reduction in lubricant stirring torque by limiting the amount of lubricant

Fig. 19 Relationship between speed and torque of each torque reduction factors

2) Torque reduction effect (actual measurement)

Fig. 20 summarizes the running torque measurement results for the standard and low-torque bearings.

In the practical speed range of 2000 to 3000 r/min, running torque was reduced by 50%.
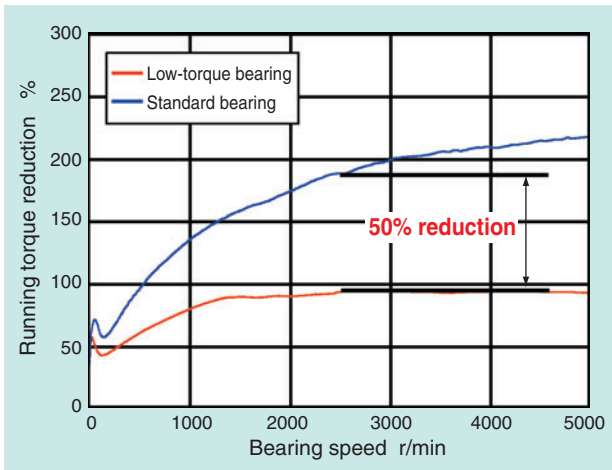
Fig. 20 Relationship between speed and torque of current bearing and low torque bearing

3) Reduction effect on running torque (calculated and actual values)

As shown in **Fig. 21**, the actual torque reductions measured at various speeds match the corresponding calculated values well.
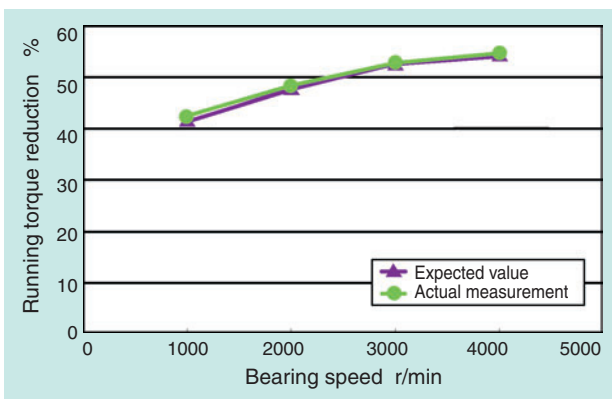
Fig. 21 Relationship between speed and torque of low torque bearing

4) Axial rigidity measurement results

Fig. 22 summarizes the axial rigidity measurement results for the standard and low-torque bearings.

The rigidity of the low-torque bearing is equivalent to that of the standard bearing.
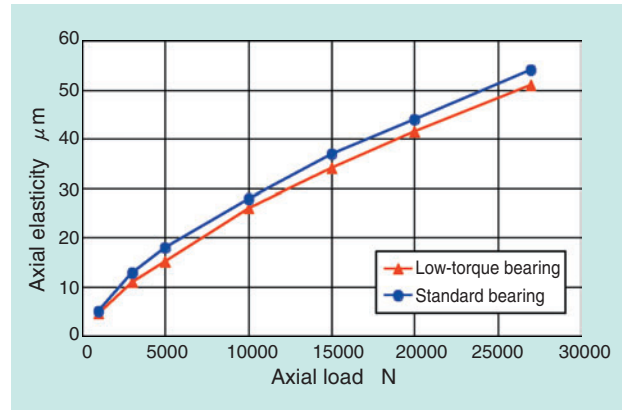
Fig. 22 Deformation of axial direction

5) Torque factor analysis for ultra-low torque/high-rigidity tapered roller bearing

Fig. 23 summarizes the torque values obtained from our verification efforts for the ultra-low torque, high-rigidity tapered roller bearing. The **NTN** ultra-low torque, high-rigidity tapered roller bearing achieved 50% reduction in bearing torque while ensuring a level of life and rigidity equivalent to that of the standard bearing.
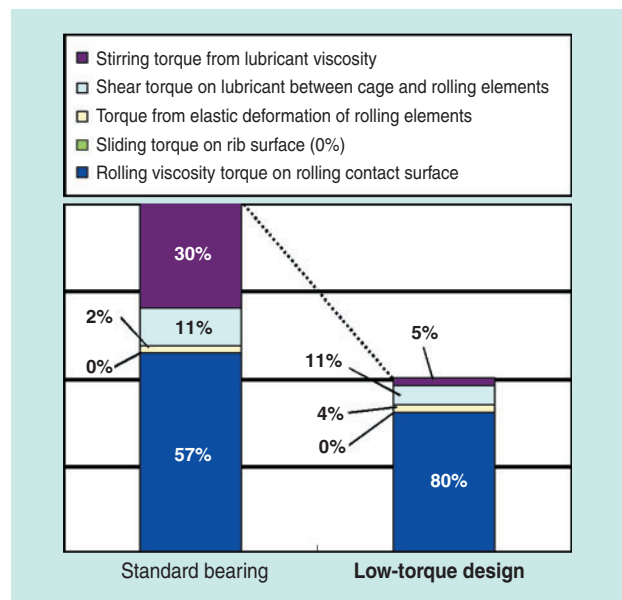
Fig. 23 Analysis of torque reduction

6. Conclusion

As explained in this thesis, we believe that our high-load capacity tapered roller bearing, which boasts longer life and higher rigidity, offers a solution to problems arising from challenges related to improving automobile fuel efficiency. We will market long-life, high-rigidity, low-torque tapered roller bearing products that combine FA and high-load bearing technologies to contribute to lower automobile fuel consumption.

References

1) Tsutomu Ohki, Kikuo Maeda, Hirokazu Nakashima: **NTN** Technical Review "Longer life with bearing steel by finer crystal size," No. 71 (2003), p2.
2) **NTN** Catalog "FA Tapered Roller Bearings" (CAT. No. 3802/E）.

Photos of authors

Takashi TSUJIMOTO

Automotive Sales Headquaters
Automotive Engineering Dept.

Jiro MOCHIZUKI

Automotive Sales Headquaters
Automotive Engineering Dept.

[**Technical Paper**]

Study of Long-Life Thrust Needle Roller Bearings Used in Low Viscosity Lubrication Conditions
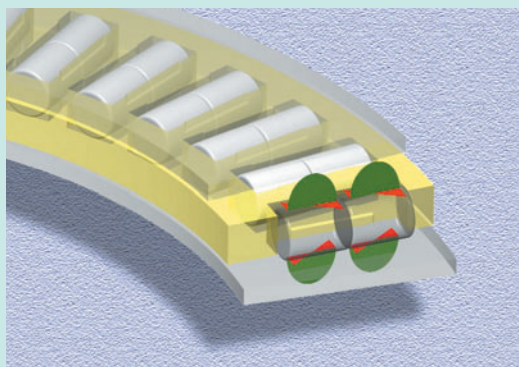
Hiroki FUJIWARA*
Kenji TAMADA**

This paper investigates the failure modes of thrust needle roller bearings lubricated with low viscosity lubricants both experimentally and theoretically, and proposes a new design of a long-life thrust needle roller bearing to meet these demands. Experimental observations reveal the occurrence of surface originated flaking at the inner edge of the raceway, which suggests that heat generation due to sliding roller-race contact and the resulting material plastic flow were the likely cause of the damage. Theoretical analysis shows that the dominant factor in bearing torque is slipping motion at the roller and raceway contact under insufficient lubrication film conditions. Consequently, the use of crowned rollers and double rows of rollers are expected to yield longer life as well as lower bearing rotational torque when compared with standard thrust needle roller bearings.

1. Introduction

Thrust needle roller bearings, boasting various advantages such as high-load carrying capacity, high rigidity and compactness, are used in a diversity of applications. Their operating conditions and performance requirements vary from application to application. Thrust needle roller bearings used for car air-conditioner compressors use a fluid mixture consisting of coolant and refrigerator oil as a lubricant. Recently, lower viscosity fluids are being used to improve the efficiency of compressors, and, as a result, lubrication performance has been decreased. To help solve this problem, long-life thrust needle roller bearings capable of low viscosity lubrication are increasingly needed.

The authors have investigated the factors that affect the lifespans of thrust needle roller bearings under low viscosity lubrication conditions and have attempted to find measures to ensure longer bearing life.

Symbols

b	Half width of contact
d_r	Roller diameter
E'	Coefficient equivalent to Young's modulus
E_E	Elastic compression workload per time unit
F_a	Friction force occurring on protruded contact area
F_r	Rolling viscous resistance
F_t	Traction force occurring on oil film
G	Material parameter
j	Roller row No.
L	Contact length
l_{rd}	Length of rolling contact per time unit
n	Number of roller rows
M_E	Friction torque resulting from elastic hysteresis loss
M_r	Frictional torque from rolling viscous resistance
M_s	Frictional torque from spinning

*New Product Development R&D Center   Mechatronics Research Dept.
**Intellectual Property Planning Dept.

P	Load
R	Equivalent radius
U	Velocity parameter
v	Absolute value of relative velocity between race and rollers
W	Load parameter
w	Load per unit length
w_0	Load at minute width in contact center
x	Coordinates in roller revolution direction relative to revolution center as origin
Z	Number of rollers per row
α_0	Viscosity-pressure coefficient
β_E	Elastic hysteresis loss coefficient
δ	Elasticity approach amount
μ	Friction coefficient
Φ_E	Heat generation ratio resulting from elastic hysteresis loss
ϕ	Elastic compression workload per distance unit
ϕ_T	Compensation coefficient for rolling viscous resistance resulting from shear heat generation
ω	Angular velocity of turning ring

2. Experimental investigation into failure causes[1]

2.1 Life test method

For this life test, the authors employed the NTN thrust needle roller bearing life test rig. This rig is schematically illustrated in **Fig. 1**, and the test conditions used are summarized in **Table 1**. The race measures dia. $\phi 60 \times$dia. $\phi 85 \times 1$ mm, and we used various race materials and heat treatment furnaces. The lubricant used was Spindle Oil ISO VG2. The oil film parameter (Λ) with this lubricant was 0.1 (surface roughness 0.084 μmRa). Thus, the lubrication used for the test was boundary lubrication.

2.2 Effects of race materials and heat treatment furnaces

Three race materials, SPCC, SCM415 and SK5, were used, and carburization/quenching was performed with three different heat treatment furnaces. The life test results with various races are shown in **Fig. 2**. The end of bearing life for every bearing tested was determined by flaking on the race. The life levels of the races tested fell in a range of approximately 11 to 17 hours in terms of 10% life (L_{10}), with no apparent difference in the life resulting from race material or heat treatment furnace differences.
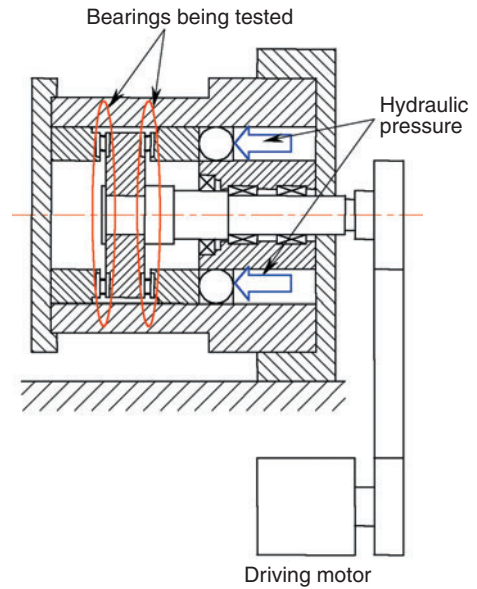
Fig. 1 NTN thrust needle roller bearing life test rig

Table 1 Life test condition

(a) Life test operating conditions

Test rig	NTN thrust needle roller bearing life test rig
Load	9.8 kN
Bearing speed	5000 min^{-1}
Lubricant	Spindle Oil ISO VG2 (70˚C)
Oil film parameter	0.1
Lubrication method	Circulating lubrication

(b) Main characteristics of bearings used in life test

Race	$\phi 60 \times \phi 85 \times 1$ mm
Rollers	$\phi 3 \times 7.8$ mm
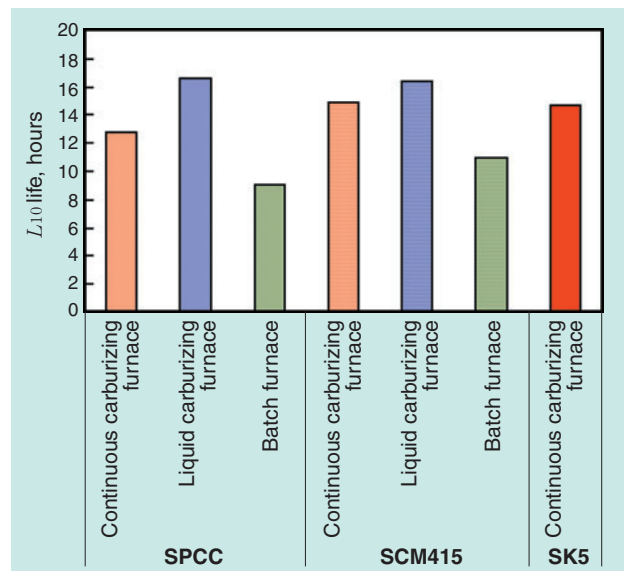
Fig. 2 Effect of race material and heat treatment furnace on bearing life

2.3 Effect of race accuracy

We investigated the effect of race surface roughness on bearing life. We assumed that the race surface roughness was in a range of approximately 0.03-0.11 μ mRa. The results are summarized in **Fig. 3**. No significant relation between surface roughness and bearing life was found under these test conditions.

Fig. 4 illustrates the results of investigation into the effects of heat treatment on the deformation of the races. The magnitude of heat treatment-induced deformation was evaluated based on the flatness of the races. Deformation had no apparent effect on bearing life.
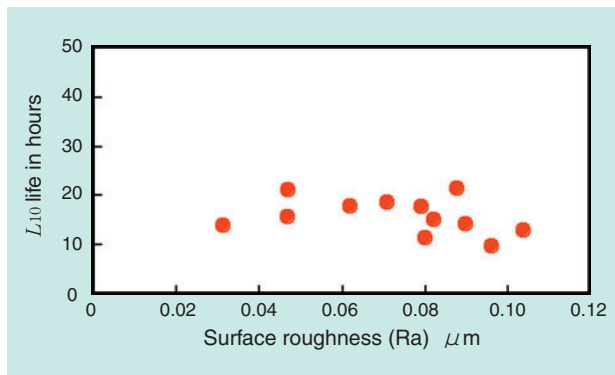
Fig. 3 Effect of race roughness on bearing life
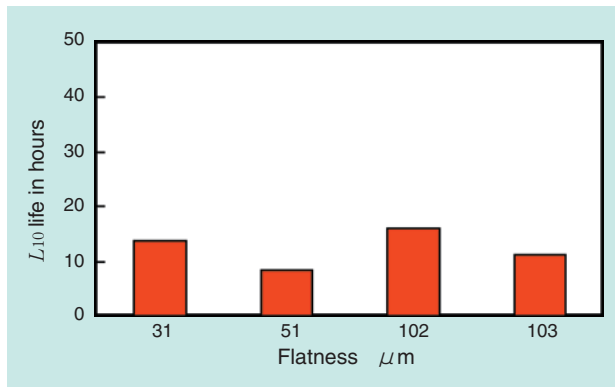
Fig. 4 Effect of race flatness on bearing life

2.4 Effects of race materials

As shown in **Fig. 2**, variation of the race steel material and heat treatment furnace type made no difference on the life of the thrust needle roller bearing. We believe the reason that no difference occurred between the samples was that a grain boundary oxidizing zone that uniformly lowered the surface strength was present on the surface of each race. The depth of the grain boundary oxidizing zone was in a range of 1.5 to 9.4 μ m. To determine the effect of the grain boundary oxidizing zone, a race

whose grain boundary oxidizing zone was removed with emery paper and buff-finished with diamond paste was subjected to the life test, and the result was as shown in **Fig. 5.**

The bearing life was not affected by the surface roughness of the race, which was 0.062 μ mRa before finishing and 0.027 μ mRa after buffing.

Furthermore, we investigated the possible connection between lifespan and other factors, including surface layer hardness, surface residual stress and residual austenitic amount, and found no significant relationships.
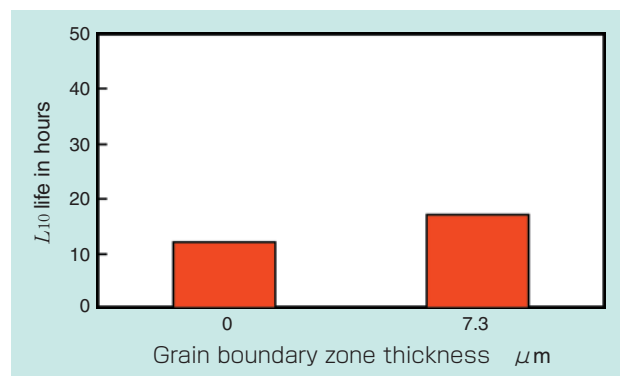
Fig. 5 Effect of race grain boundary oxidizing zone on bearing life

2.5 Failure types

The appearance of the raceway that underwent the test is shown in Photo 1. Most of the bearing failures were shallow flakings that started at the inner bore edges on the raceway rolling mark. Evidence of heat generation (discoloration) is apparent along the whole circumference of the rolling mark edge. On thrust needle roller bearings, rollers exhibited pure rolling on the pitch circle with slip occurring towards both ends of each roller. The bearing life might have been decreased by slip-induced heat generation.
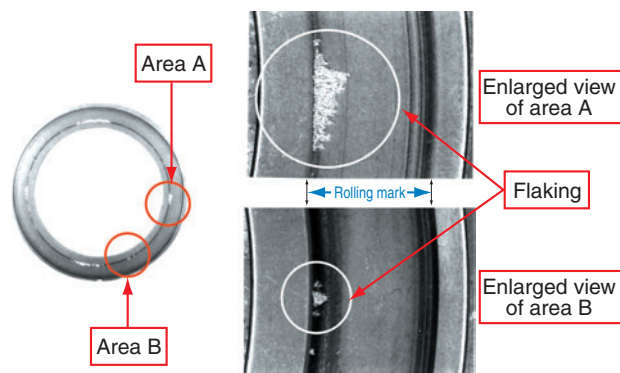
Photo 1 Raceway after life test

These tested rollers and races did not use crowning, and edge loading was considered one factor for failure. If the edge loads were a major failure factor, the failure should be internally started flaking. However, the failure that occurred in our test was flaking that started from the surface. In addition, as summarized in **Fig. 6**, the inner edge of the rolling mark on the raceway that underwent the test developed virtually no compressive residual stress, while the compressive residual stress on the outer edge reached a depth of 0.03 mm. The estimated edge stress was 2 GPa maximum, so we do not think that the edge load is a major contributing factor.
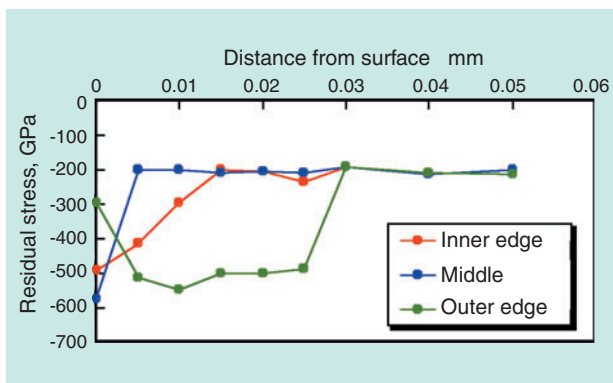
Fig. 6 Compressive residual stress in a race after test

2.6 Experimental verification of assumed failure causes

To verify our assumptions described above, we introduced crowned rollers into the bearing being tested so that the actual roller contact length was shorter than with straight rollers and subjected the bearing samples to the life test. As a result, the crowned roller bearing life was 4.5 times longer than that of the straight roller bearing, as shown in **Fig. 7**, though its surface pressure was higher. From this finding, the relative slip between the rollers and the race seems to affect the bearing life.
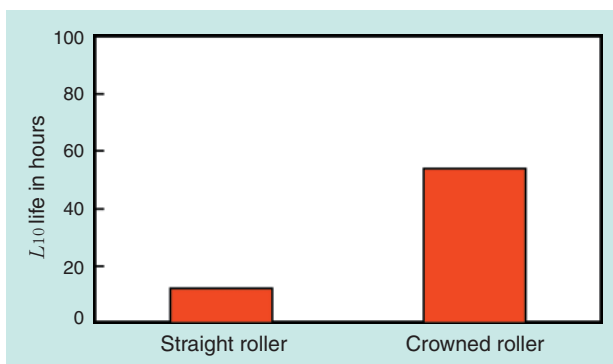
Fig. 7 Comparing bearing life with straight rollers and one with crowned rollers

Furthermore, the surface characteristics of the race on the crowned roller bearing were compared to those of the straight roller bearing. **Fig. 8** summarizes the results of X-ray half-value width measurements on the inside and outside edges and the middles of the rolling marks on the races of both bearing types that we tested. Compared to the crowned rollers, the decrease in X-ray half-value widths at the edges of the straight rollers was greater. We found that there was greater heat generation at the edges of the rolling mark on the race of the straight roller bearing compared to the crowned roller bearing.

Fig. 9 illustrates the results of X-ray anisotropy measurements on the inside and outside edges and the middles of the rolling marks on the races of both tested bearing types. "X-ray anisotropy" can be defined as a phenomenon where the crystals are oriented in a particular direction due to the plastic fluidization of the surface due to tangential force[2]. This can be qualitatively described by using the absolute value of the difference between the residual stress measured on the rolling mark surface in the roller rolling direction and the residual stress
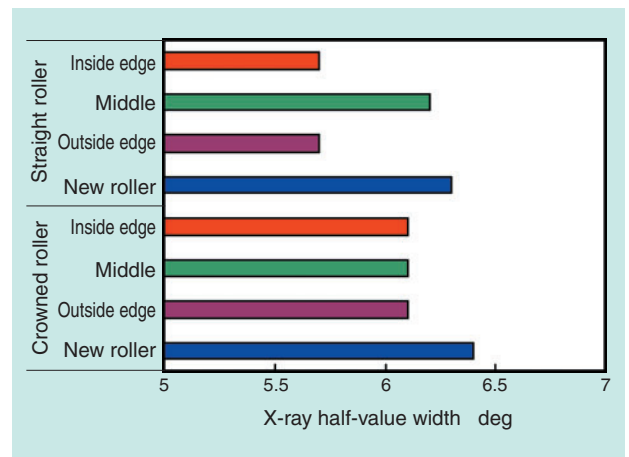
Fig. 8 X-ray half-value width of rolling marks on races
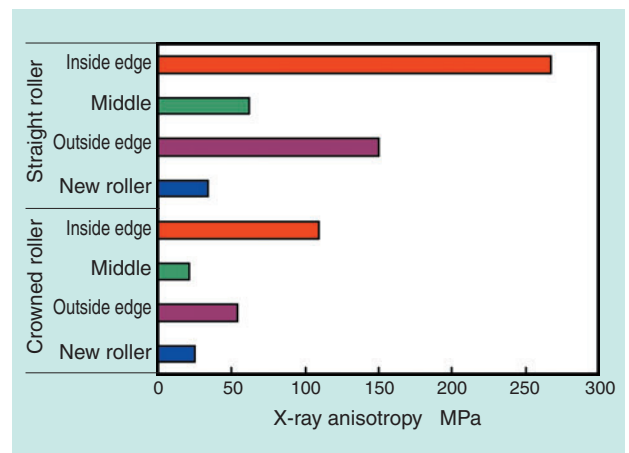
Fig. 9 X-ray anisotropy of rolling marks on races

measured in the opposite direction (for convenience, the estimated stress was determined with a simplified $\sin^2 \mu$ method). The greater this difference, the greater the plastic flow occurring on the surface.

The residual stress on the inner edge of the rolling mark on the straight roller bearing was approximately 160 MPa greater than that of the crowned roller bearing.

From these facts, we believe that the relative slip between the rollers and the race led to heat generation and plastic fluidity at the inner edge of the rolling mark on the race, resulting in the surface-initiated flaking.

3. Analysis of frictional torque[3]

The amount of heat generation can be given as the product of frictional torque and bearing speed. Given this, we will hereafter investigate the frictional torque factors and their impacts theoretically.

3.1 Frictional torque factors and methods for their calculation

3.1.1 Spin

An example of the distribution of the peripheral speed and the slip between the rollers and the race on a thrust needle roller bearing is illustrated in **Fig. 10.** If crowning is ignored, the peripheral speeds within the contact surfaces are uniformly distributed in the revolution axis. At the same time, the race velocity distribution is proportional to its radius. Accordingly, within the contact surfaces, slipping occurs in the normal direction on the contact center, and this slipping motion is known as "spin." When the friction coefficient is $\mu(x)$, the bearing torque M_s caused by spin can be described in the form of the expression (1).

$$M_s = \frac{2Z}{\omega} \sum_{j=1}^{n} \int \mu(x)\, w(x)\, v(x)\, dx \quad \cdots\cdots\cdots (1)$$
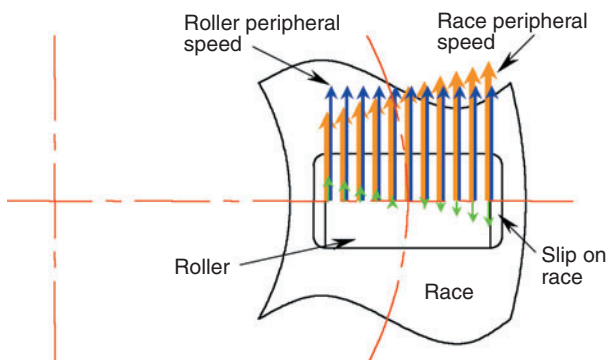
Fig. 10 Peripheral speeds and slip speed distribution in thrust needle roller bearing

The friction coefficient $\mu(x)$ can be given by a mixed lubrication theory. The frictional force on a solid-to-solid contact area was calculated using the Greenwood-Tripp theory [4], and the traction force on the fluid lubrication area was calculated using Muraki-Kimura's analysis method. [5]

Incidentally, it is usually difficult to correctly provide various parameters that represent the surface profile and lubrication state of a solid-to-solid contact model.

Therefore, with a thinner oil film and a greater proportion of solid-to-solid contact, friction coefficients and frictional torques do not necessarily coincide quantitatively with experiment results.

3.1.2 Rolling viscous resistance

According to Zhou-Hoeprich [6], shear stress on lubricant at the EHL inlet opposite the rolling direction occurs on the surface of the contact object. If converted into a surface integral, this shear stress can be evaluated as a force that causes a moment opposing the revolution to occur. This force is known as "viscous resistance." As a result of analysis of the EHL theory, Zhou-Hoeprich developed a recurrence formula for rolling viscous resistance, as shown in expression (2), which we adopted.

$$F_r = \phi_T\, 29.2\, \frac{R}{\alpha_0} L\, (GU)^{0.648}\, W^{0.246} \cdots\cdots\cdots\cdots (2)$$

For thrust needle roller bearings, the frictional torque M_r resulting from rolling viscous resistance can be expressed as:

$$M_r = 2Z \sum_{j=1}^{n} \int x\, F_r(x)\, dx \quad \cdots\cdots\cdots\cdots\cdots\cdots (3)$$

3.1.3 Elastic hysteresis loss

When elastic bodies repeatedly come into mutual contact, it is known that the relation between the resultant stress and strain can be plotted as a hysteresis loop. We determined the elastic hysteresis loss for a line-contact case.

In the contact area in **Fig. 11**, the load on the minute width dy at the center of the contact area is:

$$w_0 = \frac{2P}{\pi b}\, dy = \left(\frac{1}{2\pi} \frac{E'LP}{R} \right)^{1/2} dy \cdots\cdots\cdots\cdots (4)$$

Therefore, the elastic compression workload $d\phi$ consumed when a roller rolls by dy is:

$$d\phi = \int_0^P w_0 \frac{d\delta}{dP}\, dP = 0.65 \frac{P^{1.4}}{R^{0.5} E'^{1.4} L^{0.3}}\, dy \cdots (5)$$
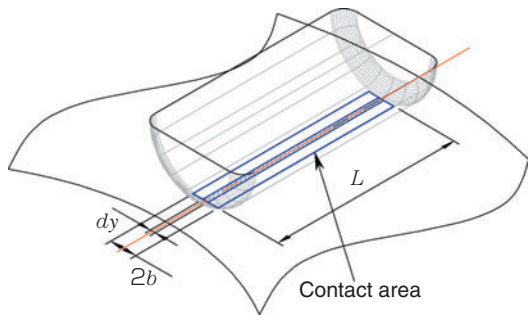
Fig. 11 Roller/race contact part

The rolling contact distance l_{rd} per time unit where a roller remains in contact with a race is:

$$l_{rd} = \frac{\omega}{2} \frac{d_r}{2} \quad \cdots\cdots\cdots\cdots\cdots\cdots\cdots\cdots\cdots (6)$$

Therefore, the elastic compression workload E_E is:

$$E_E = \phi\, l_{rd} = \frac{\phi\, \omega\, d_r}{4} \quad \cdots\cdots\cdots\cdots\cdots\cdots\cdots (7)$$

Then, if the elastic hysteresis loss coefficient is taken as β_E, the relation between the heat generation and bearing frictional torque resulting from the elastic hysteresis loss is:

$$\Phi_E = 2Z\beta_E \sum_{j=1}^{n} E_E = \omega M_E \quad \cdots\cdots\cdots\cdots\cdots (8)$$

Therefore, the frictional torque M_E resulting from the elastic hysteresis loss can be determined as:

$$M_E = \frac{2Z\,\beta_E \sum\limits_{j=1} E_E}{\omega} \quad \cdots\cdots\cdots\cdots\cdots\cdots (9)$$

3.2 Comparison between measured frictional torques and calculated results

Table 2 summarizes the test conditions for the frictional torque measurement test as well as the major technical data for the bearings tested with crowned rollers. The temperature was measured at the rear face of the race. The test rig used is schematically illustrated in **Fig. 12**.

In both experimental and calculated results with a VG2 lubricant, plotted in **Fig. 13**, the frictional torque decreases as the bearing speed increases and the frictional torque attained was lower with the single row bearing than with the double row bearing. The resultant oil film parameter fell in a range of $\Lambda = 0.7$ to 1.6.

Table 2 Frictional torque test condition

(a) Operating conditions for friction torque measurement

Test rig	**NTN** vertical torque test rig
Load	3.0 kN
Bearing speed	1000～3000 min⁻¹
Lubricant	Spindle oil ISO VG2 (31˚C)
	Turbine oil ISO VG32 (37˚C)
Lubrication method	1m ℓ coating

(b) Main data for frictional torque measurement test bearing

Race	$\phi 60 \times \phi 85 \times 1$ mm
Single row rollers	
Double row rollers	
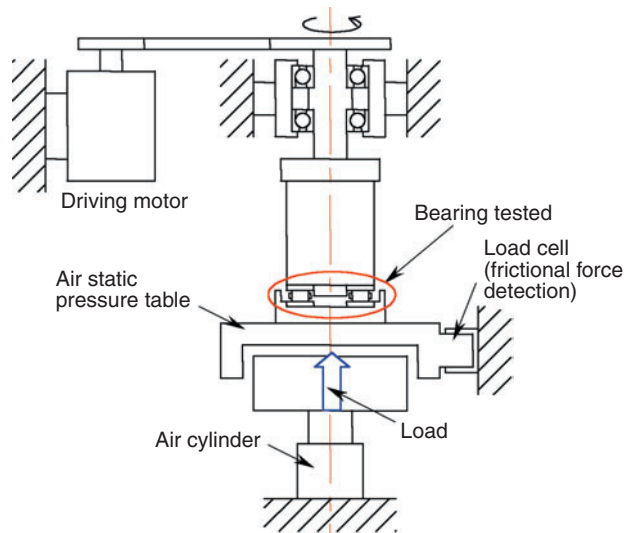
Fig. 12 NTN vertical type bearing frictional torque test rig
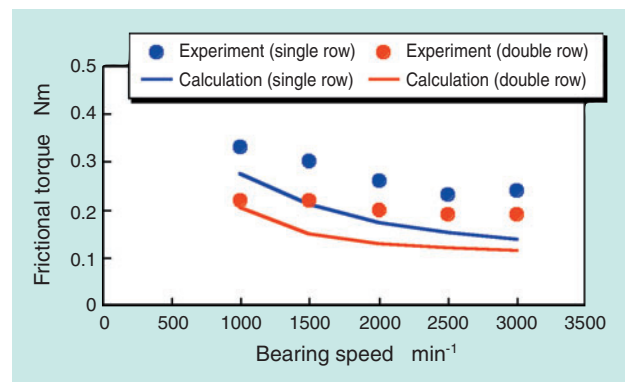
Fig. 13 Test and calculation results of bearing frictional torque with ISO VG 2 oil

The results obtained with VG32 are summarized in **Fig. 14**. The frictional torque remained unchanged or increased in the experiment, while the frictional torque increased in the calculation. There was no apparent difference between the single row bearing and the double row bearing in either the experiment or the calculation. The Λ fell in a range of 4.4 to 9.6.

With either condition, the value obtained from the experiment was greater than that obtained from the calculation. One possible reason for this is that the frictional torque resulting from cage/roller contact was not considered in our calculations. In addition, the results from VG2 shown in **Fig. 13** could not correctly reproduce the parameter of solid-to-solid contact.
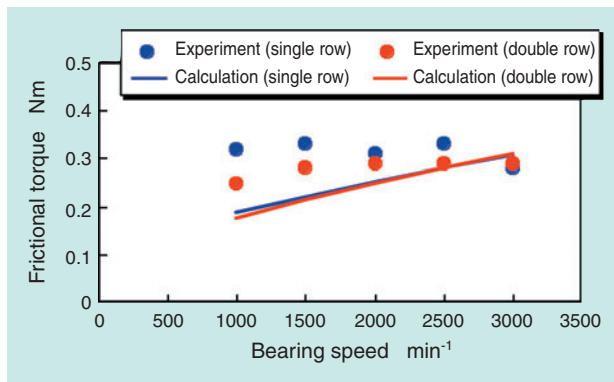
Fig. 14 Test and calculation results of bearing frictional torque with ISO VG 32 oil

3.3 Analysis and discussion of torque factors

The breakdowns of frictional torque, with a larger oil film parameter Λ and a smaller Λ are summarized in **Fig. 15.**

When Λ=9, the major frictional torque factor is rolling viscous resistance, which accounts for 80% or more of the total frictional torque. Spin does not greatly affect rolling viscous resistance. As a result, there is virtually no difference between a single row bearing and a double row bearing, both having the same effective contact length within a bearing.

When Λ=1, the lubrication condition is mixed lubrication and the solid-to-solid contact area increases. As a result, spin becomes the major frictional torque factor. Consequently, compared with a single row bearing, the torque is lower on a double row bearing, which has low spin.

The estimated temperatures on raceway surfaces obtained through FEM are summarized in **Fig. 16**. The temperature on the inner edge is higher than on the outer edge and the possibility of failure is higher with the inner edge. In addition, it is apparent that the use of crowned rollers makes the temperature lower.

In summary, we have verified theoretically that torque on a thrust needle roller bearing in mixed lubrication conditions can be decreased by introducing double row crowned rollers. A lower torque in turn helps lower the temperature on the contact surface and prevents bearing material failure.
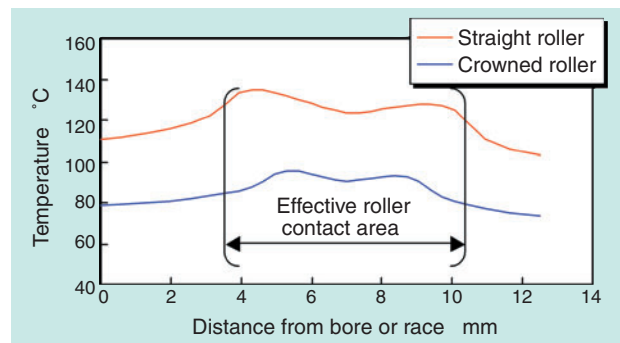
Fig. 16 Estimated temperature on raceway by FEM

Fig. 15 Oil film parameter and factors of bearing frictional torque

4. Conclusion

The authors experimentally and theoretically investigated the failure mechanism of thrust needle roller bearings in low viscosity lubrication conditions. From the results of various tests, we have verified that heat generation on the inner edge of the raceway rolling mark and the resultant plastic fluidity of the raceway surface cause surface-initiated flaking on these bearings. We have learned that under a low viscosity lubrication condition, spin is largely responsible for the frictional torque on a thrust needle roller bearing and that spin-induced slip can be decreased and excessive heat generation inhibited by introducing crowned rollers and a double row arrangement. Low heat generation helps suppress plastic fluidity of the raceway, leading to a longer bearing life.

The double row roller arrangement is described in detail in the article "Double Row Thrust Needle Bearings" in this edition of the **NTN** Technical Review.

References

1) Kenji Tamada, Factors affecting the life of thrust needle bearings, Tribology Conference Preprints (Tokyo 2002-5), 131.

2) V.M.Hauk, Evaluation of macro- and micro-residual stresses on textured materials by X-ray, neutron diffraction and deflection. measurements, Adv. X-ray Anal., 29(1986), 1.

3) Hiroki Fujiwara, Kenji Fujii, Torque analysis for double row thrust needle roller bearings, The Japan Society for Precision Engineering 2003 Spring Meeting Scientific Lectures Proceedings, (2003), 585.

4) J.A.Greenwood and J.H.Tripp, The Contact of Two Nominally Flat Rough Surfaces, Proc. Inst. Mech. Eng., Tribol., 185, 48/71(1970-71), 625.

5) Masayoshi Muraki, Yoshitugu Kimura, Research into traction characteristics of lubricants (2nd report) "Thermal analysis of traction with nonlinear viscoelasticity", Junkatsu, 28 (1983), 753.

6) R.S.Zhou and M.R.Hoeprich, Torque of tapered roller bearings, Trans. ASME, J. Tribol., 113(1991), 590.

Photos of authors
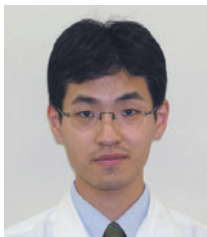
Hiroki FUJIWARA

Technical Research Dept.
Research & Development Center

Kenji TAMADA

Intellectual Property
Planning Dept.

Double-Row Thrust Needle Roller Bearings for Automotive Air Conditioners and Automatic Transmissions
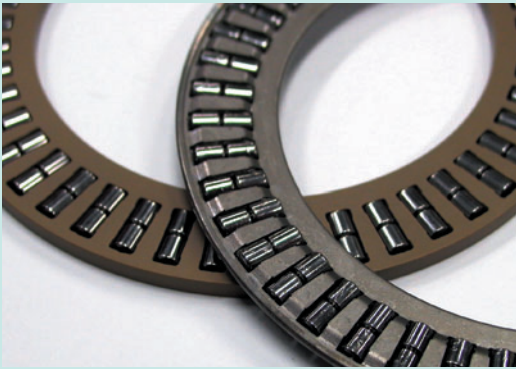
Kosuke OBAYASHI*

In order to meet the customer's need for longer service life, lower torque and lower noise bearings, **NTN** has developed double-row thrust needle roller bearings.

By using two rows of needle rollers in each retainer pocket and by optimizing the roller shape, **NTN** has successfully minimized roller slippage, achieved extended service lives and reduced torque and noise in thrust bearings.

1 Introduction

In recent automotive bearing applications, smaller amounts of lower viscosity lubricants are being used to achieve better fuel consumption. As a result, the operating conditions for bearings have become increasingly severe.

In this context, a unique problem for thrust needle roller bearings have decreased bearing life because of roller slipping. Bearings with longer lifespans are needed.

We recently developed "double-row thrust needle roller bearings" to cope with this market need. These bearings have a double-row roller arrangement to inhibit the slipping of needle rollers and to achieve longer life through prevention of surface-start failure. They also have lower torque and, through roller shape optimization, lower noise level.

For automotive air-conditioner compressors, we have developed a resin cage to achieve lighter weight and lower noise. For automatic transmissions, we designed a new sheet steel cage with inner and outer circumferences that are secured by a full enclosure technique to prevent cage loosening and to enhance cage mechanical strength. These cage types are described below.

2. Features of double-row thrust needle roller bearings (for automotive air-conditioner compressors)

The thrust bearings for automotive air-conditioner compressors are run with limited amounts of low-viscosity lubricant in order to improve the capability of the compressors. Lower viscosity lubrication will be further needed to help realize better automobile fuel efficiency. Reduced bearing life poses a problem to be solved.

In addition, as CFC refrigerant is replaced with CO_2 refrigerant to help preserve the global environment, a higher refrigerant compression ratio is increasingly needed, which in turn leads to decreased bearing life.

Our newly developed double-row thrust needle roller bearing **(Photo 1)** maintains load carrying capacity and suppresses roller slipping. The double-row roller arrangement prevents surface-start failures that result from disrupted oil film on bearing rolling surfaces. Our new bearing adopts optimal roller geometry (optimal end face shape, roller circularity and crowning) and a lightweight resin cage (of high wear resistant material) to achieve longer bearing life, lower torque and lower noise.

*Automotive Sales Headquarters   Needle Roller Bearings Engineering Dept.
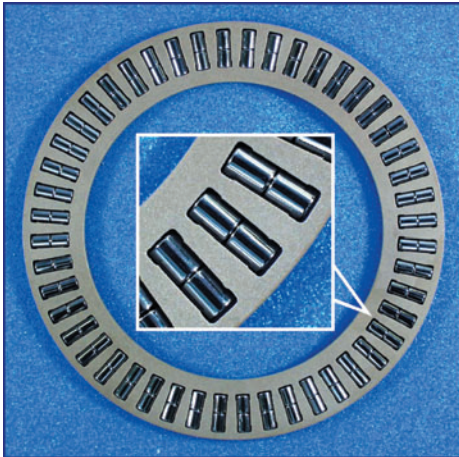
Photo 1 Double-row thrust needle roller bearings for car air conditioners
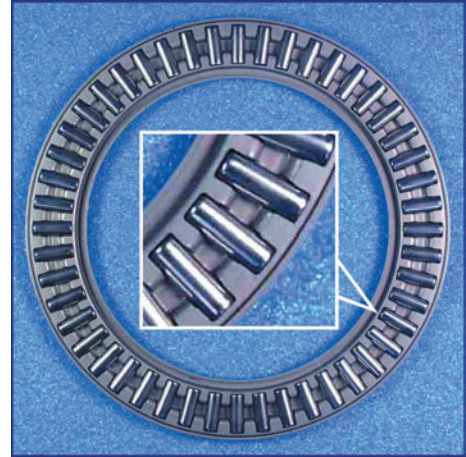
Photo 2 Current bearings

[Comparison with single-row bearing in terms of performance]

(NTN's test results for automotive air-conditioner compressors)

① **Life (surface-starting failure) : 12 times as long**
② **Rotation torque**   **: 50% reduction**
③ **Noise**   **: 8 dBA lower**

2.1 Performance evaluation

To evaluate performance of thrust needle roller bearings for automotive air-conditioner compressors, we compared our newly developed bearing with a standard bearing that has a W-type sheet steel cage and a single-row roller arrangement (**Photo 2**). We subjected both bearing types to rotation torque and running noise measurements after a bearing life test. This section summarizes the performance evaluation tests of both bearing types.

2.1.1 Bearing specification

The bearings used for the performance evaluation have 60 mm inside diameters, 85 mm outside diameters and are 3 mm wide (roller diameter).

Table 1 lists the data for both our newly developed bearing and the standard bearing.

Table 1 Comparison of bearing specifications

	Newly developed bearing (double-row type)	Standard bearing (single-row type)
Bearing size	ϕ60ID$\times$ ϕ85OD $\times$3W (roller diameter)	
Cage type	Resin cage	W-type sheet steel cage
Number of rollers	96 (48 $\times$2 rows)	48
Roller length (mm)	3.8	7.8

2.1.2 Bearing life test

For the bearing life test, we used the **NTN** vertical thrust bearing test rig illustrated in **Fig. 1** and the **NTN** horizontal thrust bearing test rig shown in **Fig. 2**.
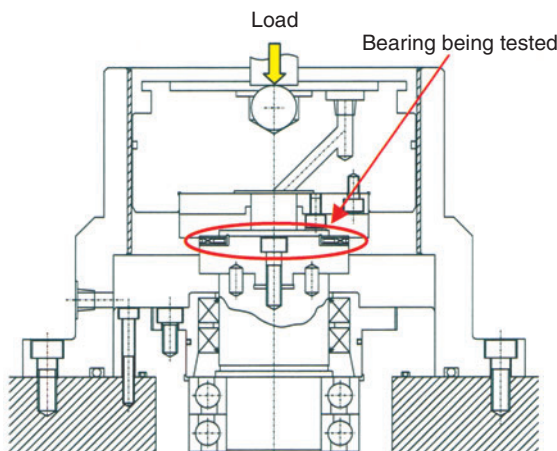
Fig 1 **NTN** vertical type thrust bearing test rig
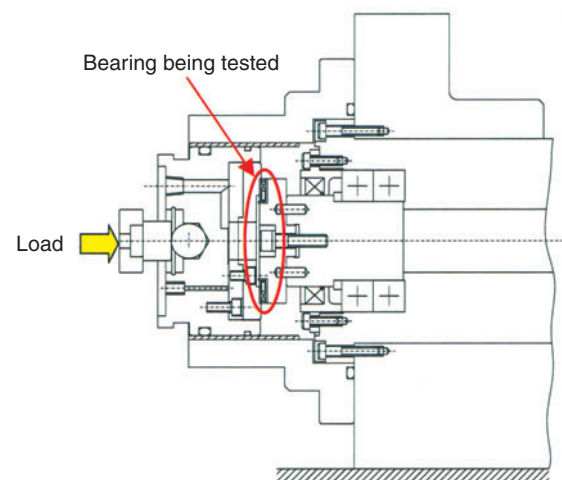
Fig 2 **NTN** horizontal type thrust bearing test rig

(1) Test conditions

Two sets of bearing life test conditions are given in **Tables 2** and **3**.

Table 2 Life test condition 1

Test rig	**NTN** vertical thrust load test rig
Axial load	P/C = 0.4 with standard bearing *
Bearing speed	5000 min⁻¹
Misalignment on race	2/1000
Lubrication	Turbine #32, circulating lubrication
Number of samples	n=8, each bearing type

*P/C : load/basic dynamic rated load

Table 3 Life test condition 2

Test rig	**NTN** horizontal type thrust load test rig
Axial load	P/C = 0.4 with standard bearing
Bearing speed	5000 min⁻¹
Lubrication	PAG (3%) + clean kerosene (97%), circulating lubrication
Number of samples	n=8, each bearing type

(2) Test results

The life test result of test condition set 1 is summarized in **Fig. 3**, and that from test condition set 2 is given in **Fig. 4**.

Compared with the standard bearing, our newly developed bearing exhibited a life more than 12 times as long in terms of L_{10} under both test condition sets 1 and 2.

2.1.3 Rotation torque measurement

For measuring the rotation torque of the bearings being tested, the **NTN** vertical thrust bearing rotation torque test rig was used.

The test rig is illustrated in **Fig. 5**

(1) Measuring conditions

The rotation torque measuring conditions are listed in **Table 4**.

Table 4 Measurement condition of rotation torque

Test rig	**NTN** vertical-type thrust torque test rig
Axial load	P/C = 0.1, 0.15, 0.2 with standard bearing
Bearing speed	1000 min⁻¹
Lubrication	Category 1 spindle oil, overall coating
Measuring duration	60 sec.
Number of samples	n=10, each bearing type
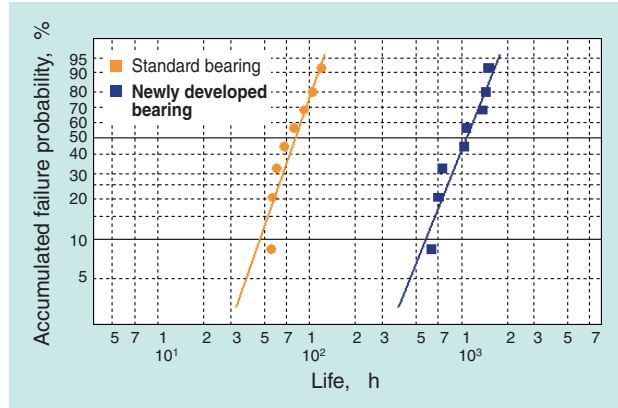
Fig 3 Result of life test condition 1 with misalignment for car air conditioners
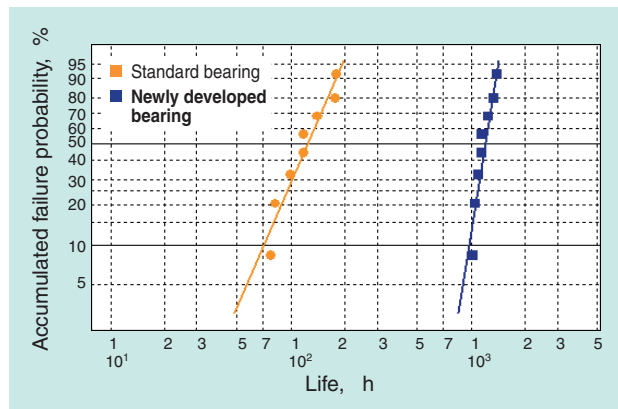
Fig 4 Result of life test condition 2 with lean lubrication for car air conditioners
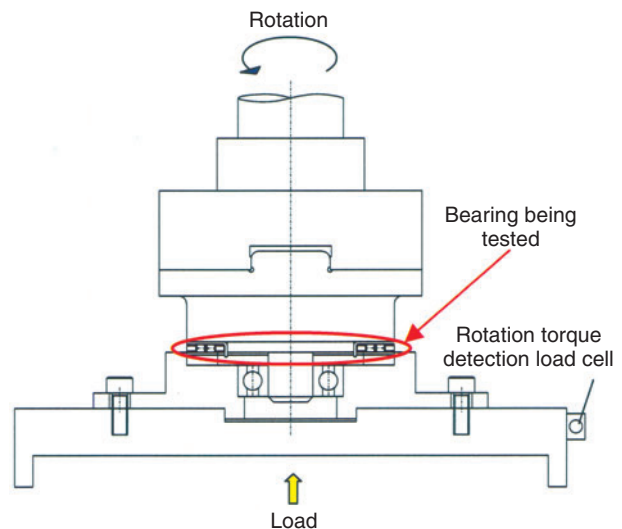
Fig 5 **NTN** vertical type thrust bearing rotation torque test rig

(2) Measurement results

The measurement results of rotation torque are plotted in **Fig. 6**.

These results verify that the newly developed bearing has achieved 47 to 51% torque reduction compared with the standard bearing.

This torque reduction was achieved by both the double-row roller arrangement, which reduced spin slippage, and the cage resin material.

The measured rotation torques were dependent on loading, but rotation speed caused virtually no variation.
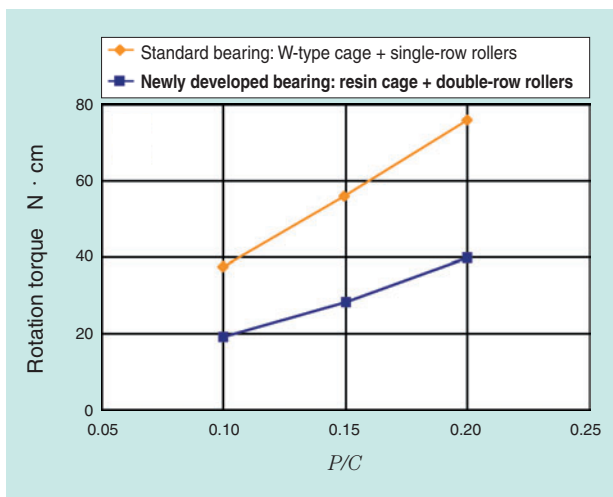
2.1.4 Sound measurement

For sound measurement, the **NTN** sound level measuring system was used.

(1) Measuring conditions

The sound level measurement conditions are summarized in **Table 5**.

(2) Measurement results

The sound level measurement results are given in **Fig. 7**.

Compared with the standard bearing, the newly developed bearing achieved a sound level reduction of approximately 8 dBA at 1800 min^{-1}, and approximately 11 dBA at 3600 min^{-1}.

The contributing factors for these reductions are the resin-made cage and the optimized roller shape.

Fig 6 Measurement result of rotation torque

Table 5 Measurement condition of sound level

Test rig	**NTN** sound level measuring system
Axial load	100N
Measurement distance	45° angle, 100mm
Bearing speed	1800 min^{-1}, 3600 min^{-1}
Lubrication	Compressor oil, droplet lubrication before running
Measuring duration	50 sec.
Number of samples	n=10, each bearing type
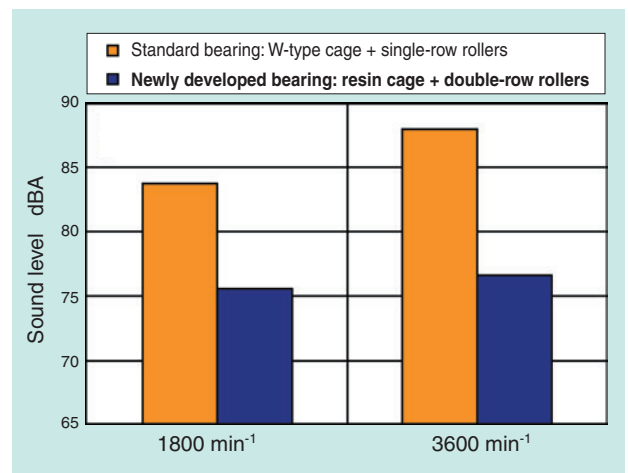
Fig 7 Measurement result of sound level

3. Feature of double-row thrust needle roller bearings (for automatic transmissions)

Featuring a lower profile in assembled units and a greater load carrying capacity, thrust needle roller bearings are often used for automatic transmissions in automobiles. However, the use of lower viscosity automatic transmission oils is increasing to alleviate shift shock and improve fuel efficiently. For this reason, the life of bearings used in this application may be shortened.

Our newly developed double-row thrust needle roller bearing (**Photo 3**) for automatic transmissions has a double-row roller arrangement to inhibit roller slipping while maintaining the necessary load carrying capacity. The newly developed bearing features optimized roller geometry (with optimized roller end face shape, roller roundness and crowning shape) to achieve a longer bearing life, lower rotation torque and quieter operation.

In addition, because thrust bearings are used in eccentric rotation conditions in automatic transmissions, cages can be pinched and damaged by bearing rings and the cage halves themselves can split apart. Therefore, higher cage strength is needed. To address this problem, we have invented and developed a new cage uniquely shaped with full enclosure of inner and outer ring circumferences, improving cage mechanical strength. This arrangement prevents separation of cage halves or displacement between the halves and allows integration of the cage with the bearing ring to form a unified structure.

[Comparison with single-row bearing]

(NTN's test results assuming application in automatic transmissions)

① **Life (surface-starting failure)**
  : **Three times as long**
② **Rotation torque** : **40% decrease**
③ **Cage strength** : **1.6 times as strong**
④ **Sound level** : **Decrease of 3 dB**

3.1 Performance evaluation

Under conditions that simulated automatic transmissions, the newly developed double-row thrust needle roller bearing was compared with a standard bearing that has a W-type sheet steel cage and single-row rollers. Performance evaluations were conducted through FEM analysis, bearing life tests, eccentric rotation tests, rotation torque measurements and sound level measurements. The results are summarized below.

3.1.1 Bearing specifications

The bearings used for performance specification were 60 mm inside diameter, 85 mm outside diameter and are 3 mm wide (roller diameter).

The bearing specifications for the newly developed bearing and the standard bearing are summarized in **Table 6**.

Table 6 Comparison of bearing specifications

	Newly developed bearing (double-row type)	Standard bearing (single-row type)
Bearing size	ϕ60ID×ϕ85OD ×3W (roller diameter)	
Cage type	Sheet steel cage of new shape	W-type sheet steel cage
Number of rollers	96 (48 ×2 rows)	48
Roller length (mm)	3.8	7.8
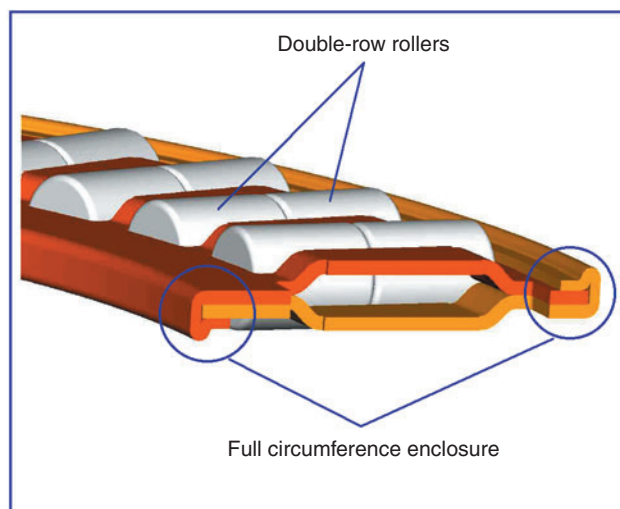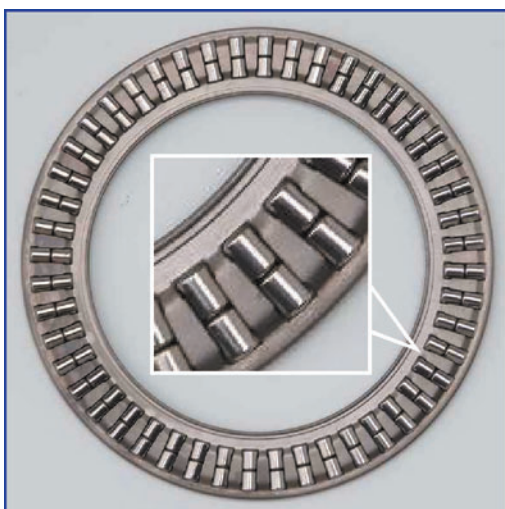
Photo 3 Double-row thrust needle roller bearings for automatic transmissions

3.1.2 FEM analysis

The results of FEM analysis for the newly developed bearing and the standard bearing are summarized below.

(1) Analysis conditions

The analysis conditions are shown in **Fig. 8**.

(2) Analysis results

The analysis results are given in **Fig. 9**.

The maximum principle stress on the standard bearing was compared with that on the newly developed bearing. As a result, the stress on the newly developed bearing was 0.62 relative to that of the standard bearing rating of 1. The cage of the newly developed bearing has increased strength.

Note: The weight of the newly developed bearing is 5% lighter than the standard bearing.

Load (50% load on the outer circumference surface and 50% load on the bars and pockets)

Fully constrained (inner circumference surface)
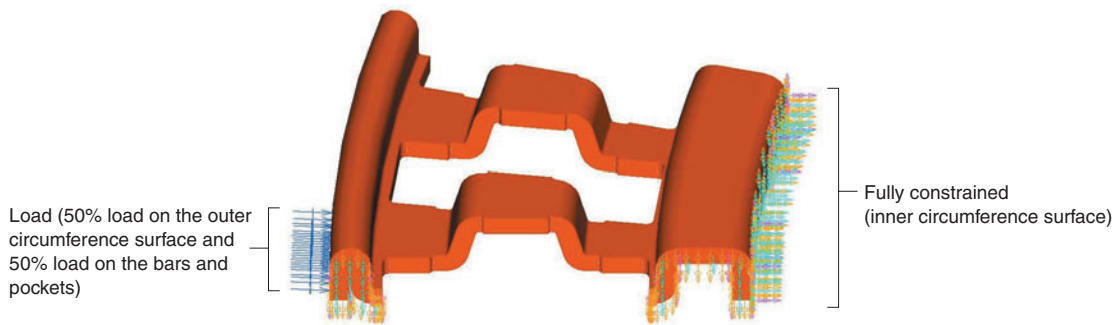
Fig 8 Analytical condition

Standard bearing

Newly developed bearing

Location where maximum principle load occurs
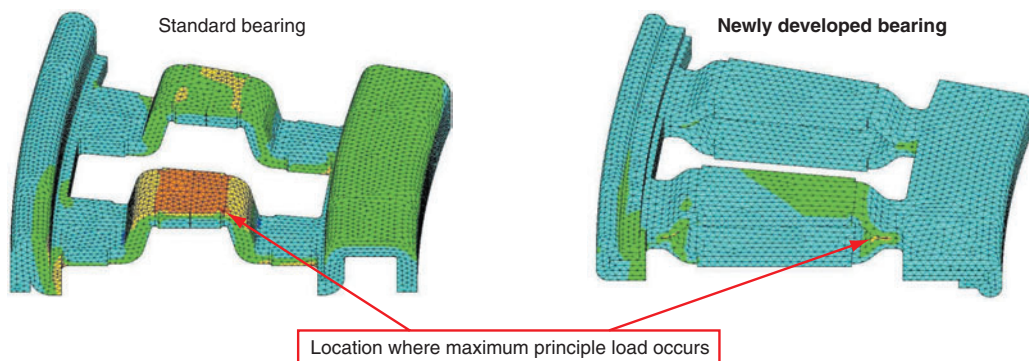
Fig 9 Analytical result

3.1.3 Bearing life test

For the bearing life test, the **NTN** vertical thrust test rig illustrated in **Fig. 1** was used.

(1) Test conditions

The test conditions are summarized in **Table 7**.

(2) Test results

The results of bearing life tests are summarized in **Fig. 10**.

In L_{10} terms, the life of the newly developed bearing was three times as long as that of the standard bearing.

Table 7 Life test condition

Test rig	**NTN** vertical type thrust test rig
Axial load	$P\diagup C$=0.4 on standard bearing
Bearing speed	8000 min^{-1}
Lubrication	ATF, circulating lubrication Oil temperature, 100˚C
Number of samples tested	n=8 each
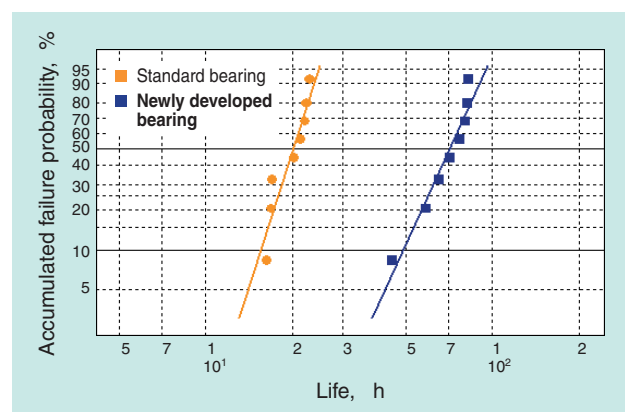
Fig 10 Result of life test for automatic transmissions

3.1.4 Eccentric rotation test

If the inner ring and outer ring rotate on an offset rotation center and the eccentricity is greater than the clearance of the bore, then the cage will be pinched between the races (inner ring and outer ring). Consequently, the cage is subjected to a compression force in the radial direction and a shear force in the rotation direction resulting from the difference between the rotation speed of the inner race and that of the outer race, leading to eventual fracture.

The situation above exists particularly in the torque converters of automatic transmissions. To address this problem, we checked the mechanical strength of the new cage shape.

Fig 11 **NTN** vertical type thrust bearing test rig for eccentricity rotation

Table 8 Eccentricity rotation test condition

Test rig	**NTN** eccentric rotation vertical thrust test rig
Axial load	$P／C$=0.3 on standard bearing
Bearing speed	3000 min^{-1}
Eccentricity (rotation axis)	0.5mm
Lubrication	ATF, circulating lubrication Oil temperature, 100˚C
Number of samples tested	n=3 each

Table 9 Result of eccentricity rotation test

	Bearing No.	Running time, h	Remarks
Standard bearing	1	53.4	Ring-shaped fracture on the cage bar bore side
	2	51.5	↑
	3	60.5	↑
Newly developed bearing	1	Suspended at 265.0 hrs.	No failure
	2	Suspended at 265.0 hrs.	↑
	3	Suspended at 265.0 hrs.	↑

For the eccentric rotation test, the **NTN** eccentric rotation vertical thrust test rig was used.

The test rig used is illustrated in **Fig. 11**.

(1) Test conditions

The test conditions for the eccentric rotation test are summarized in **Table 8**.

(2) Test results

The results of the eccentric rotation test are given in **Table 9**.

A ring-shaped fracture occurred on the bore side of the cage bar of the conventional bearing. In contrast, no fracture was found in the newly developed cage.

Compared with the conventional cage, the new cage, with a unique form created by full enclosure of inner and outer circumferences, exhibited improved strength that matches the results of FEM analysis.

3.1.5 Rotation torque measurement

The rotation torque of the bearings was measured with the **NTN** vertical thrust torque test rig illustrated in **Fig. 5**.

(1) Measuring conditions

The rotation torque measuring conditions are summarized in **Table 10**.

(2) Measurement results

The rotation torque measurement results are illustrated in **Fig. 12**.

Table 10 Measurement condition of rotation torque

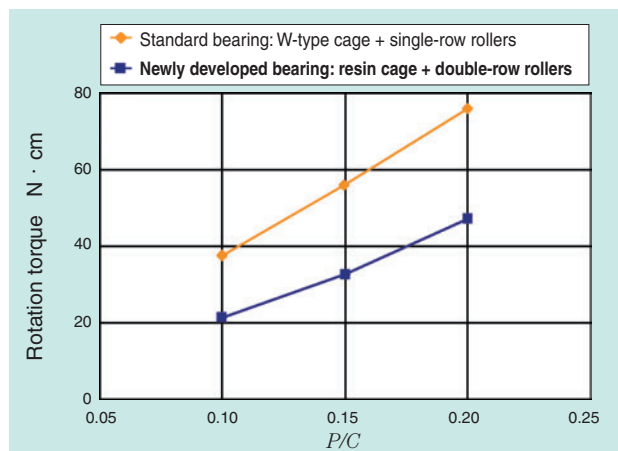| Test rig	**NTN** vertical thrust torque test rig
Axial load	$P／C$ = 0.1, 0.15, 0.2 with standard bearing
Bearing speed	1000 min^{-1}
Lubrication	Category 1 spindle oil, overall coating
Measuring duration	60 sec.
Number of samples	n=10, each bearing type

Fig 12 Measurement result of rotation torque

As a result of the measurement, we found that compared with the standard bearing, the rotational torque of the newly developed bearing is 38-43% lower.

The primary factor contributing to the torque reduction is the reduction of spin slipping due to the double-row roller design.

When comparing the newly developed cage with the conventional cage, other possible contributing factors are a smaller contact area between the cage and shaft and a smaller contact width between the cage and rollers.

We also learned that the rotation torque is dependent on the load applied to the bearing tested and is least affected by the bearing running speed.

3.1.6 Sound level measurement

For sound level measurement, the **NTN** sound level test system was used.

(1) Measuring conditions

The sound level measuring conditions are summarized in **Table 11**.

(2) Measurement results

The sound level measurement results obtained are illustrated in **Fig. 13**.

At 1800 min-1, the sound level of the newly developed bearing was approximately 3 dBA lower, and at 3600 min^{-1}, approximately 2 dBA lower.

The factor contributing to this sound suppression is optimization of the roller geometry.

Fig 13 Measurement result of sound level

Table 11 Measurement condition of sound level

Test rig	**NTN** sound level measuring system
Axial load	100N
Measurement distance	45˚ angle, 100mm
Bearing speed	1800 min^{-1}, 3600 min^{-1}
Lubrication	ATF, droplet lubrication before operation
Measuring duration	50 sec.
Number of samples	n=10, each bearing type
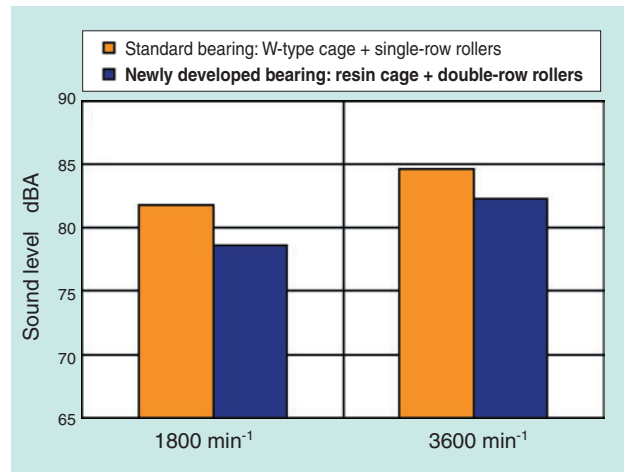
4. Conclusion

This report described our newly developed double-row thrust needle roller bearings.

In this report, the scope of application for our newly developed bearings were limited to automobile air-conditioner compressors and automatic transmissions and we evaluated them only for these applications. However, these new bearings are also capable of applications in other types of machinery.

The operating conditions for bearings will become increasingly severe. Therefore, we will remain committed to the development and marketing of novel bearing products that only **NTN** can offer, always aiming to increase customer satisfaction and satisfy market needs.

Photos of author

Kosuke OBAYASHI

Automotive Sales Headquraters
Needle Roller Bearings
Engineering Dept.

Development of In-Wheel Type Integrated Motor Axle Unit

Minoru SUZUKI*
Dawei WANG*

NTN has been developing the in-wheel type integrated motor axle unit for electric vehicles. The unit accomplishes compact size and light weight by integrating a hub bearing, a cycloid reducer and a high-speed motor, realizing least increase in the unsprung mass of in-wheel motor vehicles. This paper introduces the design concept and basic performance of the unit.

1. Introduction

Recently, fuel-cell electric vehicles (FCEV) and electric vehicles (EV) are being regarded as promising next generation automobiles because of their reduced impacts on the environment. The drive systems for EVs, including FCEVs, can be categorized into two types. One type consists of a motor situated on the chassis that transmits driving power to the tires through a drive train, like a conventional internal combustion engine. The other type is an in-wheel motor system in which a motor is incorporated into each wheel. On the positive side, an in-wheel motor system allows the provision of room space equivalent to or better than that possible in engine vehicles and helps improve vehicle stability because each wheel is driven independently. However, on the negative side, in-wheel motor system lead to greater unsprung mass that in turn results in decreased drivability and riding comfort. Therefore, this issue needs to be resolved so that EVs with in-wheel motor axle units can be more commonly used. NTN has been developing an in-wheel type integrated motor axle unit, aiming to reduce unsprung mass by creating a compacter, lighter axle unit. This report describes the design

concept and initial characteristics of this novel axle unit.

2. Newly developed axle unit specifications

We are currently developing an in-wheel type integrated motor axle unit that, when built into four wheels, has power equivalent to the 1500 cc gasoline engine of a Japanese compact car. The target specifications of our axle unit are summarized in **Table 1**. The structure of the axle unit is schematically illustrated in **Fig. 1**, and an image of the axle unit built into a tire is shown in **Fig. 2**.

Table 1 Target specification of axle unit

Max. output	20kW
Max. torque	490Nm
Max. velocity	150km/h (when built into 14" tires)）
Mass	Approx. 20 kg
Reducer type	Cycloid reducer
Reduction ratio	1/11
Motor type	Axial gap type permanent magnet synchronization motor
Max. motor speed	15000rpm

---

*New Product Development R&D Center   New Product Development Dept.
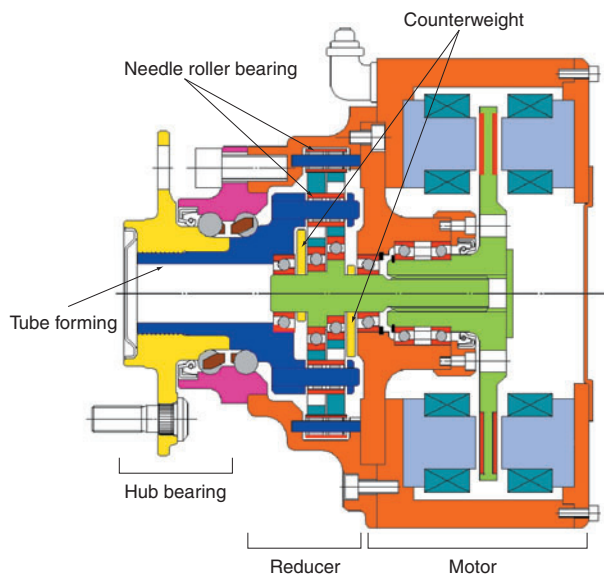
Fig. 1 Schematic of axle unit
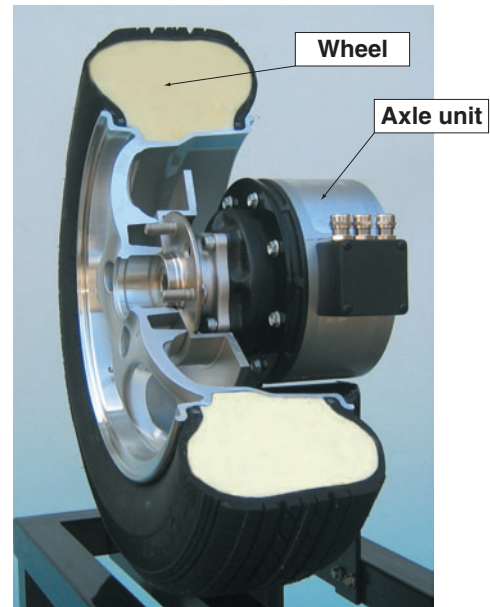
Fig. 2 Installation of the unit

3. Design concept

(1) Application of reducer

Usually, the size of a motor is dependent on the maximum torque generated. Since direct driving in-wheel motor axle units do not have reducers, the motors must provide greater torque, making the motors unavoidably larger. As a proportion of the whole axle unit weight, motor weight is large. Therefore, to design a compact, lightweight axle unit, employment of a compact, lightweight motor is necessary. We attempted to decrease the maximum torque needed for the motor by incorporating a reducer and selecting a high-speed motor so that a smaller motor could fulfill the requirements.

(2) Type of reducer

We sought a reducer type that helps satisfy the smaller space requirement and provides a greater reduction ratio. With a 2K-H planetary gear reducing mechanism, which is a type often used as a reducer system, the reduction ratio per stage is in the range of 1/4 to 1/6. To achieve a higher reduction ratio with this type, at least two stages of gear rows are necessary, and this in turn leads to a need for a large, complicated reducer.

In seeking a solution, we focused on cycloid reducing mechanisms [1-3], all of which are K-H-V planetary gear reducing mechanisms, such as the one illustrated in **Fig. 3**. With this mechanism, the final reduction ratio is dependent on the difference in the numbers of teeth between the gears. Thus, even one gear train can achieve a greater reduction ratio.

As shown in **Fig. 4**, the gears used are an external gear that features an epitrochoidal curve gear tooth profile and an internal gear with a circular arc tooth profile (hereafter referred to as an outside pin). Only autorotation motion is utilized with the inside pin situated on the bore of the eccentrically oscillating external gear.
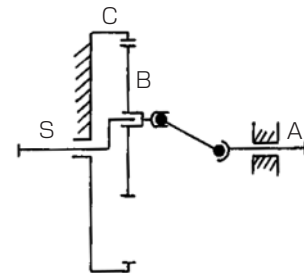
Fig. 3 Schematic of K-H-V type planetary gear
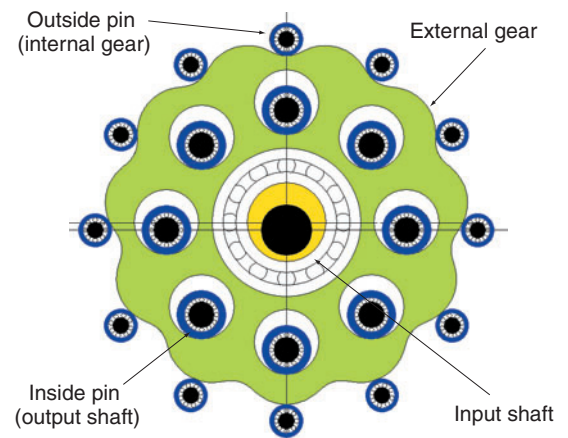
Fig. 4 Basic structure of reducer

Use of this gearing arrangement allows many teeth to remain in simultaneously meshed relations, and, as a result, transmission torque per unit volume can be greater, helping realize a compacter reducer design.

The hub bearing inner ring raceway groove is formed on the flange member to which the inside pins are secured, and the flange member and the hub bearing inner ring member with the hub flange are fastened together using **NTN**'s propriety tube forming technique, which is also applied to our 4th generation hub bearings. The tube forming technique has lead to a simple fastener structure between the hub and the reducer, allowing further reduction of the axle unit size.

(3) Higher reducer efficiency

Generally, the transmission efficiency of a two-stage 2K-H planetary gear reducer with involute gears of a reduction ratio of 1/10 to 1/20 is approximately 95%. The transmission efficiency with a cycloid reducing mechanism is said to be lower. One possible reason for this is that when the eccentrically oscillating external gear rotates, sliding contact occurs between the outside pin and the external gear and between the inside pin and the external gear.

Therefore, we attempted to reduce the loss at the meshed portions by incorporating rolling contact bearings into these sliding contact areas.

(4) Higher reducer speed

With a cycloid reducing mechanism, in principle, the external gear eccentrically oscillates and the inertial force induced by this motion causes the vibration of the component perpendicular to the rotation axis to increase. Usually, therefore, another set of reducers (external gear) acting in reverse phase is incorporated to dampen this vibration. However, the couple of force resulting from unbalanced inertia on the axes of the two external gears perpendicular to the rotation axis still remains, and the effect of the unbalance is prominent when the reducers run at higher speed. Our axle unit incorporates a counterweight to dampen the vibration induced by this couple of force resulting from unbalance inertia.

(5) Bearing layout

The motor rotating shaft has a cantilever support structure from the reducer housing. Though not shown in **Fig. 1**, the knuckle is formed around the reducer outside periphery as a part of the reducer housing, allowing the wall thickness of the motor housing to be thinner.

Thanks to this bearing layout, the space from the hub bearing to the motor bearing can be lubricated

with the same lubricant, the number of seals can be decreased, simplifying the structure of the axle unit, and the axial direction length of the axle unit can be shorter.

Though not shown in **Fig. 1**, a dog clutch or other type of parking brake, a component absolutely necessary for an axle unit, is located in the right end of the motor.

4. Performance Test Results

The results of evaluation tests are described below for the basic performance of a motor-less axle unit that consists of a reducer and a hub bearing.

(1) The efficiency of two reducer types was measured. One reducer type was a rolling contact bearing type that incorporated a needle roller bearing into the sliding contact area between each inside pin and outside pin set on the reducer. The other reducer type was a sliding contact bearing type lacking incorporated needle roller bearings. As shown in **Fig. 5**, at the input rotation speed of 3000 rpm, the rolling contact type reducer exhibited an efficiency approximately 5% better than that of the sliding contact type reducer (maximum efficiency of 94%), showing the effectiveness of the rolling contact bearing. This effect is nearly equivalent to the effect obtained from a two-stage configuration of an involute gear type 2K-H planetary gear reducer. An oil bath method was used for lubrication.
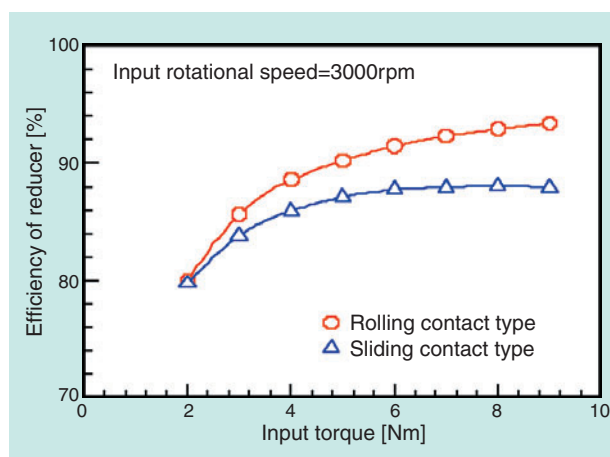

Fig. 5 Efficiency of reducer

(2) Acceleration pickup devices were installed to the outer periphery and end face of the reducer housing to measure the radial vibration and axial vibration on the running reducer. The measurement results are plotted in **Fig. 6**. Though no load was applied to the reducer, it ran smoothly without developing significant vibration at speeds up to 15000 rpm.
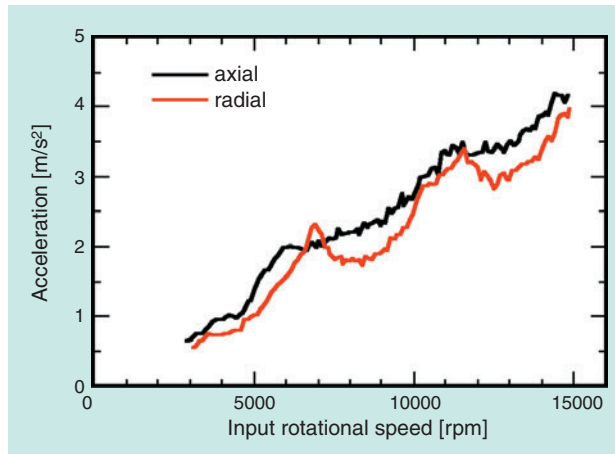

Fig. 6 Vibration of reducer

5. Conclusion

Seeking to realize a compacter and lighter in-wheel integrated motor axle unit, we adopted a cycloid reducer mechanism. By replacing the sliding contacts of the reducer with a rolling contact arrangement, a transmission efficiency of approximately 94% was achieved. We also verified that, though not under an actual load, the reducer can run smoothly without developing significant vibration at speeds up to 15000 rpm.

Since axle units are critical automotive components, we are going to improve the reliability of our unit through evaluation with various tests under actual automobile operating conditions.

References
(1) Muneharu Morozumi: Theory and design calculation technique for planetary gears and differential gears, Nikkan Kogyo Shinbun, Ltd., p1-6 (1989).
(2) Japan Institute of Plant Maintenance: Book of reducers, Japan Institute of Plant Maintenance, p22-26 (1994).
(3) Sumitomo Heavy Industries, Ltd.: Catalog C2001-5.

Photos of authors

Minoru SUZUKI

New Product Development
R&D Center
New Product Development Dept.

Dawei WANG

New Product Development
R&D Center
New Product Development Dept.

Development of the Mono Ring CVT

- Principle and Mesurement of Transmission Efficiency -

Yuichi ITOH*
Tomoya SAKAGUCHI*
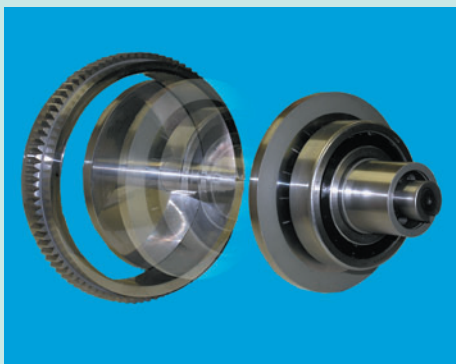
There has been several variations of CVT (Continuously Variable Transmission) designs over the years. A CVT can give high efficiency, low fuel consumption and smooth drivability to automotive applications by changing output ratios with no actual gear steps. However, the mechanism of a CVT can be intricate and contain many parts.

We have designed a new CVT, which is compact, simple and has no additional outside controllers. This CVT is composed of a ring with teeth, a set of V-pulleys, and an output cogwheel. It has been named the Mono-Ring CVT (MR-CVT) because the single ring gear carries all the torque.

This paper reports on the configuration and principle of the MR-CVT. The efficiencies of a prototype MR-CVT were also measured confirming the validity of the basic design.

1. Introduction

Various technologies have been invented for automotive continuously variable transmissions (CVT).[1][2] Recently, multi-stage designs have been increasingly used for automotive automatic transmissions (AT) in order to achieve better transmission of engine power and smooth gear change. By adopting "stepless transmission," the most advanced form of multi-stage transmission, CVTs realize higher efficiency, lower fuel consumption and extremely smooth drivability.

This report introduces a compact CVT we are currently developing that consists of a smaller number of components and does not need an external control system.

Though it resembles the Bayer CVT, our CVT can also suppress spin at the contact points. In addition, though similar to a belt type CVT because it employs V-pulleys, our CVT uses them in the drive section only and one toothed ring is inserted between the V-pulleys to transmit the power to the output gear.

We call our CVT the Mono-Ring CVT (MR-CVT) because a single (mono) toothed ring is used as the medium. The structure, operating principle and measured transmission efficiency of the MR-CVT are described below.

---

*New Product Development R&D Center   Mechatronics Research Dept.

2. Mono-Ring CVT (MR-CVT)

The internal structure of our prototype MR-CVT is illustrated in **Fig. 1**. The input shaft and the output shaft are parallel to each other in a offset relation, and both are supported by bearings fixed to the housing. The input shaft is equipped with a pair of V-pulleys that rotate concentrically and in synchronicity with the input shaft, so the V-pulleys can shift in the axial direction. The input shaft has ball splines to allow the V-pulleys to shift in the axial direction and transmit torque smoothly. A right-hand and left-hand pair of ballscrews is included on both ends of the input shaft. By turning the shafts of the ballscrews, the V-pulleys can be shifted axially.

The V-pulleys are supported on the shafts of the ballscrews by angular contact ball bearings. The pair of V-pulleys sandwich a toothed ring, where the ring has with teeth around its circumference. The two guide rollers direct the toothed ring and swing the output gear with it as a unit. This swing varies the contact radius of the toothed ring with the V-pulleys, making stepless speed change possible. The direction of rotation of the V-pulleys is regulated in the counterclockwise direction only by means of a self-adjustment mechanism described later. The toothed ring and the output shaft are linked with a spur gear.

The basic mechanism of the MR-CVT is schematically illustrated in **Fig. 2**. Since the input torque is transmitted to the toothed ring by the V-

Fig. 1 Schematic view of MR-CVT
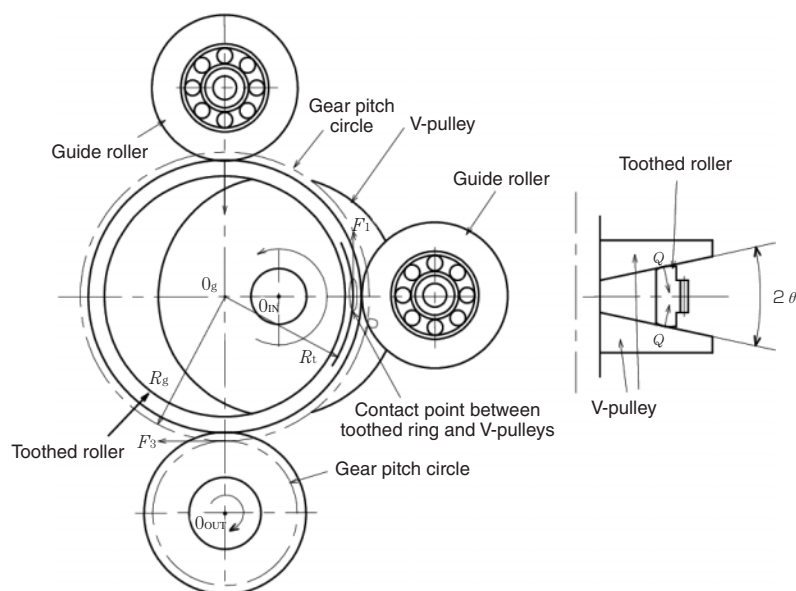
Fig. 2 Basic mechanism of MR-CVT

pulleys, the toothed ring is subjected to the frictional force F_1.

The torque transmitted to the toothed ring is further transmitted to the output shaft gear through its teeth, and, as a result, the reaction force F_3 from the transmission force acts on the toothed ring. The relation between F_1 and F_3 can be described by formula (1), where R_t and R_g are the radii from the toothed ring center at the F_1 and F_3 application points, respectively. For accuracy, the pressure angles of the gears should be considered, but for convenience of calculation, we took the pressure angles as zero.

$$F_3 = F_1 \times \frac{R_g}{R_t} \quad \cdots\cdots\cdots\cdots\cdots\cdots\cdots\cdots\cdots\cdots \quad (1)$$

The force F_3 also functions to force the toothed ring into the V-pulleys. The contact force Q caused by this force F_3 and acting from the V-pulleys onto the toothed ring can be described by formula (2) that takes the slope angle of the V-pulleys as θ.

$$Q = \frac{F_3}{2\sin\theta} \quad \cdots\cdots\cdots\cdots\cdots\cdots\cdots\cdots\cdots \quad (2)$$

If the friction coefficient at this contact area is assumed to be μ, then formula (3) holds.

$$\mu = \frac{F_1}{2Q} \quad \cdots\cdots\cdots\cdots\cdots\cdots\cdots\cdots\cdots\cdots \quad (3)$$

From formulas (1), (2) and (3), formula (4) is derived.

$$\sin\theta = \mu \times \frac{R_t}{R_g} \quad \cdots\cdots\cdots\cdots\cdots\cdots\cdots\cdots \quad (4)$$

Since the toothed ring is stable when the above relationship is valid, a self-adjustment mechanism is formed in which the friction coefficient μ is determined from the slope angle θ of the V-pulleys even if operating conditions vary.

This is because F_1 and F_3 vary according to the input torque, so the contact force Q occurring between the V-pulleys and the toothed ring automatically varies.

As shown in **Fig. 2**, when O_g-O_{out} and the O_g-O_{in} are perpendicular to each other, the optimal angle θ of the V-pulleys can be determined based on the geometrical relationship of the toothed ring alone and the friction coefficient μ as described with formula (4). However, as the toothed ring swings on the output shaft, the O_g-O_{out} and the O_g-O_{in} are no longer perpendicular as shown in **Fig. 3**. Since the contact point between the toothed ring and the V-pulleys shifts to a point on the prolonged line from the O_g-O_{in}, the relation in formula (2) is no longer valid.

Fig. 3 shows a situation where the toothed gear is in the acceleration position (top gear side). Due to the frictional force F_1, component F_4 that forces the toothed ring into the V-pulleys occurs. Thus, the resultant force F_5 is:

$$F_5 = F_3 + F_4$$

Fig. 4 illustrates the position of the toothed ring in the deceleration position. The F_5 in this situation is:

$$F_5 = F_3 - F_4$$

If angle θ between O_g-O_{out} and O_g-O_{in} is as shown in **Fig. 3**, then from this diagram, the contact force ψ derived from the push-in force F_5 can be described by formula (5).
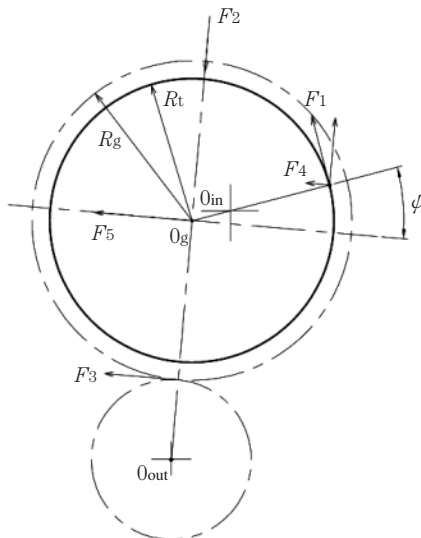
Fig. 3 Speed-up condition
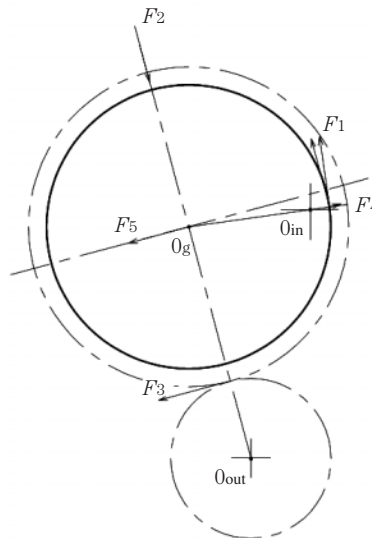
Fig. 4 Slow-down condition

$$Q= \frac{F_5}{2\sin\theta\cos\psi} = \frac{F_3+F_1\sin\psi}{2\sin\theta\cos\psi} = \frac{F_1(R_t/R_g+\sin\psi)}{2\sin\theta\cos\psi}$$
$$\cdots\cdots\cdots\cdots\cdots\cdots\cdots\cdots\cdots\cdots\cdots\cdots\cdots\cdots (5)$$

If formula (3) is substituted into the formula (5), then the optimal V-pulley inclination θ relative to ψ can be determined as a function of ψ by using formula (6) below.

$$\theta = \sin^{-1}\left[\frac{\mu\,(R_t/R_g+\sin\psi)}{\cos\psi}\right] \cdots\cdots\cdots\cdots (6)$$

In other words, the MR-CVT can have optimal efficiency if the slope angle θ, which is determined by ψ, the friction coefficient μ and the geometry of the toothed ring when it swings on the output shaft satisfy formula (6). Incidentally, the relation involving ψ, Oout-Og, R_t, Oout-Oin and the radius r from the center of the V-pulleys to the contact point is determined by the cosine theorem. In other words, the ψ can be determined based on the CVT design data.

The relation between θ and r in our prototype MR-CVT is illustrated in **Fig. 5**. As can be seen the graph as the radius of contact point r between the toothed ring and the V-pulleys increases, the slope angle also increases. Incidentally, we designed the subcurvature of the toothed ring so that the contact surface pressure between it and the V-pulleys stays below the maximum allowable level when the input torque is at maximum.

3. Test method

To verify the feasibility of the operating principle of our MR-CVT, we developed a test rig and measured the transmission efficiency of the MR-CVT.

The test rig is schematically illustrated in **Fig. 6**. Both the input and output sides of the MR-CVT were provided with a torque meter to measure the rotation speed and torque. For performance measurement of the MR-CVT, the transmission efficiency was determined based on the workload, which is the product of the rotation speed and torque of the input and output power in normal operation. On the test rig, the drive motor and the load motor were linked with an inverter, and the energy regenerated on the load motor was used for the drive motor.

The range of the gear ratio, the ratio of the rotation speed of the input shaft to that of the output shaft, was 0.3 to 1.3. The gear tooth ratio of the toothed ring (88 teeth) to the output gear (60 teeth) was 1.47. The test conditions are summarized in **Table 1**.

The lubricant used was a market-available CVT oil, and the supply inlet temperature was adjusted to 50˚C with a temperature adjustment system.
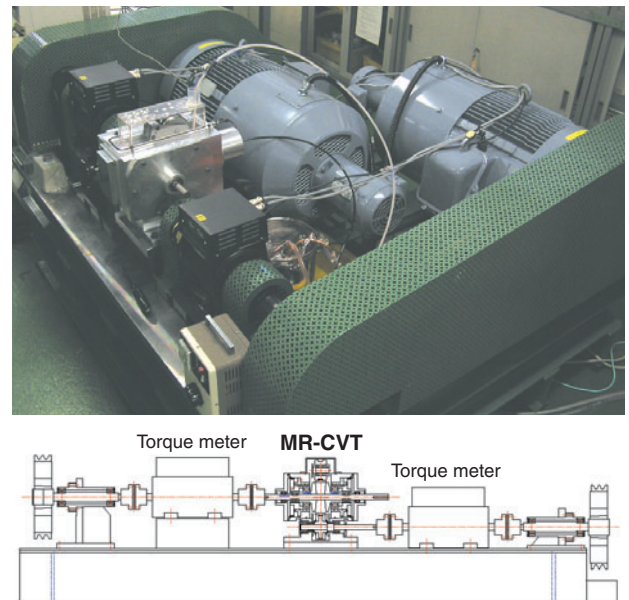
Fig. 6 Test rig for measuring transmission efficiency

Table 1 Test condition

Input rotation speed, min^{-1}	1000, 2000, 4000
Input torque, N-m	10～60
Transmission gear ratio (radius, mm)	0.4～1.2 (17～50)
Dynamic viscosity of lubricant	25.5 mm^2/s @40˚C
	5.12 mm^2/s @100˚C
Lubricant supply temperature	50˚C

Fig. 5 Relation between radius of contact point and slope angle of V-pulley

4. Test results

The measurement results for the input torque and transmission efficiency in an input rotation speed range of 1000 to 4000 min^{-1}, at gear ratios of 0.4, 0.6, 0.8, 1.0 and 1.2 are illustrated in **Figs. 7** through **9**.

Transmission efficiency increased with a greater input torque and with a higher gear ratio. At the ordinary gear ratio for automobiles of 1.0 or greater, transmission efficiency of 85% or greater was attained in almost all the torque range and the maximum transmission efficiency reached 92%. Though the transmission efficiency at the gear ratio of 0.4 was low, this gear ratio is used only when an automobile starts to run. The time when this gear ratio is used accounts for a smaller portion of the whole duration of car usage, so this low efficiency does not seem to greatly affect the overall efficiency of this MR-CVT in actual automobiles.

The reason for the increased transmission efficiency with higher gear ratios seems to be a decrease in the loss that results from spin-induced slip in the contact area between the toothed ring and the V-pulleys. The loss of input torque at 10 N-m seems to result from a greater ratio of various frictional losses to transmission efficiency in the MR-CVT.
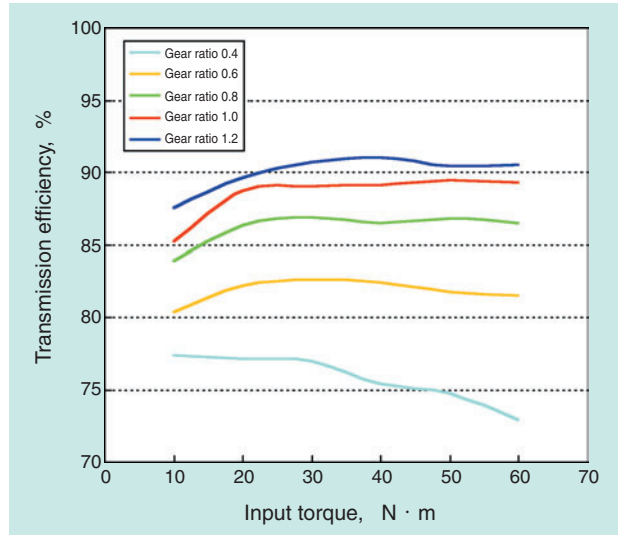
Fig. 7 Input torque and transmission efficiency (1000min^{-1})
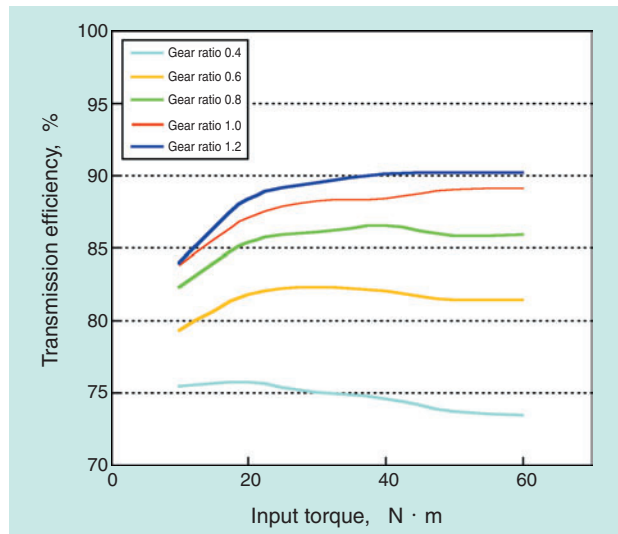
Fig. 8 Input torque and transmission efficiency (2000min^{-1})
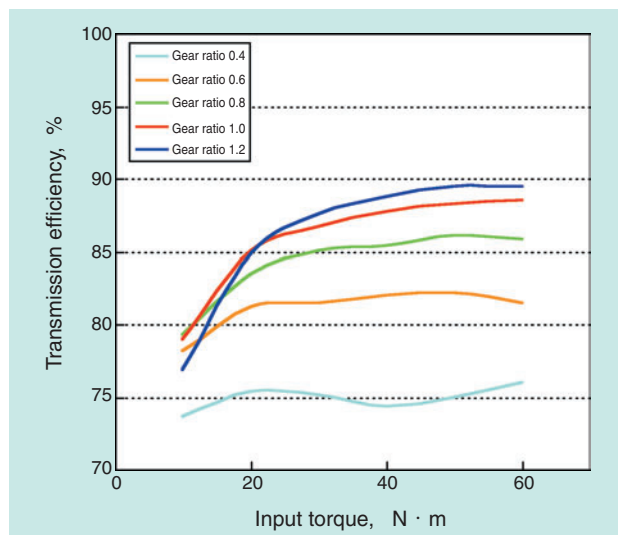
Fig. 9 Input torque and transmission efficiency (4000min^{-1})

5. Conclusion

We have invented a simple, compact MR-CVT on which a single (mono) toothed ring swings to change transmission speed. The MR-CVT features a self-adjustment mechanism that is the result of the design of the V-pulleys, guide rollers and other components. We made the following findings in the tests detailed in this report.

(1) Our MR-CVT functions correctly without need for an external pressure mechanism due to its self-contained adjustment capability.
(2) The transmission efficiency of our MR-CVT was at least 85% with a gear ratio of 1.0 or higher over nearly the entire speed range and the maximum transmission efficiency reached 92%.

References

1) S.H.Loewenthal：Advanced Power Transmission Technology NASA cp-2210（1981）79.
2) The Japan Society of Mechanical Engineers: P-SC62 Work Group for Investigation into Traction Drive (1985).

Photo of authors

Yuichi ITOH

New Product Development
R&D Center
Mechatronics Research Dept.

Tomoya SAKAGUCHI

New Product Development
R&D Center
Mechatronics Research Dept.

Hybrid Grease NA204F
for Automotive Electrical Instruments and Auxiliary Device

Masaki EGAMI*
Mitsunari ASAO*
Tomoaki GOTO**

This report introduces newly developed Hybrid Grease NA204F for automotive electrical instruments and auxiliary devices. NA204F has a unique composition that is a mixture of urea grease and fluorinated grease, and shows longer grease life at high operating temperature (up to 200°C) at lower cost than that of typical fluorinated grease. Moreover, NA204 is greatly improved on weak points of fluorinated grease, including enhanced rust prevention ability and greater resistance to grease leakage from the bearing. NA204F is expected to be applied to several kinds of automotive applications.

1. Introduction

To cope with the recent trend toward higher performance and increased power in automobiles, the need has been mounting for automotive electrical instruments and auxiliary devices that are more compact, lighter, faster and have greater functionality. As a result, the operating conditions for automotive bearings have become increasingly severe. The greases for bearings on automotive electrical instruments and auxiliary devices often consist of urea compounds as thickeners and synthetic oils as base oils. The greases used for applications in ambient temperatures of 180°C or higher sometimes use fluorine compounds as thickeners and base oils. Greases containing fluorine compounds are much more expensive than urea greases. For this reason, strong demand exists for a less expensive, high-temperature long-life grease.

To address this problem, **NTN** has developed Hybrid Grease, which features excellent cost-performance and high functionality. This paper describes the features of the Hybrid Grease and basic characteristics associated with its application in bearings for automotive electrical instruments and auxiliary devices.

2. Hybrid Grease defined

Grease prices are proportional to high-temperature life values as summarized in **Fig. 1**. In other words, greases that are more expensive also boast longer lives. With the goal of ending this commonly accepted relationship, we have been committed to developing a less expensive, high-temperature, long life grease for automotive electrical instruments and auxiliary
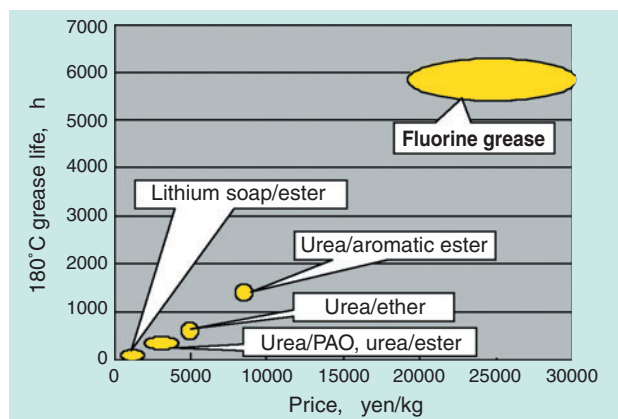
Fig. 1 Cost and high temperature life of greases

---

 *New Product Development R&D Center   Mechatronics Research Dept.
**Automotive Sales Headquarters   Automotive Engineering Dept.

devices. As a result, we have succeeded in developing our Hybrid Grease.

Our Hybrid Grease is essentially a mixture of different greases. The one introduced in this paper is a mixture of urea grease (thickener: urea compound, base oil: ester oil) and fluorine grease (thickener: ethylene tetrafluoride resin powder (PTFE), base oil: perfluoropolyether oil (PFPE)). Generally, mixing dissimilar greases needs to be avoided since it often leads to changes in grease properties such as consistency and reduced grease life. [1] However, our attempt to mix urea and fluorine greases was an exception because we have attained extremely favorable grease properties.

Fig. 2 illustrates the trend in grease life with various mixture ratios of urea and fluorine greases. The test conditions were in accordance with ASTM D 3336. A 6204 bearing with a shield plate, whose internal space was 38% filled with grease, was loaded onto the grease life test rig illustrated in **Fig. 3**, the test rig was continuously run at 200˚C, to evaluate the time until bearing seizure. As can be seen in **Fig. 2**, the life of urea grease alone is extremely short. However, the life of a mixture of urea grease and fluorine grease is longer than that of fluorine grease alone. This means that high-temperature life equivalent to or better than that of fluorine grease can be attained at a lower price.

From various analytical results, we estimated the long life mechanism of the Hybrid Grease to be as summarized in **Fig. 4**. At 200˚C, urea grease deteriorates in a short time span, and reaches the end of its life in approximately 200 hours.
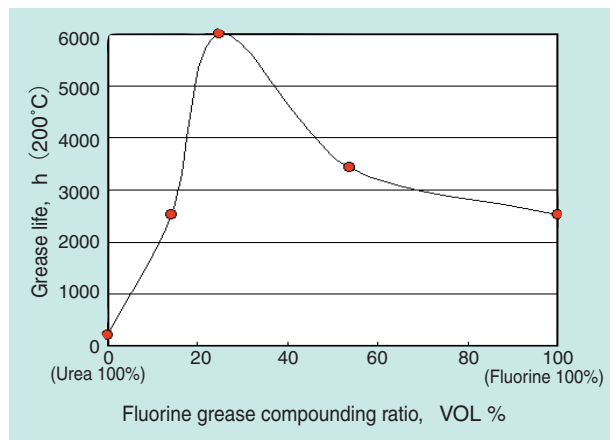
Fig. 2 High temperature life of Hybrid Grease

Test bearing   : 6204 (w/ shield plate)
Amount applied : 38% of internal space
Temperature   : 200°C (bearing outer ring end face)
Inner ring speed : 10000 min^{-1}
Load   : $F_a=F_r$=67 N
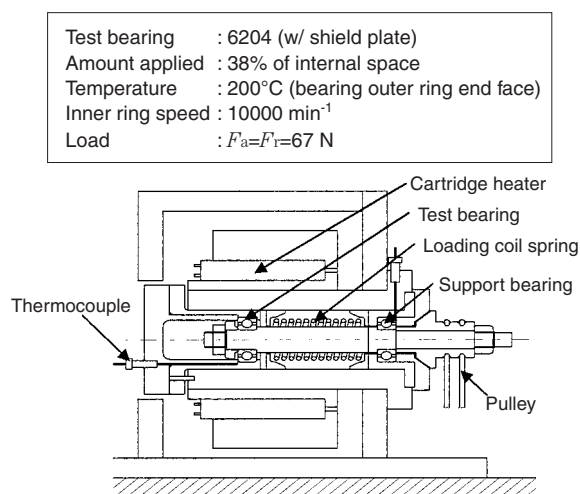
Fig. 3 Grease life test rig
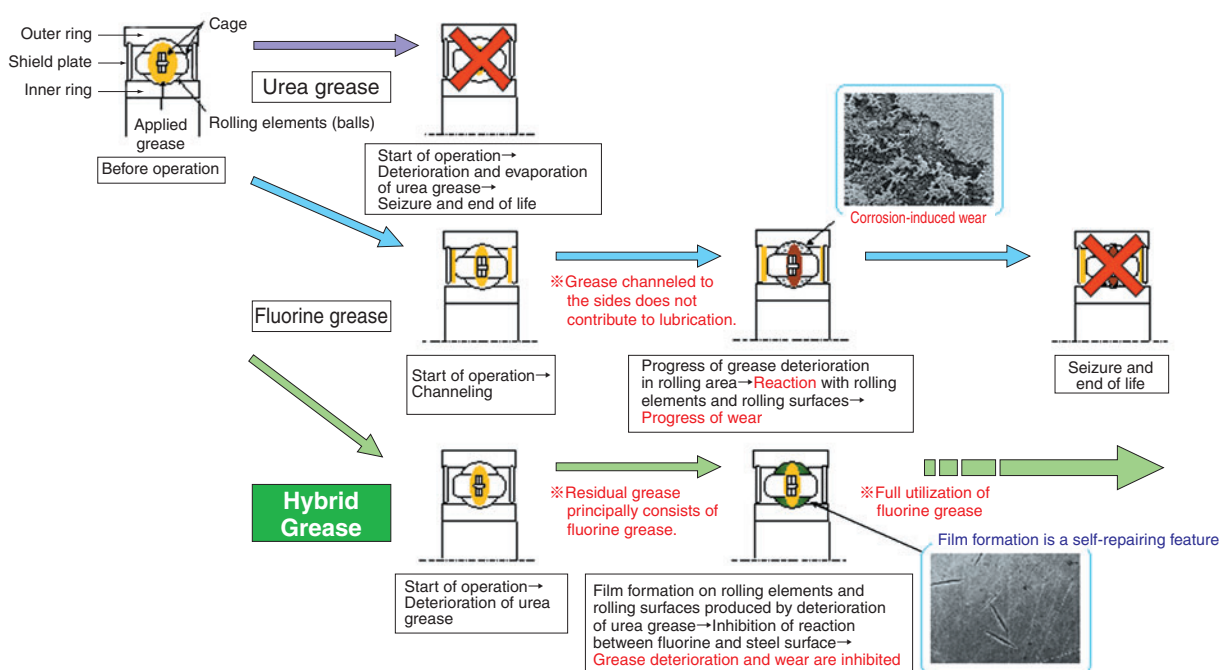
Fig. 4 Estimated mechanism for long grease life of Hybrid Grease

Immediately after the start of bearing rotation, most of the fluorine grease is shifted to the sides of the raceway, and only a small amount of grease remains on the rolling surfaces (channeling [2]). From the analysis of the bearings that underwent the test, we found that the grease adhering to the inner side of the shield plate does not contribute to lubrication and the rolling surfaces are lubricated with the small remaining amount of grease. When the grease on the rolling surfaces deteriorates and the supply of base oil to the rolling surfaces and cage pockets is insufficient, wear (corrosion-induced wear) of the steel members progresses due to the chemical reaction between the steel surfaces and PFPE [3) 4) 5], and the bearing approaches seizure and the end of life.

However, as the urea grease blended in our Hybrid Grease degrades, a film is formed on the rolling elements and rolling surfaces that inhibits the reaction between the steel parts and PFPE, preventing wear on them. Thus, the heat resistance of PFPE is fully developed to help extend the high-temperature life of the Hybrid Grease.

3. Application to automotive electrical instruments and auxiliary devices

Hybrid Grease compositions can have various fluorine grease mixture ratios as shown in **Fig. 2**. We determined the mixture ratio that leads to the longest grease life. Beginning with grease with this ratio as the base, we blended optimal amounts of additives to improve characteristics including low temperature performance and rust preventive performance in addition to high-temperature life, resulting in the development of **Hybrid Grease NA204F** for automotive electrical instruments and auxiliary devices.

3.1 General properties and high-temperature life

The general properties of our newly developed grease are summarized in **Table 1**. For comparison, this table also provides the properties of a high-temperature, long life fluorine grease A that has been performing well for automotive electrical instruments and auxiliary devices and of fluorine grease B, which features excellent cold temperature performance.

Compared with fluorine grease A, **Hybrid Grease NA204F** features a high-temperature life approximately 1.5 times as long, as well as a lower low-temperature torque. Compared with fluorine grease B, our Hybrid Grease boasts a high-temperature life approximately six times as long, though its low temperature torque is somewhat inferior.

3.2 Cold temperature noise characteristics

Depending on the pulley specifications and operating conditions, a belt pulley incorporating a deep-groove ball bearing can develop cold temperature noise known as hoot noise when started in a cold climate. With a frequency range of 500 to 1000 Hz and a sound pressure that can exceed 100 dBA, this noise is very offensive.

The cause of hoot noise seems to be that the pulley system develops resonance due to self-excited vibration of the rolling elements, causing the outer ring to vibrate in the axial direction (translational motion). Some types of grease are known to greatly promote noise generation.

For evaluation (see test conditions in **Table 2**), the test bearing incorporated into the test pulley was cooled in advance for 5 hours in a low temperature bath kept at -40˚C, then the pulley was installed in the test rig illustrated in **Fig. 5** that was at a room temperature.

Table 1 General properties of Hybrid Grease

Characteristics	Unit	Hybrid Grease NA204F	Fluorine grease A	Fluorine grease B	Test method
Thickener	—	Diurea compound PTFE	PTFE	PTFE	—
Base oil	—	Special ester oil PFPE PAO	PFPE	PFPE	—
Base oil dynamic viscosity (@40°C)	mm²/s	148	160	90	JIS2220.23
60-times worked penetration	—	Category 1 (310〜340)	Category 2 (265〜295)	Category 2 (265〜295)	JIS2220.7
Dropping point	˚C	more than 250	—	—	JIS2220.8
Oil separation (100˚C×24 h)	mass %	0.0	4.8	4.7	JIS2220.11
Specific gravity		1.22	1.85	1.94	—
Low temperature torque Starting (-30˚C) Steady	N · m	Start 16.9	37.6	4.9	JIS2220.18
		Running 7.0	28.0	2.6	
Grease life ＊	h	6000	4050	965	Per ASTM D3336

＊Evaluation test shown in **Fig. 3**

Belt tension was applied and operation was started when the bearing temperature rose to -20°C and was maintained until the bearing temperature reached 10°C. During this period, the noise level (cold temperature noise) was checked by listening. For each grease, evaluation was repeated 5 times for each of two bearings (n=10).

As can be seen by the data in **Table 3**, like the fluorine grease B that excels in cold temperature performance, our **Hybrid Grease NA204F** did not develop cold temperature noise and was found to exhibit excellent cold temperature noise prevention ability.
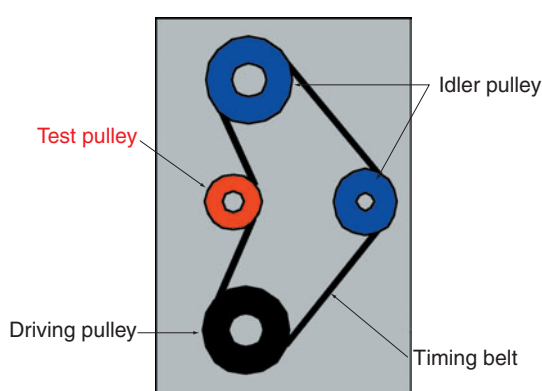
Fig. 5 Tension pulley type test rig

Table 2 Test condition of hoot noise at low temperature

Test bearing	6203 (light-contact type, w/ rubber seal)
Radial clearance, μm	12~16
Amount of applied grease	38% of internal space
Outer ring speed, min^{-1}	2700
Pulley load, N	127
Test temperature, °C	−20~10
Number of repetitions	n=2×5 times

Table 3 Rate of hoot noise generation at low temperature

Grease / Item		1	2	3	4	5	Occurrence %
Hybrid Grease NA204F	No.1	○	○	○	○	○	0
	No.2	○	○	○	○	○	
Fluorine grease A	No.1	○	○	×	×	×	60
	No.2	○	△	×	×	×	
Fluorine grease B	No.1	○	○	○	○	○	0
	No.2	○	○	○	○	○	

Symbols
○: No noise occurrence
△: Noise other than hoot noise (grease sound)
×: Hoot noise

3.3 Rust prevention ability

Since ordinary rust preventing grease additives do not dissolve in PFPE, they cannot be used in fluorine greases. As a result, the rust prevention ability of fluorine grease is inferior to that of other grease types. Since a rust-preventing additive is dissolved in the urea grease base, however, our Hybrid Grease has powerful rust prevention ability.

Fig. 6 summarizes rust occurrence percentages obtained from an evaluation test conducted according to ASTM D1743 in which salt water was used instead of pure water. For evaluation, a 4T-30204 tapered roller bearing coated with each of the test greases was immersed in 1% aqueous sodium chloride solution for 10 seconds, and was allowed to stand for 48 hours in an atmosphere of 40°C and 95% relative humidity. Then, the rust spots on the outer ring rolling surface were counted. The rolling surface was circumferentially divided into 32 equal segments, and the number of segments with rust was divided by 32 to determine the rust occurrence rate.

Compared with the rust prevention ability of fluorine greases A and B, **Hybrid Grease NA204F** exhibited excellent rust prevention ability.
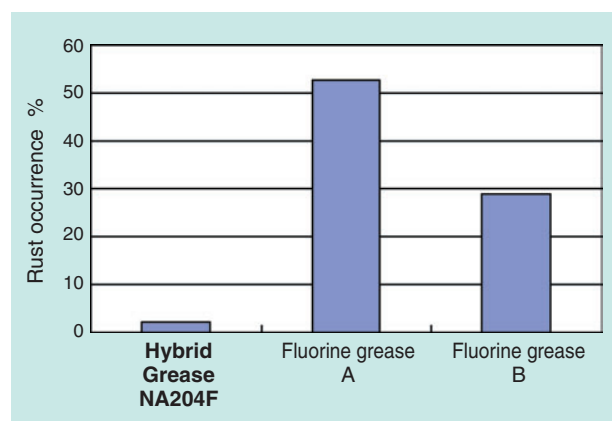
Fig. 6 Rust prevention ability of greases

3.4 Leakage characteristics of greases

Fluorine grease is not compatible with the base oil (mineral oil) in rust-preventive oil that is used in the bearing manufacturing process. As a result, if fluorine grease is inserted in a bearing coated with such rust-preventive oil, the fluorine grease will slip on the oil film and may leak out of the bearing in a short period of time. To prevent this problem with fluorine grease application in bearings, it is common to limit the amount of residual rust preventive oil within the bearing.

By following a manufacturing practice for applying common grease, we inserted the same amount of grease into a bearing whose inside was coated with a rust-preventive oil (internally rust-proofed bearing) and into a degreased bearing. Each bearing was run for 10 minutes. The resultant grease leakage percentages (expression [1]) are summarized in **Fig. 7**.

$$\text{Leakage percentage} = \frac{\text{amount of leakage}}{\text{original inserted amount}} \times 100 \text{ (\%)}$$

<div align="right">Expression (1)</div>

Large amounts of fluorine greases A and B leaked from the internally rustproofed bearing. In contrast, only a small amount of **Hybrid Grease NA204F** leaked from the internally rustproofed bearing.

As mentioned in Sec. 3.3, with its powerful rust-prevention ability, Hybrid Grease will help contribute to bearings that are more resistant to rust compared to fluorine grease-filled bearings.
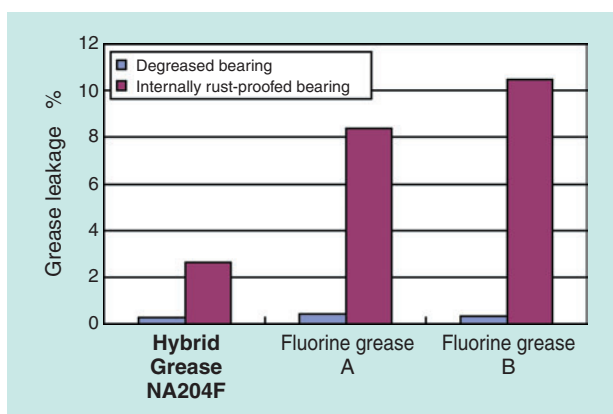
Fig. 7 Leak rates of greases during rotation

Test bearing   : 6204 (w/ non-contact rubber seal)
Applied amount : 38% of internal space
Inner ring speed : 10000 min^{-1}
Load   : F_a=39 N
Temperature   : room temperature
Operating time   : 10 min.

4. Compatibility with seal rubber material

The rubber seal material in bearings with fluorine grease is usually a fluorine-containing rubber in order to satisfy heat-resistance requirements. The most commonly used fluorine-containing rubber materials are so-called FKMs (an ASTMD1418 abbreviation representing fluorine-containing rubber) that include a binary copolymer of vinylidene fluoride and hexafluoropropylene (VDF-HFP) and a ternary copolymer comprising VDF-HFP and tetrafluoroethylene (VDF-HFP-TFE). These common FKMs exhibit sufficient durability when combined with fluorine grease and do not pose any problem. However, when an FKM contacts urea grease in a high-temperature situation, its vinylidene fluoride component is attacked by the urea thickener and amine, developing a cross-linking reaction. As a result, the FKM becomes hardened, its strength is degraded and its sealing performance is eventually lost. Our Hybrid Grease also affects common FKMs in the same way as urea grease.

To address this problem, the authors developed a novel fluorine rubber seal material, NUF (**NTN** anti-urea fluorine rubber), with a base rubber that consists of fluorine rubber made of components immune to urea. **Fig. 8** illustrates the time-dependent variations in hardness and tensile strength with dumbbell test pieces made of NUF and common FKM that were immersed in Hybrid Grease NA204F at 200˚C. While the physical properties of the common FKM greatly degraded in a short time, those of the NUF did not degrade much, remaining stable for a prolonged time. This feature of FKM is valid not only when used with Hybrid Grease, but also when it is used together with urea grease.

5. Conclusion

By combining urea and fluorine greases, we have successfully developed **Hybrid Grease NA204F**, which features exceptionally long high-temperature life that has no precedent in conventional grease technology. At a temperature as high as 200˚C, its life is longer than that of conventional fluorine greases. At the same time, it is free from the drawbacks associated with fluorine greases, including poor rust prevention ability and a tendency toward leakage induced by rust preventive oil within bearings. Furthermore, it helps prevent occurrence of cold temperature noise when applied to pulley bearings. Being less expensive than fluorine greases, **Hybrid Grease NA204F** boasts extremely high cost performance, and when used together with our newly developed urea-resistant
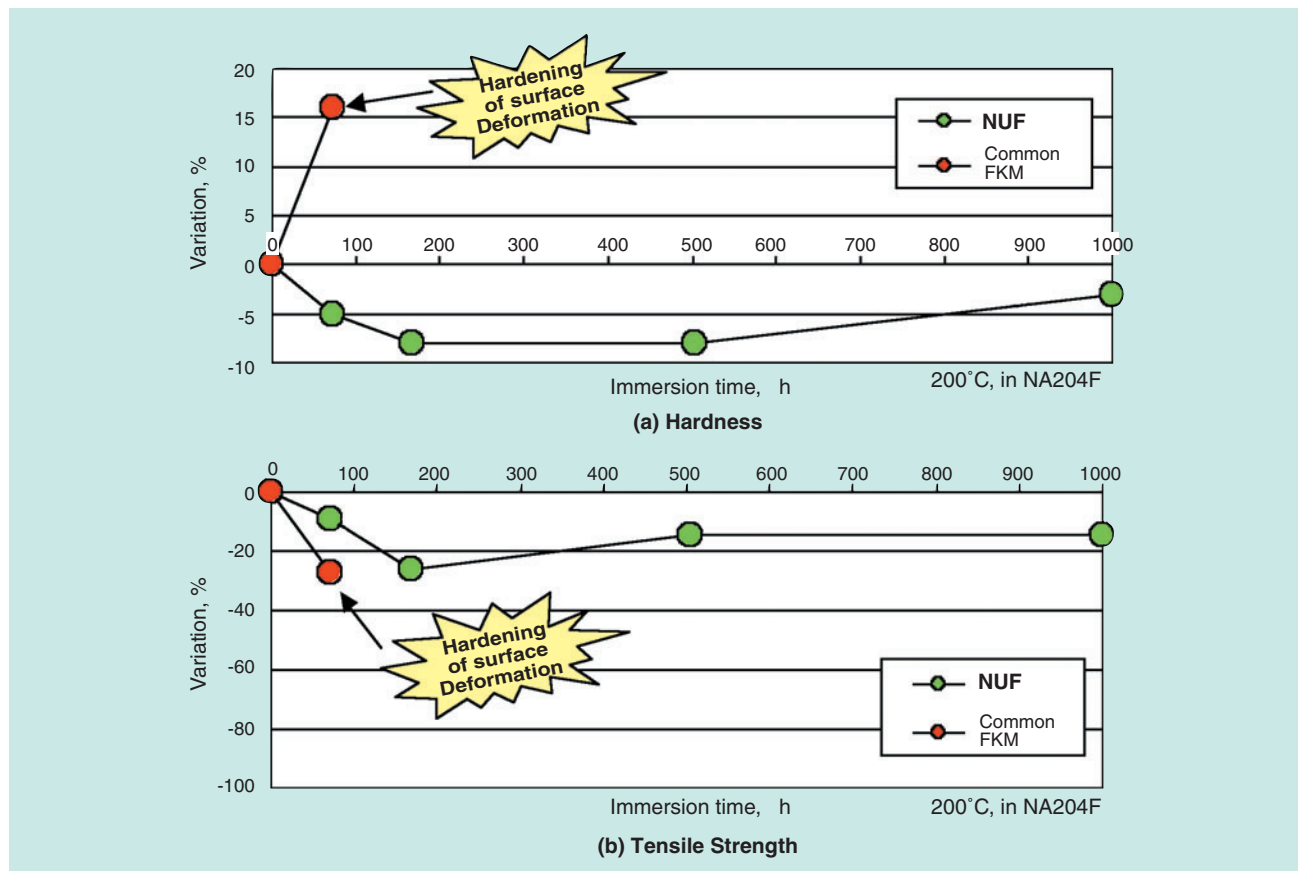
Fig. 8 Deterioration of fluorinated rubbers dipped into Hybrid Grease at 200˚C

fluorine rubber, NUF, it does not develop incompatibility problems with seal rubber material. Thus, we believe that **Hybrid Grease NA204F** will greatly contribute to performance enhancement and cost reduction for automotive electrical instruments and auxiliary devices.

References

1) Tadashi Hatakeyama: Mixing of dissimilar greases, and variation in properties, Junkatsu, 19, 4 (1974) 331.

2) Japanese Society of Tribologists: Tribology Handbook, Yokendo Co., Ltd. (2001) 715.

3) Shigeyuki Mori, Mariko Ito, Yuji Shitara, Yuji Enomoto: Relation between lubricity and molecular structure with perfluoroether oil (2nd report), Tribologist, 40, 15 (1995) 923.

4) William R. Jones Jr., Mariko Ito (translation), Shigeyuki Mori (translation): Perfluoroether-based lubricants, Tribologist, 42, 3 (1997) 205.

5) Mineo Suzuki, Philippe Plat, Koji Matsumoto: JAXA research and development report, Performance of ball bearings having a retainer impregnated with space lubricants and their outgassing properties, JAXA-RR-03-014 (2004).

Photos of authors

Masaki EGAMI
New Product Development
R&D Center
Mechatronics Research Dept.

Mitsunari ASAO
New Product Development
R&D Center
Mechatronics Research Dept.

Tomoaki GOTO
Automotive Sales Headquarters
Automotive Engineering Dept.

Ballscrew for Automated Manual Transmission

-72-

Koji TATEISHI*
Keisuke KAZUNO*

Recently , the use of automated manual transmissions (AMT) are expanding in the automotive market. Of the many methods of automation in the market, the ball screw and driven by DC motor are methods that have the quickest response and largest system output.

Mitsubishi FUSO truck & bus and Bosch Co. ltd have developed a new small and medium sized truck that incorporates the AMT system. **NTN** has started to supply ball screw and support bearings for this application.

This article documents the development and future applications.

1. Introduction

Recently, an increasing number of automobiles models have been incorporating automated manual transmissions (AMT) to improve fuel efficiency and ride comfort.

In the past, most automated gear change systems for AMT were driven hydraulically or pneumatically. These systems have recently been superseded by electric motors in order to achieve more compact, lighter weight units. Various attempts had been made by combining electric motors with reducers that are centered on worm gears or sliding screws. these attempts had drawbacks including higher cost due to the increased number of components, inability to offer greater driving power due to relatively large friction, lower efficiency, and poor response.

To solve these drawbacks, Mitsubishi Fuso Truck and Bus Corporation and Bosch Corporation developed a gearshift actuator for a compact truck

automated manual transmission (INOMAT-Ⅱ) in which the actuator is driven with ball screws. This actuator uses **NTN** ball screws and support bearings.

This paper describes the ball screws specifically developed for this AMT.

2. Structure of automated manual transmission

2.1 AMT appearance

Photo 1 shows the AMT appearance. The gearshift actuator is mounted to the top of the transmission, which had previously required manual operation for gear shifting. This automatization has been achieved without significant change to the transmission structure. The significantly altered area is shown encircled by a dashed line.

*Automotive Sales Headquarters   Automotive Engineering Dept.
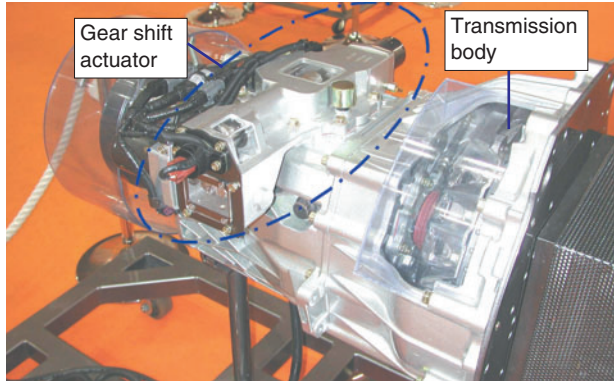
Photo 1 Transmission

2.2 Overall layout of gearshift actuator

Fig. 1 illustrates the general structure of the gearshift actuator.[1]

The gearshift actuator achieves gear change by synchronously driving the two ball screws perpendicular with each other by means of DC motors. The gearshift actuator is capable of rapid response thanks to the advantages of low friction ball screws. The response times are 0.06 sec. for the shift side, and 0.08 sec for the select side.
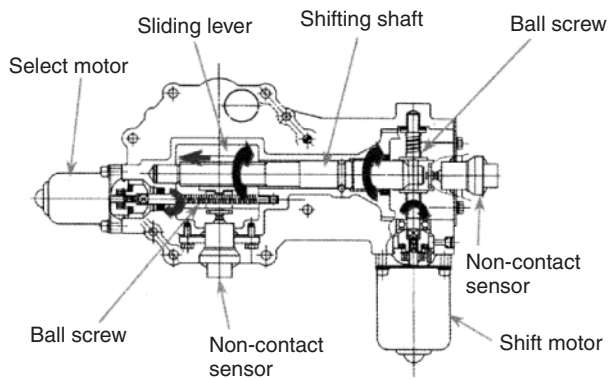
Fig. 1 Construction of gear shift actuator

3. Features of ATM ball screws

The ball screws used in this ATM are shown in **Photo 2.**
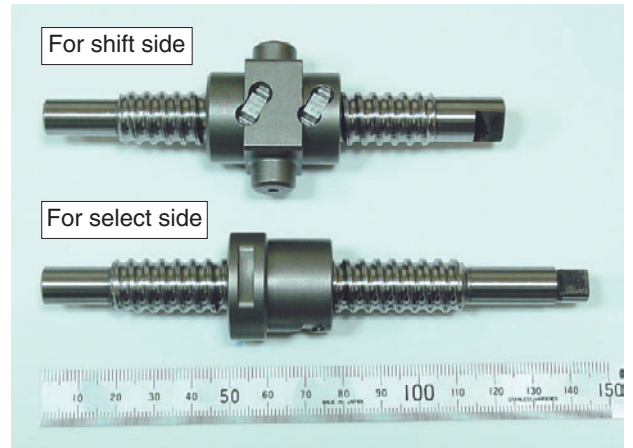
Photo 2 Ball screw for AMT

3.1 Ball screw circulation sections

The circulation section on each of the ball screws is a deflector type. Thanks to a new staking method each deflector **Photo 3**. is very compact with a radial dimension approximately 20% smaller than ordinary return tubes.

The deflector staking assembly is shown in **Photo 4**. The deflector is inserted from the inside of the nut, and the wing is fit into the thread groove where the balls do not roll, and then the wing is fixed by staking (**Photo 5**). This structure is less expensive compared with conventional gluing or assembly with a screw, but is reliable because it has sufficient strength against loosening of the deflector member toward the outside of the nut. The deflector is formed with high-precision metal injection molding (MIM), guaranteeing stable ball circulation.

Photo 3
New deflector

Photo 4
Appearance of deflector
staking assembly

Photo 5
Appearance of deflector staking

3.2 Durability

When the gearshift actuator is running, the fork-shaped arm of the shift axle and the trunnion on the ball nut come into contact and form a point of application (**Fig. 2**).

If the arm and the nut trunnion are in an ideal contact relationship, the ball screw receives a pure axial load. However, in reality, a moment load acts on the ball screw from the trunnion because of factors including the gearshift unit clearance and the inclination induced by the ball screw backlash.

As a result, greater load occurs on the balls situated at both sides of the nut. Therefore, to ensure a longer ball screw life, improving the load distribution on the balls is important.

To address this problem the authors have changed the ball circulation system from a return tube system to a deflector system that optimizes the span and circumferential phase of the circulation deflector relative to the position of the trunnion.

Comparison of both ball circulation systems in terms of ball contact pressure has been examined under the conditions summarized in **Table 1**.
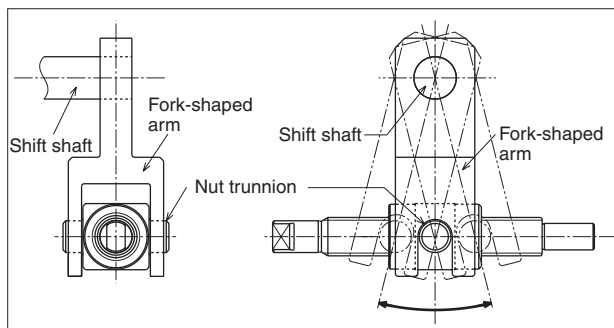
Fig. 2 Driving way of ball nut

Table 1 Specification of ballscrew

Characteristics	Tube type	Deflector type
Shaft dia. (mm)	ϕ14.5	
Lead (mm)	4.0	
Ball dia. (mm)	ϕ2.778	
Number of circulations (rounds×rows)	3.5×1	1×4
Moment load (N-m)	17	

The results of the test are summarized in **Fig. 3**. There are two main advantages to application of a deflector system. [1] The deflector can be arranged in a longer nut-axis direction, and [2] the maximum number of balls can be placed in the phase where moment load is applied. As a result, the contact pressure on balls can be reduced by as much as 20%. Sufficient durability was not attained with any return tube system, but the **NTN** deflector system has achieved the necessary durability.

4. Evaluation test

We developed a unique purpose-specific test rig that can simulate the possible operation conditions of actual automotive AMTs, and evaluated our ball screws with it.

4.1 Operability (efficiency)

Shift side ball screws must be capable of developing sufficiently large thrust because they are meshed with a shift gear. **Fig. 4** summarizes the results of the relationship between the ball screw backlash and the resultant thrust.
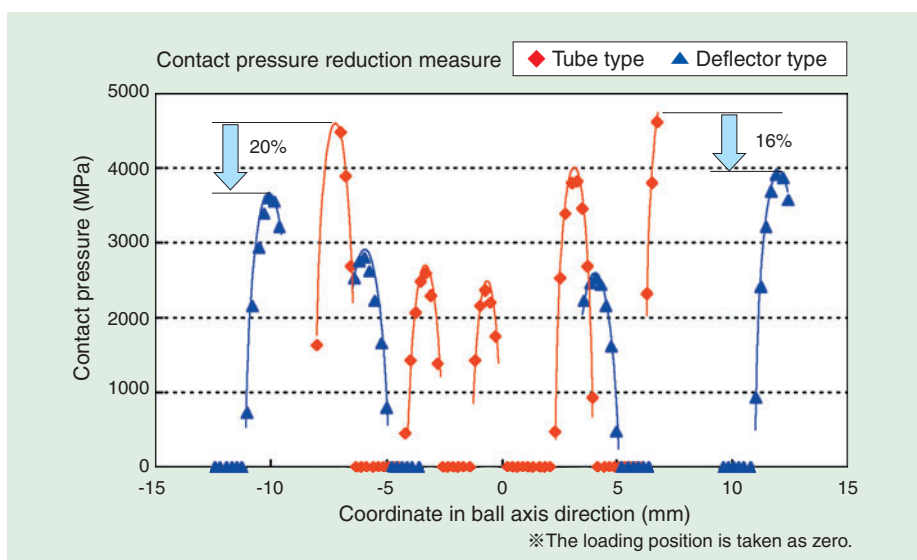
Fig. 3 Comparison of ball contact pressure
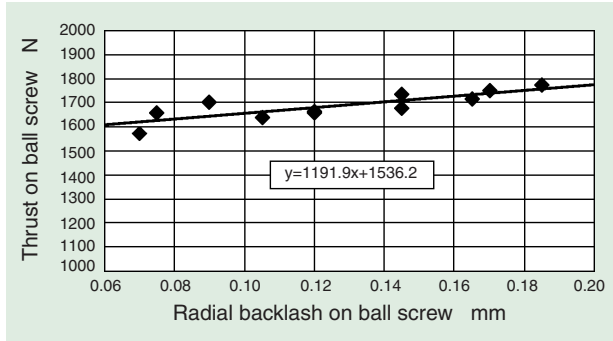
Fig. 4 Relationship between ballscrew's lash and thrust

Table 3 Durability test condition of select side ballscrew

Test		Test conditions	
Durability test	Max. load	Inertia load by acceleration and deceleration of nut	
	Stroke	±7mm	
	Drive motor	24 VDC motor	
	Ambient temperature	110˚C	
	Lubrication	Contaminated transmission oil	
	Number of operations	2,200,000	
Fretting test	Vibration frequency	25～400Hz	
	Acceleration	3.7～96.1m/s^2 *In three directions	
	Ambient temperature	Room temperature	
	Lubrication	Contaminated transmission oil	
	Duration of vibration	12h	

Because a smaller radial backlash on any ball screw reduces the degree of freedom of the nut, the friction on the sliding surface of the actuator will increase and as a result the thrust will decrease.

When the backlash on the ball screw is large, the life of the actuator can become shorter because of the moment load.

From the test results, we determined an optimal backlash on the ball screw that ensures thrust necessary for shifting action.

4.2 Durability

The tests and test conditions for evaluating the durability of the ball screws are summarized in **Tables 2** and **3**. When the shift gears start meshing, on rare occasions an impact load may act on the shift side ball screw, so a strength tests was performed on this ball screw. The ball screw successfully passed the durability test.

5. Conclusion

In this report, we have introduced unique ball screws that are used for novel, compact, less expensive actuators that are used in mechanical manual transmissions for compact and midsized trucks. We have developed these ball screws through design improvements and innovations for the ball circulation section. By applying these improvements, **NTN** is currently developing ball screw units for use in the electrically driven automotive actuators of engine brake controllers in an attempt to expand the scope of applications for these ball screws.

Table 2 Durability test condition of shift side ballscrew

Test		Test conditions	
Durability test	Max. load	2800N	
	Stroke	±5mm	
	Drive motor	24V DC motor	
	Ambient temperature	110˚C	
	Lubrication (grease)	Ether-based synthetic oil + aromatic diurea	
	Number of operations	2,310,000	
Strength test	Impact load	8000N (two directions)	
	Ambient temperature	Room temperature	
	Lubrication (grease)	Ether-based synthetic oil + aromatic diurea	
	Number of operations	2000	
Fretting test	Vibration frequency	25～400Hz	
	Acceleration	13.7～96.1m/s^2 *in three directions: up-down, right-left, front-rear	
	Ambient temperature	Room temperature	
	Lubrication (grease)	Ether-based synthetic oil + aromatic diurea	
	Duration of vibration	12h	

Reference

1) Nakamura, et al. : Development of new INOMAT, Mitsubishi FUSO Technical Review (2004, No. 1), p. 49-54

Photos of authors

Koji TATEISHI
Automotive Sales Headquarters
Automotive Engineering Dept.

Keisuke KAZUNO
Automotive Sales Headquarters
Automotive Engineering Dept.

[New Product]

Drawn Cup Needle Roller Bearings for Throttle Bodies

Hideki AKAMATSU*

Drawn cup needle roller bearings have an outer ring that is precisely drawn from a thin steel plate. Of all bearings with outer rings, drawn cup needle roller bearings have the smallest cross sectional height, which enables both space and cost savings.

This chapter introduces the features as well as the performance of sealed, low friction, low air leak drawn cup needle roller bearings for use in throttle bodies.

1. Introduction

A throttle valve is a device that controls the amount of air fed into an engine. To cope with recent growing needs for better fuel efficiency and lower emissions, electronically controlled throttle valves that are capable of fine adjustment of an air/fuel ratio are being used increasingly.

As a result of the employment of electronic control, the means for driving throttle valves has changed from wires to motors. Rolling contact bearings, which feature decreased friction, are also being used increasingly to enable both a compact lightweight design and an improved response with the motor used for this purpose.

Rolling contact bearings are being used in the systems that control the airflow into automotive engines as well. The support for the throttle blade must not allow air to leak, therefore rolling contact bearings must have good sealing performance.

To address these needs, we have developed drawn cup needle roller bearings for throttle bodies that have seals with lower friction and less air leakage. This paper introduces the features and performance of these drawn cup needle roller bearings.

2. Structure and features

The rolling bearings used for electronically controlled throttle valves can be categorized as deep grooved ball bearings (hereafter, referred to as "ball bearings") and drawn cup needle roller bearings (hereafter, referred to as "drawn cup bearings") (**Fig. 1)**.

Compared with ball bearings, drawn cup bearings have smaller outside diameters, and as a result, the radial space of the housing can be smaller and the housing can be lighter. Ball bearings are narrower than drawn cup bearings, but their built-in seals alone cannot completely prevent air leakage so additional seals must be incorporated, which leads to the need for additional space and expense.

Our newly developed drawn cup bearing assembly consists of a drawn cup bearing fabricated by the pre-bent technique* and a seal that does not have a core metal. This bearing does not need additional sealing, and it can contribute to environmental protection through cost reduction, space conservation and reduced weight.

*Pre-bent technique: a technique in which a cage and rollers are fit into a drawn cup outer ring, and then the assembly is subjected to heat treatment.

---

*Automotive Sales Headquarters　Needle Roller Bearings Engineering Dept.
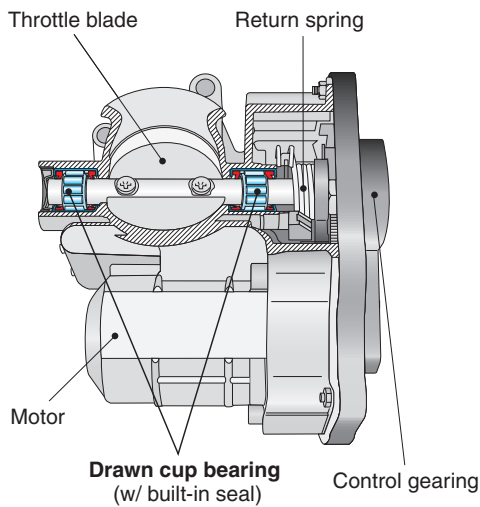
Drawn cup bearing application example
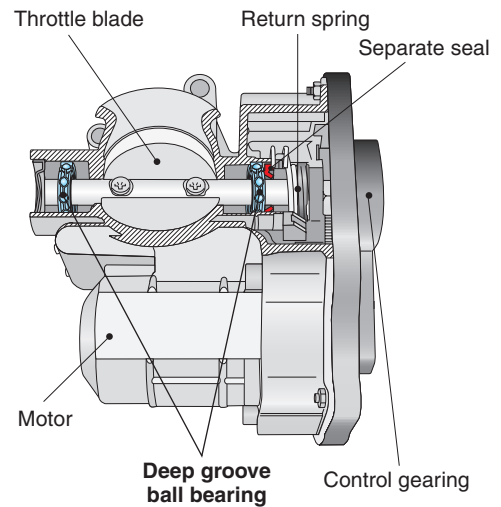
Deep groove ball bearing application example

Fig. 1 Structure of electronic throttle bodies
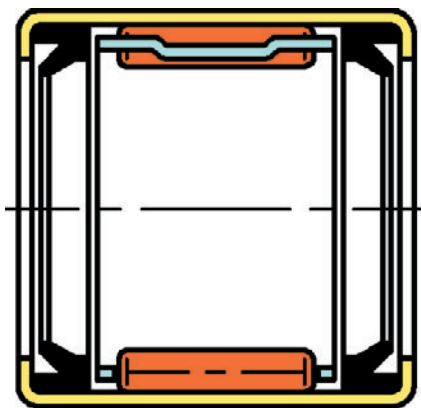
Fig. 2 Structure of drawn cup needle roller bearings for throttle bodies

Table 1 Specification of drawn cup needle roller bearings for throttle bodies

Specifications	Dimensions	Inscribed circle dia. 10 × outside dia. 14 × width 14 mm
	Outer ring	Chromium molybdenum steel
	Cage	V-type welded cage
	Rollers	Crowned
	Seal	Fluorine rubber, no core metal
	Rated load	Dynamic rated load C_r 4500 N Static rated load C_{0r} 5100 N
	Others	High performance grease applied
Development target	Friction	1.1 N-cm max.
	Air leakage	0.8cm^3/min. max.

3. Friction Performance

The friction performance of the bearings that support the throttle blade is a critical factor in adopting a compact design and achieving quick response with the motor.

A friction measurement value is obtained by inserting a torque gauge with a shaft of a specified diameter into a drawn cup bearing that is press-fitted into a standard ring, and turning the gauge 90 degrees. The friction value of these bearings is approximately 0.8 N-cm, which is sufficiently lower than the development target of 1.1 N-cm (**Table 2**)

Table 2 Test result of friction

Development target	1.1 N-cm max.
Number of samples (n)	30 pcs.
Mean value	0.78 N-cm
Max. value	0.85 N-cm
Min. value	0.70 N-cm
Standard deviation	0.054 N-cm

4. Air Leakage Prevention Performance

Because the throttle valve regulates the amount of air fed into the engine, the amount of air leakage from the supports of the throttle blade must be strictly controlled.

The measuring method and resultant measurements of the air leakage on drawn cup bearings are summarized below.

Before starting the air leakage measurements, each drawn cup bearing was press-fit into a ring of specified dimensions, and the shaft was inserted into the bearing of a specified diameter. This set was then mounted to a sufficiently rigid measuring head. The other measuring head was shut with a lid, and was used as a standard control. These heads were connected to an air leakage tester, the open space in each head was adjusted to a negative pressure, and then air leakage was measured. **Photo 1** shows the air leakage tester, and **Fig. 3** illustrates the measurement heads.

The amount of air leakage with our drawn cup bearing was 0.01 cm^3/min. or lower, which is sufficiently lower than the development target of 0.8 cm^3/min (**Table 3**).
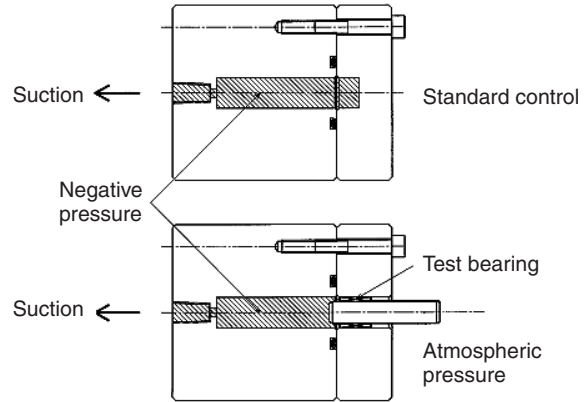
Fig. 3 Measurement part

Table 3 Test result of air leakage

Bearing No.	Diameter of shaft inserted (mm)	Air leakage Development target: 0.8 cm^3/min. max.
No.1		0.01cm^3/min. max.
No.2	ϕ 9.975	0.01cm^3/min. max.
No.3		0.01cm^3/min. max.
No.4		0.01cm^3/min. max.

5. Conclusion

This paper has introduced our unique drawn cup bearing assembly for a throttle valve. This assembly incorporates a compact, less expensive drawn cup bearing and a seal that features lower friction and air leakage prevention capabilities. Use of this bearing helps reduce the size of the throttle valve and improve the response speed. We believe that this bearing will offer better control of air-fuel ratios for automotive engines, helping realize better fuel efficiency and lower emissions and thus contributing to global environmental protection.

Photo 1 Air leakage tester

Photos of author

Hideki AKAMATSU

Automotive Sales Headquraters
Needle Roller Bearings
Engineering Dept.

Compact & Smooth

For New Technology Network

NTN®

B E A R I N G S

www.ntn.co.jp

Compact and Shudderless Constant Velocity Joint (EPTJ)

Tatsuro SUGIYAMA*
Yuuichi ASANO*

NTN Corporation has successfully developed a new, high efficiency Pillow Journal Tripod Joint (EPTJ). This type of joint drastically improves the NVH (Noise, Vibration, Harshness) characteristic in vehicles. The high efficiency E-series PTJ, what we call EPTJ, is also lighter and more compact than a conventional PTJ. The EPTJ maintains the excellent vibration characteristics of the ultra-low vibration plunging tripod joint PTJ that **NTN** brought into the market in 2002. Moreover, it is smaller (4% reduction in outer diameter) and lighter (weight reduced by 8%) than the PTJ.

1. Introduction

Constant velocity joints (CVJ) used for automotive drive shafts are categorized as fixed-type CVJs, which enable a greater operating angle and are used on the tire side, and sliding-type CVJs, which are capable of axial sliding and are used on the engine side.

The shudder that occurs when a vehicle is started or accelerated and the vibration that occurs during idling of A/T cars are affected by vibration characteristics that result from the induced thrust and slide resistance of sliding-type constant velocity joints.

In an attempt to solve these problems, in 2002, **NTN** develops the revolutionary PTJ constant velocity joint with vibration characteristic values that have been reduced by more than 50% compared to conventional low-vibration joints. Since then, the production of this novel constant velocity joint has been expanding.

With our PTJ products, the roller cassette in the joint slides smoothly on the outer race roller groove while maintaining specific attitude even when the joint is operating at an angle, making it possible to suppress the frictional resistance and reliably maintain the vibration characteristic values at lower levels. As a result, the induced thrust from the running PTJ has been reduced by more than 70% (at an operating angle of 6° or greater) compared to conventional tripod joints, greatly reducing the shudder that occurs when a vehicle is started or accelerated.

In addition, our constant velocity joint design has greatly reduced sliding resistance, and significantly improved the idling vibration quality of A/T vehicles.

Retaining a mechanism similar to that of the PTJ, our newly developed EPTJ features a more compact, lighter CVJ design that has been realized through

Fixed-type CVJ

Sliding-type CVJ

Front wheel drive axle

---
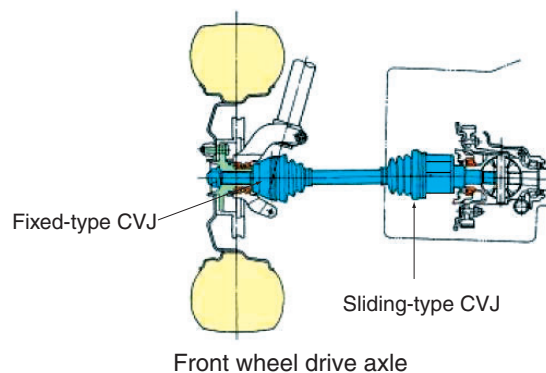
*Automotive Sales Headquarters   C.V.Joint Engineering Dept.

optimization of the internal design and heat treatment of joint components that fully utilize CAE techniques including FEM and dynamic mechanism analysis, as well as by adopting quality engineering (robust design).

2. EPTJ structure

The structure of our newly developed EPTJ is illustrated in **Fig. 1.**

With an internal structure similar to that of the PTJ, the EPTJ features lower frictional force through improvement in contact states and stabilization of roller cassette attitude.

The internal structure of the EPTJ, being similar to that of the PTJ, is structured as [roller cassette (inner race/outer race/snap ring/needle rollers) + trunnion + outer race] to promote ease of assembly.

The outer race diameter of the EPTJ is approximately 4% smaller than that of the PTJ (**NTN** data: one size reduction) (**Fig. 2**). The weight of the EPTJ is approximately 8% less than that of the PTJ through size reduction of the outer race and inner components.
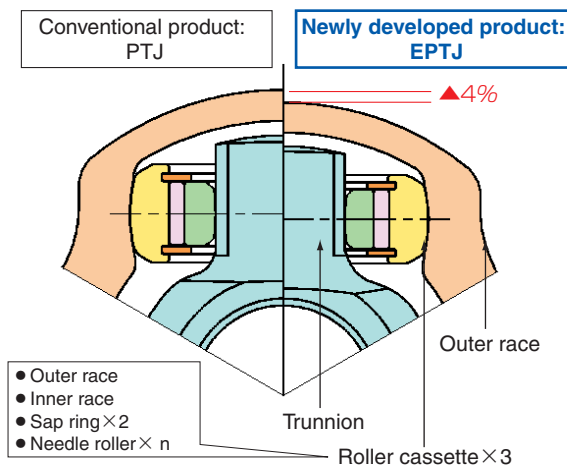
Fig. 1 Construction of PTJ and EPTJ
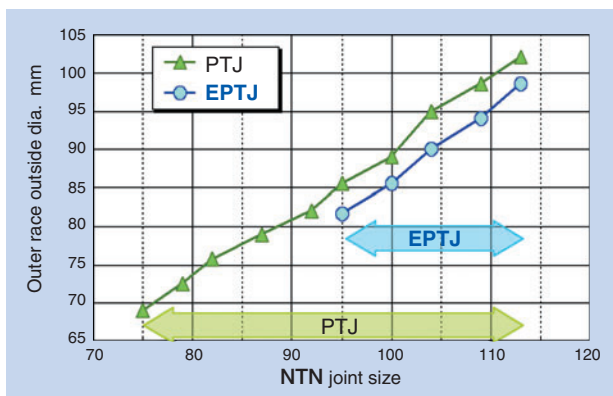
Fig. 2 Outer-diameter comparison between PTJ and EPTJ

3. EPTJ functions

Making CVJs more compact and lightweight leads to reduced vibration performance, mechanical strength and bearing life. We have overcome these drawbacks and our EPTJ has attained functionality comparable to the PTJ.

3.1 Reduction of induced thrust load (Countermeasure against accelerating vehicle shudder)

Induced thrust load on a CVJ is an axial force induced by mutual friction between joint components when the shaft rotates at an angle with the outer race. This thrust is associated with shudder in an accelerating car, so reducing it can help suppress car shudder.

Like the PTJ, the trunnion journal of the EPTJ is an elliptical cylinder (loading point: major axis side), and the bore surface of the inner race in contact with the journal is outwardly curved. Thanks to this contact relationship, the moment of roller cassette tilt while the CVJ is running is smaller and the attitude of the outer race and roller cassette is stable. As a result, the induced thrust on the EPTJ is always small regardless the operating angle as shown in **Fig. 3**. Incidentally, in this diagram, the induced thrust values with the EPTJ are nearly equivalent to those with the PTJ.
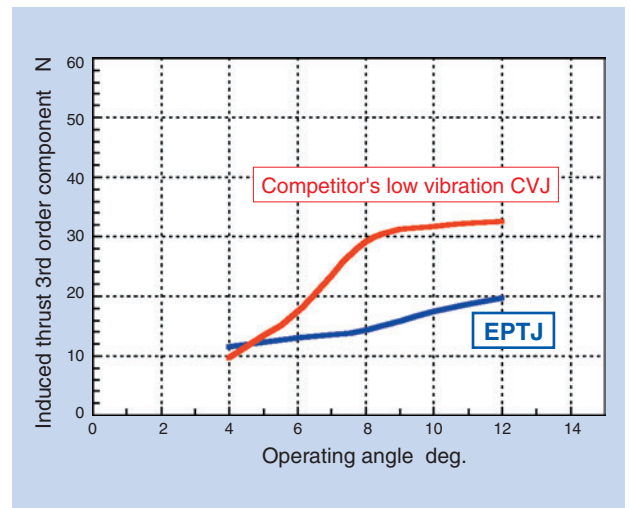
Fig. 3 Measurement of insulation resistance

3.2 Reduction in static plunging slide resistance (Countermeasure against D range idling vibration with A/T cars)

Slide resistance on a CVJ, which occurs when the outer race is vibrating and allowed to slide in the axial direction, is a cause of D range idling vibration in A/T cars. Therefore, idling vibration can be suppressed by controlling the slide resistance.

Like the PTJ, the EPTJ is capable of oscillation on the roller cassette bore and the trunnion journal. In other words, with the EPTJ, the roller cassette rolls only in the axial direction on the outer race, and the plunging force in the axial direction on the outer race is borne only by the rolling motion of the needle rollers, thereby keeping the slide resistance of the EPTJ low regardless of the operating angle (**Fig. 4**). Incidentally, in this diagram, the slide resistance values with the EPTJ are nearly equivalent to those with the PTJ.
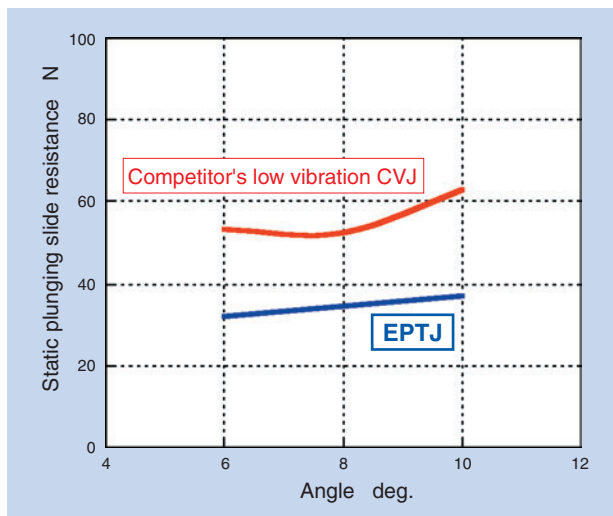
Fig. 4 Static plunging resistance vs operating angle under torque and stimulated vibration condition

3.3. Strength

The mechanical strengths of the internal components of the EPTJ, including static torsion strength and torsion fatigue strength, are greater than those of outer race stems and shafts, meaning that the internal components are strong enough for use in real cars.

3.4 Durability

The high and low load oscillation durability of the EPTJ is equivalent to or better than that of the DOJ, which boasts many years of good reputation. In addition, the EPTJ durability is equivalent to or better than that of a competitor's CVJ.

4. FEM stress analysis and mechanical analysis

To improve the overall strength, durability and NVH characteristics in good balance, we determined the optimal geometry of the major components (outer race, trunnion and needle rollers) through full utilization of FEM stress analysis. We sought lower stress levels and compared evaluation results with actual components.

We have also fully utilized dynamic mechanism analysis, as shown in **Fig. 6**, to understand the internal forces and component motions that occur in operation of the EPTJ in order to optimize its internal dimensions.
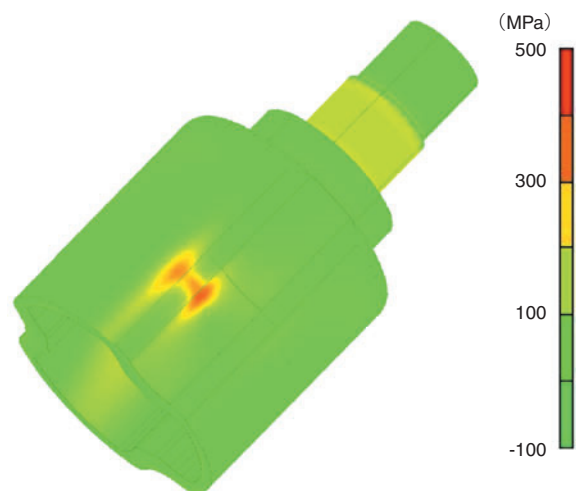
Fig. 5 FEM stress analysis for outer-race
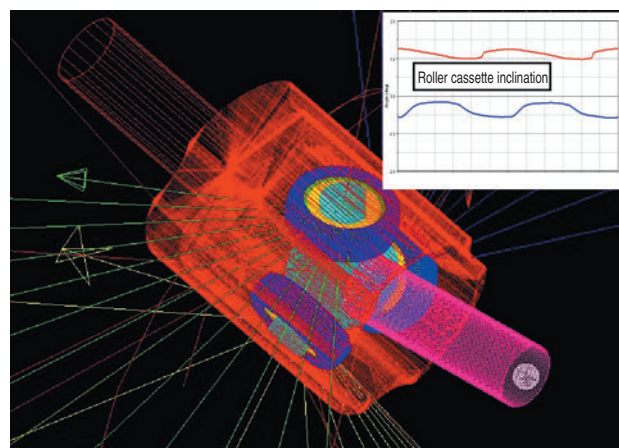
Fig. 6 Dynamic mechanism analysis

5. Application of quality engineering

The EPTJ is essentially a compact version of the PTJ. Size reduction can cause problems including decreased component rigidity and adverse effects on bearing functions and characteristics due to the increased contact pressure. In particular, the compact design significantly affected the NVH characteristics, and the induced thrust at a high torque load. To address this problem, we applied quality engineering to achieve a robust design.

In application of quality engineering, we first clarified the functions of low vibration constant velocity joints, and then listed the controllable factors, operating conditions and variations in manufacturing that could affect their functionality, before performing an experiment using the L18 orthogonal matrix. We selected the factors that significantly affect the functions of constant velocity joints and adopted our findings in designing the EPTJ.

As shown in **Fig. 7**, the induced thrust on the EPTJ was decreased by approximately 50% through application of quality engineering.

6. Conclusion

EPTJ features:

(1) The magnitude of induced thrust is not affected by the operating angle of the joint, and the EPTJ can attain low vibration comparable to the PTJ.

(2) The magnitude of static plunging slide resistance is not affected by the operating angle of the joint, and the EPTJ can attain low vibration comparable to the PTJ.

(3) The outside diameter of the outer race is approximately 4% smaller than the PTJ (NTN data: one size reduction).

(4) The weight is approximately 8% lighter than the PTJ.

(5) The maximum operating angle is the same as that of the PTJ (26˚).

The EPTJ is a low vibration CVJ that is much smaller and lighter compared with conventional CVJs and that is minimally affected by the operating angle. EPTJ units will fully demonstrate their design performance in conditions when better space efficiency is needed and a larger operating angle is required due to the layout limitations of a particular car, and when greater torque is applied to the CVJ when the car is idling, starting or accelerating.
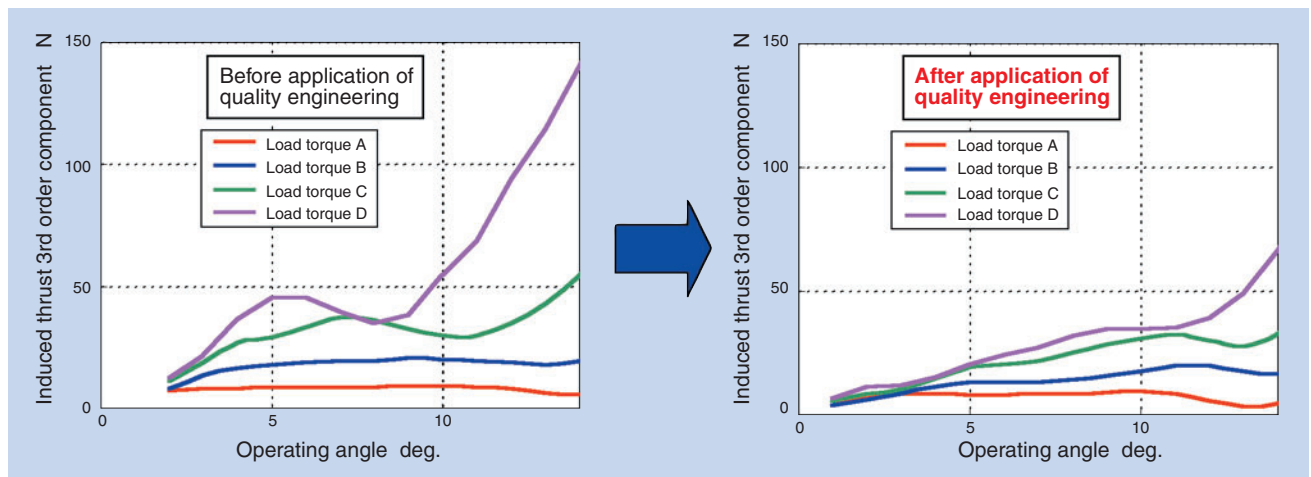
Fig. 7 Quality engineering for induced cyclic load reduction

Photos of authors

Tatsuro SUGIYAMA

Automotive Sales Headquarters
C.V.Joint Engineering Dept.

Yuuichi ASANO

Automotive Sales Headquarters
C.V.Joint Engineering Dept.

Constant Velocity Steering Joint (CSJ)

Kenta YAMAZAKI*

In an automotive steering system, Cross or Cardan joints typically were used. However, because of the nature of non-constant velocity joints, we are required to use two joints with special geometrical construction to obtain constant velocity performance. To improve this situation, a new constant velocity steering joint (CSJ) has been developed.

This paper reports the summary of the concept, design and characteristics of this new joint developed by **NTN**. Adding the original idea to the reliable know-how of constant velocity universal joint, a smooth and non-backlash feeling has been achieved.

1. Introduction

Cross joints, also known as Cardan joints, (see **Fig. 8**) have been used for automotive steering systems. Since a cross joint is not a constant velocity joint, if only one cross joint is used to provide a larger operating angle for an automotive steering system, then variation in rotational angle and resultant variation in torque occurs, leading to uncomfortable steering. To avoid this problem a feature similar to that obtained with constant velocity joints can be achieved if two joints are combined such that their operating angle is the same. They are positioned in rotational phases where the deviation in rotational velocity of one joint is counterbalanced by the other joint.

With recent automotive models, the available space in engine compartments is becoming smaller and smaller due to the conflicting needs for both compact, lightweight car bodies and greater passenger space. As a result, there has been increased difficulty in realizing two-joint system steering layouts that provide constant velocity features.

Using our expertise with constant velocity joints that have performed outstandingly with automotive drive shafts and in unique constructions, **NTN** has become the first in the world to develop a **CSJ constant velocity ball-type steering joint** that is capable of smooth, constant velocity actuation over the entire operating range. This report describes the features of our CSJ and the results of basic functionality tests.

2. Conventional technology

Steering joints are expected to operate smoothly and free from backlash in the rotational direction, while greater operating angles and compactness are desired. Currently double Cardan joints (D-CJ) (see **Fig. 9**) are mass-produced as constant velocity steering joints that consist of two cross joints with a centering mechanism so that one D-CJ unit can function as a constant velocity joint. However, the double Cardan joints have problems including greater size, heavier weight and low torsional rigidity. D-CJs can be categorized into two types: pseudo constant velocity and full constant velocity. Both types have drawbacks, including unreliable constant velocity with angles outside the preset operation angle range and a narrower oscillating angle (see **Table 1**).

*Automotive Sales Headquarters   C.V.Joint Engineering Dept.

3. CSJ structure

The basic structure of the CSJ resembles that of the BJ (fixed constant velocity joint of track offset type) that is often used for drive shafts. However, with an ordinary BJ, clearance between the ball groove (formed between the outer race and inner race) and the balls is small, and as a result, backlash occurs in the rotational direction. Because of this, the BJ is not suitable for automotive steering systems that need to be free from backlash. Another problem is that if a tightening allowance is provided for clearance between the ball groove and the balls in order to reduce backlash, assembly of the BJ into the steering system may not be possible.

To solve these conflicting problems, we have added a plunger and a spherical plate to the joint (see **Fig. 1**). More specifically, a plunger comprised of a spring and a ball is provided at the shaft end, and the force of this spring is applied through the ball to the spherical plate fitted into the cage. As a result, as shown in Fig. 2, the inner race alone shifts to the right, causing the ball to be lifted until it touches the outer race, thereby the clearance on the ball groove is reduced.

With this structural arrangement, even when minor wear occurs on contact areas between the components due to extended steering system use, associated clearances are automatically reduced through the action of the spring, maintaining the steering system in a backlash-free state.

NTN has also attempted to optimize the shapes of the components and the clearance between them, and have optimized the force of the spring accordingly. In this way, we have achieved both reduction in rotational backlash throughout the operating angle range and smoother steering system rotational motion.

4. Performance characteristics

4.1 Rotational backlash

The results of comparison of our CSJ with a D-CJ are illustrated in **Fig. 3**.

Since it is free from excessive backlash, our CSJ boasts higher torsional rigidity, compared to currently used double Cardan joints (D-CJ), for automotive steering systems.

Fig. 1 Structure

Fig. 2 Structure to reduce rotational play
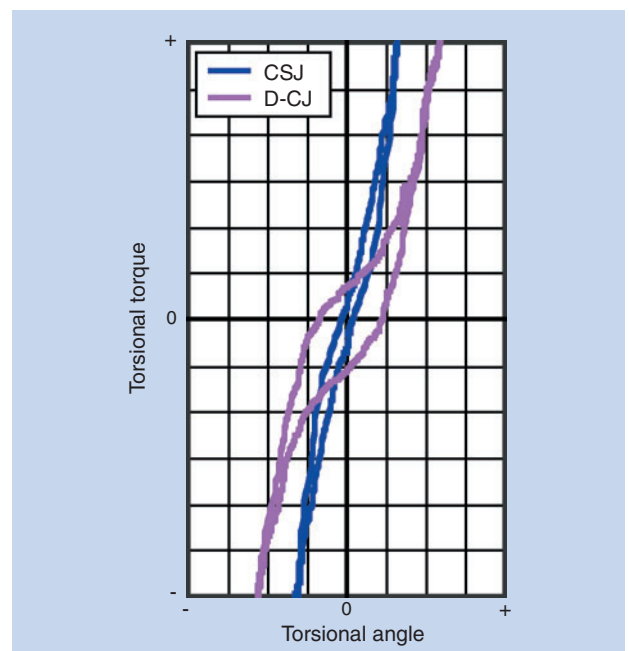
Fig. 3 Rotational back lash

4.2 Rotational torque

The results of the comparison of the CSJ and the D-CJ are summarized in **Fig. 4**.

Though somewhat greater than that of the D-CJ, the rotational torque of the CSJ falls in a permissible range and has less variation. Therefore, these CSJ characteristics are suitable for steering joints.
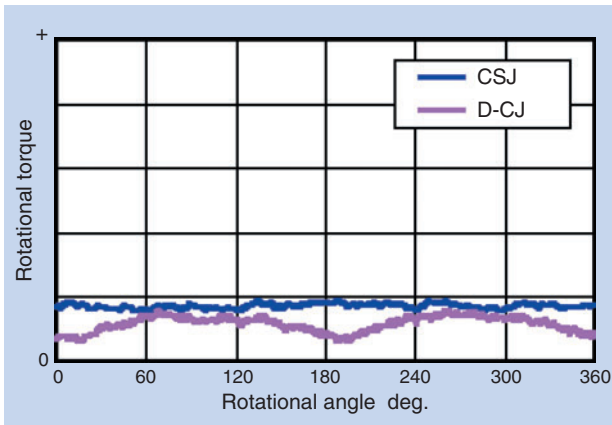
	Operating time		Test result
	Targeted life	Targeted life×2	
Condition A			No problem
Condition B			No problem

Fig. 5 Endurance test results

Fig. 4 Rotating torque
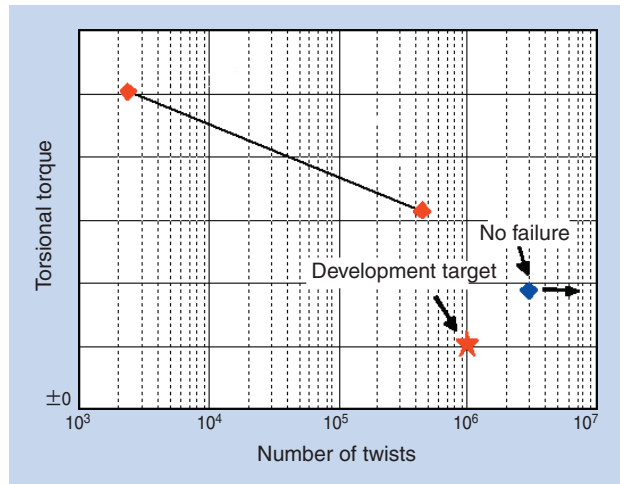
Fig. 6 Torsional fatigue strength

5. Endurance and strength

The results of an endurance test are summarized in **Fig. 5**, and the results of strength tests are plotted in **Figs. 6** and **7**.

In terms of both endurance and strength, the CSJ satisfies targeted levels, and we believe that the CSJ can be used in applications on actual automobiles.

6. Comparison with other constant velocity steering joints

Compared with competitors' double Cardan joints, the CSJ is lighter and more compact, and has a greater permissible operating angle. Therefore, the CSJ can greatly improve the freedom of layout for automotive steering systems.
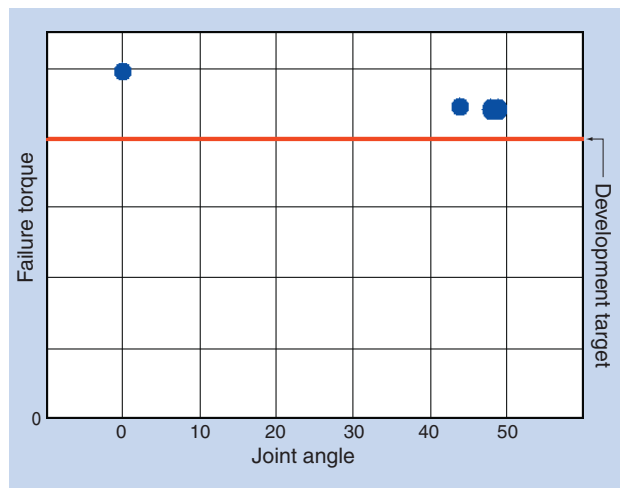
Fig. 7 Static torsion strength

Table 1 Comparison of constant velocity steering joint

	CSJ	Double Cardan joint from competitor A	Double Cardan joint from competitor B
Outside dia.	ϕ 64 mm	ϕ 61.5 mm	ϕ 70 mm
Weight	441 g	970 g	830 g
Volume occupied	160 cm³	327 cm³	270 cm³
Operating angle	0～48 deg (Fully constant velocity over whole range)	0～47 deg (Pseudo constant velocity type)※	40～48 deg (Fully constant velocity type)

※Constant velocity feature is lost when the angle is outside the permissible range.

① Bearing
② Cross spider
③ Bearing seal
④ Yoke

Fig. 8 Crose joint (Cardan joint)

Socket
Socket yoke
Centering ball
Needle rollers

Outer seal
Inner seal

Inner seal
Bearing cup

Coupling yoke
Bushing
Socket yoke

Needle rollers

Spider
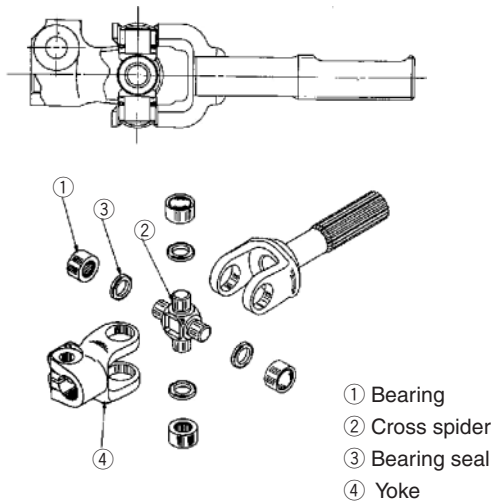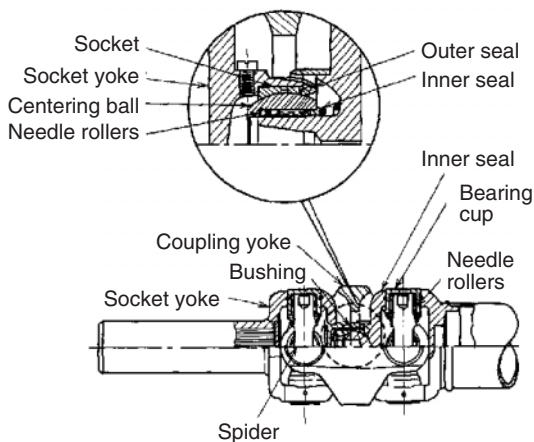
Fig. 9 Double cardan joint

7. Conclusion

Developed as a dedicated constant velocity steering joint for automobiles the **NTN** CSJ is characterized by a unique preload applying mechanism incorporated into the joint and internal clearance optimized to realize not only inhibition of rotary-direction backlash but also the capability for smooth rotational operation over the entire operating angle up to the maximum operating angle of 48 degrees. These features, which are lacking in conventional BJs, make the CSJ capable of providing an ideal constant velocity for automotive steering systems, while maintaining sufficient endurance and mechanical strength.

With the CSJ, one joint unit provides smooth, constant velocity transmission of rotation, adjustment of joint angles and phase matching in the rotational direction. In contrast, two Cardan joints are needed for this application. Furthermore, compared with double Cardan joint arrangements, the CSJ features lighter weight and a more compact design, allowing significantly greater freedom for steering system design layout. We believe that our CSJ is the constant velocity joint type that can satisfy mounting needs for advanced functionality and more compact size in automotive steering systems.

Reference

1) The Society of Automotive Engineers of Japan, Automotive Engineering Handbook, Design Volume (1991)

Photos of author

Kenta YAMAZAKI

Automotive Sales Headquarters
C.V.Joint Engineering Dept.

[New Product]

Summary of E Series, Constant Velocity Joint for Propeller Shaft

Tomoshige KOBAYASHI*
Teruaki FUJIO*

Automotive manufacturers are trying to develop automobiles with better fuel efficiency and comfort. **NTN** developed E series CVJs for propeller shaft based on the design of mass-produced E series high efficiency constant velocity joints for drive shafts.

This paper summarizes the E series CVJs for propeller shaft products.

1. Introduction

To satisfy automotive performance requirements, including higher efficiency and lower vibration, **NTN** has been mass-producing E series constant velocity high-efficiency joint products for drive shafts. The need has been mounting to satisfy these requirements for constant velocity joints for propeller shafts in complicated 4WD car drive systems. To address this trend, we have developed E series constant velocity joints (CVJ) for propeller shafts. The features of various E series CVJ subtypes are described below.

Photo 1 Example of Propeller shaft. (2 joint design)

2. Overview of E Series CVJ products for propeller shafts

We have developed high-speed variants of the E series -the HEBJ, HEDJ and HETJ- whose basic structure derives from that of other E series drive shaft products. Compared with conventional mass-produced CVJs for propeller shafts (BJ, DOJ and TJ), the HEBJ, HEDJ and HETJ series products boast high efficiency, light weight and compact size while maintaining the load carrying capacity and durability of the conventional products. The features of the E series CVJs for propeller shafts are summarized in **Table 1**.

Incidentally, in consideration of the environment, **NTN** uses a lead-free grease prepared especially for propeller shaft CVJs and employs a hexavalent

Table 1 Characteristics of E series

New series	Maximum allowable angle	Outside dia.	Mass	Torque loss	Heat generation	Subject of comparison
HEBJ	+	+++	+++	++	++	BJ
HEDJ	+	++	++	++	++	DOJ
HETJ	+	++	+++	+	++	TJ

+++ ···Excellent   +++··· Good   +··· Equivalent

*Automotive Sales Headquarters   C.V.Joint Engineering Dept.

chromium-free material for CVJ components that need surface treatment.

3. E Series Propeller Shaft CVJ product features and future developments

3.1 HEBJ

3.1.1 Features

When a CJ (cross joint) cannot satisfy requirements for a greater operating angle, a BJ type CVJ for propeller shafts is used together with a sliding type CVJ.

Like the EBJ for drive shafts, the HEBJ for propeller shafts features temperature increase and transmission efficiency that is much improved over conventional BJ products.

The construction of HEBJ is illustrated in **Fig. 2**. A size comparison of the HEBJ and a conventional BJ for propeller shafts is provided in **Fig. 2**, and their outside diameters are shown in **Table 2**.

Table 2 Comparison of outer-diameter between HEBJ and BJ

Unit: mm

NTN joint size	BJ	HEBJ
87	79.9	72.6
100	91.0	83.7

Flange type design of Constant Velocity Joint for Propeller Shaft was compared with the outer-diameter.

The flange type and disk type designs are available for the HEBJ in order to cope with user requirements. (See **Figs. 3** and **4**.)
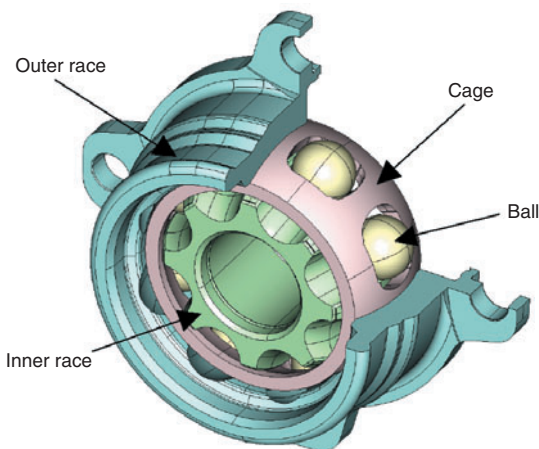
Fig. 1 Composition of HEBJ
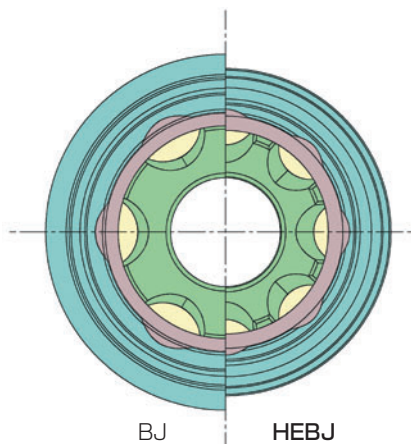
Fig. 2 Comparison of structure between BJ and HEBJ
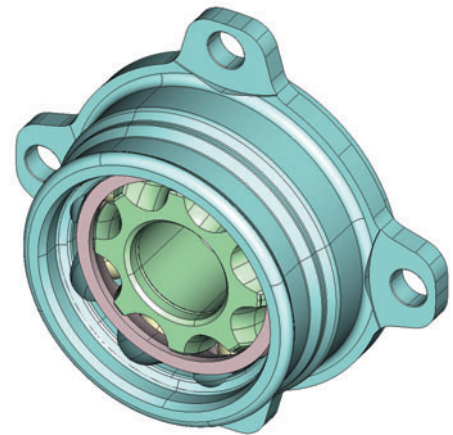
Fig. 3 HEBJ flange type design
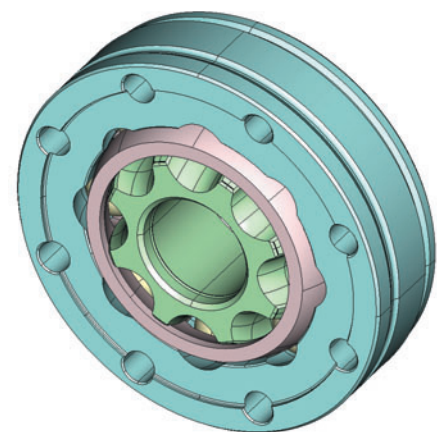
Fig. 4 HEBJ disc type design

3.1.2 Future development

We will make HEBJ products the standard bearings for fixed constant velocity joints for propeller shafts, and will increasingly replace conventional BJ and CJ (cross joint) products with HEBJ products.

3.2 HEDJ
3.2.1 Features

The DOJ type CVJs for propeller shafts are capable of a greater axial slide, and can absorb minute axial vibration.

Like the EDJ products for drive shafts, the temperature increase on the HEDJ is limited and an induced thrust on the HEDJ is lower compared with the conventional DOJ. The size of the HEDJ is approximately 4% smaller than that of the DOJ. To cope with varying CVJ use specifications for propeller shafts, the HEDJ is available in sizes #71, #82, #92 and #95. The standard HEDJ forms available are the pressure-welding type and flange type, both of which are in demand.

The joint construction (pressure-welding type) is illustrated in **Fig. 5**, and a comparison of outside diameters with the DOJ is given in **Table 3**.

3.3 HETJ
3.3.1 Features

The permissible slide amount is greater with TJ type constant velocity joints for propeller shafts. TJ products feature smaller slide resistance over the whole sliding range as well as lower heat generation.

As for the ETJ for drive shafts, the internal design of the HETJ has been improved based on data obtained from FEM analysis. As a result, the HETJ products for propeller shafts feature a smaller outside diameter, while their strength, durability and NVH characteristics are equivalent to those of the conventional TJ.

The standard form is a pressure-welding type.

The construction of the joint is illustrated in **Fig. 6**, a comparison of proportions of the TJ and HETJ for propeller shafts is given in **Fig. 7**, and a comparison of outside diameters of the TJ and HETJ is given in **Table 4.**

Fig. 5 Composition of HEDJ
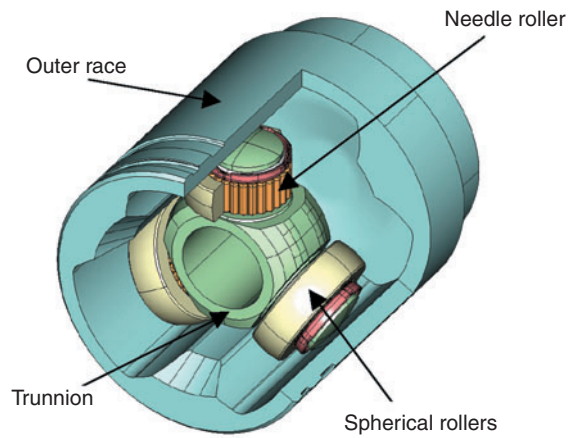
Fig. 6 Composition of HETJ

Table 3 Comparison of outer-diameter between HEDJ and DOJ

Unit: mm

NTN joint size	DOJ	HEDJ
71	—	63
75	73	—
82	—	73
87	79	—
92	—	79
95	—	83
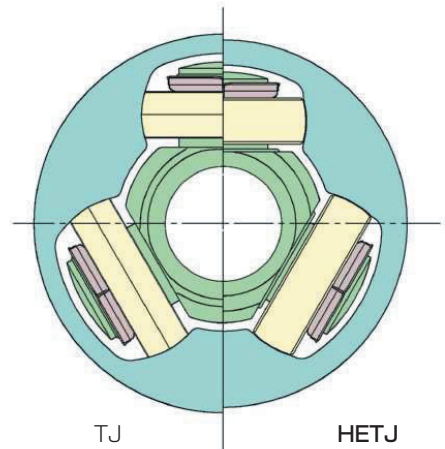
Fig. 7 Comparison of structure between TJ and HETJ

Table 4 Comparison of outer-diameter between HETJ with TJ

Unit: mm

NTN joint size	TJ	HETJ
75	68	66
79	73	68

4. Conclusion

By applying the experience and expertise accumulated through the development of the E series CVJs for drive shafts to CVJs for propeller shafts, **NTN** has successfully developed the lightweight, compact E series CVJs for propeller shafts.

NTN will further improve the CVJs for propeller it is possible shafts, for which demand will increase, so that to supply constant velocity joints that best satisfy the customer needs.

3.4 Future development of sliding types

An optimal choice can be selected from the sliding types (HEDJ and HETJ) and other sliding joint types (HLJ and LJ), according to the required slide amount, outside diameter size and CVJ characteristics (see **Table 5**).

Table 5 Comparison of characteristics between propeller shaft CVJ

		Fixed type	Sliding type			
		HEBJ	HEDJ	HETJ	HLJ	LJ
Slide amount		—	◎	◎	○	△
Permissible angle		◎	◎	△	○	◎
High speed operation		○	○	△	◎	◎
Heat generation		○	○	◎	△	△
NVH characteristics	Slide resistance	—	○	◎	△	△
	Induced force	8th order	8th order	3th order	6 and 3th order	6 and 3th order
Backlash	Radial direction	—	○	△	◎	◎
	Rotation direction	○	○	△	◎	◎

◎：Excellent　　○：Good　　△：Average

Photos of authors

Tomoshige KOBAYASHI

Automotive Sales Headquarters
C.V.Joint Engineering Dept.

Teruaki FUJIO

Automotive Sales Headquarters
C.V.Joint Engineering Dept.

[**Technical Paper**]

NVH Analysis Using Full Vehicle Multi Body Dynamic Model*
-Influence of Constant Velocity Universal Joints on Shudder Vibration–
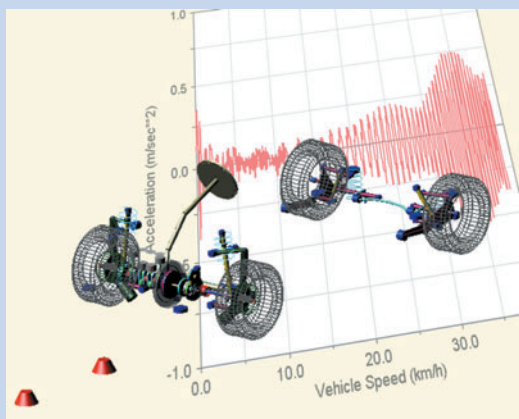
Yoshihiko HAYAMA**
Takashi NOZAKI***
Masafumi NAKAKOUJI***
Satoshi FUJIKAWA****
Komaki FUKUSHIMA****

Vehicle NVH characteristics have been analyzed using a full vehicle simulation model. This model consists of engine, drive train and chassis components that are respectively accurate multi body dynamic models. This paper focuses on a shudder vibration analysis, specifically on the influence of constant velocity universal joints (CVJs) on shudder vibration characteristics.

1. Introduction

In developing automobiles, the mode of NVH problems varies significantly depending on engine and chassis types, with many problems occurring only in completed vehicles. In addition, the NVH problems to be solved during development of a particular car require many hours of work and pose a significant challenge in expediting vehicle design completion. Furthermore, since the NVH problems of a given vehicle are often the result of complex mechanisms, determination of the root causes of each NVH problem through experiments with actual vehicles is very difficult.

Recently, various structural and mechanism analysis techniques have been applied to vehicle development, [1] contributing to the simplification of prototyping and reduction of labor time required for vehicle development. As for NVH problems, examples of analysis techniques applied to idling vibration

analysis have been reported. [2] Analysis techniques are used not only for vehicle development but also for automotive component development. [3][4]

We have developed a full vehicle dynamic model using mechanism analysis to analyze vehicle vibration. The NVH problem we analyzed this time was the shudder vibration that occurs when a vehicle starts and runs straight ahead. This full vehicle dynamic model is a detailed mechanism analysis model that incorporates virtually all the elements usually included in automobiles, including a power train ranging from the engine to tires as well as a steering and suspension system. Using this full vehicle model, we have reviewed the effects of a drive shaft constant velocity joint on shudder vibration. The constant velocity joint model also reflects nonlinear elements in its mechanism simulation. We have verified that this model reproduces the forces that act on the interior of actual constant velocity joints. [3][4]

---

2. Shudder vibration in starting vehicles

Shudder vibration occurring in a starting vehicle is generally defined as the phenomenon in which a car body is excited by resonance between the engine vibration and the induced thrust on a sliding constant velocity joint.

Results of shudder vibration measurements obtained on an actual vehicle are summarized in **Fig. 1**, where **Fig. 1 (a)** illustrates vehicles speeds, **Fig. 1 (b)**, torques acting on the drive shaft, and **Fig. 1 (c)**, lateral acceleration below the driver's seat floor.

The area encircled with a dotted line represents a state where lateral vibration occurred and the vehicle accelerated while vibrating left and right. The conditions that induced shudder on the test vehicle were a time of 2.5 to 3.5 seconds after starting, vehicle speed of 28 to 40 km/h, and drive shaft torque of approximately 700 Nm, and the associated drive shaft speed was in a range of 230 to 330 rpm.

Fig. 2 illustrates the results of tracking analysis with the drive shaft torque values provided in **Fig. 1 (c)**.

As shown in **Fig. 2**, the major component of the shudder vibration is clearly the drive shaft rotation 3rd order. The drive shaft of the test vehicle is equipped with a tripod type constant velocity joint (hereafter, TJ) on its inboard side and a fixed constant velocity joint (hereafter, EBJ) with eight balls on its outboard side. Because of this, it appears that the inboard side constant velocity joint is responsible for shudder vibration on starting vehicles.

A non-mass-production sliding constant velocity joint was used in our experiment in order to analyze the shudder vibration phenomenon accurately.
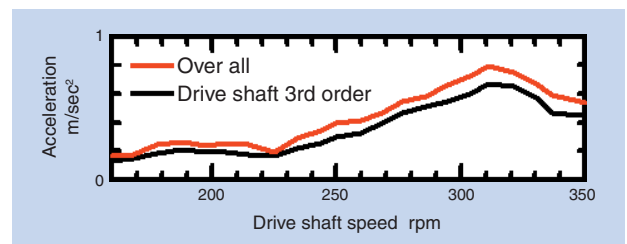
Fig. 2 Tracking result of fig.1 (c)

3. Full vehicle model

3.1 Power train and chassis model

To theoretically forecast the shudder vibration phenomenon, analyses of engine vibration characteristics and induced thrust on a constant velocity joint, as well as transmission of the engine vibration and the induced thrust to the car body via the mount and suspension, are also necessary. To this end, we developed a detailed full vehicle mechanism simulation model and performed analysis by applying a drive torque from the engine output in order to simulate an induced thrust occurring from rotation of the constant velocity joint.

Fig. 3 schematically illustrates the power train and chassis model used for our analysis work. The engine model simulated the piston and crank motion resulting from the pressure of the fired fuel. The model for the torque-transmitting transmission includes the simulated torque amplification by a torque converter, speed reduction by planetary gearing and motion of a differential. The model for suspension includes a spring mass capable of simulating the suspension resonance characteristics, and a suspension mass capable of simulating the rigidity of the stoppers on a starting vehicle. Furthermore, the tire model accurately simulates tire rigidity, thus allowing the simulation of a complete vehicle running on a road, including friction with the road surface.
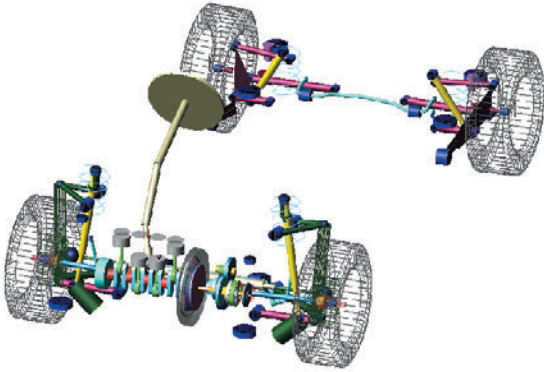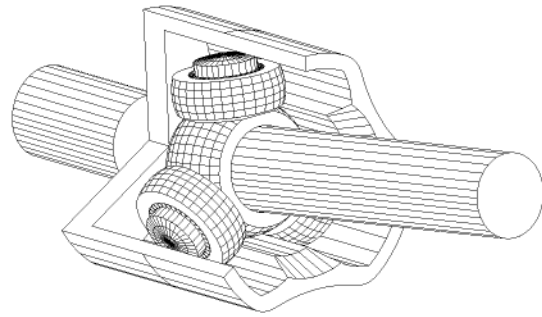

(a) Vehicle speed

(b) Drive shaft torque

(c) Acceleration of floor
(Lateral direction; 50Hz LP Filter)

Fig. 1 Experimental Results of Shudder Vibration
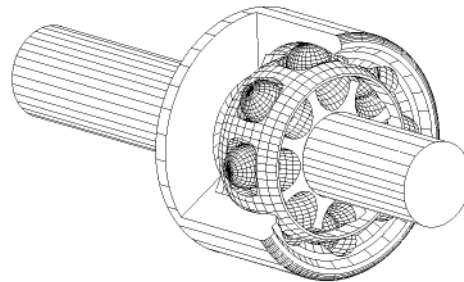
Fig. 3 Multi body Powertrain & Chassis model

Our vehicle model was developed with consideration for not only shudder vibration but also possible application for evaluation of other vehicle NVH performance. Thus, the vehicle model includes detailed simulation of sections not associated with prediction of shudder vibration.

3.2 Drive shaft model

As described in Sec. 2 above, we learned that the drive shaft 3rd order component affects shudder vibration. The test vehicle has the TJ on its inboard side. In order to simulate the drive shaft 3rd order, the constant velocity joint model must be a detailed mechanism simulation model. **Fig. 4** shows the constant velocity joint models (TJ and EBJ) that were used in our full vehicle dynamic model. Thus, this configuration provided mechanism simulation-capable inboard and outboard constant velocity joint models. Each of these mechanism models simulated the clearance, contact force and friction between the related components in the CVJs. [3) 4)]

4. Verification of analysis accuracy

Fig. 5 shows a comparison between the analysis results for lateral acceleration below the floor at the driver's seat and the actual experiment results. Though the amplitude obtained from the simulation is smaller than that obtained from the experiment, the results of analysis match those of the experiment well.

5. Analysis of shudder vibration phenomenon

5.1 Relation between engine and drive shaft

We found that shudder vibration on a starting vehicle is related to the drive shaft rotation 3rd order component. The speed of a drive shaft that triggers shudder vibration is in the range of 230 to 330 rpm. The frequency of the 3rd order component falls in a
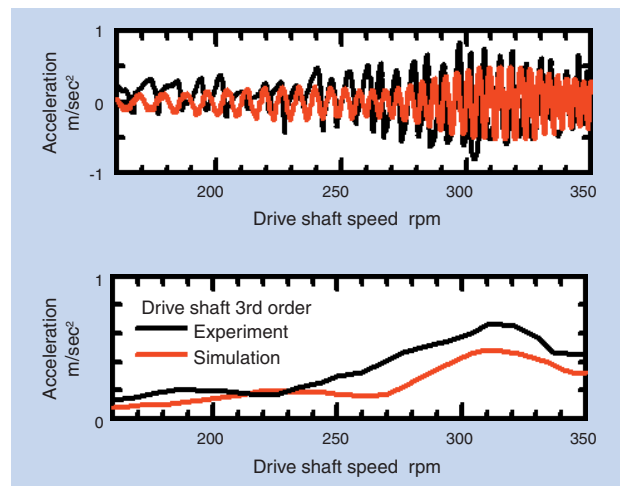

(a) Inboard CVJ (TJ)

(b) Outboard CVJ (EBJ)

Fig. 4 Multi body CVJ model

Fig. 3 Acceleration of floor (Lateral direction)

range of approximately 11.5 to 16.5 Hz. To investigate the vehicle vibration mode in this frequency range, we performed model analysis with the full vehicle model.

Fig. 6 illustrates the lateral direction engine mode. The characteristic frequency of the lateral engine motion was approximately 15 Hz. The drive shaft speed was approximately 310 rpm when the acceleration was greatest as shown in **Fig. 5**, and the frequency of the drive shaft rotation 3rd order component was approximately 15.5 Hz.

Because of this, shudder vibration seemed to occur from the resonance between the lateral acceleration of the engine and the drive shaft rotation 3rd order component.

For further clarification, we altered the rigidity of the engine mount in the mechanism simulation model, and again performed modal analysis and lateral shudder analysis. **Fig. 7** shows an engine vibration mode with reduced engine mount rigidity. The alteration to rigidity can be understood to change the characteristic vibration frequency and mode. **Fig. 8** offers a comparison of the magnitudes of shudder vibration between these two modes. In summary, for each particular engine mode, there is a unique vibration frequency and a unique magnitude of shudder vibration.

5.2 Influence of CVJ type

Induced thrust, which is one of the drive shaft rotation 3rd order components, typically occurs with the TJ. When the TJ is run, an induced thrust occurs along the rotational axis of the outer race and that mainly consists of the rotational 3rd order. This induced thrust is a force that results from frictional forces occurring because of the mutual friction of the rotating internal components on the TJ.[5] Therefore, we executed shudder vibration analysis with two sliding constant velocity joints with unique friction characteristics. **Fig. 9** summarizes the results of analysis for lateral acceleration below the floor at the driver's seat. As can be seen from this diagram, it seems that use of a low friction CVJ can alleviate shudder vibration.
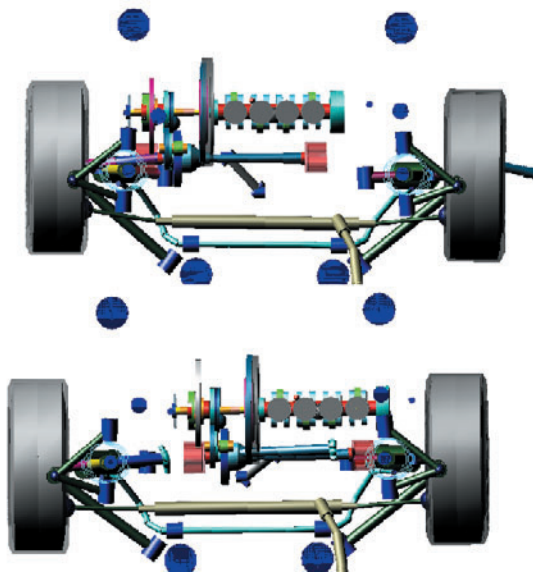
Fig. 6 Lateral engine mode shape (14.93Hz) of original model
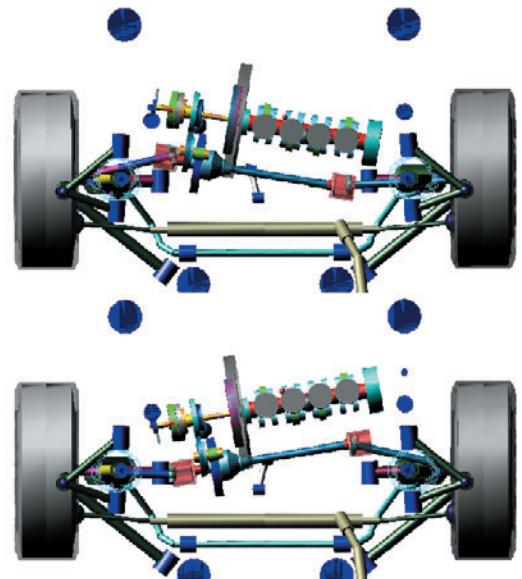
Fig. 7 Lateral engine mode shape (12.33Hz) of modified model
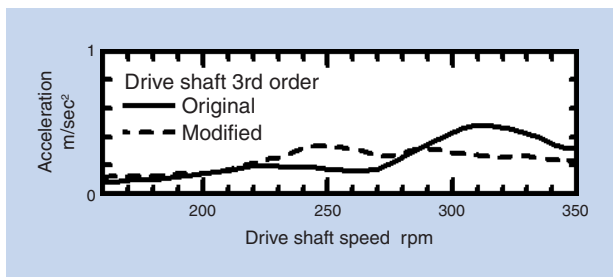

Fig. 8 Effect of engine mode on shudder vibration
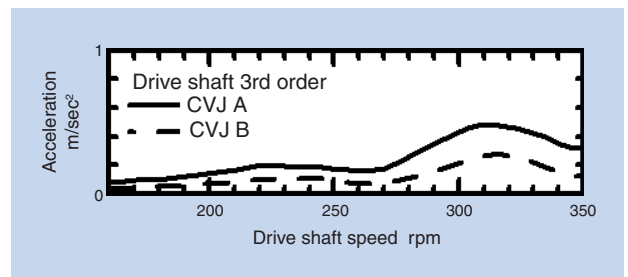

Fig. 9 Effect of CVJ on shudder vibration (Induced Thrust CVJ A>CVJ B)

5.3 Effect of phase gap with right-hand and left-hand CVJs

The shudder vibration test with an actual car was a forward traveling-only starting and acceleration test. When the vehicle turned, the resultant measurement values greatly varied. **Fig. 10** illustrates the running pattern used in the shudder test and the resultant maximum measurements of shudder vibration. The measurement operation was repeated 30 times for each constant velocity joint type. Each CVJ type exhibited measurement variation and had unique vibration characteristics. Notwithstanding, the lowest shudder measurements for both CVJ types were nearly same.

There are right-hand drive and left-hand drive shafts. The right hand and left hand TJs are incorporated via the differential box. The resultant force of the induced thrusts from the two TJs varies depending on the phase gap between both TJs. **Fig. 11 (a)** shows the definition of phase gap, and **Fig. 11 (b)** plots induced thrusts resulting from the phase gap angles between the two TJs. As can be seen in Fig. 11(b), when the relative phase of one TJ coincides with that of the other TJ, the resultant force of the induced thrusts theoretically becomes zero, and reaches the maximum level when the phase gap angle is 60 degrees.

With our full vehicle model, the effect of the phase gap between the right-hand TJ and the left-hand TJ was analyzed. As shown in **Fig. 12**, it was found through simulation that the magnitude of shudder vibration was largest when the phase gap was in a range of 45 to 60 degrees and was smallest when the phase gap was in a range of 100 to 120 degrees. As

is apparent from **Fig. 12**, this trend was validated in the experiment with an actual vehicle. Consequently, we learned that this variation in shudder vibration level occurred when the differential gearing was activated as the vehicle turned and, as a result, phase gap between the right hand and left hand TJs varied.
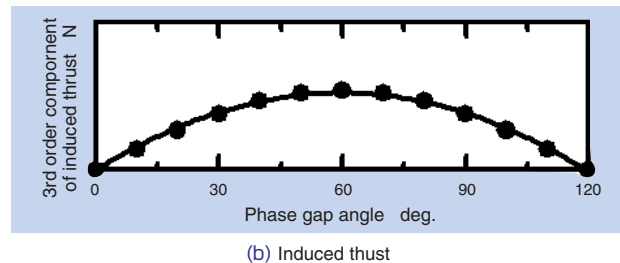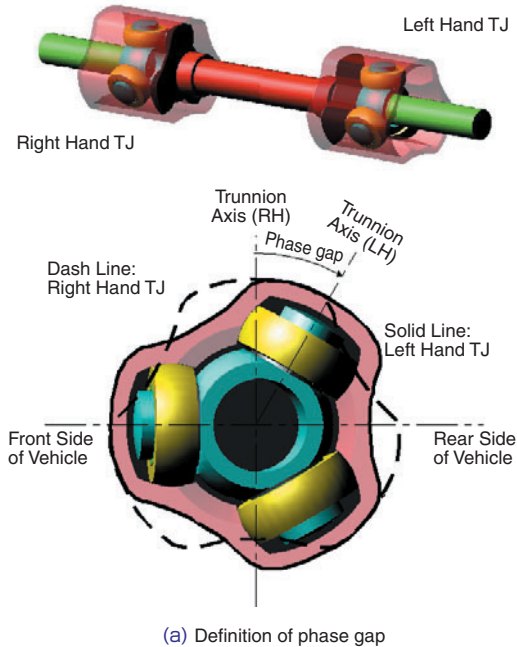

(a) Definition of phase gap

(b) Induced thust

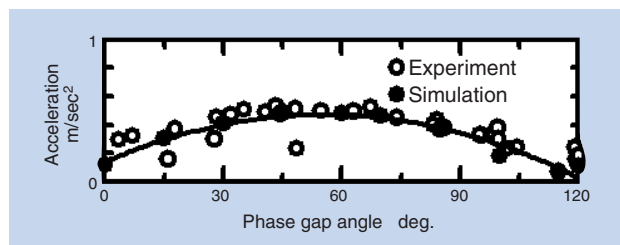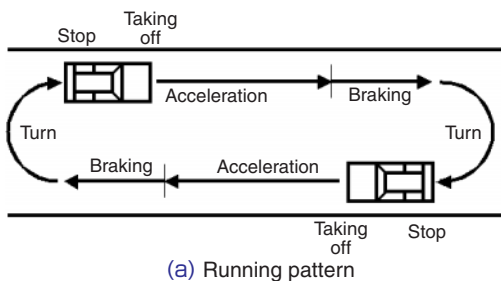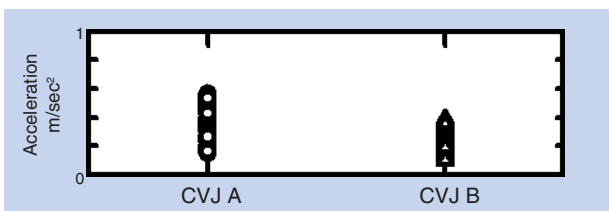**Fig. 11** Theoretical effect of CVJ phase gap on induced thrust

(a) Running pattern

(b) Experimental data (30 times par each CVJ)

Fig. 10 Mesurement summary of shudder test

Fig. 12 Effect of CVJ phase gap on shudder vibration

6. Conclusion

We developed a full vehicle running-capable mechanism simulation model and performed a simulation for vehicular NVH (analysis of shudder vibration).

We identified and verified the relationship between the shudder vibration mechanism on a starting vehicle and engine vibration modes.

We qualitatively and quantitatively clarified the interrelation between induced thrusts and shudder vibration levels on constant velocity joints.

References

1) Kurisu, Fujikawa, Miyauchi, Koizumi, Hirobe, Fukushima: Application of ADAMS mechanism analysis software to power trains, Mazda Technical Review, No. 22, p44-49 (2004).

2) Matsumoto, Suzuki, Kitani, Kanuma: Idling shudder analysis using a full vehicle model, the Society of Automotive Engineers of Japan, 2003 Spring Scientific Lecture Session preprints, No. 39-03, p1-4 (2003).

3) Hayama: Dynamic internal force analysis for constant velocity joints considering nonlinear elements, the Japan Society for Computational Engineering and Science, lecture proceedings, Vol. 8, No. 1, p393-396 (2003).

4) Hayama: Internal force analysis for constant velocity joints, the Society of Automotive Engineers of Japan Journal, Vol. 34, No. 4, p157-162 (2003).

5) Nozaki, Kobara: Experimental determination of forces acting on tripod constant velocity joint housings, the Japan Society of Mechanical Engineers, 2003 annual meeting proceedings, IV, p155-156 (2003).

Photos of authors

Yoshihiko HAYAMA

New Product Development
R&D Center
New Product Development Dept.

Takashi NOZAKI

Automotive Sales Headquarters
Automotive Engineering Dept.

Masafumi NAKAKOUJI

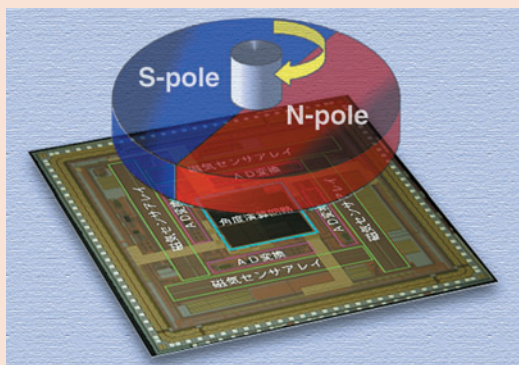Automotive Sales Headquarters
Automotive Engineering Dept.

Satoshi FUJIKAWA

Mazda Motor Coproration
Powertrain Advance
Development Dept.

Komaki FUKUSHIMA

Mazda Motor Coproration
Powertrain Advance
Development Dept.

[**Technical Paper**]

Development of a High Precision Angle Sensor

Toru TAKAHASHI*
Yoshitaka NAGANO*
Shoji KAWAHITO**

Small and high-resolution encoders capable of absolute angle detection are required for many applications such as automotive, industrial, consumer products, and robots. For automotive applications, these sensors are used not only for the motion control of mechanical parts and motors, but also for sensing the human operating motion such as steering sensors or pedal sensors. However, commonly used rotary encoders using magneto-resistive devices or Hall devices combined with a multi-pole magnet have difficulty in meeting these requirements because they have a large cylindrical structure and need a fine-pitched magnetic scale. Furthermore, they can not detect absolute angles. This paper presents a single-chip CMOS magnetic rotary encoder system that operates on a new working principle based on magnetic pattern analysis with a statistical calculation method. The developed chip can detect the absolute angle at a resolution of 10bits per rotation, which leads to a promising solution for compact high-resolution rotary encoders.

1. Introduction

Rotary encoders for rotational angle detection have been used in a variety of industrial applications, including detection of actuation and travel amounts and motor speed control. In automotive applications, rotary encoders are utilized for steering system angle detection, accelerator pedals and throttle valves to improve vehicle operability and safety. For every automotive application, the need has been mounting for more compact rotational angle detection sensors that are capable of higher detection accuracy and are less expensive.

The detection schemes of rotary encoders can be categorized as contact and non-contact types. Components on a contact type rotary encoder can deteriorate from wear. Non-contact rotary encoders can be further subcategorized into optical rotary encoder types that utilize transmission or reflection of light beams and magnetic rotary encoder types that

detect magnetic field variations. Since they are less susceptible to the effects of dust, magnetic rotary encoders are used more often in automotive applications.

On many commonly used magnetic rotary encoders, a magnetic sensor, such as a Hall sensor or an MR device, is used to detect the magnetic field variation that results from rotation of a multi-pole magnet. Most of the **NTN** bearings equipped with rotary encoders use this type of a magnetic sensor. However, this arrangement poses an obstacle to creating more compact rotary encoders because the pole pitch of the multi-pole magnet would be too small for the magnetic sensor to detect magnetic field variations. Therefore, a new sensor that operates on a different principle has been needed to provide a compact detection system that is capable of high precision angle detection.

In cooperation with Professor Shoji Kawahito of the Shizuoka University Research Institute of Electronics,

*New Product Development R&D Center   Mechatronics Research Dept.
**Shizuoka University   Research Institute of Electronics   Professor

NTN has developed a unique compact magnetic array rotary encoder that measures 5 mm square and is capable of detecting an absolute angle of ±0.36˚. At the International Solid-State Circuits Conference 2005 (ISSCC 2005) held in February 2005, this sensor won the Beatrice Winner Award for Editorial Excellence.[1] This paper provides an overview of our sensor and reports the results of angle detection with a compact bearing that incorporates this sensor.

2. Magnetic array sensor operating principles

2.1 Structure of sensor

The rotary encoder we have developed consists of a permanent magnet (using sintered NdFeB) at the tip of a rotary shaft and a 5 mm square sensor chip opposite the permanent magnet with a gap of approximately 0.5 to 1 mm between them (**Fig. 1**).

The internal configuration of the sensor circuit formed on the sensor chip is schematically illustrated in **Fig. 2**. The integrated sensor chip is comprised of a magnetic sensor array (MAGFET Array) consisting of multiple miniature sensor elements arranged along the four edges of a tetragon. These include a sample-and-hold amplifier (SHA) circuit that amplifies sensor
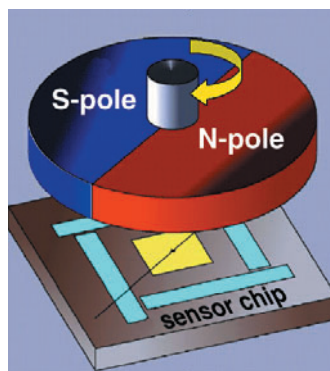
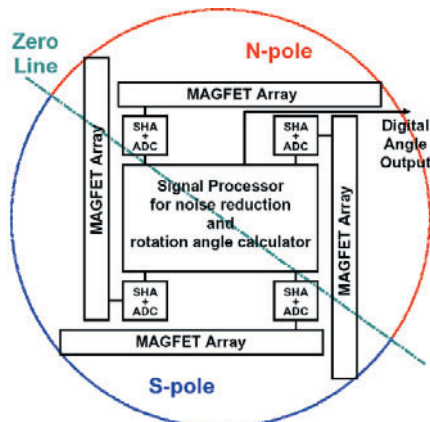signals, an analog-to-digital converter (ADC) circuit that converts analog signals into digital signals and a digital processor circuit that calculates rotational angles. This integrated sensor chip has all the functions needed to detect the absolute rotational angle of a magnet and output detection results as numerical data.

2.2 MAGFET magnetic sensor element

Our sensor chip uses a split-drain MAGFET (Magnetic Field Effect Transistor) for each magnetic sensor element. MAGFETs can be manufactured by a CMOS (Complementary Metal-Oxide Semiconductor) process similar to that used for ordinary logic circuits. They can also be incorporated into chips that also include amplifier and calculator circuits.

The MAGFET structure and corresponding circuit are illustrated in **Fig. 3**.

Like common transistors, each MAGFET has four terminals, including a source (S), a gate (G) and two separate drain (D) terminals. This sensor is sensitive to magnetic fields that are perpendicular to the sensor elements, and functions because of the Lorentz force used for the current within the transistor. When a magnetic field is not present, the current levels of the two drain terminals are the same and the relation $I_1=I_2$ holds. When a magnetic field B_z is applied, electrons will flow in the direction of the red arrow in **Fig. 3**, and there will be a bias between the currents of both drain terminals, resulting in a difference between the drain currents (I_1-I_2) that occur in accordance with the magnetic field applied.

When assuming that the magnetic field intensity is B_z [T], the sensor sensitivity is S_R [1/T] and the sensor bias current holds a relation of $I_{bias} = I_1+ I_2$, then the sensor output signal can be defined as follows:

$$I_{signal} = I_1 - I_2$$
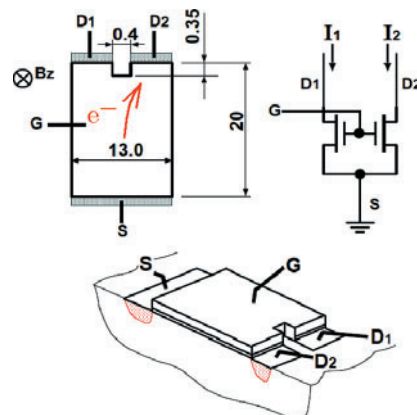$$= S_R\, B_Z\, I_{bias} \cdots\cdots\cdots\cdots\cdots\cdots\cdots\cdots (1)$$

Fig. 1 Rotary encoder setup

Fig. 2 Block diagram of the sensor chip

Fig. 3 Structure of MAGFET (unit μm)

2.3 Angle detection scheme

The arrangement of the sensor arrays is shown in **Fig. 4**. This diagram illustrates a state where the magnet is at a standstill with a rotational angle θ. The blue line in this diagram shows the border between the N-pole and the S-pole. The magnetic field perpendicular to the page from this line is zero, so this line is called the "Zero-Line."

When the sensor signals from the multiple MAGFETs arranged on the sensor chip are sequentially read in a clockwise direction, beginning with the No. 1 position in the upper left corner of **Fig. 4**, and the read signals are plotted, the wave pattern shown in **Fig. 5** is obtained. The relation between the magnetic field distribution and the sensor signals is shown in **Fig. 6**. By detecting two points, Z_1 and Z_2, where the obtained sensor signal level is zero, the angle of the Zero-Line can be calculated based on their coordinates.

$$\theta = \tan^{-1}(\triangle y / \triangle x) \cdots\cdots\cdots\cdots\cdots\cdots (2)$$
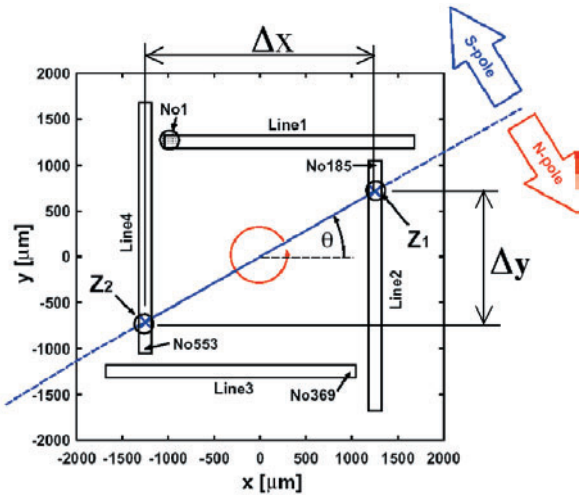
Fig. 4 Arrangement of sensor arrays
(magnet is set at an angle θ)
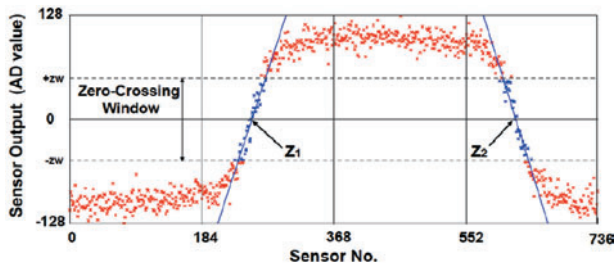
Fig. 5 Output signal of the sensor arrays

Two points where no magnetic field exists are detected.
→ Boundary angle is calculated.
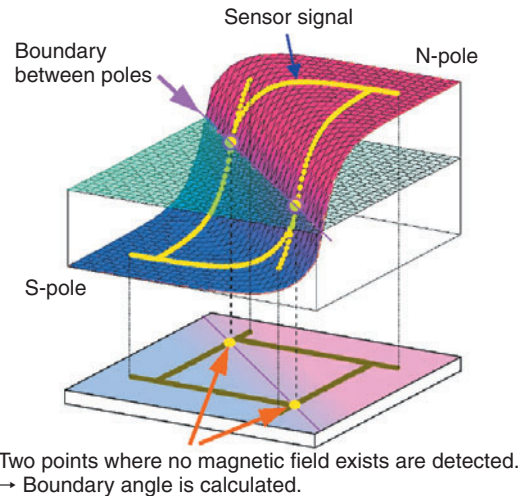
Fig. 6 Detection of the Zero-Line

To improve the detection accuracy of two zero-crossing points in the actual calculation process, the Zero-Crossing Window, the area subjected to calculation shown with dotted lines in **Fig. 5**, is set, and the multiple sensor signals included in this window are statistically processed.[2] A block diagram of the angle calculator circuit is shown in **Fig. 7**. The sensor data AD1 through AD4 obtained from the sensors on the four edges are stowed in the memory. Then the data within the zero-crossing window are sampled and subjected to calculation. In the calculator circuit, the positions of the two zero-crossing points are determined accurately to enable linear approximation based on a Least Mean Square (LMS) method. Using the coordinates of the two determined points, calculation is executed as per expression (2) (arctan CORDIC circuit), and then the calculated 10-bit angle data is output to an external system. Since this calculator circuit includes a communication circuit (Comm.I/F), it can output angle data through a serial communication means.
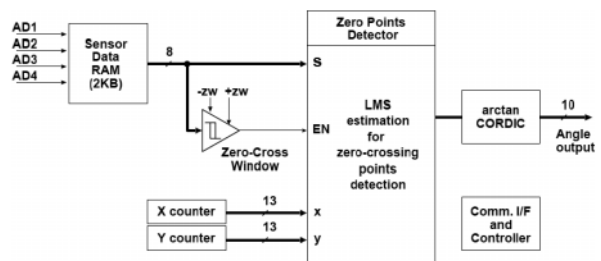

Fig. 7 Block diagram of the angle calculator

2.4 Features of our sensor system

Our sensor system calculates an angle based on magnetic field distribution measured by multiple magnetic sensors, and has the following advantages.

(1) Since it is intended to detect a position where a magnetic field does not exist (position where the level of magnetic sensor output is zero), our sensor system is not affected by sensitivity variation or the non-linearity of the sensor elements. As a result, a complicated compensation process is not necessary.

(2) Since multiple sensor signals are statistically processed, the effect of signal noise is minimized, resulting in the improved angle detection accuracy.

(3) Since the angle is calculated from the coordinates of two zero-crossing points, our sensor system is not much affected by the positional difference between the magnet and the sensor elements.

(4) The MAGFET magnetic sensor chip can be manufactured by a common CMOS process. As a result, related circuits can be incorporated into the same chip, reducing manufacturing costs.

3. Native-MAGFET

As explained above, our MAGFET magnetic sensor chip can be manufactured by an ordinary CMOS process. However, because it is made from a silicon material, its magnetic sensitivity is lower than Hall sensors and other sensor chips made from chemical compound semiconductor materials. In addition, variations in the characteristics of the MAGFET are unavoidable because the chip is manufactured through an ordinary CMOS process.

To attain sufficiently accurate angle detection with our sensor system, it was necessary to improve the sensor performance by enhancing the magnetic sensitivity of the sensor elements. To achieve this, we invented a native-MAGFET structured as shown in **Fig. 8**.[3] This diagram shows cross-sectional views of CMOS circuit transistors and the native-MAGFET.

Structured identically to an nMOS transistor, a "normal-MAGFET" is usually formed on the p-well region. In contrast, native-MAGFET is formed directly on the p-substrate, and its impurity concentration directly beneath the gate differs from that of a normal-
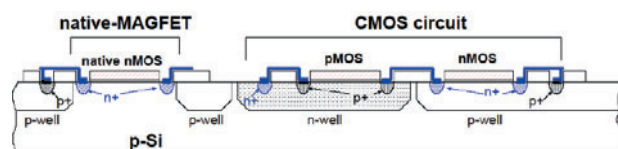
MAGFET. Use of a native-MAGFET leads to the following advantages.

(1) Compared to the p-well region, the impurity concentration on the p-substrate is lower. This in turn leads to higher electron mobility within the native-MAGFET, causing the MAGFET chip to have higher magnetic sensitivity.

(2) Because the p-well region is formed through an ion implantation process, the concentration of implanted ions can vary, which leads to variation in the characteristics of the sensor elements formed in this region. Native-MAGFETs are free from this problem, so variation of characteristics is minimized.

The results of measured magnetic sensitivities of normal and native MAGFETs are plotted in **Fig. 9**. In this diagram, IMAGFET represents bias currents carried by the MAGFET. While the magnetic sensitivity of the normal-MAGFET was 2.7%/T, that of the native-MAGFET was approximately 5%/T%. The sensitivity of the native-MAGFET is approximately twice as high as that of the normal-MAGFET. At the same time, we learned that the magnetic sensitivity of the native-MAGFET decreased as the bias current increased. Because the sensor elements were formed directly on the p-substrate, the channel structure of regions with lower gate voltage seems to be similar to that of embedded channels. We believe that with a higher gate voltage, the distribution of channels shifts to the surface. Since the channels are affected by diffusion at the interface, decreasing electron mobility, magnetic sensitivity is reduced.
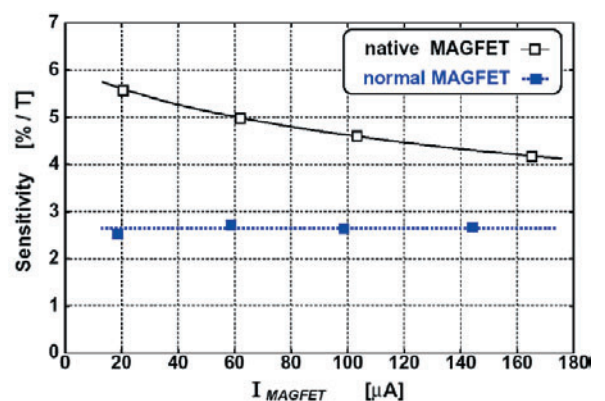

Fig. 9 Magnetic sensitivity of the MAGFETs
(I_{MAGFET} : bias current in a MAGFET)

Fig. 8 Cross section of native-MAGFET

4. Verification of our prototype chip operation

The prototype sensor chip is shown in **Photo 1**. This chip was fabricated through a standard $0.25\,\mu$ m CMOS process [5-layer metal wiring, 1-layer polysilicon, MiM (Meal-Insulator-Metal) capacitor]. The sensor chip measures 5 mm by 5 mm, and the sensor array measures approximately 4.2 mm square.

The technical data of the prototype sensor chip are as follows.

(a) Number of sensor elements: 184 pixels×4 lines
(b) Structure of one pixel: six MAGFETs connected in parallel
(c) Chip size: 5×5 mm
(d) Chip thickness: approx. $300\,\mu$ m
(e) Number of IO terminals: 100 (including test terminals)
(f) Angle detection resolution: ±0.36 degrees

The result of angle detection with our sensor chip is summarized in **Fig. 10**. The horizontal axis corresponds with one revolution of the magnet (360 degrees). The angle resolution was within ±0.36 degrees, and accuracy of 10 bits per revolution was achieved.
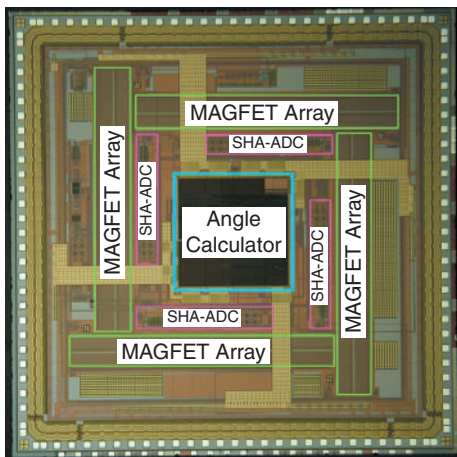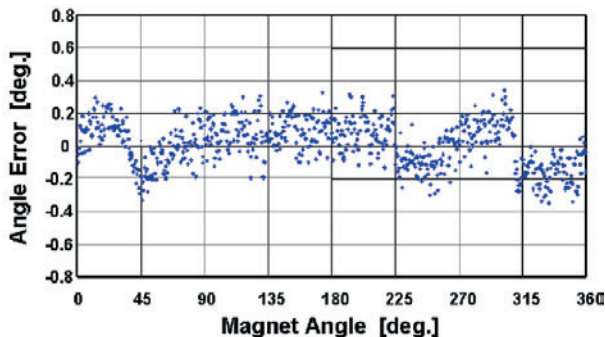

Photo 1 Micrograph of a prototype chip

Fig. 10 Angle detection result

5. Sensor bearing sample

A sample sensor bearing that incorporates our sensor chip is shown in **Photo 2**. Its structure is shown in **Fig. 11**, together with the structure of a conventional sensor bearing.
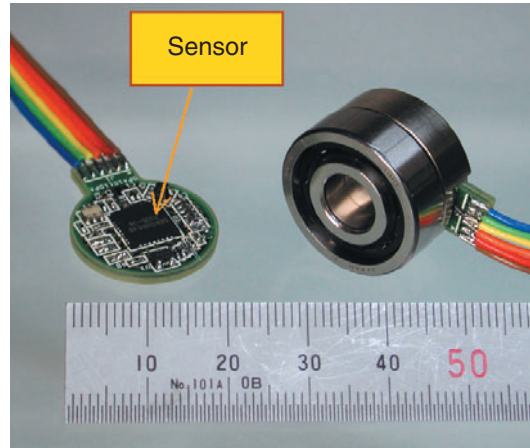

Photo 2 Picture of a sensor bearing sample

(a) Conventional sensor bearing
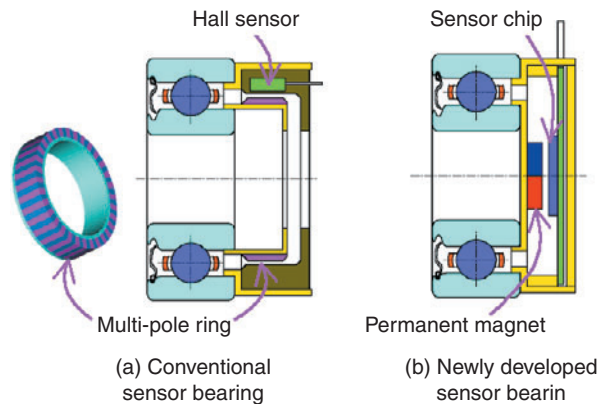
(b) Newly developed sensor bearin

Fig. 11 Cross section of sensor bearings

The optimal resolution with conventional sensor bearings was approximately 2 degrees (180 pulses/revolution). As pulse output types, they cannot detect absolute angles. In contrast, our sensor bearing is capable of 0.36-degree resolution and can detect an absolute angle and output this angle as a digital value. The sensor chip can be installed easily, and the sensor bearing can be of a more compact design. The angle detection accuracy of the new sensor bearing is plotted in **Fig. 12**. The detection error at a sampling speed of 10 kHz was within ±0.3 degrees.
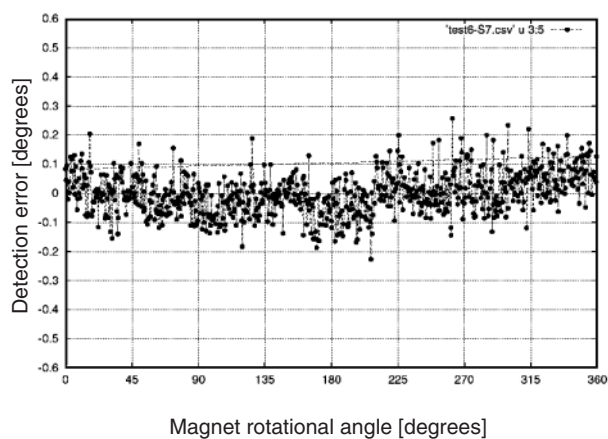

Fig. 12 Angle detection result using a sensor bearing

6. Conclusion

We have developed a novel rotational angle sensor that employs magnetic sensor arrays. To improve the characteristics of sensor elements on silicon substrates, we developed a new sensor structure using a native-substrate MAGFET to enhance the magnetic sensitivity of the sensor elements, thereby achieving a very high angle detection accuracy of 10 bits per revolution (0.36 degrees). This degree of angle detection accuracy was also achieved with a sensor bearing that incorporates a MAGFET sensor chip sealed in a compact package.

Automotive components are becoming increasingly more compact and functional. We intend to apply our simple, compact sensor chip to automotive applications including steering systems and accelerator pedals.

References

1）S. Kawahito, T. Takahashi, Y. Nagano, and K. Nakano, "CMOS Rotary Encoder System Based on Magnetic Pattern Analysis with a Resolution of 10b per Rotation," ISSCC2005, Dig. Tech. Papers, IEEE Int. Solid-State Circuits Conf., pp.240-241, 2005.

2）K. Nakano, T. Takahashi, S. Kawahito, "Angle Detection Methods for a CMOS Smart Rotary Encoder," Journal of Robotics and Mechatronics Vol.17(4), pp.469-474, 2005.

3）Toru Takahashi, Kazuhiro Nakano, and Shoji Kawahito, "CMOS Magnetic Sensor Arrays Using Native-Substrate MAGFETs for a Smart Rotary Encoder," Proc. IEEE SENSORS 2004, pp.973-976, 2004.

Photos of authors

Toru TAKAHASHI

New Product Development
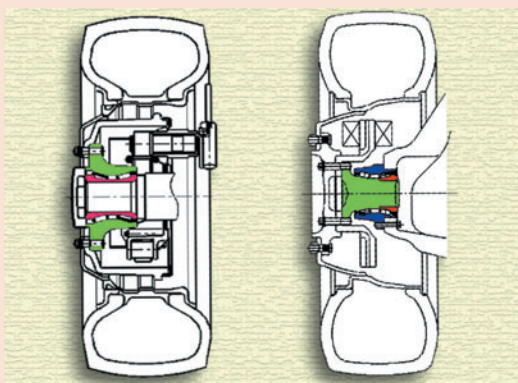R&D Center
Mechatronics Research Dept.

Yoshitaka NAGANO

New Product Development
R&D Center
Mechatronics Research Dept.

Shoji KAWAHITO

Shizuoka University
Research Institute of Electronics
Professor

Tapered Roller Hub Bearings for Large Truck

Hiroshi KAWAMURA*
Akira FUJIMURA*

Hub bearings for larger commercial vehicles have advanced to unit type for the purpose of reliability and easy assembling. This article features the transition of continuous improvement in hub bearings for larger commercial vehicles and technology of the newly developed Tapered Roller Hub Bearing, that has supposed the largest diameter in the world.

1. Introduction

Recently, unit designs have been increasingly implemented in front axles for large trucks in order to improve reliability and assembly ease. Previously, two single-row tapered roller bearings had been used for this purpose. However, this arrangement occasionally posed safety problems. Incorrect adjustment of preload on an assembled bearing during truck repair caused premature flaking or seizure. To address this problem and improve truck safety, unit designs for axle bearings have been increasingly introduced. Following European truck manufacturers, Japanese truck manufacturers also began developing unit design axles, and now some Japanese truck manufacturers are using 2nd generation tapered roller hub bearings (hereafter, GEN2 HUR). This paper describes the current trend in axle bearings on large trucks as well as the GEN2 HUR that **NTN** has recently developed. This unit consists of an outer race integrated with a hub ring and has the largest flange diameter in the world.
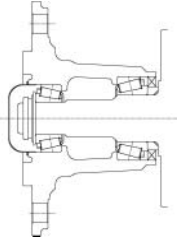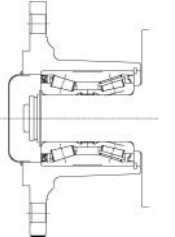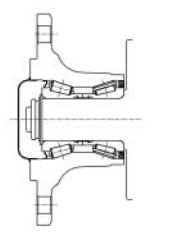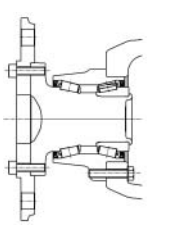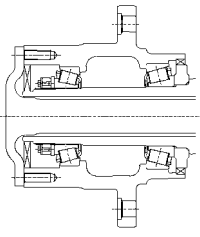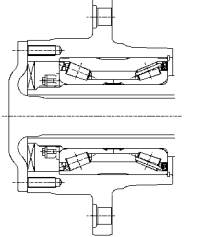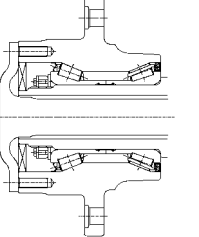
2. Construction and features of large truck axles

Previously, two single-row tapered roller bearings were usually used for large truck axles. Then, GEN1 units composed of two bearings and set light bearings were adopted. Compared to previous designs that use two single-row tapered roller bearings, these designs boast higher reliability and ease-of-assembly. In 2000, **NTN** began mass-production of GEN2 HUR for the first time in Japan. This bearing type includes a unit comprised of a bearing and a hub ring mounting flange (a bearing accessory). **Table 1** summarizes the history of HUR development by **NTN**, and the features of HURs of various generations. We believe that the trend for large truck axle bearings will be a shift to GEN2 HURs. To satisfy this need, **NTN** has developed a GEN2 HUR that features the world's largest flange diameter. Furthermore, to attain higher reliability, **NTN** is currently developing GEN3 HURs that do not need axle nut tightening control.

---

*Automotive Sales Headquarters   Automotive Engineering Dept.

Table 1 Features of Tapered roller hub bearings in each generation

Ranking：☆＜☆☆＜☆☆☆

	Non-driven wheel use			
Generation	Conventional	GEN1	GEN2	GEN3
Rotation system	Outer race rotation	Outer race rotation	Outer race rotation	Inner ring rotation
Assembly and service ease	−	☆	☆☆	☆☆☆
Compactness	−	☆	☆☆	☆☆
Built-in seal	−	☆☆	☆☆	☆☆
Preload control	−	☆	☆☆	☆☆☆
	Driven wheel use			
Generation	Conventional	GEN1		GEN2
Rotation system	Outer race rotation	Outer race rotation		Outer race rotation
Assembly and service ease	−	☆		☆☆
Compactness	−	☆		☆☆
Built-in seal	−	☆☆		☆☆
Preload control	−	☆		☆☆

3. NTN HUR development status

3.1 Mass-production of GEN2 HUR

GEN2 HUR technology is described in **NTN** Technical Review No. 70. **NTN**'s GEN2 HUR mass-production record is summarized in **Table 2**.

Table 2 GEN2 HUR Mass production results

Truck manufacturer	Truck type	Application	Beginning of mass-production
Company A (Japan)	Large truck (24 t)	Front wheel (non-driven wheel)	2000〜
Company B (Europe)	Large truck (24 t)	Front wheel (non-driven wheel)	2001〜
	Medium truck (12 t)	Front wheel (non-driven wheel)	2002〜
Company C (Europe)	Trailer	Trailer rear wheel (non-driven wheel)	2003〜

3.2 GEN2 HUR Development

NTN has developed a large size GEN2 HUR that can be used not only for large truck front axle non-driven wheels, but also for driven wheels on rear full floating axles. We will describe this newly developed product in more detail. This GEN2 HUR is a lightweight tapered roller hub bearing that has an outer race integrated with a hub ring, and features the largest GEN2 HUR flange in the world.

(1) Bearing structure and assembly

Fig. 1 illustrates the structure of GEN2 HUR for non-driven wheels, and **Fig. 2** shows the structure of GEN2 HUR for driven wheels. Featuring an outer race integrated with a hub ring, the newly developed HUR has been optimally designed to reduce the stress that occurs on the hub due to high load when the truck turns as well as to lighten the bearing. **Fig. 3** shows an example of GEN2 HUR application. The assembly
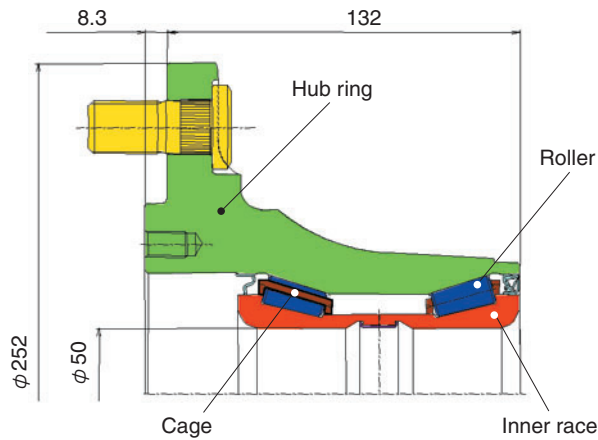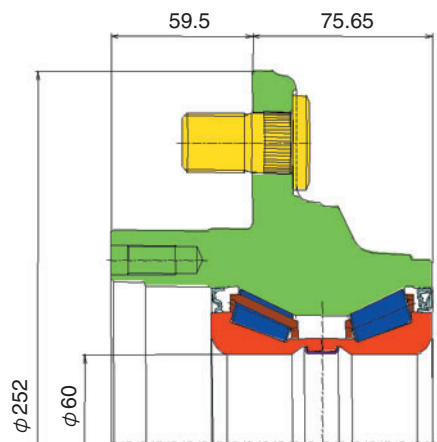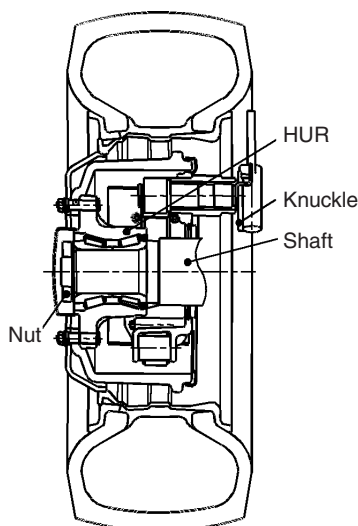
Fig. 1 Front non-driven GEN2 HUR structure

Fig. 2 Rear driven GEN2 HUR structure

<Assembly of GEN2 HUR on trucks>
① The GEN2 HUR is inserted over the shaft.
② The nut at the shaft end is tightened
　　with a predetermined torque.

Fig. 3 Structure of axle assembled GEN2 HUR

method for the GEN2 HUR is the same for both driven and non-driven wheels.

(2) Hub ring, inner race and roller materials

The hub ring is made of a unique **NTN** bearing material that features good castability and excellent shock resistance. Areas where greater stress can occur when the bearing operates are treated with an induction heating process to give them higher static strength and rotary bending fatigue strength. The material for the inner ring and rollers is SUJ2.

(3) Lubricant

For axle bearings on large trucks, we are adopting a newly developed grease that boasts fretting resistance, high temperature resistance and long life. **Table 3** summarizes the grease's general characteristics, and **Table 4** provides the results of a high temperature durability life test.

① The grease includes a base oil that excels in oil film formation performance at high temperature and under high bearing pressure in order to prevent overheating and scuffing-induced wear that tends to occur on inner race larger ribs.

② With a urea-based thickener featuring excellent shear stability, the grease boasts good durability.

Table 3 General characteristics of grease

Thickener	Urea-based thickener
Base oil	Mineral oil + synthetic oil
Operating temperature range	$-30 \sim +150$°C
Hue	Yellow

Table 4 Test result of grease fatigue

Grease type	Life test result (hr)
Current representative grease for trucks (Sunlight 2)	46
HUR grease	1618

※ **NTN** test data
　Test method = ASTM D3336 modified
　Bearing = 6204, amount of prefilled grease = 1.8 g,
　test temperature =150°C
　Speed = 10,000 r/min, F_r= 67 N, F_a= 67 N

(4) Cage

The polyamide resin cage used can be easily assembled into the bearing and has excellent heat resistance, flexibility and durability. This makes possible a lighter weight at a lower price. Its shape has also been optimized to promote ease of assembly into the bearing.

(5) Seal

A double-lip high-pack seal has been adopted to provide good seal performance against mud water, which trucks traveling long distances often experience, and to simplify the bearing assembly process. **Table 5** summarizes the results of a mud water resistance test with various seal types. The seal material for our newly developed bearing is fluorine rubber (FKM) to ensure better high temperature durability. The slinger material that provides the sliding surface of the lip is stainless steel, making it rust-resistant.

Table 5 Test result of seal performance against mud water

Seal type	Cross-section	Mud water resistance (durability cycle)	Durability ratio
Conventional seal		2	1
Double-lip seal		4〜7	2〜3.5
High-pack seal		18〜20	9〜10
New seal (double-lip high-pack seal)		30〜38	15〜19

※ **NTN** test data
 Speed = 1100 r/min, shaft eccentricity = 0,
 as mounted eccentricity = 0.05 TIR,
 Liquid level = to the shaft center
 Material blocked = Kanto loam powder, JIS class S8, 10 wt%,
 Test cycle = 20 h run + 4 h standstill

(6) Hub ring (outer race), inner race raceway surface, and roller rolling surface and large end face forms

When a truck turns, a greater load acts on its hub, and an edge load can occur on the hub. To avoid this problem, the hub ring (outer race) and inner race raceway surfaces, as well as the roller rolling surfaces, have optimal complex crowning (example of contact stress calculation in **Fig. 4**).

In addition, the roundness of the large end face of each roller has been optimized to prevent scuffing and seizure caused by slippage between it and the inner race large ribs.

3.3 Test rig and evaluation result

Axle bearings are important safety components that support vehicles so that they can run safely. A bench test is very important in ensuring the functionality and reliability of bearings. **NTN** possesses various test rigs for evaluating axle bearings, and can evaluate HURs for large trucks through various tests such as rolling fatigue life test. One of the **NTN** test rigs and a part of the HUR evaluation results are described below.

(1) Evaluation test rig

The **NTN** durability test machine for large trucks is schematically illustrated in **Fig. 5**. This machine is capable of applying a maximum radial load of 196 kN and a maximum axial load of 98 kN. In executing tests, a strain gauge and a measuring instrument are used to measure stresses occurring in various areas. Since this machine can run with a program that can vary the load and bearing speed during the test run, it is capable of simulating cyclic loads or actual vehicle running modes.
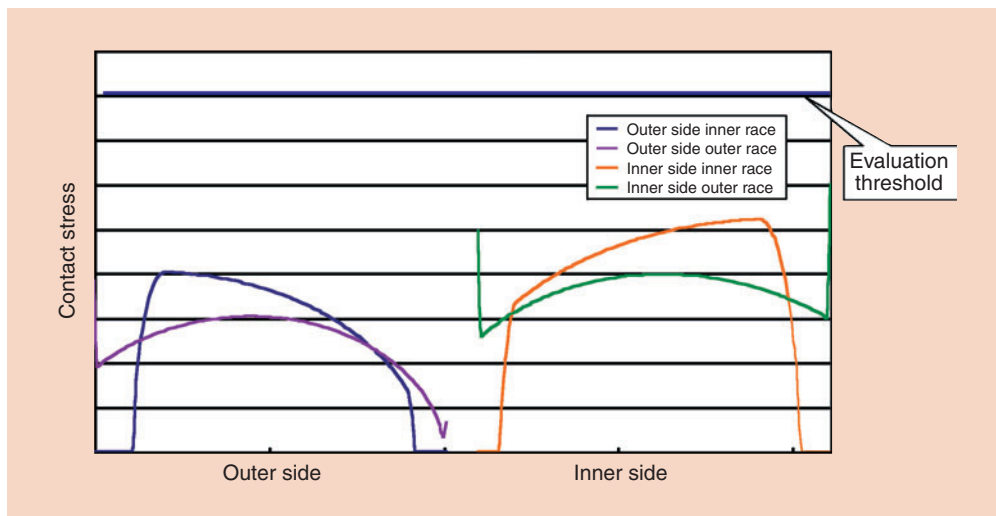

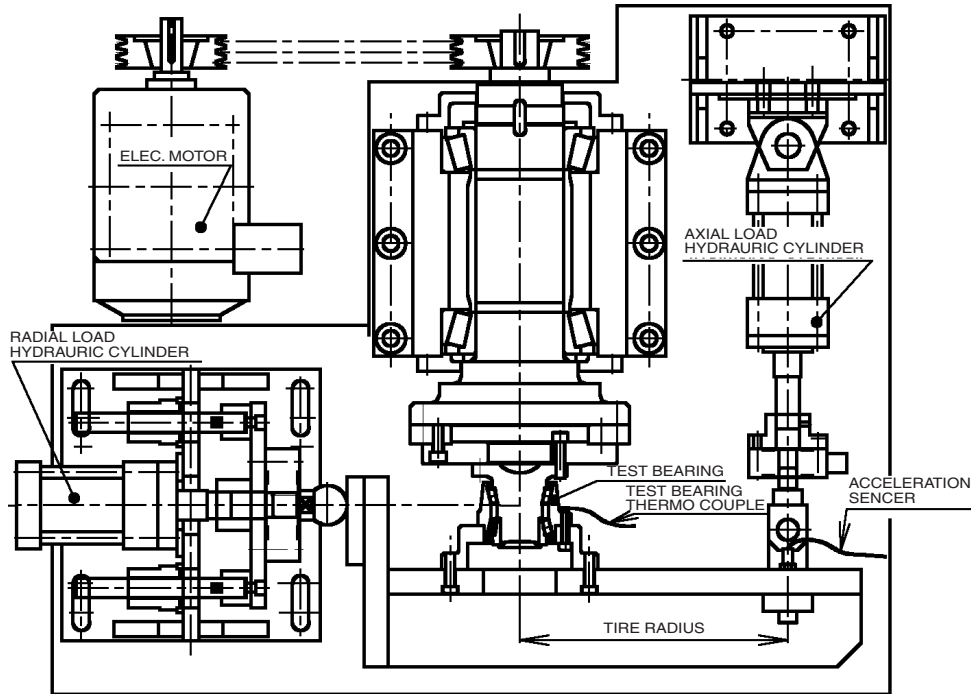**Fig. 4** Example of contact stress calculation

Fig. 5 Test machine structure

(2) HUR analysis and testing results

The results of analysis and testing of the HUR illustrated in **Fig. 2** are described for three aspects–hub ring stress analysis, heavy load durability and high speed durability. In designing the hub ring, wall thickness was thinned through the counterboring of flanges and the optimization of rib shape. For this effort, we employed FEM to limit the stresses to levels below standard values, thereby we have succeeded in

weight reduction of approximately 20%.

① **Hub ring stress analysis**

Predetermined moment loads were applied to various areas, a set number of times, to measure the stress occurring in each area. We verified that each area successfully withstood load application and did not reach the fatigue limit. An example of hub ring stress analysis is provided in **Fig. 6**.
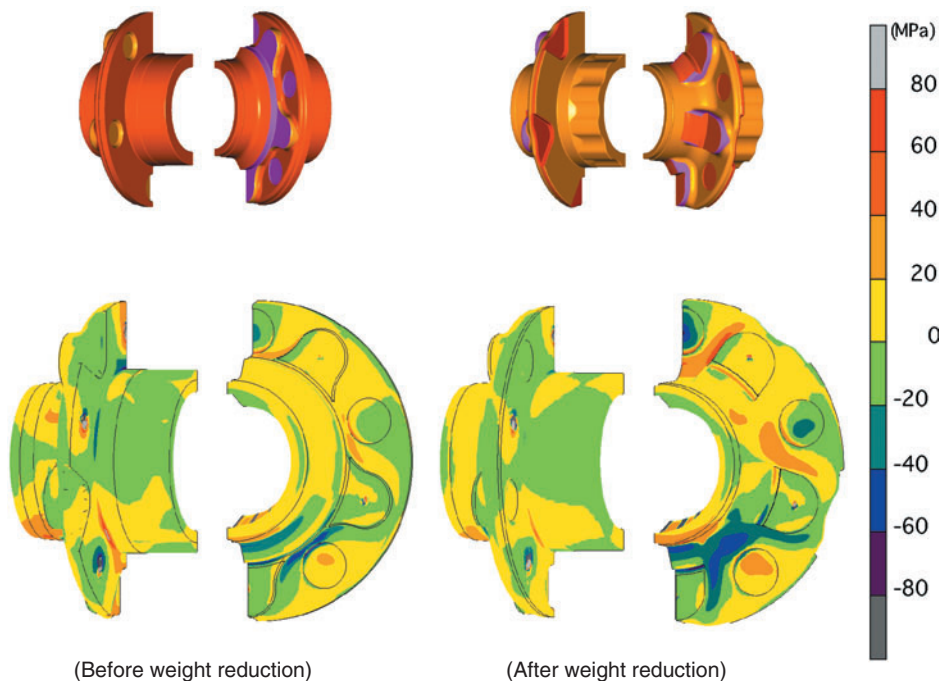
(Before weight reduction) (After weight reduction)
Fig. 6 FEM analysis example

② **Heavy load durability test (0.6 G turning moment durability test)**

The results of this test are summarized in **Table 6**. The actual life with each sample was more than three times the targeted life (calculated life), showing that each sample had sufficient durability.

③ **High speed durability test**

The results of a high speed durability test are summarized in **Table 7**. Even if the bearing was operated at the maximum vehicle speed (160 km/h) for 20 hours, it did not seize and there was little oil leakage. Thus, we verified that our bearing has sufficient durability.

Table 6 Test results of 0.6G turning moment durabirity

Bearing	Number of revolutions $L(\times 10^4 \mathrm{rev})$	Calculated life $L_0(\times 10^4 \mathrm{rev})$	Calculated life ratio L/L_0	State after test
Front non-driven wheel	2545		3.0	Suspended
	2545	848	3.0	Suspended
	2545		3.0	Suspended
Rear driven wheel	867		3.0	Flaking on inner side inner race
	2382	289	8.2	Suspended
	867		3.0	Suspended

Table 7 Test results of high speed durabirity

Bearing	Speed (r/min)	Running time (h)	Test result	State after test
Front non-driven wheel	326 (vehicle speed 160 km/h)	20	Suspended	n=2 No problems such as seizure
Rear driven wheel			Suspended	n=2 No problems such as seizure

4. Conclusion

NTN has been mass-producing GEN2 HURs as axle bearings for large trucks, and has recently developed a unique GEN2 HUR product that is the largest in the world. Furthermore, **NTN** is currently developing GEN3 HUR products that boast greatly enhanced reliability. We believe that these HUR products are excellent axle bearings capable of satisfying requirements for long life, improved reliability and ease-of-assembly. We expect the demand for them will steadily increase in Japan. **NTN** is also mass-producing HURs for driven wheels for rear semi-floating axles on compact commercial vehicles. We intend to supply various HUR products to satisfy user needs.

Photos of authors

Hiroshi KAWAMURA

Automotive Sales Headquarters
Automotive Engineering Dept.

Akira FUJIMURA

Automotive Sales Headquarters
Automotive Engineering Dept.

The Auto-tensioner Market and Technical Trends

Satoshi KITANO*
Tadahisa TANAKA*
Tomokazu NAKAGAWA*

Automotive engines generally use accessory drive belts, timing belts, or timing chains to transmit crankshaft rotation to the camshaft and accessories. An auto-tensioner can act to keep the tension of the belt or chain constant, and has shown to be effective at improving belt and chain life as well as reducing noise generation.

Although the cost of the system and the number of components increases when auto-tensioners are implemented, improvements in system reliability and reductions in maintenance are achieved.

Auto-tensioners are required to add constant tension, but also have damping characteristics to allow for rapid tension changes. If the driving methods of the camshaft and accessories are to improve in the future, the application of an auto-tensioner to increase life and reduce noise will be necessary. Consequently, the design of the **NTN** auto-tensioner has been improved to help reduce cost and increase reliability.

1. Introduction

To transmit the revolutions of crankshafts to camshafts and auxiliary mechanisms, ordinary automotive engines are equipped with engine components such as timing belts, timing chains and accessory drive belts. Recently, as automotive engine performance is being greatly enhanced, the requirements for their components have become increasingly demanding. In this context, auto-tensioners play an important role in extending the belts and chain service lives and in suppressing noise. This report covers technical trends related to automotive auto-tensioners.

2. Drive systems

Examples of automotive engine camshaft and auxiliary shaft drive systems are illustrated in **Fig. 1**.

Camshaft drive systems for automotive engines can be categorized into timing belt drive systems and timing chain drive systems. Both types transmit power by meshed components. Auxiliary drives systems are usually frictional transmission systems using V-belts.

In all these drive systems, auto-tensioners are placed in slack spans where the tension is lowest.

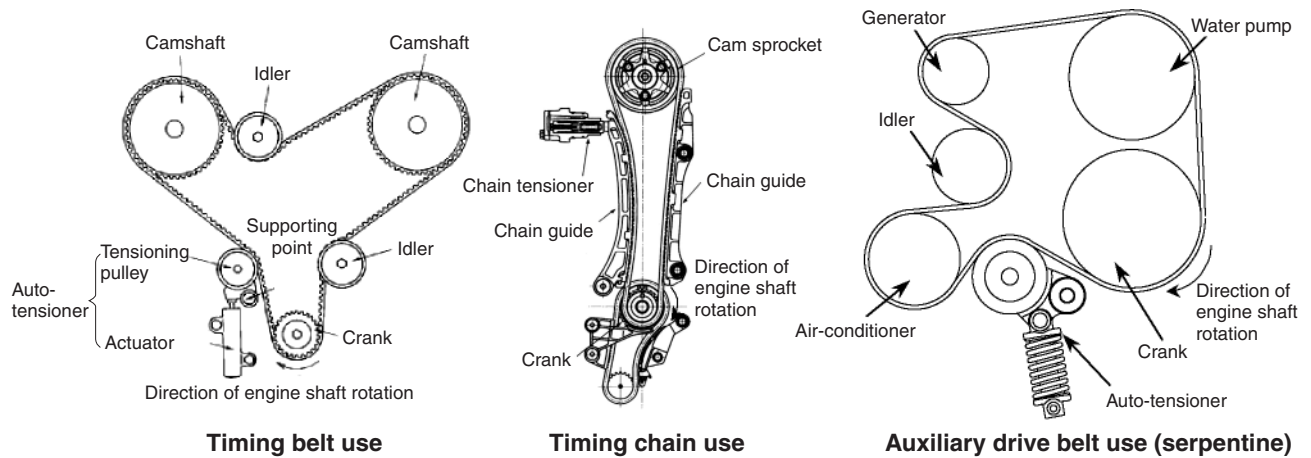*Automotive Sales Headquarters　Automotive Engineering Dept.

Timing belt use　　　**Timing chain use**　　　**Auxiliary drive belt use (serpentine)**

Fig. 1 Layout of Auto-tensioner (example)

3. History of camshaft drive systems

The first timing belt drive system in the world was used commercially in 1946 in the USA, and the first automotive application there was in 1965. In Japan, this system was first adopted in 1971. In the 1980's, this new system began quickly capturing market share from timing chain drive systems.

Through the 1970's, the timing chain drive system was the main type, but in the 1980's, timing belt systems became dominant. However, timing chain drive systems began to be adopted again in the 1990's thanks to the development of high-performance chains. The current market shares for timing chain drive systems and timing belt drive systems are about 50% each in Japan.

Fig.2 illustrates the direction of camshaft drive systems.

In the past, all accessory drive systems involved several belts. In the 1980's, though, serpentine systems began to be used in the USA. The market share for this drive system type is expanding in Japan currently.

4. Importance of auto-tensioners

Unlike conventional fixed-tensioners, when auto-tensioners are assembled into drive systems they are capable of maintaining a belt or chain tension at a constant level. This is done by absorbing variations in tension, including changes in tension due to expansion and shrinking from engine temperature changes and decreased tension resulting from drive system aging. Thus, auto-tensioners provide an effective means for extending the lives of drive belts and chains and for suppressing noise. Although, when compared with fixed-tensioner systems, adoption of auto-tensioners can lead to higher actuator valve system costs and more complicated structures auto-tensioners have significant advantages. Drive systems that use auto-tensioners boast improved reliability and greatly reduced maintenance needs.
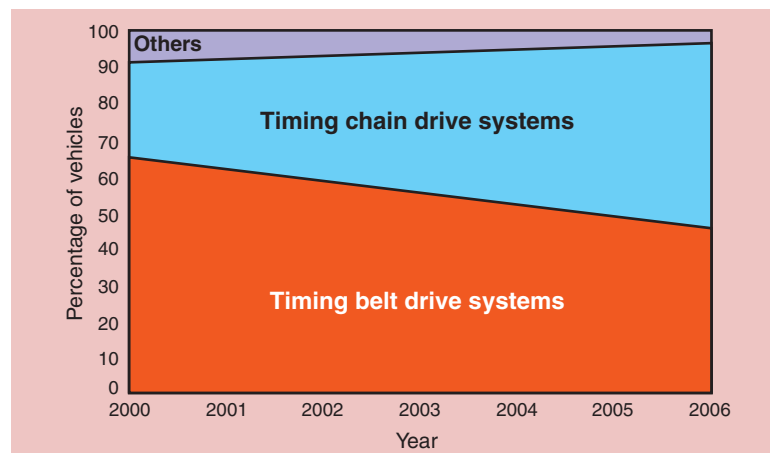

Fig. 2 Direction of a cam-shaft drive system

5. Auto-tensioner types and structures

5.1 Timing belt auto-tensioners

The actuation systems for timing belt auto-tensioners include hydraulic, screw, and friction systems. **NTN** auto-tensioners employ a hydraulic actuation system that excels in durability and tension adjustment capability to cope with temperature variations.

Fig. 3 illustrates the structure of an **NTN** auto-tensioner. The cylinder is die-cast aluminum to reduce weight.
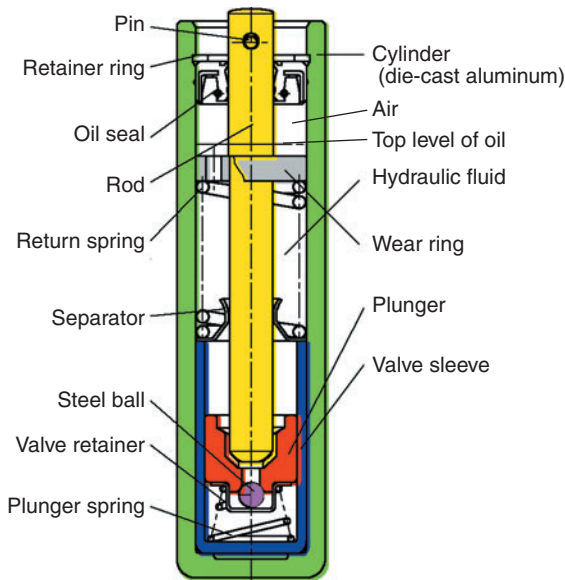
Fig. 4 illustrates various timing belt auto-tensioners.

NTN has been developing various hydraulic dampers including a standard type, a short type that is compact in the axial direction, and an ultra-compact type.

The integrated pulley-arm type is a unit design complete with a hydraulic damper and a tension pulley that reduces costs and has smaller space requirements. The built-in pulley type helps save space since the hydraulic damper is built into the pulley, and it can replace a fixed tensioner.

A performance comparison of various timing belt auto-tensioners is shown in **Table 1**.

Fig. 3 Sectional view of Auto-tensioner

Table 1 Performance comparison (for timing belt)

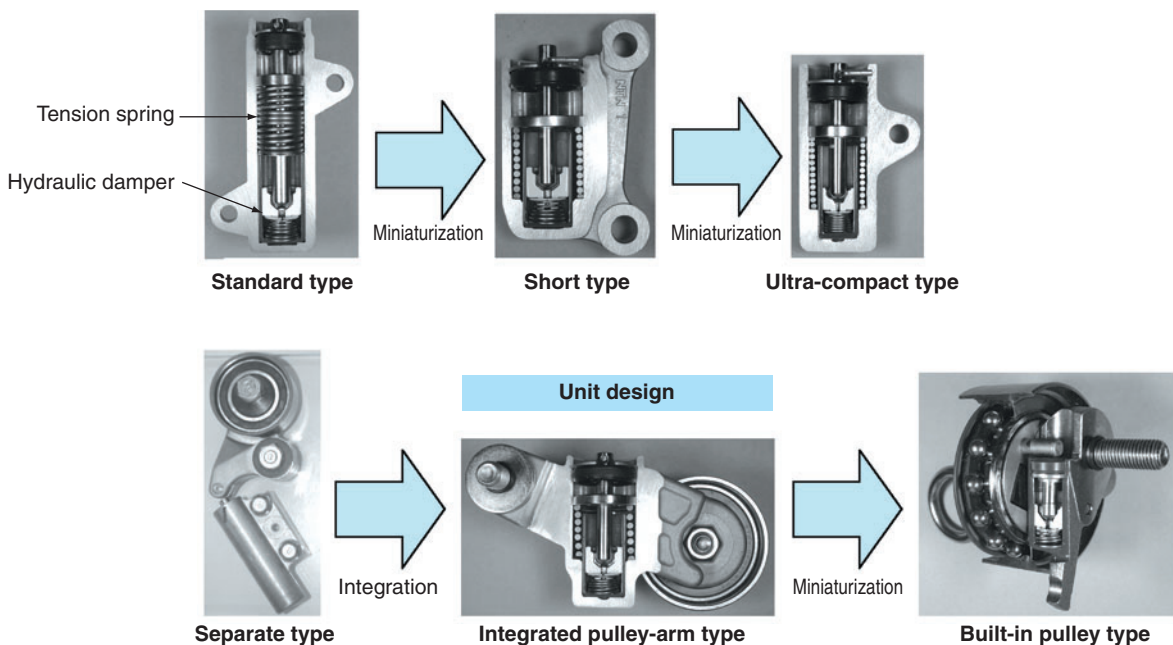|	Type	Manufacturer	Function※	Reliability	Weight	Cost
Element	Hydraulic type	**NTN**	◎	◎	◎	◎
Element	Hydraulic type	A	◎	○	○	△
Element	Hydraulic type	B	○	○	○	△
Element	Screw type	C	△	△	◎	◎
Unit	Hydraulic type	**NTN**	◎	◎	○	○
Unit	Viscosity type	D	△	○	○	△
Unit	Friction type	E	△	△	△	○
Unit	Friction type	F	△	△	◎	◎

※Tension adjustment function

Fig. 4 Various Auto-tensioner's for timing belt

NTN auto-tensioners employ a hydropneumatic construction that is free from oil leakage. However, if this type of auto-tensioner is mounted at an angle close to horizontal, the liquid can approach the pressure chamber, possibly letting air enter and leading to damper failure. Therefore, the mounting angle of this auto-tensioner is limited, and the recommended mounting angle range is ±45° from vertical.

If a greater mounting angle is unavoidable, an auto-tensioner with a reservoir is available (see **Fig. 5**).

In the design phase, we create 3D models for the cylinder and pulley bracket of the auto-tensioner to check for the possibility of interference. (See **Fig. 6.**)

Through FEM analysis techniques, we have achieved both a high level of durability and a compact, lightweight design. (See **Fig. 7**.)

5.2 Timing chain auto-tensioners

Recent camshaft drive systems employ timing chains rather than timing belts so that the whole engine length can be shortened and because reliability is high and running noise is low with timing chains.

With ordinary timing chain auto-tensioners (hereafter referred to as chain tensioners), engine oil supplied from the engine is introduced into the chain tensioner to generate hydraulic damping power. A no-back mechanism is included to prevent inward pressure before engine oil is supplied after the engine is started. No-back mechanisms can be categorized as ratchet, serrated screw, ring, and screw types.

NTN uses serrated screw and ring types. To reduce weight, die-cast aluminum cylinders are used. Mass production of the serrated screw type began in 1999, and that of the ring type started in 2003.

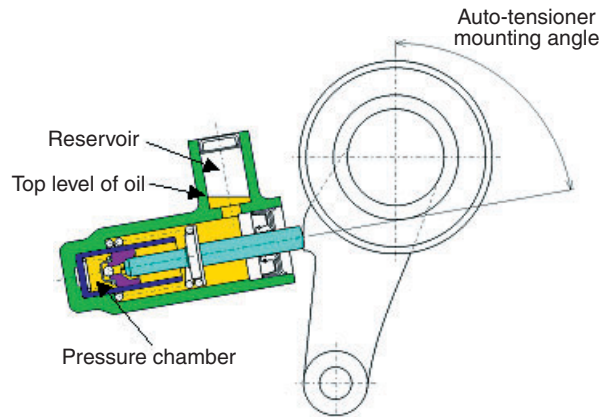The constructions of our chain tensioners are illustrated in **Fig. 8**.

Fig. 5 Auto-tensioner with reservoir room
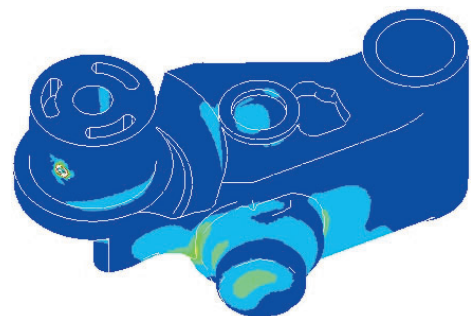

Fig. 6 3D-model
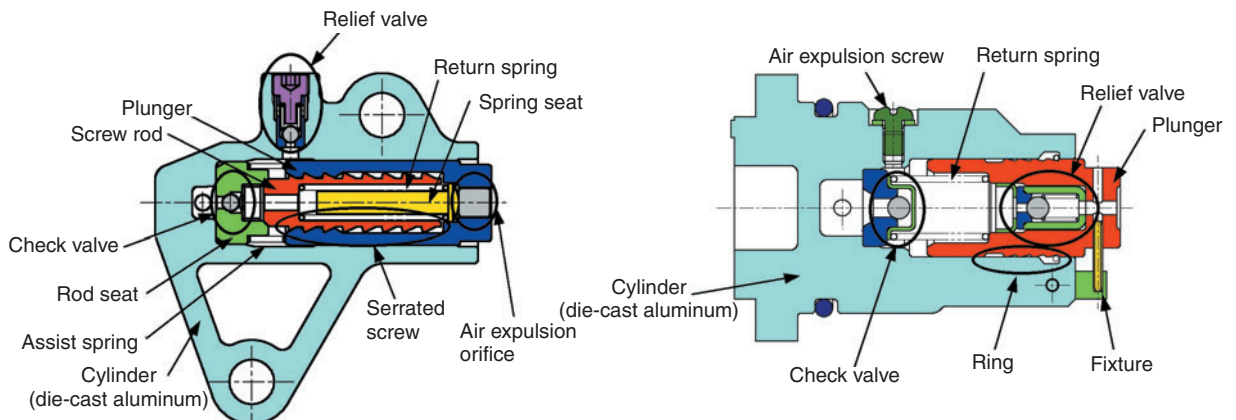

Fig. 7 FEM analysis result

Fig. 8 Various Auto-tensioner for timing chain

The results of a performance comparison of various timing chain auto-tensioners are summarized in **Table 2**.

Table 2 Performance comparison (for timing chain)

Type	Manu-facturer	Basic structure					Cost
		Damper		No-back			
Serrated screw type	NTN	Hydraulic and serrated screw	◎	Serrated screw (stage-less)	◎	△
Ring type	NTN	Hydraulic	○	Ring	○	◎
Ratchet type	A	Hydraulic	○	Ratchet	○	○
Ring type	B	Hydraulic	○	Ring	○	○
Ratchet type	C	Hydraulic	○	Ratchet	○	○
Screw type	D	Screw	△	Screw	△	△

5.2.1 Serrated screw functions

With a no-back mechanism that employs rings, there are actuation stages, and the return allowance is greater. In contrast, with serrated screw types, the no-back mechanism can function regardless of the screw position, actuation is stage-less, and the return allowance is equivalent to the backlash and can be set very small.

Unlike ordinary screws, serrated screws are constructed so that they are still when a static load is applied in the inward pressure direction, but operate swiftly in the outward direction.

The results of an investigation into the functions of serrated screws are described below.

① **Results of plunger tracking verification**

Any auto-tensioner must be able to quickly absorb changes in tension due to engine thermal expansion or due to chain or belt slackening when the engine starts.
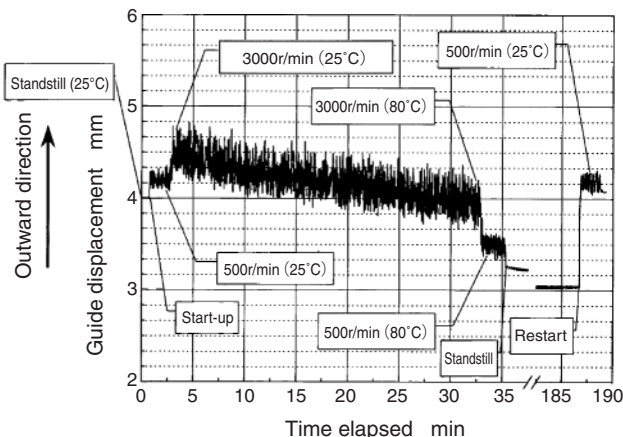
As shown in **Fig. 9**, the chain running position fluctuates greatly (the guide position changes) as the temperature and running speed vary after the engine starts. The chain tensioner clearly responds quickly to changes in the chain running position, and presses or pulls accordingly.

② **Static no-back characteristics**

When the engine is at a standstill, and if the span where the chain tensioner is present is in a tensioned state because of a phase difference between the camshaft and the valve, then the tensioner will be pressed in. Then, after the engine is started, and before the engine oil is supplied, the amplitude of vibration could be greater due to the amount of inward pressure, possibly causing abnormal noise. **Fig. 10** summarizes measured static characteristics of the no-back mechanism.

The results in this chart were obtained by allowing a static load to be applied to the plunger tip and measuring the resultant plunger displacement until a particular load was reached. Though the amount of inward pressure relative to the screw axial clearance is apparent, no further inward pressure occurred because the screw remained locked.
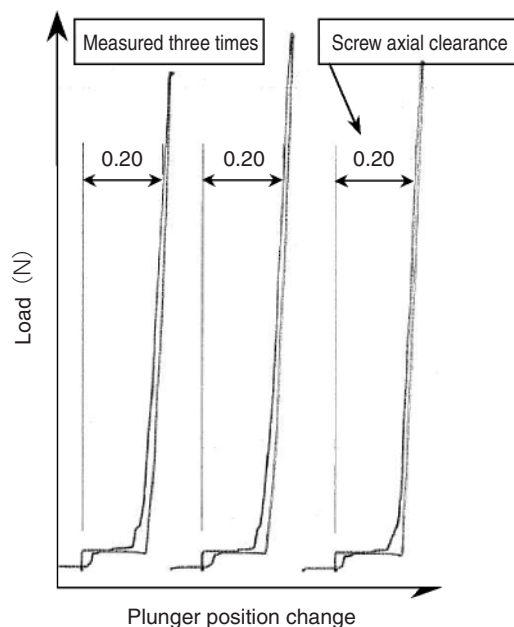

Fig. 10 Static characteristic of 'No-back' mechanism

Fig. 9 Plunger position during engine operation

③ Dynamic inward pressure characteristics

While the engine is running, the chain tensioner plunger pushes in to prevent chain snaking, but over-tensioning the chain must also be avoided.

The results of measurements of the inward pressing on the actuated chain tensioner are summarized in **Fig. 11.**

As shown in this chart, when the chain tensioner is actuated, the screw is unlocked, and the plunger is pushed in, preventing the chain from becoming over-tensioned.
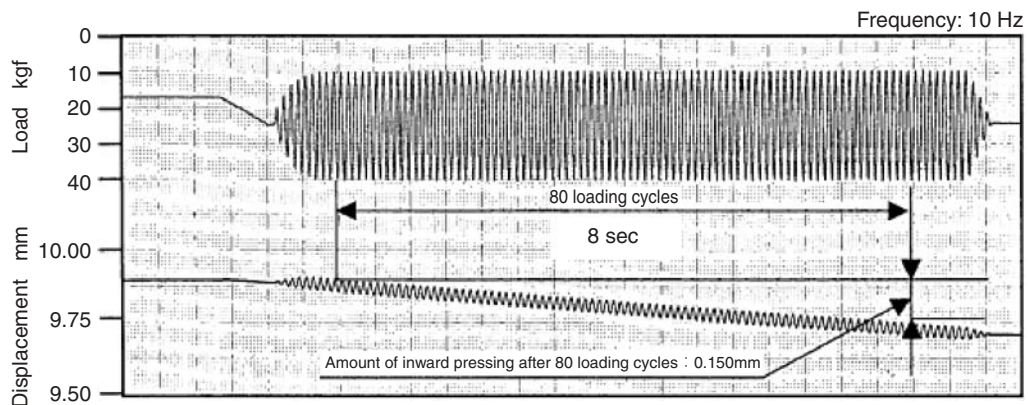

Fig. 11 Dynamic characteristic of screw plunger

5.2.2 Damper adjustment mechanism

The chain tensioner receives a varying load from the chain via a hydraulic damper. The hydraulic damper setup is optimized based on the relationship between the chain tension and the guide amplitude (plunger amplitude).

① Method for adjusting the hydraulic damper

The damping force is determined by the leak clearance and relief valve opening pressure.

The user must check the effect of the leak clearance and relief valve opening pressure in advance and optimize the tensioner reaction force settings.

② About tracking

The varying load acting on the chain tensioner is governed by the number of engine cylinders.

The currently available **NTN** chain tensioners are for four-cylinder and six-cylinder engines. With a four-cylinder engine, a rotational 2nd-order varying load is applied to the chain tensioner, and with a six-cylinder engine, a rotational 3rd-order varying load is applied. With a six-cylinder engine, the maximum vibration frequency of a varying load can reach 300 Hz. When the speed of a four-cylinder engine on a motorcycle reaches 15,000 r/min, the frequency of the varying load can reach 500 Hz. Every chain tensioner must be capable of coping with this high-frequency range.

Fig. 12 illustrates the results of response relative to vibration frequencies applied.

This graph shows that the load is generated stably to a maximum frequency of 500 Hz, and that the chain tensioner reliably responds to the varying load.
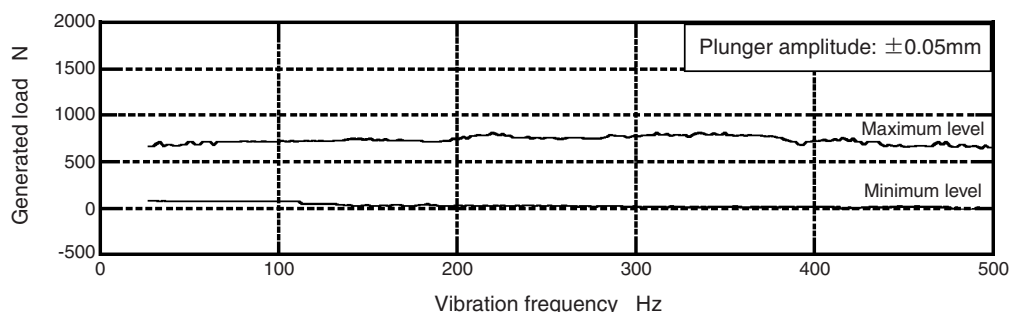

Fig. 12 Dynamic-characteristic evaluation result

5.3 Auto-tensioners for accessory drive belts

Previously, commonly employed belt tensioners used multiple belts with one or two auxiliary mechanisms driven by each belt. With this arrangement, it was necessary to adjust the tension of each belt while running the auxiliary mechanisms and turning an idler pulley and measuring the tension by observing the amount of belt sag or by measuring the belt tension with a tensiometer.

Recently, serpentine designs have frequently been used to drive all the auxiliary mechanisms with one belt because of reduced maintenance needs, ease of belt installation, reduced weight and shorter total engine length. At first, serpentine designs were used for large gasoline engines with six or more cylinders, but they have been increasingly used for gasoline engines and diesel engines with four or fewer cylinders.

However, the longer belts of serpentine systems are associated with elongation that occurs when driving the auxiliary mechanisms or as a result of aging. Therefore, an auto-tensioner must be incorporated to automatically adjust the belt length and maintain the tension at a constant level. Because belt tension changes due to variations in the load from auxiliary mechanisms and in the engine speed, the auto-tensioner must be able to provide a damping force. Insufficient auto-tensioner damping power leads to greater belt snaking or belt slip (squeaking).

Friction and hydraulic are the two types of mechanisms available for generating damping forces. **NTN** employs a hydraulic type because of its greater damping force and higher reliability.

The construction of an **NTN** auto-tensioner is illustrated in **Fig. 13**.

A performance comparison of various auto-tensioners for automotive auxiliary mechanisms is summarized in **Table 3.**

In the design phase, we developed a 3D model for assessing the shapes of pulleys and pulley brackets, checked for interference with engine-related components and performed FEM analysis to achieve both reduced weight and higher rigidity.

In order to help promote environmental conservation by improving automobile fuel economy, an idling-stop mechanism for automotive engines is available. With this scheme, the integrated starter generator (ISG) drives the accessory belt to turn the crank to restart the engine. **NTN** has been developing hydraulic type accessory belt auto-tensioners optimized for ISG engines.

We believe that the demand for hydraulic auto-tensioners will be increasing because they will enable longer drive belt life as loads from auxiliary mechanisms, including larger alternators and greater air-conditioner capacities, increase.

Table 3 Performance comparison (for accessory belt)

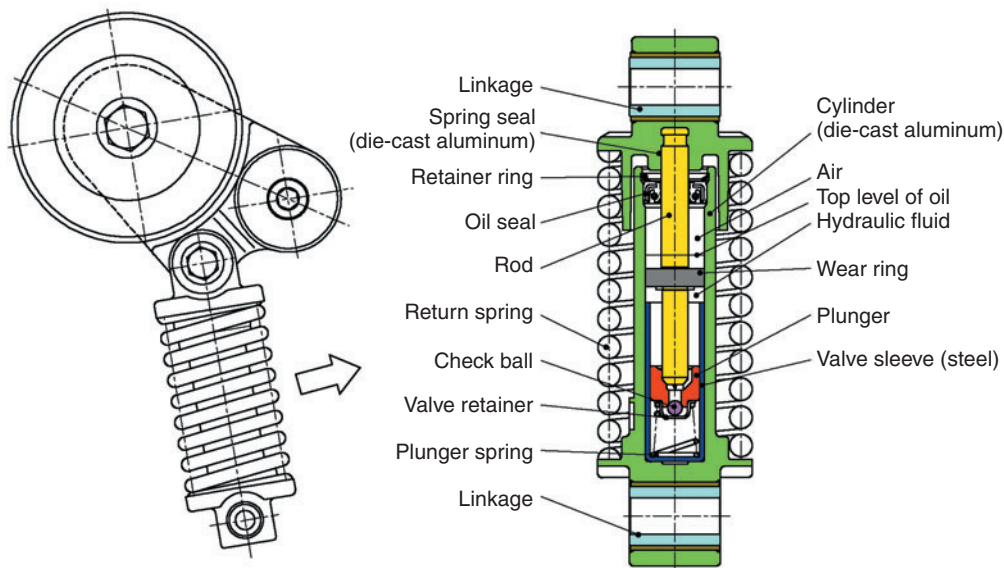| Type	Manufacturer	Function	Reliability	Weight	Cost
Hydraulic	**NTN**	◎	◎	○	○
	A	○	○	○	○
Frictional	B	△	△	◎	◎

Fig. 13 Auto-tensioner for accessory belt

6. Conclusion

We have introduced the trend for various auto-tensioners related to improved reliability in driving camshafts and accessory shafts. We are determined to develop less expensive, highly reliable auto-tensioners that feature improved functionality and construction.

References

1） Kazuki Kawashima, **NTN** Technical Review No. 61 (1992)
2） Katsumi Furutani, Kazuki Kawashima, **NTN** Technical review No. 65 (1996)
3） Satoshi Kitano, Tadahisa Tanaka, Tomokazu Nakagawa, Monthly Tribology (2004, 10)

Photos of authors

Satoshi KITANO

Automotive Sales Headquarters
Automotive Engineering Dept.

Tadahisa TANAKA

Automotive Sales Headquarters
Automotive Engineering Dept.

Tomokazu NAKAGAWA

Automotive Sales Headquarters
Automotive Engineering Dept.

[New Products Information]

Advanced Technology Deep-Groove Ball Bearings for High-Speed Servomotors

Higher speeds are capable with these prelubricated deep-groove ball bearings!

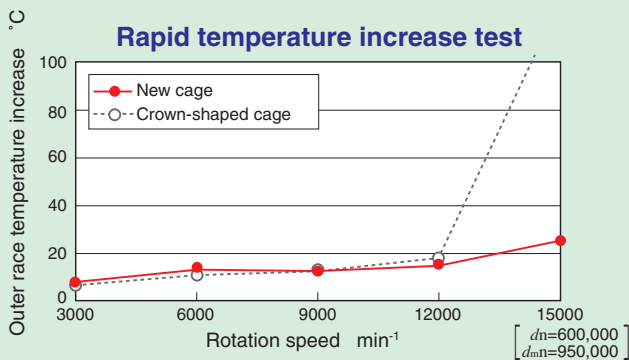### Prelubricated Deep Groove Ball Bearings
62XX and 63XX series

Capable of d_mn value 95×10^4

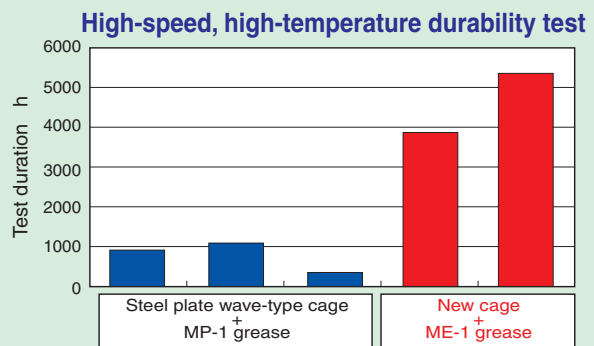Newly-shaped synthetic resin cage
High-speed, long-life grease

Features

- Optimal design improves lubrication reliability

Maintenance-free: No need to grease or clean, and usable life is three times the length

Rapid temperature increase test

- ● New cage
- ○ Crown-shaped cage

Outer race temperature increase °C

Rotation speed   min⁻¹

$$\begin{bmatrix} d_n = 600,000 \\ d_m n = 950,000 \end{bmatrix}$$

Bearing description	6308 with non-contact seals on both sides （φ40mm×φ90mm×23mm）
Grease	ME-1 grease common to both cage specifications

High-speed, high-temperature durability test

Test duration h

Steel plate wave-type cage + MP-1 grease	New cage + ME-1 grease

Bearing description	6209 with non-contact seals on both sides （φ45mm×φ85mm×19mm）
Rotation speed	Blue：n=11,111min⁻¹，Red：n=13,333min⁻¹
Bearing temperature	130°C (bearing outer ring)

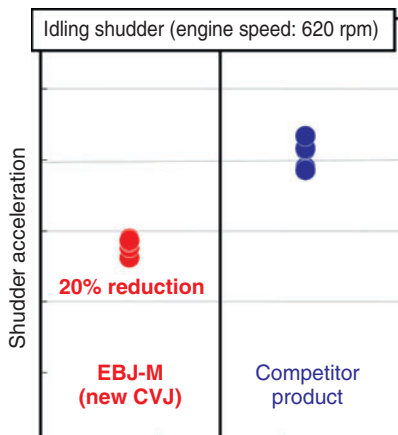# Idling Shudder-Suppressing Fixed Constant Velocity Joint

We have developed a constant velocity joint that features the lowest level of idling shudder in the world.

Features

● Compared to similar competitor products, the new NTN fixed type constant velocity joint features a 40% reduction in bending load in the operating angle direction, and a 20% reduction in actual vehicle idling shudder.

Performance

Idling shudder (engine speed: 620 rpm)

Shudder acceleration

20% reduction

EBJ-M (new CVJ)

Competitor product

Application on actual vehicle

Improvement by adoption of low slide-resistance CVJ (PTJ)

Differential gearing

Absorption by sliding

Vibration from engine

Absorption by bending

Shaft

Sliding joint

Fixed joint

By means of bending rigidity-reduced CVJ
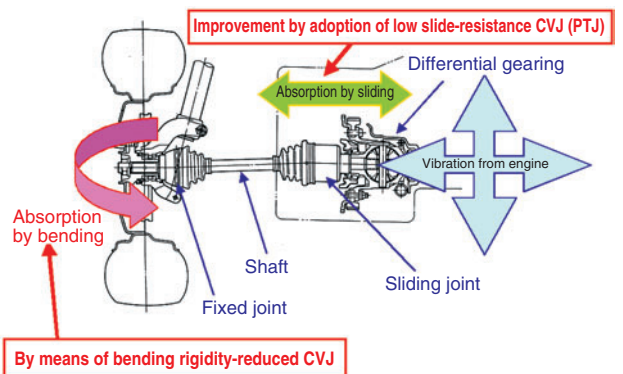
Low Profile Thrust Needle Roller Bearings

NTN has developed the world's thinnest low profile thrust needle roller bearing!
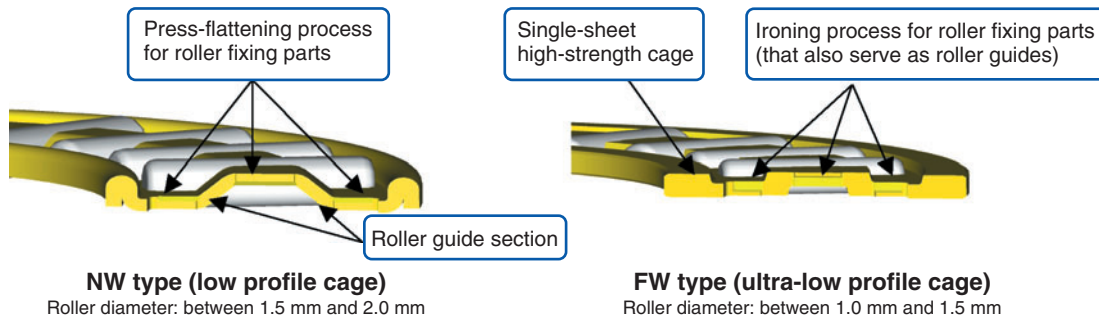

Features

● **These thrust needle roller bearings with sheet steel cages possess thicknesses as low as 1 mm, the thinnest in the world.**

Part design: The roller fixing parts of the cage were optimized to eliminate possible interference

Press-flattening process for roller fixing parts

Single-sheet high-strength cage

Ironing process for roller fixing parts (that also serve as roller guides)

Roller guide section

NW type (low profile cage)
Roller diameter: between 1.5 mm and 2.0 mm

FW type (ultra-low profile cage)
Roller diameter: between 1.0 mm and 1.5 mm

W type (conventional cage)	(New) NW type (low profile cage)	(New) FW type (low profile cage)
●No interference between the roller fixing parts on the cage and the rollers	●Interference avoided by press-flattening the pockets of the cage ●Though having the same sheet thickness as the W type cage, this bearing cage features both low profile and increased strength	●Interference is avoided by ironing the cage pockets ●The single sheet form has a low profile, as well as higher strength from increased thickness
Roller diameter: 2.0 mm	Roller diameter: 1.5 mm	Roller diameter: 1.0 mm
Sheet thickness: 0.4 mm	Sheet thickness: 0.4 mm	Sheet thickness: 0.7 mm
(Cage strength) 1.0	(Cage strength relative to W type) 1.3 ● Reduction of moment load at stress concentration areas by low profile design	(Cage strength relative to W type) 3.0 ● Reduction of moment load at stress concentration areas by increased sheet thickness and low profile design

S-TITAN™ Series of Self-Aligning Roller Bearings

Sets new standards with longest life and greatest load capacity in the world!


Features

● High temperature long-life bearing steel that was developed with consideration for the global environment has been adopted for the standard series of self-aligning roller bearings. The internal design of the bearing employs a center-rib free inner race and symmetrical rollers.
   ● Long life in ordinary to high temperatures
   ● Strong resistance to surface failure
   ● Better dimensional stability at higher temperatures
   ● Increased crack fatigue strength
   ● Simplified replacement inventory management
Optimization of internal design and surface finish ensures consistent high performance.

High temperature life

Test conditions
Test temperature:
   200˚C
Test piece:
   dia. 47×7 mm
   flat plate
Contact stress:
   5.5 GPa
Load frequency:
   3000 r/min
Lubrication:
   Ether oil
   (oil bath)

More than 30 time longer

No. of load (cycle)

Current   S-TITAN™
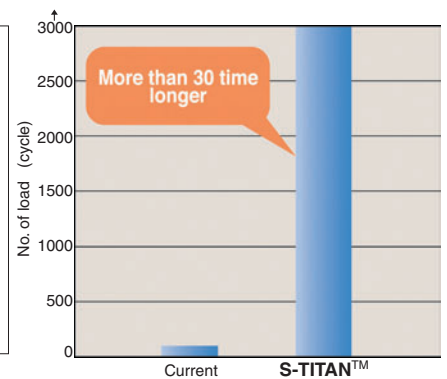
Load capacity comparison (dynamic load rating) with competitor product

(%) 160

Comparison of dynamic load ratings (NTN/Company A)

World-greatest dynamic load rating

■ 222
▲ 223
■ 240
◆ 241

Bore, mm
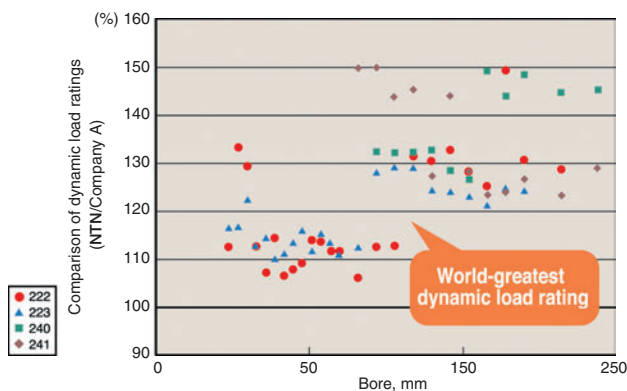
Ordinary temperature life

Test conditions
Test bearing:
   22208
   (dia. 40×dia. 80×23)
Test load:
   Dynamic load
   rating ratio = 0.5
Rotation speed:
   2000 min⁻¹
Lubrication:
   Turbine oil
   (oil bath)

World-longest life

Life (h)

Current   Company A   S-TITAN™
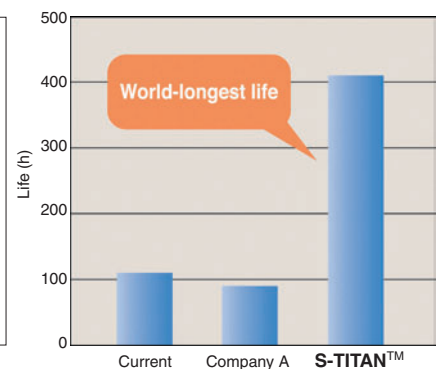
Bearing with Magnetic Field Resistant Rotary Sensor

## Magnetic field resistance: three times that of previous products

Features

- Sensor can be built into a high-torque motor, allowing very compact systems
- Sensor rarely malfunctions even in environments with strong external magnetic fields
- Built-in sensor allows greater compactness and easier assembly
- Sensor can detect rotation even at speeds near 0 rpm
- Sensor output signal can be mathematically processed, allowing calculation of rotational angle and velocity and detection of rotational direction
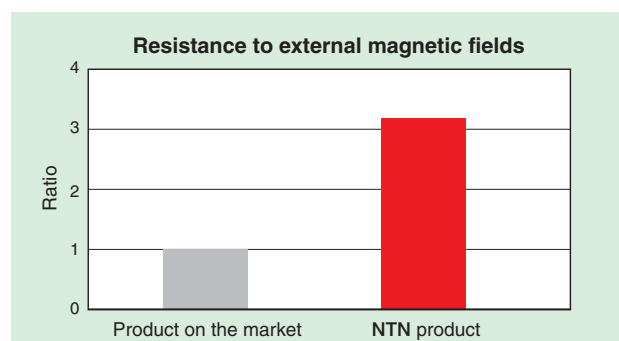
Structure

Magnetic sensor

Magnetic encoder

Performance

Resistance to external magnetic fields

Specifications

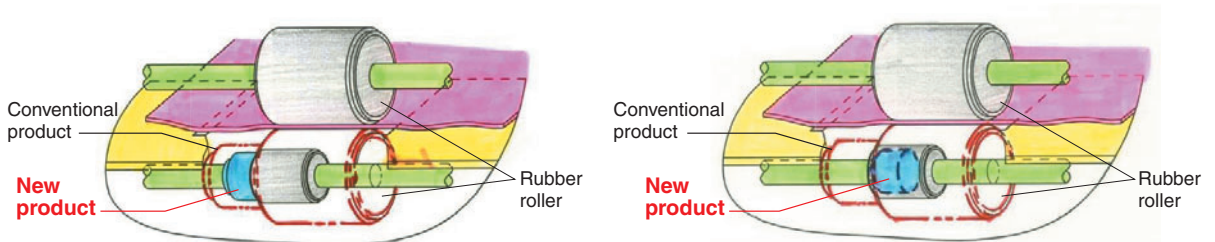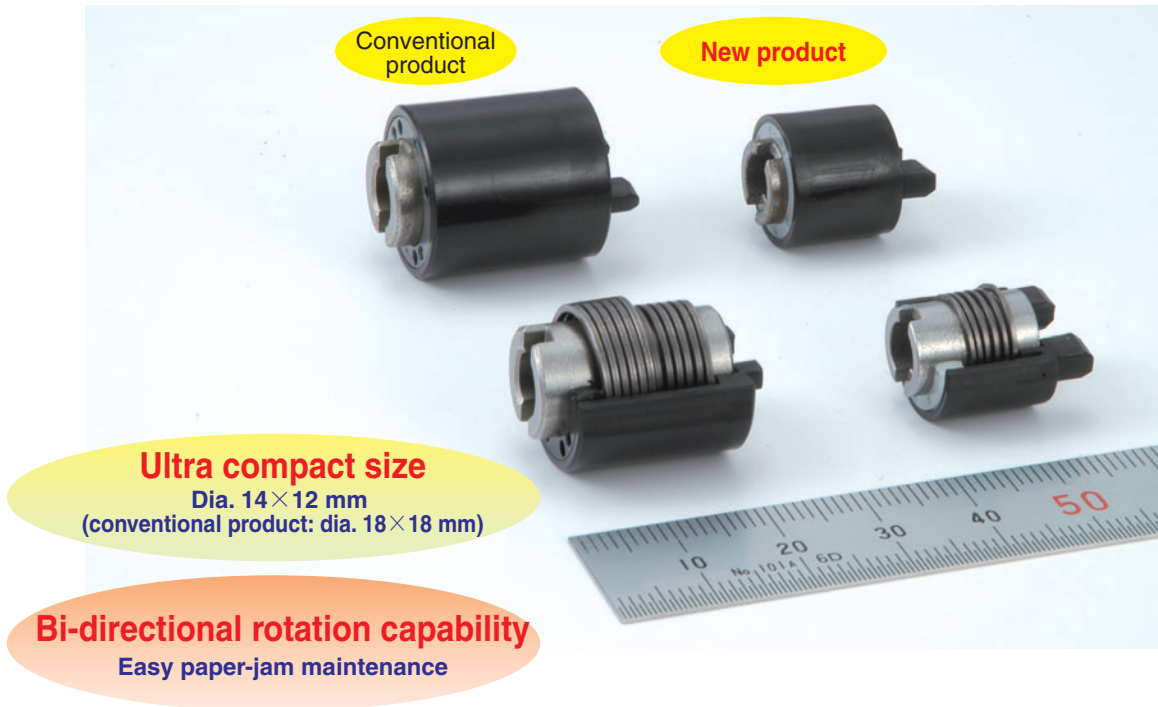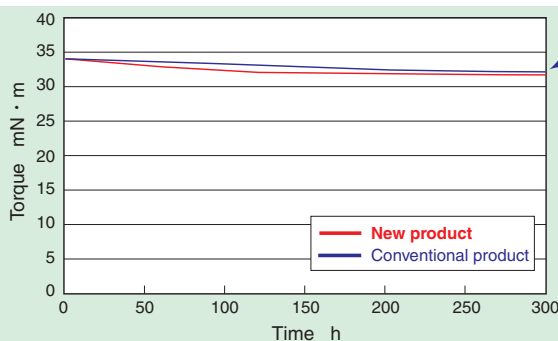|	
Supply voltage	5～24V, DC
Allowable temperature range	−40˚C～120˚C
Output types	Rectangular wave, open-collector
	Phases A and B
Applicable bearing numbers	6202～6209
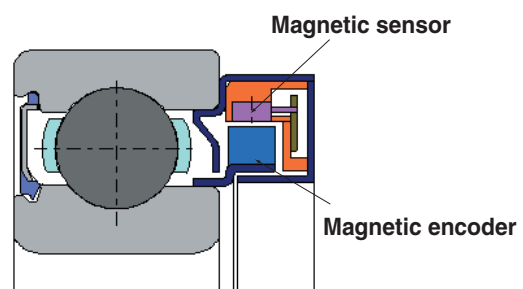
"Ultra" Compact Torque Limiter for Office Automation Equipment

First in the bearing industry! Development of an ultra compact size of dia. 14✕12. Great space savings in office automation equipment.

Conventional product

New product

Ultra compact size
Dia. 14✕12 mm
(conventional product: dia. 18✕18 mm)

Bi-directional rotation capability
Easy paper-jam maintenance

Conventional product

New product

Rubber roller

Conventional product

New product

Rubber roller

Rubber roller diameter can be made smaller and the axial direction more compact (red line shows a conventional torque limiter).

NTN's new torque limiter can be built into rubber rollers, allowing reduction of the number of components (blue area shows NTN''s new torque limiter).

Performance

Torque stability is equivalent to that of conventional products

— New product
— Conventional product

Torque mN・m (y-axis: 0 to 40)
Time h (x-axis: 0 to 300)

<**Test conditions**>
Temperature: Ambient / room temperature
Operation pattern: Actuation for 1.1 seconds and no motion for 0.2 seconds
Rotation speed: 220 min⁻¹

-123-

RustGuard™ Highly Corrosion-Resistant Bearing for Steelmaking Machinery

Special coating improves bearing corrosion-resistance and extends life to 3.5 times that of conventional products.


Features

● **Longer bearing life with improved corrosion resistance**

With our newly developed coating technique that forms a special manganese phosphate film, we have succeeded in creating a protective film that is two to three times thicker than that attained with other bearing products. In situations where corrosion (such as roller mark rusting*) can occur, RustGuard bearings boast a life 3.5 times longer than conventional bearings.
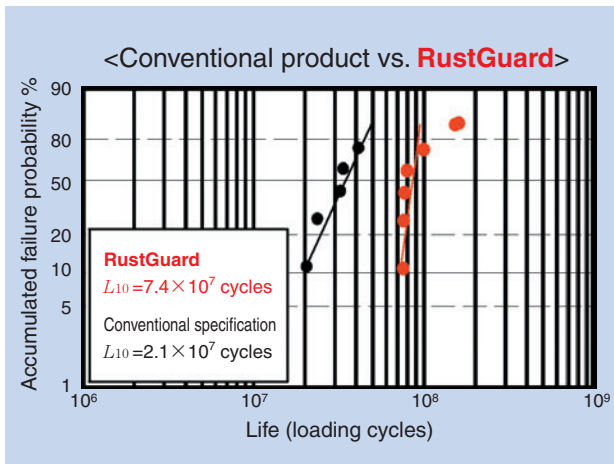
***Roller mark rusting**: Each roll neck bearing on a rolling machine is left stationary water present on it during roller maintenance work. As a result, streak-patterned axial rusting occurs at equal intervals (roller-to-roller pitches) on the raceway surfaces on inner and outer races. This phenomenon is called "roller mark rusting."

Roller mark rusting

Flaking

Evidence of bearing failure on actual machinery
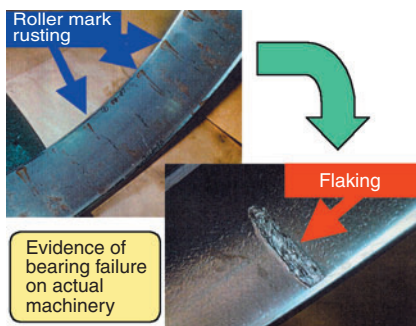
Application

● **Use in steelmaking and papermaking machinery parts that are exposed to water**

Results of failure mode reproduction test on actual machines

<Conventional product vs. **RustGuard**>

Accumulated failure probability %

RustGuard
$L_{10} = 7.4 \times 10^7$ cycles

Conventional specification
$L_{10} = 2.1 \times 10^7$ cycles

Life (loading cycles)
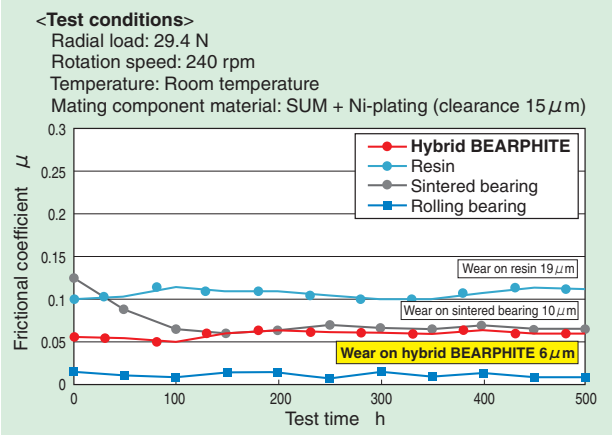
Hybrid BEARPHITE Bearings

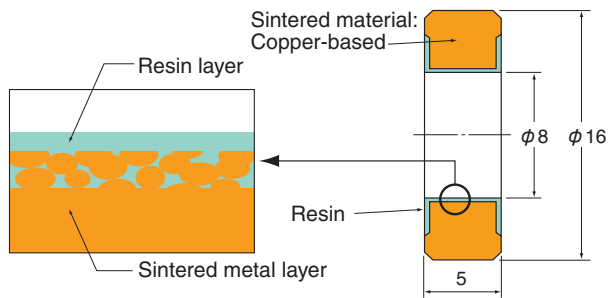## Hybrid structure of resin and sintered metal achieves low friction, high precision and quiet running!

Features

- Low friction (μ = 0.05)
- Higher precision than ordinary resin bearings
- Quieter running compared with rolling bearings
- Capable of carrying an axial load
- Can be applied to an aluminum shaft

## Performance (frictional characteristics for carrying radial loads)

<Test conditions>
Radial load: 29.4 N
Rotation speed: 240 rpm
Temperature: Room temperature
Mating component material: SUM + Ni-plating (clearance 15 μm)

Frictional coefficient μ

- Hybrid BEARPHITE
- Resin
- Sintered bearing
- Rolling bearing

Wear on resin 19 μm
Wear on sintered bearing 10 μm
Wear on hybrid BEARPHITE 6 μm

Test time   h

Structure

Sintered material: Copper-based
Resin layer
Resin
Sintered metal layer

ϕ8 ϕ16

5

Dimensions

	Bore diameter	Bearing outside diameter	Length	Roller bearing number
1	ϕ 6	ϕ 12	4	**WBC6-12ZZA**
2	ϕ 8	ϕ 12	3.5	**W678ZZA**
3	ϕ 8	ϕ 16	5	**W688ZZ**
4	ϕ 10	ϕ 15	4	**W6700LLFV4**

Mono-Drive Two-Way Feeder™

Breakthrough two-way feeding unit achieves parts storage, aligning and feeding functions in one linear feeder!
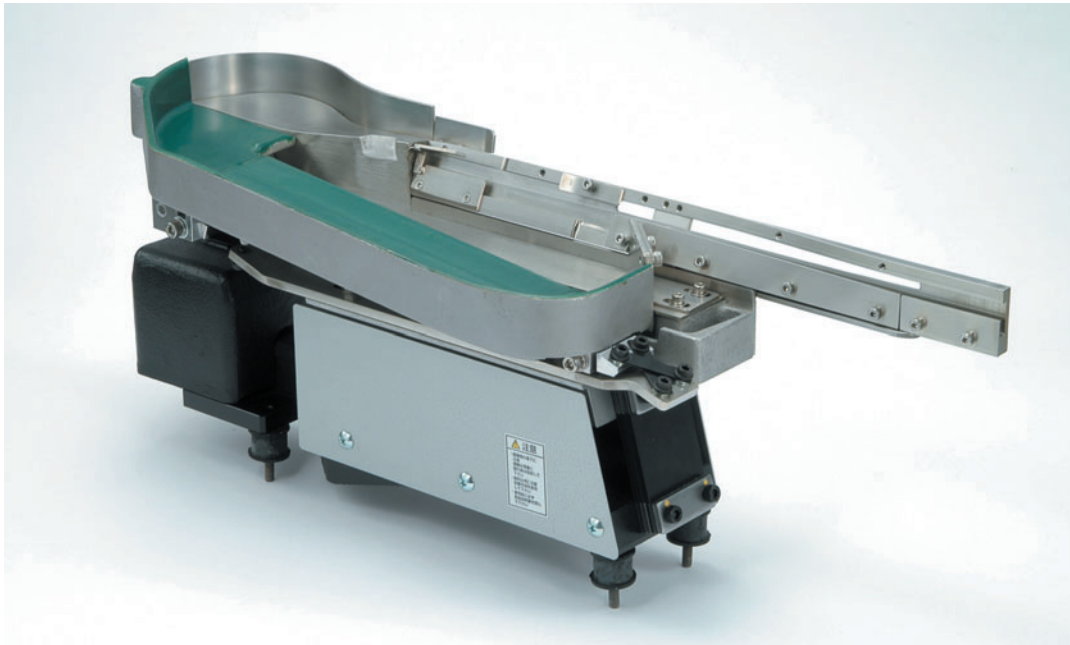
Features

● **Single linear feeder drives two chutes: one for aligning/feeding and one for returning**

This novel return feeder is comprised of a newly developed leaf spring unit installed on a conventional linear feeder to generate inclined vibration in two dissimilar directions and achieve parts feeding and aligning. (Patent pending)

● **Space saving and lightweight**

Compared with conventional bowl feeders, this linear aligning feeder is simple and compact, requiring less than half the floor space. Since this single linear feeder unit is capable of storage, aligning and feeding, it can contribute to overall equipment weight reduction.

● **Simple construction makes it the optimum choice for handling multiple work piece types and small lot production**

The simple construction allows easier maintenance. The feeder can handle multiple work piece types by simply installing chutes that are suitable for the work pieces handled.

Plan view

Bowl system (conventional)

Mono-drive two-way feeder
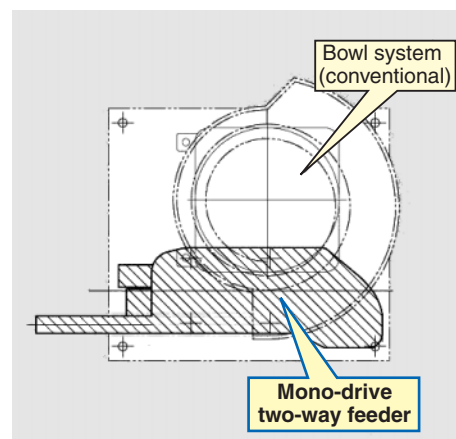
Applications

This feeder is capable of handling various small or medium-sized work pieces, including machine components, electronic components and plastic parts.

Ultra Compact Grinding Sludge Solidification System

Low power consumption, easy operation, and environmental impact alleviation!

Features of ultra compact type

- **Floor space required (approx. 0.8 m²) is 40% that of the compact type (approx. 2 m²)**
- **Size allows for direct connection to a machining line or a grinding machine**
- **Capable of handling amounts of delivered sludge as small as 10 kg/h**
- **Very economical at 50% the cost of, and using less power than, the compact type**

Benefits from adoption of the ultra compact type (equivalent to conventional systems)

- **Cost reduction by recycling and reuse of oil-based coolant**
  Grinding liquid recovery ratio of 90% or higher
- **Reduction of industrial waste emissions**
  Capable of reducing sludge volume to 20% and weight to 55%
- **Reduction of waste transportation and landfill disposal expenses**

Capacity and applications by type

Both types can be used according to needs.

Type	Handling capacity for liquefied grinding sludge	Applications
Ultra compact	10 kg/h (1.8 ton/month)※	Local processing (easy direct connection to grinding sludge filtration systems)
Compact	20 kg/h (3.6 ton/month)※	Centralized processing, batch processing

※These values were obtained by assuming that the equipment is operated 8 hours per day, 22 days per month.

Dimensions and weight of ultra compact type

Dimensions: W1,000×D800×H1,530 (mm)
Weight: 1 ton